Towards Magnetic Resonance Imaging for Detection of Nerve Agent Adducts

by Viliyana Lewis

A thesis submitted to the University College London for the degree of Doctor of Engineering

May 2023

I, Viliyana Georgieva Lewis confirm that the work presented in this thesis is my own. Where information has been derived from other sources, I confirm that this has been indicated in the thesis.

"Somewhere, something incredible is waiting to be known."

Carl Sagan

Abstract

Nerve agents are the deadliest class of chemical warfare agents known to mankind. Currently, detection techniques such as LC-MS are readily available, however real-life cases have shown that these detection methods take too long considering the severity of nerve agent poisoning. Magnetic Resonance Imaging (MRI) is a non-invasive technique which could offer an alternative approach to nerve agent detection and this thesis seeks to explore the possibility of such sensing using MRI. A range of analytical techniques were utilised to investigate binding of oxyanion analogues of nerve agent adducts to a Gd^{3+} metal centre in a chelate. Furthermore, amplification of the MRI signal of Gd^{3+}−doped nanomaterials, based on porous silica nanoparticles was investigated using NMRR. Finally, inorganic ligands proposed to bind phosphotyrosine residues were synthesised and their binding to sarin- and cyclosarin-tyrosine adducts was tested using MRI. We discovered weak binding interactions between the contrast agent Gd^{3+}–DOTA and an excess of oxyanions, such as tyrosine, ibuprofen, and lysine. Interestingly, phosphate and phosphoserine showed a formation of a second hydration sphere instead, which led to increase in relaxivity. The addition of mesoporous silica nanoparticles (MSNs) incorporating Gd^{3+}–DOTA, to excess lysine resulted in significant increase in relaxivity, which resulted in amplification of the detection response (signal increased from 40 mM^{-1} s^{-1} to 59 mM^{-1} s^{-1}). The final part of this project sought to directly observe interactions between nerve agent adducts (produced by Dstl) and

Gd^{3+}chelates, incorporating aromatic groups in their structure. We demonstrated that the presence of G-type nerve agent adducts causes a significant modulation of the MRI signal arising from Gd^{3+} chelates in very short timescales.

In conclusion, this work offers a powerful alternative method for the detection of nerve agent poisoning which can easily be used by both – scientists at Dstl and healthcare professionals.

Impact Statement

Currently, detection of nerve agent poisoning takes minimum two to three days, resulting in delayed treatment and reduced chances of survival for victims, as well as secondary poisoning in medical and police personal. This is because the current detection techniques, namely liquid chromatography-mass spectrometry (LC-MS) and gas chromatography-mass spectrometry (GC-MS) require lengthy sample preparation, specialised equipment available only in research laboratories, as well as an expert data interpretation.

Our work aims to improve the detection approach of nerve agent poisoning, addressing specifically G-type nerve agents with the potential to expand the novel detection technique to other nerve agent classes. Magnetic resonance imaging (MRI) requires little-to-no sample preparation. The spectral acquisition as well as data interpretation are much less time consuming than traditional methods and will provide a robust initial nerve agent poisoning detection. Furthermore, MRI machines are available in most hospitals in the UK and around the world offering the possibility to expand this detection technique globally and offering the possibility of immediate detection at the site where victims are most likely to be taken first – hospitals. The ability of MRI detection of nerve agents through protein adducts as biomarkers also allows for retrospective detection which can be used as evidence in subsequent court cases.

This means that our novel method can serve as both a first line of defence by detecting poisoning immediately, as well as retrospective detection to bring the offensive parties to justice. Abrupt detection means timely treatment of victims, as well as enabling the placement of appropriate control measures, reducing the chances of secondary poisoning. This will significantly increase chances of survival, and subsequent life quality. Because our detection offers a simple on/off switch visual inspection as well as the quantitative evaluation through relaxivity, non-specialised staff can visually inspect the data and determine whether or not nerve agent poisoning has taken place. This will reduce stress amongst medical personal which currently have no way of identifying nerve agent poisoning victims as proven by recent cases in the UK.

Acknowledgements

I would first and foremost like to thank my supervisor Dr Gemma Louise Davies, who believed in me from the moment of my first interview. She gave me the amazing opportunity to work on something I am really passionate about, and was not only my supervisor, but also my mentor. Dr Davies shared her expertise and knowledge but also gave me space to explore my own research ideas and independent thinking. I am immensely grateful, fortunate, and honoured to have had such a great EngD supervisor.

Secondly, I would like to address all members of Davies Group, especially Dr Aaron King, who was always supportive of me and provided training on our equipment, including the bench-top relaxometer Frankie. I would like to thank Marwa and Connor for being there for me as an emotional support as well as for anything to do with silica nanoparticles. And of course, all other members of Davies Group for the great time!

I would also like to thank Shreya for the training on the glove box and all the cups of coffee together.

I would like to thank Saeed from Security, who always said 'hello' and 'goodbye' and these small greetings made a difference during a lot of hard days. I would like to thank Tony from Stores for all the problem solving around orders, the humour and our little chats that often brightened my day.

I would like to thank Martyn Towner from Turner lab for the technical support with talking through complex experimental set up. I would also like

Abbreviations

Ach   – acetylcholine (neurotransmitter)

AChE   – acetylcholinesterase (enzyme)

ADP   – adenosine diphosphate

ADC   – analogue-to-digital converter

AMP   – adenosine monophosphate

ANOVA   – analysis of variance

APTES   – 3-aminopropyltriethoxysilane

ATP   – adenosine triphosphate

B_0 – external magnetic field used during magnetic resonance

B_1 – external magnetic field at 90° to B_0

BChE   – butylcholinesterase (enzyme)

BJH   – Barret–Joyner–Halenda (method)

CA   – contrast agent (MRI)

cAMP   – cyclic adenosine monophosphate

CDEPAT   – U.S. Army's Chemical Defence Equipment Process Action Team

CIP   – ciprofloxacin

CTAB   – cetrimonium bromide

CWA   – chemical warfare agent

DCP   − diethyl chlorophosphite

DLS   – dynamic light scattering (characterisation technique)

DMF   − dimethylformamide

DMSO   − dimethylsulfoxide

DOTA   – 1,4,7,10-tetraazacyclododacane-1,4,7,10-tetraacetic acid (ligand)

DOSY   − diffusion ordered spectroscopy

DSTL   – Defence Science Technology Laboratories (Porton Down)

DVLO   − Derjaguin, Verwey, Landau and Overbeek (theory)

EDX   − Energy Dispersive X-Ray Analysis

FFC NMR   − fast-field cycling nuclear magnetic resonance

FID   − free induction decay

FISP   − fast imaging with steady-state free precession

GA   – tabun (nerve agent)

GB	– sarin (nerve agent)
GC	– gas chromatography
GD	– soman (nerve agent)
GF	– cyclosoman (nerve agent)
GRE	– gradient echoes
HPLC	– high-performance liquid chromatography (characterisation technique)
HRP	– horseradish peroxidase
HSA	– human serum albumin
ICP–AES	– inductively coupled plasma atomic emission spectroscopy
IMPA	– Isopropyl methyl phosphonic acid (biomarker)
IR	– infrared spectroscopy; also, inversion-recovery (pulse sequence)
IS	– inner sphere of a co-ordination complex
J	– energy transition (spectrofluorimetry)
K_A	– association constant (equilibrium binding)
k_D	– dissociation constant (binding)
KF	– potassium fluoride
LC	– liquid chromatography
LC-MS/MS	– tandem liquid chromatography – mass spectrometry (two linked mass spectrometry detectors)
Ln	– lanthanide (any of the series)
MCM–41	– mobile composite material 41 (type of silica nanoparticles)
MPO	– myeloper-oxidase
MRI	– magnetic resonance imaging
MRM	– multiple reaction monitoring (from mass spectrometry)
MSNs	– mesoporous silica nanoparticles
M	– net magnetisation
M_0	– the maximum value of the net magnetisation in the z-direction
m/z	– mass-to-charge ratio
NA	– nerve agents
NHS	– N-Hydroxysuccinimide
$N_{LOWER/UPPER}$	– energy states (Boltzmann)
NMR	– nuclear magnetic resonance (characterisation technique)
NMRD	– nuclear magnetic resonance dispersion

NMRR   – nuclear magnetic resonance relaxometry

NP   – nanoparticles (general)

OP   – organophosphates (nerve agents)

OPCW   – Organisation for the Prohibition of Chemical Weapons

OS   – outer sphere of a co-ordination complex

PDI   – polydispersity index (statistics)

POSS   – polyhedral oligomeric silsesquioxane

PPE   – personal protective equipment

PS   – phosphoserine

R.T.   – room temperature

R_1 – longitudinal relaxation rate during magnetic resonance (s^{-1})

R_2 – transverse relaxation rate during magnetic resonance (s^{-1})

r_1 – longitudinal relaxivity during magnetic resonance (mM^{-1} s^{-1})

r_2 – transverse relaxivity during magnetic resonance (mM^{-1} s^{-1})

RCF   – relative centrifugal force (in a centrifuge)

RBC   – red blood cells

RF   – radiofrequency

RIME   – receptor-induced magnetisation effect

SAP   – square antiprism

SBM   – Solomon-Bloembergen-Morgan

SF   – spectrofluorimetry

SPD   – solid phase derivatization (chemical process)

SS   – second sphere of a co-ordination complex

T_1 – longitudinal relaxation time constant during magnetic resonance (s)

T_2 – transverse relaxation time constant during magnetic resonance (s)

TEM   – transmission electron microscopy

TEOS   – tetraethyl orthosilicate

TGA   – thermogravimetric analysis

THF   – tetrahydrofuran

TLC   – thin layer chromatography

TOCSY   – total correlation spectroscopy

TR   – repetition times (in a pulse sequence)

TSAP   – twisted square antiprism

Tyr−OP   – phosphotyrosine

UV-Vis   − ultraviolet visible (spectroscopy)

VR   – nerve agent from V-series, prototype for the series of Novichok agents.

VX   – nerve agent from V-series, "venomous agent X"

WWII   – world war two

Table of Contents

Table of Figures

1 Introduction

1.1 Nerve agents

1.1.1 Short History of Nerve Agents

The discovery of nerve agents emerged from the discovery of organophosphorus compounds by the German scientist Dr Willy Lange and his PhD student Gerda von Krüger in 1932. Dr Lange's original research was based on fluorine chemistry. He proposed that fluorine could be used as a pesticide due to its mildly toxic properties and patented the idea in 1930. In 1932 Gerda von Krüger joined Dr Lange's research and started working on phosphorus chemistry. More specifically, their research focused on the organophosphorus compounds, where two of the valence electrons of phosphorous have formed a double bond with an oxygen and the other three were available for organic modification. They soon noticed that these compounds can be toxic in very small amounts. They had a "pleasant aromatic odour", however caused difficulty breathing, high sensitivity to light (possibly due to miosis, constriction of the pupils) and blurred vision. Seven years after they started their research, Dr Lange had to emigrate to the United States because his wife was Jewish, and the Nazi government held this against him. He had to leave academia and his research and worked in a soap and detergent factory.

The compounds Dr Lange made got the attention of a young scientist in the Bayer division of IG Farben when he was assigned to work on pesticides. His name was Dr Paul Gerhard Heinrich Schrader, and he synthesised over 2, 000 organophosphorus compounds. His original research was based on organic compounds containing sulfur and fluorine. His fluorinated candidates for pesticides were toxic, however they were also strong irritants and so he started experimenting with the new class of compounds – organophosphates, building upon Dr Lange's research. In November 1936 he incorporated cyanide, which was the already toxic, into the organophosphate frame and accidently discovered tabun (**Figure 1.1**). Driving home after the synthesis Schrader felt acutely ill and suffered from shortness of breath and miosis. He was hospitalised for several weeks, not knowing that what he experienced were typical symptoms of nerve agent poisoning.[1] Symptoms of nerve agent exposure include mild loss of muscle control such as miosis, tightness in the chest, runny nose, nausea, salivation and loss of consciousness. This can quickly escalate to respiratory distress, bradycardia (slow heart rate) and vomiting. High dose exposure left untreated can lead to death by asphyxiation (lack of oxygen) or cardiac arrest.
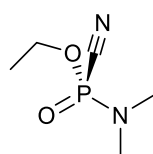
Figure 1.1 *Chemical structure of the nerve agent tabun.*

Upon return from the hospital Paul Schrader tested to see exactly what he had synthesised. He submitted a sample for routine toxicology test he used to do for all his pesticide candidates and the results came back disappointing – the substance was so toxic that it would kill not only the pesticides but also workers who tried to use them. Tabun got the attention of the military and Paul was asked to disclose the synthesis to them and help with scale up. Next, Paul Schrader was sent home for few months and then assigned to a different laboratory at IG Farben. He was asked to continue his work on organophosphorus pesticides and report to management if he discovered another toxic chemical.

In late 1938 Schrader discovered Sarin (**Figure 1.2**). He incorporated a fluorine into the organophosphorus framework by combining the new class of compounds with the old chemistry he used to investigate. Sarin was originally named "substance 146" in Schrader's lab books. It was superior to tabun in every single way, including toxicity. In the unclassified German documents, it was called "Trilon 146" after a detergent that was produced in IG Farben. In the secret Nazi files, it was called Sarin. Sarin is an abbreviation from <u>S</u>chrader, <u>A</u>mbros, <u>R</u>ittler and von der L<u>in</u>de (Foreign Office 1031/105 Schrader interrogation, available in Kew Archives).[1] Otto Ambros ('A' in Sarin) was an executive in IG Farben and later on led the mass production of nerve agents at factory close to Dyhernfurth. Rittler and von der Linde were government officials who worked in Spandau (gas protection laboratory, offence/defence of Germany at the time).[1]
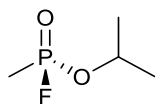
***Figure 1.2** Chemical structure of the nerve agent Sarin.*

1.1.2 Toxicity of Sarin

In order to understand the toxicity of nerve agents, a few definitions are summarized in **Table 1.1**. Detailed information on the toxicity of tabun and sarin are shown in **Table 1.2**. In short, Sarin requires half of the lethal vapor concentration of Tabun to be inhaled to cause lethal effects (ICt_{50}). Concentration vapour as little as less than a drop of Sarin per cubic meter of air (64 μL, 70 mg/ m^3) could kill in one minute. Similarly, the estimated values for lethal dose absorbed through the skin is 10 grams of Sarin vapor per cubic meter of air causing death in 1 min *vs* 15 grams of vapor/m^3 for Tabun. Mild symptoms could appear only after 0.5 mg-min/m^3 of vapor for both nerve agents, however Tabun requires twice the concentration of Sarin vapor to cause threshold and severe effects (**Table 1.2**, ECt_{50}). The dose of liquid Sarin for percutaneous exposure causing lethal and defined effects is not well understood. Estimates point towards 1 g of liquid applied to the skin for defined severe effects and 1.7 g for lethal effects, however in 1997 the U.S. Army's Chemical Defence Equipment Process Action Team (CDEPAT) stated in their report that they have a low confidence in these estimates due to lack of data.[2]

Table 1.1 *Toxicity exposure definitions*[2]

Toxicity Type	Definition	Units
LCt_{50}	The exposure to vapour causing death in 50 % of chosen population due to percutaneous or inhalation exposure. The units are air concentration (C, mg/m^3) per time (t, min). It refers to both inhalation and percutaneous vapour exposure.	mg-min/m^3
ECt_{50}	Similar parameter to LCt_{50}, however it refers to exposure having defined effect (rather than lethal effect) and can include threshold, mild or severe effects. Mild effects include symptoms such as miosis, whereas severe effects include but are not limited to incapacitation, convulsions, and collapse.	mg-min/m^3
LD_{50}	Percutaneous liquid lethal dose to 50% of given population and the units are milligrams per kilogram of body weight.	mg/kg
ED_{50}	Dose of liquid causing defined effects in 50 % of given population, including threshold, mild and severe effects.	mg/kg

Table 1.2 *Toxicity of Sarin and Tabun*[2]

	Toxicity	Tabun	Sarin
LCt_{50}, mg-min/m^3	Percutaneous, vapour	15,000	10,000
	Inhalation, vapour	70	35
ECt_{50}, mg-min/m^3	Severe effects, inhalation vapour	50	25
	Mild effects, inhalation vapour	0.5	0.5
LD_{50}, mg	for 70 kg man	1,500	1,700
ED_{50}, mg	for 70 kg man	880	1,000

1.1.3 Ronald Maddison and British investigation of Sarin ED_{50} and LD_{50}

In 1951 Porton Down started testing for Sarin toxicity on humans. An

accident with a volunteer, Ronald Maddison in 1953 exposed the danger of this

type of testing. Maddison was 20 years old at the time and participated in a gas chamber test where bare skin was exposed to drops of sarin and the inhibition of AChE in red blood cells (RBC) was monitored. The experiments aimed to corelate the amount of Sarin on the skin to the amount of inhibited AChE in RBC that causes mild to severe effects (ED_{50}) and from that to estimate the lethal dose of liquid Sarin in milligrams per body weight (LD_{50}, mg/kg). Large monetary rewards were delivered to volunteers for the experiments and Ronald was planning to buy an engagement ring for his girlfriend with the reward. Maddison died within 45 minutes from being exposed to Sarin. Other volunteers exposed to the same experimental conditions as Maddison did not suffer the same effects. A post-mortem examination concluded that the reason for this is either that his skin had incredibly fast absorption rate of chemicals or that he was extra sensitive to poisons.[1,3] It is not clear when did human experimentation with nerve agents stop or if there was valuable data generated on ED_{50} and LD_{50} from the 1950s.

1.1.4 Why is Sarin so toxic? Biological effects

In order to understand the effects of Sarin and other nerve agents on the nervous system, it is important to understand how signals are passed from one neuron to another in healthy humans. Neurons have three functional parts related to signalling: dendrites, cell body and axon(s). The function of the dendrites is to receive electrical signals from other neurons. The cell body is used for the synthesis of neurotransmitters (signalling molecules) and the axon contains tau protein fibers which transport macrovesicles full of

neurotransmitters, subsequently secreted by the axon through exocytosis. The junction between the axon of the transmitting neuron (presynaptic terminal) and the dendrite of the receiving neuron (postsynaptic terminal) is called the synapse.[4]

The neurotransmitters typically synthesised in the cell body of cholinergic neurons are kept in vesicles until needed. Acetylcholine is synthesised from acetyl coenzyme A and choline. Vesicular acetylcholine transporters load approximately 10,000 ACh molecules in each vesicle. In cholinergic neurons the signal is mediated through the following events (**Figure 1.4**):

1. A signal depolarises the membrane of the presynaptic terminal.

2. This results in opening of the voltage-gated Ca^{2+} ion channels and efflux of Ca^{2+} into the presynaptic neuron.

3. Ca^{2+} causes the vesicle containing acetylcholine (ACh) to fuse with the presynaptic membrane and release the neurotransmitter through exocytosis.

4. The transmitter fills the synaptic cleft and binds the postsynaptic receptors which are ligand-gated ion channels (**Figure 1.4**, bottom).

5. This allows Na^+ ions to enter the cell and K^+ ions to leave the cell in a way that excitatory or inhibitory postsynaptic potential is generated.

6. The hydrolytic enzyme acetylcholinesterase (AChE) breaks down ACh into acetate and choline and choline is transported back to the neural terminals for recycling and re-synthesis of ACh.[5]

AChE plays a key role in the correct functioning of cholinergic neurons. Inhibition of AChE by sarin occurs through nucleophilic attack mediated by serine hydroxyl groups present on the enzyme (**Figure 1.3**). This causes build-up of ACh in the synapse, which in turn causes depolarisation in the postsynaptic cell, making it unable to release ACh and pass the signal on. This results in neuromuscular paralysis and other symptoms of nerve agent (NA) poisoning. Cholinergic neurons are present at neuromuscular junctions, variety of sites in the central nervous system and the synapse between the vagus nerve and the cardiac muscle fibers and their dysfunction affects all these areas of the human body. This is the reason why nerve agents are so damaging.[5]
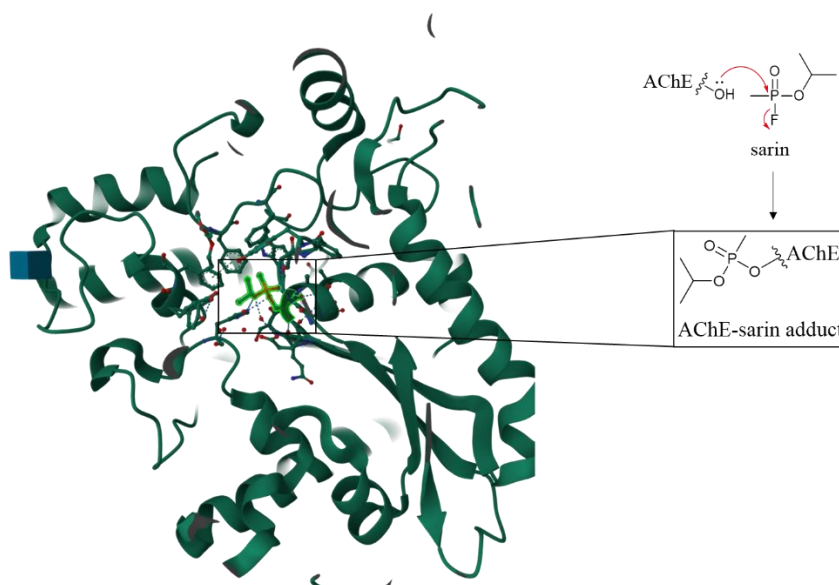
Figure 1.3 *Schematic representation of AChE enzyme inhibition by sarin at the serine residue of AChE and the formation of protein-nerve agent adduct.*[6]
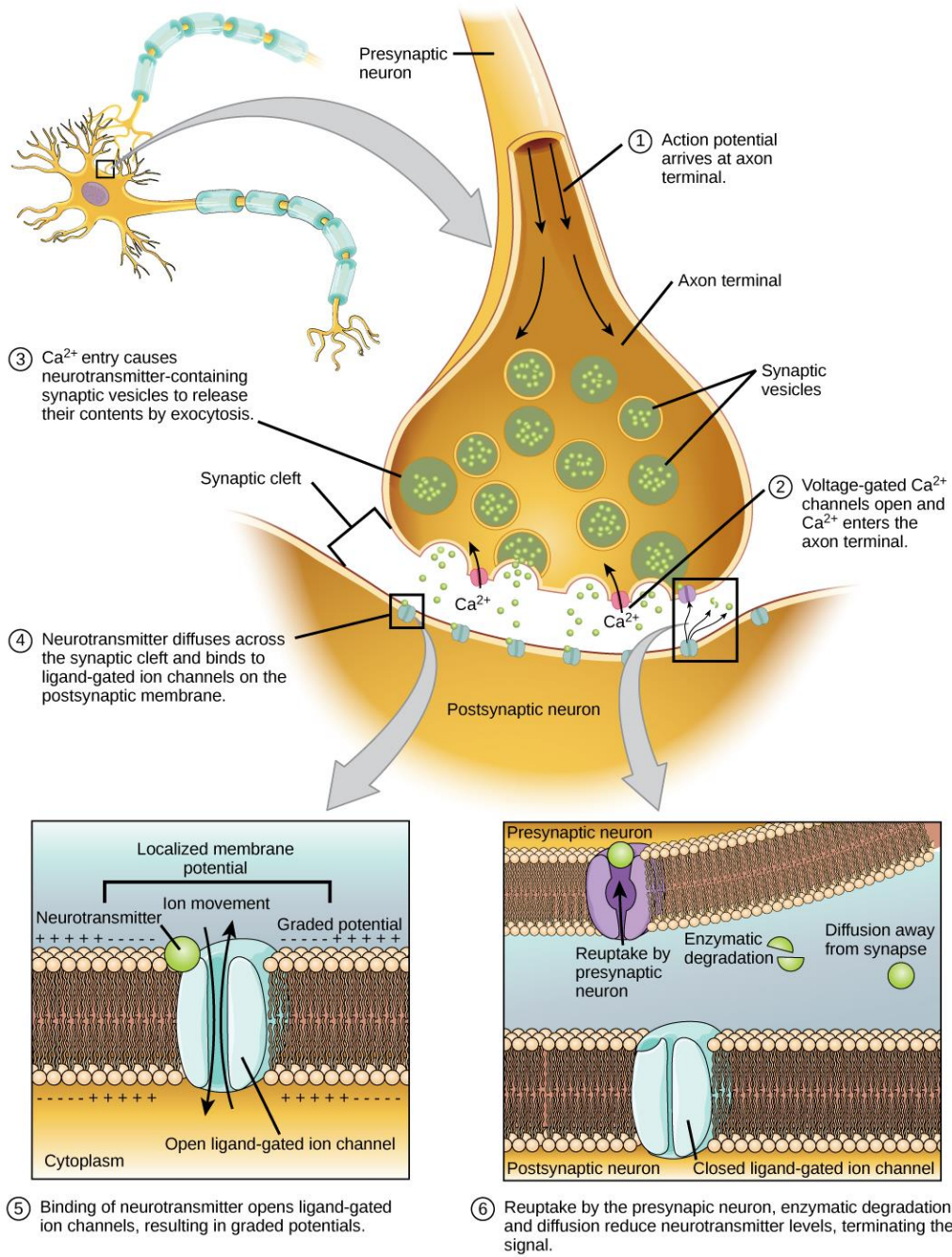
Figure 1.4 *Neural transmission of signal: general description of the sequence of events.*[7]

1.1.5   Sarin and Other Nerve Agents in the Modern world

In 1995 Sarin was released in the Tokyo subway. One hour after the attack the fire service concluded that the substance released was acetonitrile, due to a false positive test result. On this occasion 640 people were admitted into hospital and 12 people died, the impact exacerbated by the mis-classification of the attack.[8] Secondary poisoning due to inappropriate personal protective equipment (PPE) thankfully did not lead to any additional deaths due to the low concentration of sarin in the substance released and therefore exposure levels were low (only 35% of the mixture was Sarin). After this incident it was clear that an international law is needed to control chemical weapons, such as nerve agents.

In 1997 The Chemical Weapons Convention was signed in Geneva for the prohibition of the development, production, stockpiling and use of chemical weapons and for initiating their destruction. The implementing body for the Convention is the Organisation for the Prohibition of Chemical Weapons (OPCW) which currently has 193 Member States. This means that 193 countries have signed the convention. Their mission is to 'to achieve a world permanently free of chemical weapons and to contribute to international security and stability, general and complete disarmament, and global economic development'.[9] In 2013, the OPCW was awarded the Nobel Peace Prize for its efforts to eradicate chemical weapons.

Despite OPCW efforts the use of sarin has been implemented on at least five occasions since the Convention was signed.[10] In April 2017 sarin was used on the civilians in Khan Shaykhun, Syrian Arab Republic. OPCW concluded that "a large number of people, some of whom died, were exposed to sarin".[11] The report showed that total of 292 people were exposed to sarin, 50 of which lost their life (23 victims were under the age of 16).[11]

Other nerve agents were also used in the past five years, the two most famous cases being the Novichok agent poisoning on the 4th of March 2018 in Salisbury, UK and the Novichok attack on the Russian Opposition Coordination Council member Alexei Navalny on the 20th of August 2020. Both cases were confirmed as nerve agent poisonings by OPCW.[12]

It has been well-documented that although detection of chemical weapons is possible, tests are expensive and there exists no single instrument which can perform qualitative and quantitative analyses for toxic agents.[8] In addition, in cases when an attack has been carried on a single person or small groups of people, severe symptoms can be mistaken with opioid overdose. It is extremely difficult for medical staff to recognize organophosphate poisoning from the presenting symptoms, this can easily lead to secondary poisoning in staff.[13]

1.1.6 Current detection capabilities of Nerve agents

Current detection techniques for nerve agent exposures include five main approaches: (i) analysis of cholinesterase activity, (ii) direct measurement of

intact nerve agent,[14] (iii) detection of degradation products of NA present in the urine/blood,[15,16] (iv) fluoride re-activation method[8,15,17,18] and (v) analysis of nerve agent-protein adduct.[17,19] Each one of these methods will be discussed below.

1.1.6.1 Cholinesterase Activity

Nerve agents inhibit the activity of cholinesterase enzymes (AChE) and prevent them from breaking down acetylcholine to acetyl and choline. Ellman's assay is a colorimetric test used to detect cholinesterase activity (**Figure 1.5**).
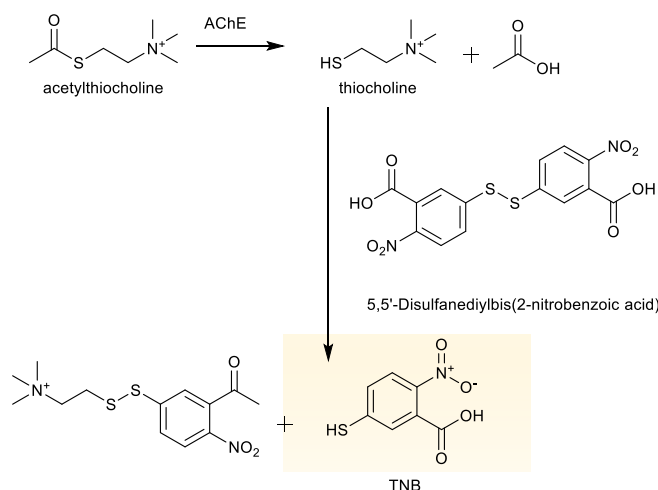
Figure 1.5 *Detection of acetylcholinesterase activity using Ellman's assay. Acetylthiocholine is hydrolysed to thiocholine and acetic acid. Next, thiocholine reacts with 5,5'-disulfanediylbis(2-nitrobenzoic acid) to yield a coloured compound 2-nitro-5-thiobenzoate (TNB^{2-}).*

In this assay acetylthiocholine is used instead of acetylcholine to form a thiol after the molecule is broken down by the enzyme. By mixing serum samples with acetylthiocholine and Ellman's reagent, the coloured compound 2-nitro-5-thiobenzoate (TNB^{2-}) is released as a result of the thiol breaking down the

disulphide bridge of Ellman's reagent. (**Figure 1.5**). If the enzyme is active, acetylthiocholine is broken down to produce an acetyl and thiocholine. The thiol reacts with the Ellman's reagent and gives a yellow colour. In the case of inhibited enzyme, no colour change is observed.

1.1.6.2 Intact Nerve Agent

Intact nerve agent has been successfully detected in concentration range of 10^{-3} - 10^{-6} mol/L using a colorimetric enzyme inhibition immunoassay. The signal was generated by HRP (horseradish peroxidase). The assay required the immobilization of antigens on the surface of a well plate and incubation with a mixture of antiserum containing HRP-antibodies. Following a peroxide wash the sample becomes coloured if no sarin is present due to the binding of the antibody to the antigen. If sarin is present it competitively binds the antibody which is subsequently washed away and no colorimetric response is detected.[14] This assay has a very good specificity for sarin (GB) over soman (GD) and VX.

Efforts to develop fluorescent-based sensing were also made by a number of groups.[20–25] Some interesting examples utilised on/off strategies and concentration-dependent detection methods. Detection limits of 10^{-8} M of a nerve agent-mimicking drug diethyl chlorophosphite (DCP, **Figure 1.6**, A) were achieved using a triphenylamine-benzimidazole (TPIM) fluorescent probe (**Figure 1.6**, A). In the presence of DCP the probe undergoes internal charge transfer, which leads to increased fluorescent intensity at 573 nm with increasing DCP concentration. Interestingly, this probe showed a colorimetric

response to DCP vapour, making it suitable for environmental testing.[23] Indirect sensing of sarin, tabun and VX in soil samples was also developed by the utility of an oxime/ferrocenyl dye dual reagent detection method (**Figure 1.6**, B). [24] The ferrocenyl dye changes colour from pink to yellow (sarin), colourless (tabun) or orange-yellow (VX) in the presence of the corresponding nucleophilic hydrolised species (F[-], CN^{-} and $SCH_2CH_2N(CH_3)_2$).

Iminocoumarin-benzothiazole-based probes have also been developed and their fluorescent detection efficiency tested against the nerve agent mimic drug DCP (**Figure 1.6**, C).[25] The lowest detection limit was found to be 0.065 µM of DCP. Addition of the DCP to the probes resulted in dramatic reduction of signal intensity at 526 nm and 521 nm.
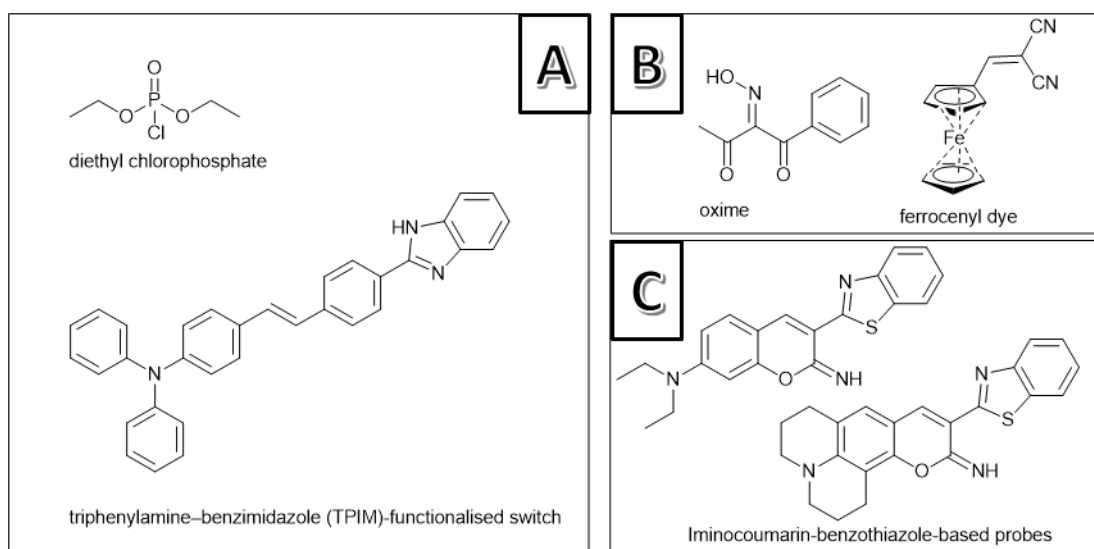
Figure 1.6 A) Structure of diethyl chlorophosphite (DCP) and B), and C) fluorescent probes used to detect nerve agents and DCP.

Lanthanides have also been used in the design of sensing probes for the detection of nerve agent-mimicking drugs. In a recent example Abbas *et al.* developed two luminescent europium-based probes for the detection of DCP.[26] These luminescent probes react with DCP in a similar manor to the way sarin and other G-type nerve agents react with the serine residue on AChE, shown on **Figure 1.3**. The structure and reactivity of these lanthanide probes with DCP is shown on **Figure 1.7**. The probes allowed for 'naked eye' detection of DCP in the nanomolar range. Additionally, the probes were immobilised on a strip of filter paper and were able to detect DCP aerosol at volume of 20 μL. Unfortunately, concentration of DCP in this volume was not stated and cannot be determined how the detection limit compared to the LCt_{50} of G-type nerve agents described in **Table 1.2**.
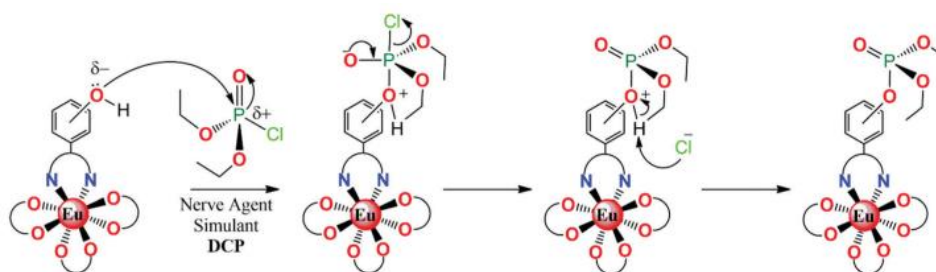
Figure 1.7 *Eu^{3+}-based probes designed by Abbas et al. for the detection of intact G-type nerve agents and their reaction with the nerve agent-mimicking drug DCP.*

A plethora of other examples of on/off fluorescent-based switches were reviewed by Martinez-Manez,[22] Yoon,[21] and Kumar *et al.*,[20] however, most of these strategies could only be applied to environmental testing due to the type of solvents required and the short longevity of intact nerve agents in the body.

Disadvantages of the colorimetric enzyme inhibition immunoassay include low sensitivity (detection limit for sarin concentration on the mM scale), laborious reagent synthesis (antigen, antibodies) and long incubation times (hours) resulting in inefficiency. Following exposure, it would be more useful to detect the sarin in patient samples, where it is unlikely to remain as an intact nerve agent but convert to a bioconjugate version (a biomarker).

1.1.6.3 Degradation Products of NA present in the Urine

Most sarin in the body is hydrolysed to isopropyl methyl phosphonic acid (IMPA). IMPA is an excellent biomarker for sarin poisoning and can be found distributed throughout the body, including hair, blood, skin, lung, heart etc. and detected in the urine (**Figure 1.8**).[15] Presence of IMPA is a clear indication that sarin poisoning has taken place and can be extracted from the urine using solid phase derivatization (SPD). This method has been combined with gas chromatography mass spectrometry/mass spectrometry (GC-MS/MS, tandem mass spectrometry) detection system to achieve detection limit of 0.02 ng/mL. In MS/MS spectrometers, two or more mass analysers are coupled together to deliver improved accuracy and precision as well as better selectivity.
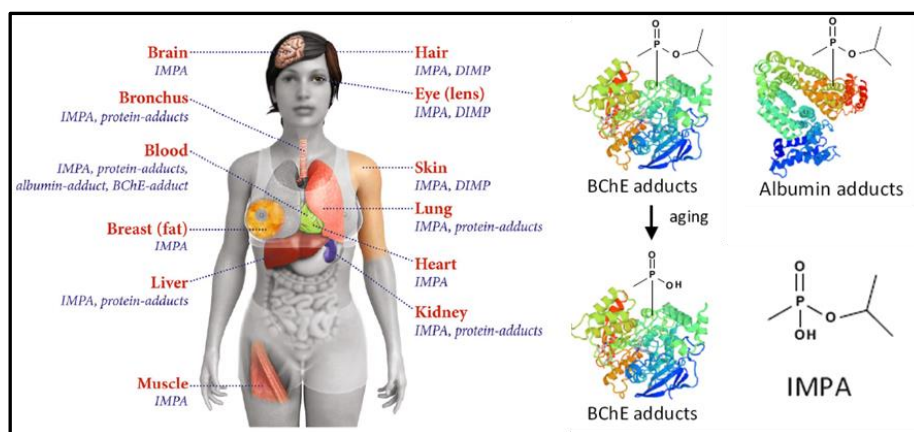
Figure 1.8 *Distribution of sarin poisoning biomarkers throughout the body (left) and some of their structures (right). Isopropyl methyl phosphonic acid (IMPA) was found to be the most common biomarker of sarin poisoning. Albumin and BChE (butylcholinesterase) adducts are examples of protein adducts.*[15]

The disadvantage of choosing IMPA as a biomarker for Sarin poisoning is that it is not as long-lived as other biomarkers, for example sarin-protein adducts. The extraction/derivatization includes three separate steps of sample preparation, including centrifugation and sonication, which are time consuming. In addition, if the specialized MS/MS detector isn't available the detection limit will fall lower. [16]

1.1.6.4 Fluoride reactivation method

One way this can be improved is by recovering the enzyme-bound sarin in the sample prior to detection and in this way increasing the amount of free sarin in the sample. This is achieved by the fluoride re-activation method (method iv). The fluoride reactivation method involves extraction of the protein-bound sarin present in a sample (this can be from serum or whole blood) and subsequent detection of the agent in its pure form using

chromatography (gas or liquid)/mass spectrometry (MS) systems. The principle of the fluoride reactivation is outlined in **Figure 1.9**.[17]

Sarin was successfully detected using this method by recovery from a blood serum sample and subsequent detection with GC/MS.[17] The detection limit was 4% inhibition of BChE. In short, blood serum sample containing methyl phosphonylated (inhibited) enzymes such as AChE, BChE, albumins and general proteins was incubated with excess fluoride ions. Nucleophilic attack on the phosphorus resulted in recovery of the enzyme's original, active form and the sarin molecule which was extracted for detection. The sarin was detected using a GS/MS system. This method recovered only 63-66 % of the original nerve agent in the sample. [15] The disadvantage of using serum samples is that they lack red blood cells which contain a large amount of AChE expressed on their surface. In this way a lot of the AChE-bound sarin residing there is missed during detection. Sarin was successfully extracted from whole blood using the fluoride method by Blanca *et al.* [18] Furthermore, the typical GC/MS was replaced by LC-MS/MS (multiple reaction monitoring (MRM)) machine which greatly improved the sensitivity of detection to 5 pg/mL. An extra step in the sample preparation was added (**Figure 1.10**).
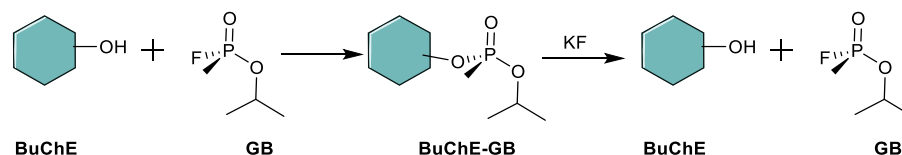
Figure 1.9 *Fluoride Reactivation method. Hydroxyl group on an enzyme – in this case BChE, is phosphonylated by GB. The inhibited enzyme is next incubated with KF and nucleophilic attack on the phosphorus recovers GB and BuChE.*[17]

During this step Sarin is reacted with 2-[(dimethylamino)methyl]phenol (2-DMAMP). The final product is much safer to handle for LC-MS/MS analysis and provides a better target for detection.[18] The disadvantage of this approach is that at present MRM systems are expensive specialist equipment and very few laboratories have them.
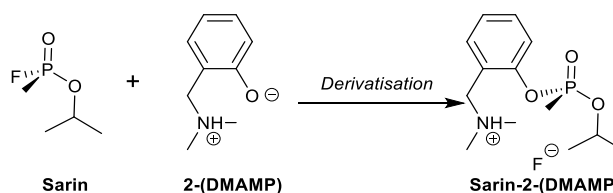
Figure 1.10 *Principle of derivatization adopted by Blanca et al. The final product GB-2-DMAMP is detected by LC-MS/MS.*[18]

A great disadvantage of the methods described above include the necessity to work with very toxic chemicals (sarin), long sample preparation times and use of expensive specialized equipment. In cases such as the Tokyo gas attack these tests can be extremely useful as a retrospective study but are less useful as a first response. In addition, a great disadvantage of the fluoride method is its inability to detect sarin/NAs in aged form. In the aged products the aliphatic isopropane group is replaced by the electron-dense hydroxyl group. The

oxygen hinders the phosphorus from the nucleophilic attack of fluoride and therefore recovery of the nerve agent cannot be achieved. This provides a very narrow window for the detection efficiency of the tests in terms of time after exposure. The time required for sarin bioproducts to "age" is not well understood, however agents like Tabun may take only minutes.[15] One way to overcome this problem is to use another enzyme – pepsin, to hydrolyse the Sarin-enzyme bond.[19]

1.1.6.5 *Analysis of Nerve Agent-protein Adduct*

The presence of nerve agent-protein adducts within the body following NA exposure represent excellent biomarkers for detecting nerve agent poisoning due to their high concentrations in blood.[19] Current techniques for the detection of these bioproducts include digestion of the enzyme butyl cholinesterase (BChE) using pepsin and subsequent analysis of the harvested peptides using liquid chromatography tandem mass spectrometry (LC-MS/MS). This method has been used to successfully detect 0.2 ng/mL VR following exposure. VR protein adducts are particularly convenient for research as they are stable to storage for up to six years without aging. As with most of the other detection methods the sample preparation and analysis involve long and laborious preparation – extraction of the enzymes includes immunomagnetic separation which is followed by the pepsin digestion, sample preparation and LC-MS/MS analysis (**Table 1.3**). Accordingly, cheaper, faster, and more easy-to-use techniques are required for NA detection, both in the immediate and longer-term aftermath of attacks.

Table 1.3 *Summary of current detection methods for nerve agent poisoning, their detection limits, and disadvantages.*

Method	Detection limit	Disadvantages
Cholinesterase Activity	Not clear	• non-specific
Intact Nerve Agent	μM-mM	• low sensitivity. • laborious reagent synthesis (antigen, antibodies). • long incubation times (hours).
Degradation Products of NA present in the Urine	0.02 ng/mL	• short-lived biomarker. • time consuming sample preparation. • specialized laboratory equipment (if the specialized MS/MS detector isn't available the detection limit will fall lower).
Fluoride reactivation method	0.005 ng/mL	• work with very toxic sarin. • long sample preparation times. • use of expensive specialised laboratory equipment. • not suitable as a first response due to inability to detect sarin/NAs in aged form (narrow window for detection).
Analysis of Nerve Agent-protein Adduct	0.2 ng/mL	• long sample preparation and analysis. • specialised laboratory equipment

1.2   Principles of MRI

In this work, we aim to offer an alternative detection methodology for nerve agent-protein adducts by exploiting the capability of imaging techniques to deliver fast results. **Figure 1.11** shows the structure of human albumin and how this protein reacts with sarin. Zoomed-in is the location for binding of G-type

nerve agents, including sarin (Tyr 411). Sarin- and Cyclosarin-tyrosine adducts were provided for testing in this project by dstl (**Figure 1.12**).
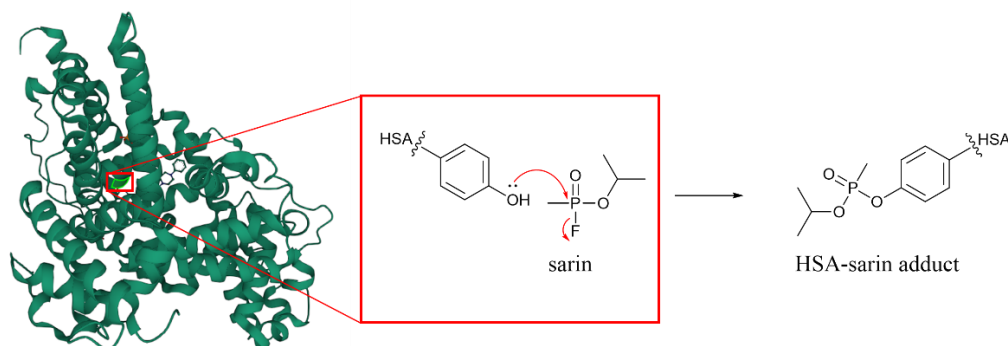
Figure 1.11 *The location for sarin binding at the Tyr411 residue of unmodified human serum albumin and subsequent reaction of the hydroxyl group on tyrosine with sarin nerve agent resulting in protein-nerve agent adduct.*[27]

Magnetic resonance imaging (MRI) can produce images quickly and it is already widely used by clinicians for a range of applications. Additionally, MRI scanners are present in most hospitals making MRI a suitable technique for use in peace and war. There are plethora of examples in the literature of using MRI contrast agents for the detection of binding of specific molecules, discussed in detail sections 1.4.2 and 1.5.1.[28–30]
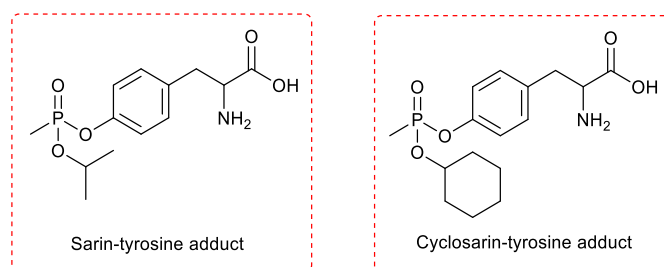
Figure 1.12 *Structure of sarin-tyrosine adducts provided by dstl Porton Down.*

MRI is an excellent diagnostic tool widely used in the clinical setting. Its application includes soft tissue scans and monitoring disease progression by recording tomographic images. It is non-invasive, has a high spatial resolution (<1 mm), high tissue contrast and uses non-damaging radiofrequency radiation. MRI also has the potential to be used for sample analysis of blood and hair.[31] Its basic principles arise from the nuclear magnetic resonance (NMR) phenomena.

1.2.1 Basic principles of nuclear magnetic resonance (NMR) phenomena

This subsection describes the behaviour of proton nuclei when placed in an external magnetic field and introduces the importance of Larmor frequency.

A nucleus with spin I has $2I+1$ energy levels equally spaced by energy ΔE:

$$\Delta E = \mu B_0 / I, \qquad (1.1)$$

Where B_0 is the external magnetic field. The nuclear magnetic moment, μ equals:

$$\mu = \frac{\gamma h I}{2\pi}, \qquad (1.2)$$

where γ is the gyromagnetic ratio and h is Plank's constant. Proton nuclei have a quantum spin $I = \frac{1}{2}$, and 2 energy levels ($2I+1$). The frequency that induces transitions between energy levels is given by:

$$\omega_0 = \frac{\Delta E}{h} = \frac{\gamma B_0}{2\pi} \quad (Hz) \qquad (1.3)$$

or

$$\omega_0 = \gamma B_0 \quad (rad\ sec^{-1}) \qquad\qquad (1.4)$$

This shows that when placed in an external magnetic field with strength B_0, proton nuclei align and spin at a constant Larmor frequency (ω_0) according to their gyromagnetic ratio. For protons γ = 42.58 MHz/T. Conventionally B_0 points along the z-axis, as illustrated in **Figure 1.13**.[32,33] In the initial equilibrium state μ is aligned with B_0. From classical mechanics[34] when a second radiofrequency (rf) field is applied at angle θ to μ, a torque is exerted over the magnetic moment causing it to precess about the new magnetic field, B_1. This field is typically rf pulse applied perpendicularly to B_0, in the xy plane. Energy is absorbed from B_1 only if it is in the Larmor frequency (ω_0). The magnetic vector of B_1 can be thought to rotate in the xy plane (**Figure 1.13**), tipping M in an angle, however the precession frequency remains constant.
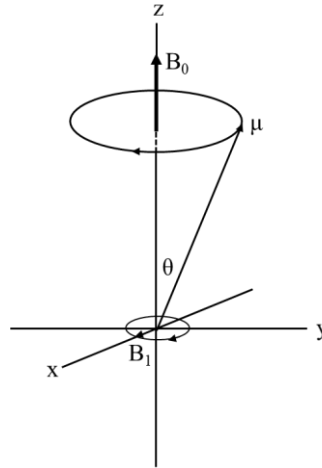
Figure 1.13 *Nuclear magnetic moment μ precess about the static magnetic field, B_0. The radiofrequency field B_1 rotates in the xy plane.*[35]

When placed in B_0 proton nuclei develop net magnetisation (M) vector with maximum value (M_0) over several seconds. Net magnetisation is a result of the small majority (1.381×10^{-23} Joules/K at body temperature) of nuclear magnetic spins oriented in the lower energy state (N_{UPPER}) parallel to B_0 in accordance to Boltzmann distribution (Equation (1.5)) and it is a representation of the average angular momenta of all spins in the sample (**Figure 1.15**A).[36]

$$\frac{N_{UPPER}}{N_{LOWER}} = \exp\left(\frac{-\Delta E}{kT}\right) \qquad (1.5)$$

When describing MRI, it is more accurate to consider M as opposed to individual proton nuclei due to the complexity of quantum mechanics, as Heisenberg's uncertainty principle states that the exact direction any given proton magnetic moment is pointing at any given time is unknown.[37]

When describing the motion of magnetisation, it is useful to use a rotating frame of reference with coordinates x', y' and z', as opposed to the

static coordinate system of the laboratory (x,y,z). The rotating frame is a coordinate system that rotates about the external magnetic field (B_0) in the same direction as the precession of the nuclear magnetic moments. By using the rotating frame, the net magnetisation vector M would describe a much simpler motion path compared with the static laboratory frame. To understand the rotating frame, one might consider the trajectory of a football being thrown upwards from the perspective of a distant observer positioned in space (**Figure 1.14**, left) vs from the perspective of the person positioned on Earth, throwing the football (**Figure 1.14**, B). From space, the football will follow a complex parabolic path being drawn back to Earth by its gravity. From the perspective of the person standing 'at rest' on Earth the football will simply follow a straight vertical line path and fall back at its original starting point.

Figure 1.14 *Trajectory of a football thrown upwards from the perspective of a distant observer (left) vs a person standing 'at rest' on Earth (right).*

In the initial equilibrium state M is aligned with B_0 and at this point there is no resonance taking place (**Figure 1.15** A). To introduce resonance the system requires an external energy which is supplied through the application of the radiofrequency field (B_1), typically in the form of a pulse, perpendicular to B_0. B_1 is assigned in the x' plane in the rotating frame and must be at Larmor

frequency to induce interaction with proton nuclei. The extra energy from B_1 is absorbed and results in statistically significant proportion of proton nuclei moving into the higher energy state (N_{LOWER}, anti-parallel to B_0). From the Larmor equation (Equation (1.5)) the precession frequency is γB_1 about the x' axis. At this point, nuclear magnetic resonance has occurred which is evident by the energy transfer between B_1 and M. In a time t_p (sec) the precession angle θ of the net magnetisation is given by:

$$\theta = \gamma B_1 t_p \ (rad) \qquad\qquad (1.6)$$

In **Figure 1.15** B the net magnetisation M recesses about x' by $\theta = \pi/2$ (left) and $\theta = \pi$ (right) rad. Originally, there was no phase coherence in the x'y' plane and therefore M had no component in this plane. After B_1 pulse is turned off M is tipped in the y' plane and y' component of M is generated ($M_{y'}$). Due to energy exchange between the magnetic moments through natural processes (spin-spin relaxation) $M_{y'}$ decays with a time constant T_2. Inhomogeneity of the magnetic field B_0 causes some magnetic moments to precess slightly faster or slightly slower than the rotating frame in different parts of the sample, causing $M_{y'}$ to decay with time constant T_{2*}. Energy is also lost to the surroundings (spin-lattice relaxation) as M tips back to the z' axis. M decays to equilibrium state M_0 with time constant T_1. In general, $T_{2*} \leq T_2 \leq T_1$.[35]
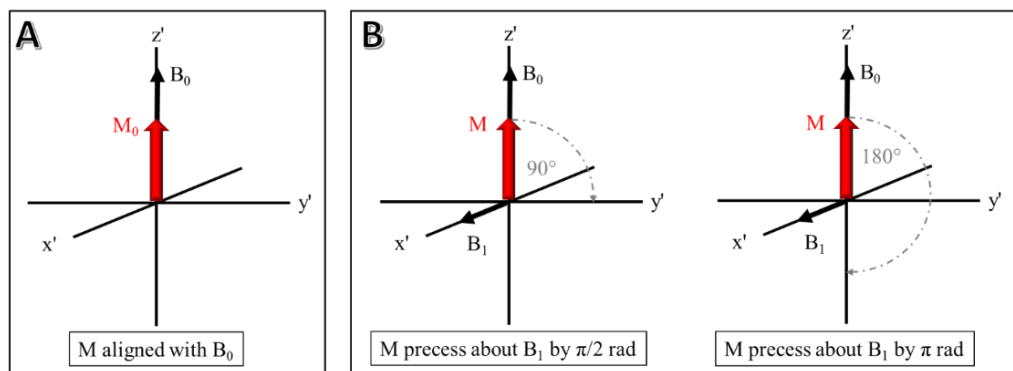
***Figure 1.15 A**- Net magnetisation vector aligned with B_0, M has only z-components (M_0); **B**-precession of M about B_1 in the rotating frame by π/2 rad (90 °) and π rad (180°).*

Longitudinal relaxation (spin-lattice, T_1) and transverse relaxation (spin-spin, T_2) occur simultaneously. Transverse relaxation (T_2-relaxation) describes the behaviour of the xy component of M, specifically the decay of M_{xy} due to loss of spin coherence (entropic process). The time constant T_2 (sec) represents the time required for M_{xy} to fall to approximately 37% of its maximum value reached during the RF pulse (**Figure 1.16**).[36]

Longitudinal relaxation (T_1-relaxation, spin-lattice) is a thermal (enthalpic) process whereby energy in the form of heat flows from the excited nuclei (N_{LOWER}) to the surroundings (nuclei, atoms, molecules). The heat is transferred through collisions, rotations and electromagnetic interactions and results in the recovery of the z-component of M to its original maximum value of M_0. The time constant T_1 is defined as the time required for M_z to reach 63% of M_0 (1-1/e), equation, and it has units of seconds (**Figure 1.17**).[36,38]
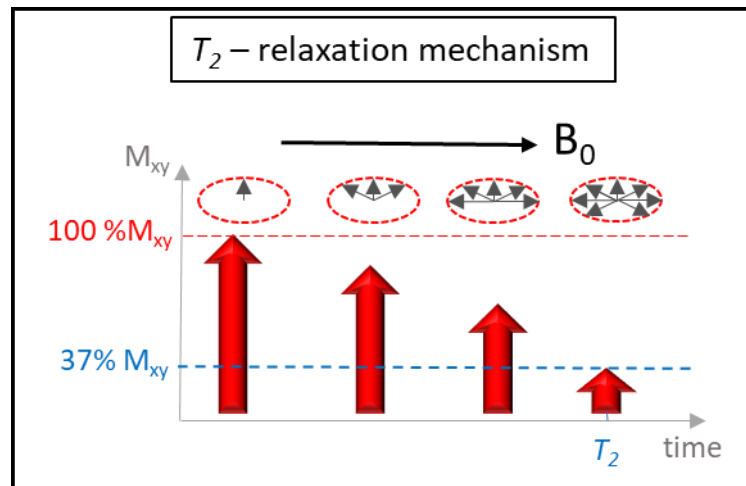
Figure 1.16 *Transverse relaxation mechanism. Spins falling out of coherence shown on top represented by grey arrows. When phase cohesion is disrupted, the spins cancel each other out in the xy-plane and M_{xy} decays. T_2 constant is shown in blue, representing the time required for M_{xy} to decay to 37% of its maximum value.*
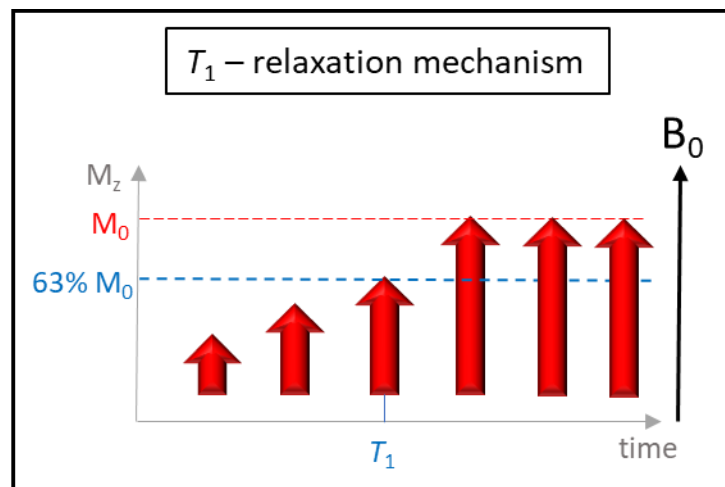
Figure 1.17 *Longitudinal relaxation mechanism. Thermal energy is lost, and the z-component of M grows back to M_0 due to larger proportion of protons returning to the lower energy state N_{UPPER}. The time constant T_1 is shown in blue and represents the time required for M to reach 63% of M_0.*

1.2.2 Free induction decay

In the ideal case of perfectly homogeneous static magnetic field B_0 the transverse decay of $M_{x'y'}$ following a 90° B_1 pulse looks like the one shown in **Figure 1.18** A. In reality due to inhomogeneities of B_0, chemical shifts and spin-spin coupling the rf pulse differs slightly from the Larmor frequency. The exponential decay is still observed; however, the signal also contains interference effects as $M_{x'y'}$ and the reference frequency come in and out of phase with each other (**Figure 1.18** B). This signal is termed free induction decay (FID) and it contains all information we are used seeing from the NMR spectrum. FID resulting from pulse sequences from two or more pulses are used to determine relaxation times and to generate MRI images.
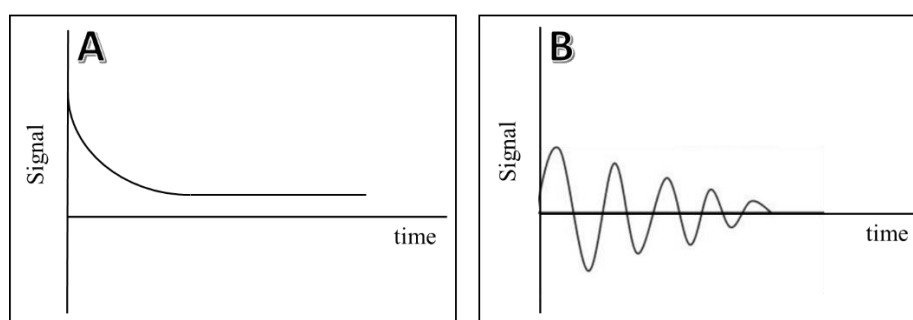
Figure 1.18 *Free induction decay (FID) A- for B₀ precisely at the Larmor frequency; B- for B₀ off resonance.*

1.2.3 Measuring T_1 – Relaxation and Pulse Sequences

The most common way to measure T_1 in NMR Relaxometry is by employing the Inversion-Recovery (IR) pulse sequence. IR sequence consists of a 180 ° pulse, followed by a wait time τ and another 90° pulse (180°, τ, 90°). The initial 180° pulse is applied along the x' axis and inverts the net

magnetization M_0 along the z' axis to a value of -M_0. After a time τ a 90° pulse is applied, which rotates M to the y' axis so it can be detected. An FID with initial height proportional to M is generated and this value is the value of $M_{z'}$ at time τ. By recording systematically the value of M at different τ until τ is around five times T_1 (at this value $M_{z'}$ = 0.993 M_0), we can obtain a curve corresponding to the decay of M.[35] To quantify T_1 we can then use Bloch equations:

$$\frac{\partial M_z}{\partial t} = -\frac{M_z - M_0}{T_1}.$$

(1.7)

Integrating this equation by stating that M_z = -M_0 at t=0 gives:

$$M_z = M_0 \left(1 - 2e^{\frac{-t}{T_1}}\right).$$

(1.8)

In MRI other pulse sequences are also used to measure T_1, for example Fast Imaging with Steady-state free Precession (FISP) is particularly popular.[39] This is a type of coherent gradient echo with FID refocusing pulse sequence. Gradient echoes (GRE) are just clever manipulations of the FID (**Figure 1.19**). By dephasing and then rephasing the FID signal, an 'echo' is produced. GREs are used to improve signal-to-noise and to access T_1, T_2, and T_{2*}. The name FISP was used by Siemens, other names of this sequence include GRASS (GE Healthcare), FFE (Philips), SARGE (Hitachi) and FE (Toshiba).[39] This pulse sequence is a bit more complicated and involves the generation of steady state free precession by producing a train of excitation rf pulses with very short repetition times (TR). The repetition times are defined as the cycle time between corresponding points (in milliseconds). For example, in IR sequence

(180°, τ, 90°) the TR will be from the middle of the 180° pulse to the middle of the next 180° pulse. Using short repetition times would mean that the first FID won't be ended before the next excitation rf is applied which results in a signal like the one shown on **Figure 1.20**. In FISP the excitation pulses are alternating in phase (+α, -α. +α…). The -α gradient helps to restore the longitudinal magnetisation. FISP also includes extra gradients and "rewinders" which help with image artifacts and resonant offset effects (**Figure 1.21**). The FID part of the signal contains information on T_1 and T_{2*}, whereas the echoes contain T_2.
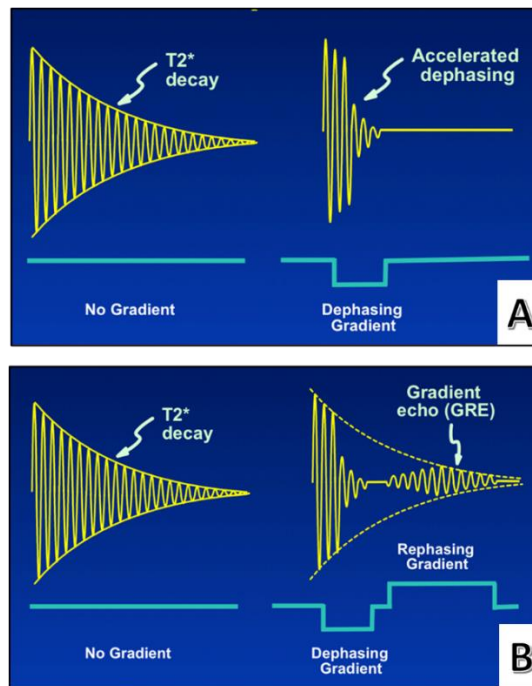
Figure 1.19 *Formation of GRE:* **A-** *Dephasing gradient is applied to the FID, resulting in trampling of the FID.* **B-** *Rephasing gradient is applied (polarity is inverse to dephasing gradients). This reverses the phase changes caused by the gradient of dephasing and revives the FID as GRE.*[40]
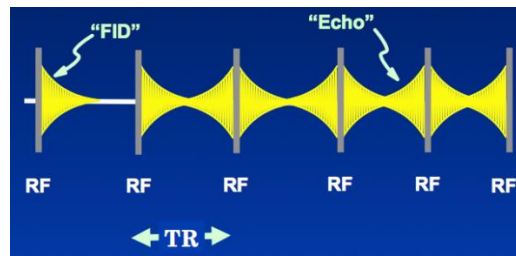
Figure 1.20 *Steady-state precession.*[40]
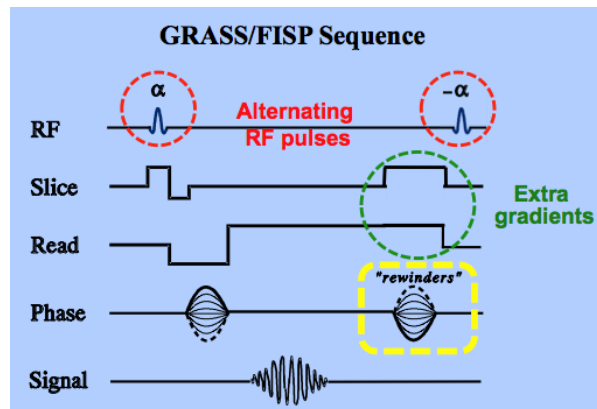
Figure 1.21 *FISP pulse sequence.* [40]

1.3 MRI contrast agents

MRI contrast agents (CA) are frequently employed to improve the sensitivity and enhance the signal of the technique. CAs work to reduce the transverse or longitudinal relaxation times resulting in better image contrast.

Negative contrast agents predominantly enhance T_2 relaxation times and produce darker images. They are based mainly on iron oxide and work by creating a strong local magnetic field, which contributes to the faster loss of phase cohesion, interpreted by the receiver coil as weaker electronic signal (hence darker pixels).[41]

Gd^{3+} is the most frequently used paramagnetic ion in both clinical and research setting due in-part to seven unpaired electrons and isotropic S-ground state. The magnetic dipole of these electrons forms dipole-dipole interactions with nearby water protons and introduce significant enhancement (reduction) of T_1 relaxation times. As a result areas enhanced with Gd^{3+}-based CAs appear brighter on the image due to increase in electronic signal passed to the receiver coil of the instrument.[42] However, Gd^{3+} has a very similar size to Ca^{2+} (r_{ionic} (Gd^{3+}) = 0.99 Å, r_{ionic} (Ca^{2+}) = 1.12 Å),[43] which means that it can easily interfere with Ca^{2+} pathways and inhibit their function leading to toxic physiological responses.[44] Thermodynamically stable and kinetically inert Gd^{3+}-chelates, such as $Gd^{3+}-DOTA$ (Dotarem®, **Figure 1.22**) bypass this problem by occupying eight of the nine coordination sites of Gd^{3+},[43] leaving a single coordination site in the inner sphere for a water molecule to bind.[28] Octadentate chelates from thermodynamically stable complexes, and series of these ligands have been approved for clinical use (**Figure 1.23**).[45,42] Thermodynamic stability is characterised by the Gibbs free energy required for the complexation reaction and is typically reported as a rate constant. In addition to thermodynamic stability, kinetic stability has also been found to be crucial for the design of a safe contrast agent. The kinetic stability is reported in the form of half-lives and describes the time required for the metal to dissociate from the chelate. Transmetallation plays a key role when considering the kinetic stability of contrast agents. It has been found that open-chain contrast agents, such as $Gd^{3+}-DTPA$ and its derivatives, are less kinetically

stable than macrocyclic contrast agents, such as Gd^{3+}−DOTA. In 2006 tens of reports connecting the use of Gd^{3+}−DTPA−BMA (Omniscan®, **Figure 1.23**) with the development of nephrogenic systemic fibrosis (NSF) in patients with renal failure, due to leakage of Gd^{3+} in the bloodstream. [46,47] This was exclusive to open-chain contrast agents. In our work contrast agents are designed for use in patient samples and not *in vivo*, therefore complex dissociation is only relevant in the context of signal modulation. Nevertheless, all contrast agents used in this study were based on macrocyclic chelates to ensure high stability of these complexes. Contrast agents are also extremely useful for molecular recognition and their structure can be easily manipulated to bind specific ions/molecules.[30,48–50]

The efficacy of positive contrast agents is quantified by their relaxivity (r_1, mM^{-1} s^{-1}) defined as the T_1-relaxation time enhancement standardised to a 1 mM concentration of the paramagnetic ion (Equation(1.9),[13,44] where R_1 is the relaxation rate ($1/T_1$, s^{-1}) and [CA] is the concentration of Gd^{3+}.[31]

$$r_1 = \frac{\Delta R_1}{[CA]}, mM^{-1}s^{-1} \qquad\qquad (1.9)$$
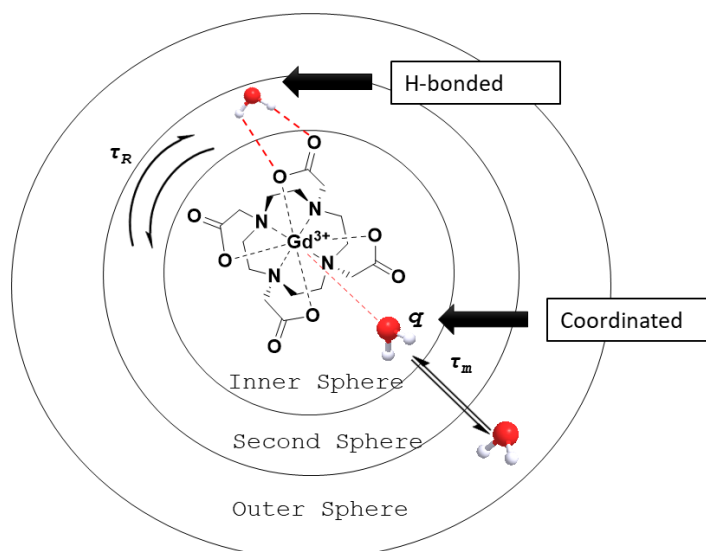
Figure 1.22 Structure and inner, second and outer coordination sphere of the positive contrast agent Dotarem® (Gd^{3+}–DOTA).[31]

The factors governing the r_1 parameter are described by Solomon-Bloembergen-Morgan (SBM) theory.[51,52] In short, the overall observed relaxation rate ($R_{1(obs)}$) enhancement is a sum of the effects of water molecules coordinated in the inner sphere of the complex (IS), hydrogen bonded water in the second sphere of the complex (SS) and diffusing bulk water situated in the outer coordination sphere (OS) (Equation (1.10), **Figure 1.22**).[53,54,31,42,55] The following subsections describe in detail the equations governing relaxivity from the OS and IS.

$$R_{1(obs)} = R_1^{IS} + R_1^{SS} + R_1^{OS} \qquad\qquad (1.10)$$
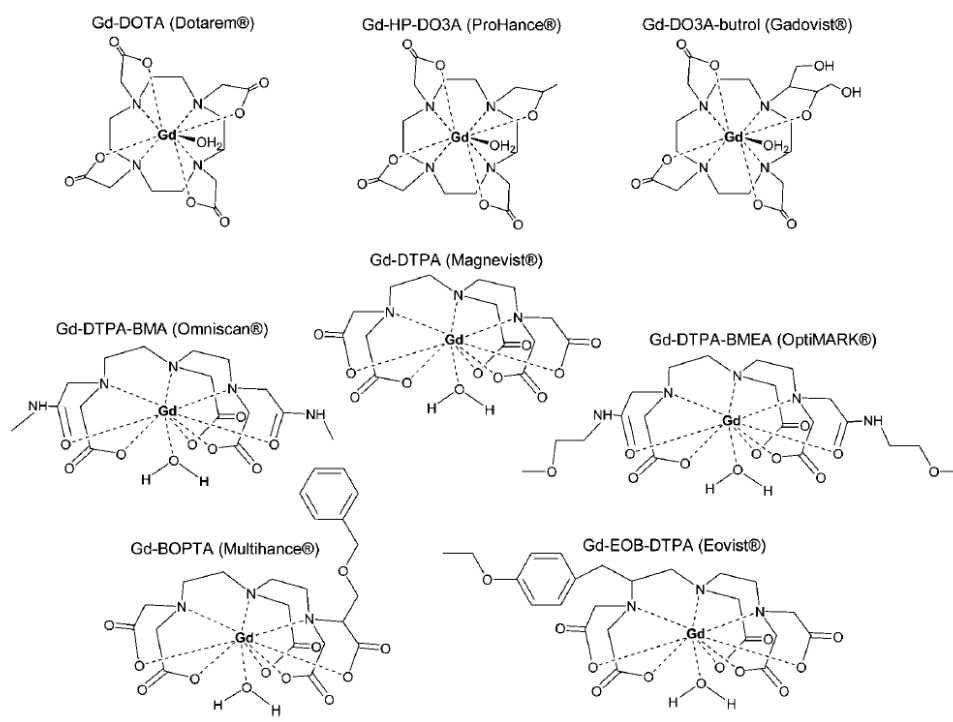
Figure 1.23 *Clinically approved MRI Contrast Agents*[42]

1.3.1   Outer Sphere Relaxation Mechanism for Longitudinal Relaxation Rate

The outer sphere relaxation theory describes the contribution of the bulk solvent water molecules to the overall relaxation times. Outer sphere relaxation rates depend heavily on the relative diffusion between the two interacting spins (D), which in the case of Gd^{3+}-based contrast agents are the electron spins of the seven unpaired electrons of the Gd^{3+} ion and the spins of the water protons. At higher temperatures relaxation rates reduce slightly and relaxation enhancement by the contrast agent is decreased because both the correlation time for the relative translational diffusion (τ_D) and the electronic relaxation

times ($T_{1,2e}$) decrease.[56] The expression for outer sphere longitudinal relaxation

rate is shown in equation (1.11):

$$R_1 = \frac{32\pi}{405}\left(\frac{\mu_0}{4\pi}\right)^2 \frac{N_A[CA]}{dD}\gamma_I^2\gamma_S^2\hbar^2 S(S+1)[j_2(\omega_I - \omega_S) \qquad (1.11)$$

$$+3j_1(\omega_I) + 6j_2(\omega_I + \omega_S)$$

Where μ_0 is the vacuum permeability, N_A is Avogadro's number, [CA] is

the molar concentration of the paramagnetic metal (Gd^{3+} in this report), d is the

closest distance of approach of spins I and S, D is the diffusion coefficient for

relative diffusion ($D = D_I + D_S$), γ_I and γ_S are the gyromagnetic ratios of the

proton and electron spin respectively, S is the total spin of the paramagnetic

atom ($Gd^{3+} = 7/2$), ω_I and ω_S are the proton and electron Larmor frequencies

respectively. The spectral densities $j(\omega)$ can be expressed as:

$$j_{1,2}(\omega) = R_e\left\{\frac{1 + z/4}{1 + z + \frac{4z^2}{9} + \frac{z^3}{9}}\right\} \qquad (1.12)$$

Where:

$$z = \sqrt{i\omega\tau_D + \frac{\tau_D}{T_{1,2e}}}; \tau_D = \frac{d^2}{D} \qquad (1.13)$$

Where τ_D is the correlation time for the relative translational diffusion,

$T_{1,2e}$ is the longitudinal/transverse electron spin relaxation time.

Outer sphere relaxation rate contribution to overall T_1 is typically lower

than that of the inner sphere, however there are exceptions. The outer sphere

contribution becomes more important where the inner coordination sphere has

no water molecules coordinated to the metal centre. Outer sphere contributions

can be easily seen on NMR diffusion (NMRD) profiles generated using Fast-Field Cycling NMR (FFC-NMR). **Figure 1.24** shows the NMRD profiles of Gd^{3+}−TETA, which has a hydration number of 0 and therefore displays only outer sphere contributions to relaxivity. The relaxivity across all frequencies was lower compared with ligands containing inner-sphere water molecule ($q \neq$ 0), however outer-sphere contribution is clearly present.
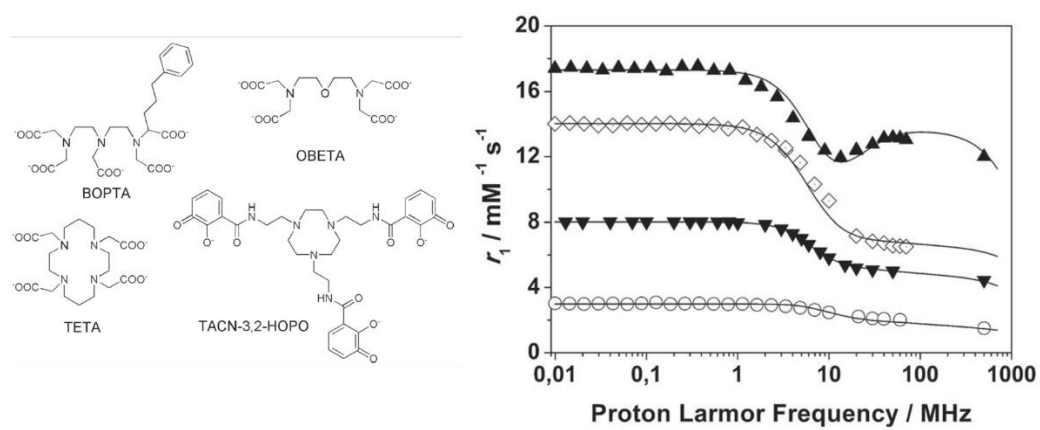
Figure 1.24 *Proton NMRD profiles of MRI contrast agents Gd^{3+}-TETA (○)*
with q=0, Gd^{3+}-BOPTA (▼)with q=1, Gd^{3+}-OBETA (◇) with q=2, and Gd^{3+}-
TACN-3,2-HOPO (▲)with q=3.[57]

1.3.2 Inner Sphere Relaxation Mechanism for Longitudinal Relaxation

Rate

The inner sphere relaxation rates of water in solutions containing Gd^{3+} based contrast agents mainly depend on the hydration number q, which represents the number of water molecules directly coordinated to the metal centre, the lifetime of water residence time τ_m, the rotational correlation time of the contrast agent, τ_R and the relaxation rate of the water molecule coordinated directly to the metal centre of the contrast agent $1/T_{1m}$ (Equation (1.14), **Figure 1.22**). The dependence on the hydration number (q) can be clearly seen on the NMRD profiles shown on **Figure 1.24**, where relaxivity increases across all frequencies as the q number is varied from 0 to 3. The lifetime of water residence time is simply the reciprocal of the exchange rate of the inner-sphere water molecule and the bulk water in the outer hydration sphere $\tau_m = 1/k_{ex}$. The effect on water exchange can be observed using FFC-NMR where longer water residence times result in lower relaxivities at high frequencies. [57]

$$R_1^{IS} = \frac{[CA]q}{55.5} \frac{1}{T_{1m} + \tau_m} \qquad (1.14)$$

Most molecular contrast agents based on Gd^{3+} are in the fast water exchange regime ($\tau_m < T_{1m}$) where the lifetime of water residence time is in the nanosecond region. When this condition is met the T_{1m} term dominates equation (1.14). In some cases, the water exchange regime could be intermediate/fast ($\tau_m \geq T_{1m}$) where τ_m moves into the microsecond region and becomes the more important parameter in the equation. Because the IS and OS

contributions to relaxivity have different dependency on temperature it is possible to investigate the water exchange regime using temperature-variable relaxometry. OS contribution decreases exponentially with increasing temperature because both the Gd^{3+} electronic relaxation and the correlation time for the relative translational diffusion (τ_D) decrease with temperature. Thompson *et al.* have demonstrated that in the fast exchange regime the relaxivity (r_1, mM^{-1} s^{-1}) decreases exponentially with increasing temperature for both IS and OS contributions. In case of intermediate/slow exchange regimes, OS maintains this trend, whilst the inner sphere contribution (r^{IS}) increases with increasing temperature. The resultant overall profile starts off with exponential decrease until a certain temperature and then the relaxivity starts to increase again.[57,58]

The relaxation rate of the inner-sphere water molecule ($1/T_{1m}$) is dependent on both through-space interactions described by the dipolar term, DD; and through bond interactions which are described by the scalar term, SC (equation (1.15)).

$$R_{1m} = R_1^{DD} + R_1^{SC} \qquad (1.15)$$

The DD term, driven by dipole-dipole interactions between spins I and S is described by equation (1.16):

$$R_1^{DD} = \frac{2}{15}\left(\frac{\mu_0}{4\pi}\right)^2 \frac{\gamma_S^2 \gamma_I^2 \hbar^2}{r_{IS}^6} S(S+1)\left[\frac{3\tau_{c1}}{1+\omega_I^2\tau_{c1}^2} + \frac{7\tau_{c2}}{1+\omega_S^2\tau_{c2}^2}\right] \qquad (1.16)$$

Where μ_0 is the vacuum permeability, $\hbar = (h/2\pi)$, τ_{c1} and τ_{c2} are the dipole-dipole correlation times for the longitudinal and transverse relaxation respectively. The correlation times describe the orientation of the electron spin-nuclear spin vector and play a key role in the change in inner-water relaxivity and contain three terms: the electron relaxation times ($T_{1,2e}$), the lifetime of water residence time (τ_m) and the rotational correlation time, τ_R (equation (1.17)).

$$\frac{1}{\tau_{c1}} = \frac{1}{T_{1e}} + \frac{1}{\tau_m} + \frac{1}{\tau_R} \qquad\qquad \frac{1}{\tau_{c2}} = \frac{1}{T_{2e}} + \frac{1}{\tau_m} + \frac{1}{\tau_R} \qquad \textit{(1.17)}$$

In small molecules characterised by fast tumbling τ_R is small and the relaxation times are relatively slow compared with nano contrast agents, which tumble more slowly and have a large τ_R. **Figure 1.25** shows the dependence of relaxation on the size of the contrast agents (f_0 indicates the Larmor frequency). Other important factors that follow from equation (1.17) are the electron relaxation times (T_{ie}, i=1,2), the water and protic exchange(τ_m).

In contrast, the scalar term is unaffected by the molecular reorientation as it describes through-bond effects and is dependant only on the electron spin relaxation times and the water exchange (equation (1.18)):

$$R_1^{SC} = \frac{2}{3}\left(\frac{A}{\hbar}\right)^2 S(S+1)\left[\frac{\tau_{e1}}{1 + \omega_s^2 \tau_{e1}^2}\right] \qquad \textit{(1.18)}$$
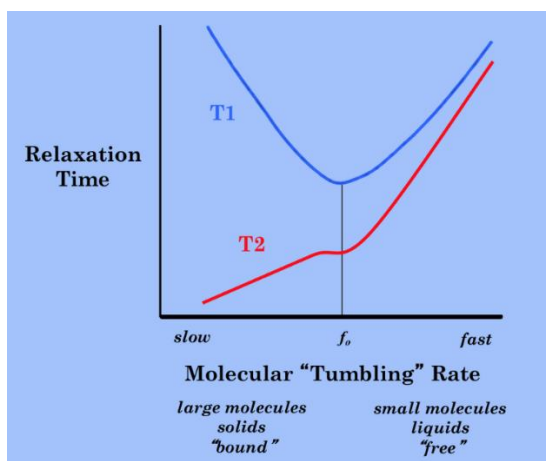
Figure 1.25 *Molecular tumbling effects on T_1 relaxation times. Typically, T_1 gets progressively shorter as structures reach nanometer sizes and then starts to increase again region as species move towards the micrometer sizes.*[40,59]

The Fermi contact coupling constant (A\ℏ) has energy in the MHz region. It is responsible for the isotropic hyperfine coupling and the fermi contact is the magnetic interaction between the Gd^{3+} electrons and the proton nucleus. Expression for A is shown in equation (1.19):

$$A = -\frac{2}{3}\mu_0\langle \mu_n . \mu_e \rangle |\Psi(0)|^2 \qquad (\textit{1.19})$$

$$\frac{1}{\tau_{e1}} = \frac{1}{T_{1e}} + \frac{1}{\tau_m} \qquad (\textit{1.20})$$

Where $\Psi(0)$ is the value of the electron wavefunction at the nucleus and τ_{e1} is the electron correlation time for the longitudinal correlation (equation (1.20)).

It was observed that in systems where water exchange of the solvent molecule in the IS is too slow (high τ_m) relaxivity is dominated by second-sphere effects where τ_m is much faster. This can be due to lower residual

negative charge on the complex or the presence of phosphonate arms on the chelate.[60,61]

1.4 Ion recognition using lanthanides

Methods of recognising the presence of specific species in solution are very important in industry and medicine. It is clear that there is an opportunity within lanthanide chelates, with their tuneable structure and variable coordination sphere, to facilitate binding of different species, with some kind of measurable output. This is most popularly exploited through emissive lanthanide species including Sm^{3+}, Eu^{3+}, Tb^{3+} and Dy^{3+}. Spectrofluorimetry is often employed to evaluate whether a given molecule would bind to the metal centre of a lanthanide chelate, such as $Eu^{3+}-DOTA$, and perturb q. Titrations of a fluorescent species (containing Eu^{3+} ions, for example) with a binding moiety can yield association constants (K_A) by monitoring changes in q and/or luminescent intensity.[62] A typical equilibrium is defined in Equation (1.20) and association constant in Equation (1.21), where A represents a lanthanide ligand, B represents a guest binding moiety and AB the association between them.[63]

$$A + B \rightleftharpoons AB \qquad (1.20)$$

$$K_A = \frac{[AB]}{[A][B]} \qquad (1.21)$$

The association constant can be found by solving series of equations through linear algebra and DynaFit and other software packages can calculate

K_A effortlessly.[63,64] This approach has been widely used in the literature to observe binding between lanthanide chelates and guest binding moieties, with some examples shown in the following sections. Specifically, these sections focus on phosphate and oxyanion binding as these functional groups are present on the nerve agent-tyrosine adduct investigated in this thesis.

1.4.1 Spectrofluorimetry and design of lanthanide complexes for phosphate and oxyanion detection

Spectrofluorimetry is a technique used for the detection of photoluminescent emission and photoluminescent analysis of liquid mixtures. Fluorescent emission is observed in aromatic molecules (fluorophores), whereas phosphorescence arises from metal complexes, including rare earth materials. Lanthanide complexes containing europium and terbium trivalent ions have been excessively studied in literature as phosphorescent dyes. Their longer emission lifetimes compared with organic fluorophores offers the ability to separate their signal from the signals of common biological molecules during fluorescent spectroscopy. Their line-like emission lines due to well-defined transitions enable ratiometric studies and the calculation of binding kinetics.

The most important transitions in Eu^{3+} emission in the context of binding detection are the hyperfine transition $\Delta J = 2$, which is sensitive to binding at the Eu^{3+} centre and the $\Delta J = 1$ transition which is used as an internal reference. Ratiometric studies of the binding kinetics of a large range

of molecules with biologically relevant anions such as phosphate, citrate, bicarbonate, acetate, and others have enabled the detection of these anions in solution and real-time monitoring of biologically relevant chemical reactions, such as enzymatic activity.[65] Detection of larger molecules, such as insulin receptors and energy carriers such as ATP and ADP (which play an important role in disease detection and progression) have also been reported.[66]

Several ligands incorporating lanthanides have been developed for the detection of phosphate in this way.[67,68,65] Phosphate has been shown to bind in different modes, depending on the type of ligand and functionalisation, unlike other ions which exhibit the same binding mode independent of the ligand. One factor influencing the binding of phosphate appeared to be the size of the binding pocket: all complexes designed to bind phosphate are characterised with a large binding pocket with $q > 1$.[67,68,65] Inorganic phosphate was successfully detected using series of tripodal ligand scaffolds (**Figure 1.26**).[69] The tripodal ligand scaffolds ranged between $q = 2$ and 3. Inorganic phosphate showed both bimodal and trimodal binding to $q = 3$ tripodal ligands depending on the functionalisation of their side arms. In neutral residues (R$-$H and R$-$CH$_2$OH) phosphate displaced all three inner-sphere water molecules, with K_A of 14.5 and 15.9 respectively. In the scaffold containing positively charged cationic lysine residue (R$-$CH$_2$CH$_2$CH$_2$CH$_2$NH$_3^+$) only two out of the three inner-sphere water molecules were displaced, leaving a single water coordinated to the Eu^{3+} ion and yielding and association constant K_A of 11.3. Interestingly negatively charged groups such as glutamic acid (R

$= CH_2CH_2COO^-$) and cysteine (R = $CH_2SO_3^-$) binding to phosphate was not observed, possibly due to repulsion between the residues and the phosphate anion. Phosphate binding did not show any affinity discrimination between q = 2 and q = 3 tripodal ligands.

R =		Log k_A
serine	OH	15.9
glycine	H	14.5
lysine	$NH_3^{\oplus}$	11.3
glutamic acid	$O^{\ominus}$	N/A
cysteine	$SO_3^{\ominus}$	N/A
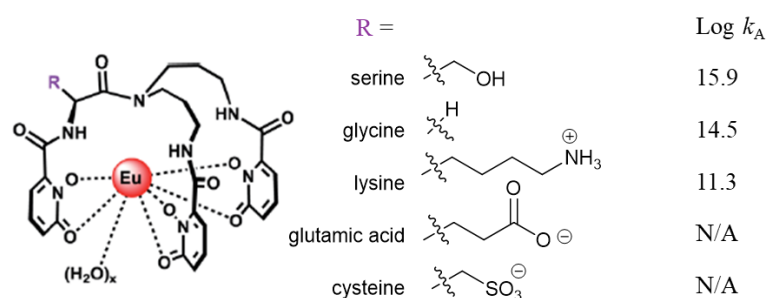
Figure 1.26 *Tripodal type ligand for the detection of phosphate. R = H, CH₂OH or CH₂CH₂CH₂CH₂NH₃⁺. x = 2,3.*[70]

A Tb-based receptor,[71] cyclen-based Ln^{3+} receptor[72] and a complex detection system constructed from Eu^{3+}, ciprofloxacin (CIP) and a surfactant[68] were also developed by three different groups to bind phosphate (**Figure 1.27**). The Tb-based receptor had an interesting mechanism of action. [71] The presence of H_2PO_4 caused initially a displacement of one of the cyclen-based Tb^{3+} moieties from the receptor with initial association constant log $K_{A\ 1:1}$ = 6.6, followed by a displacement of the second moiety with log $K_{A\ 1:2}$ = 13.8. The displacement causes a quenching of the fluorescent intensity by the solvent, which enabled the detection of H_2PO_4 (**Figure 1.27** a). [71]
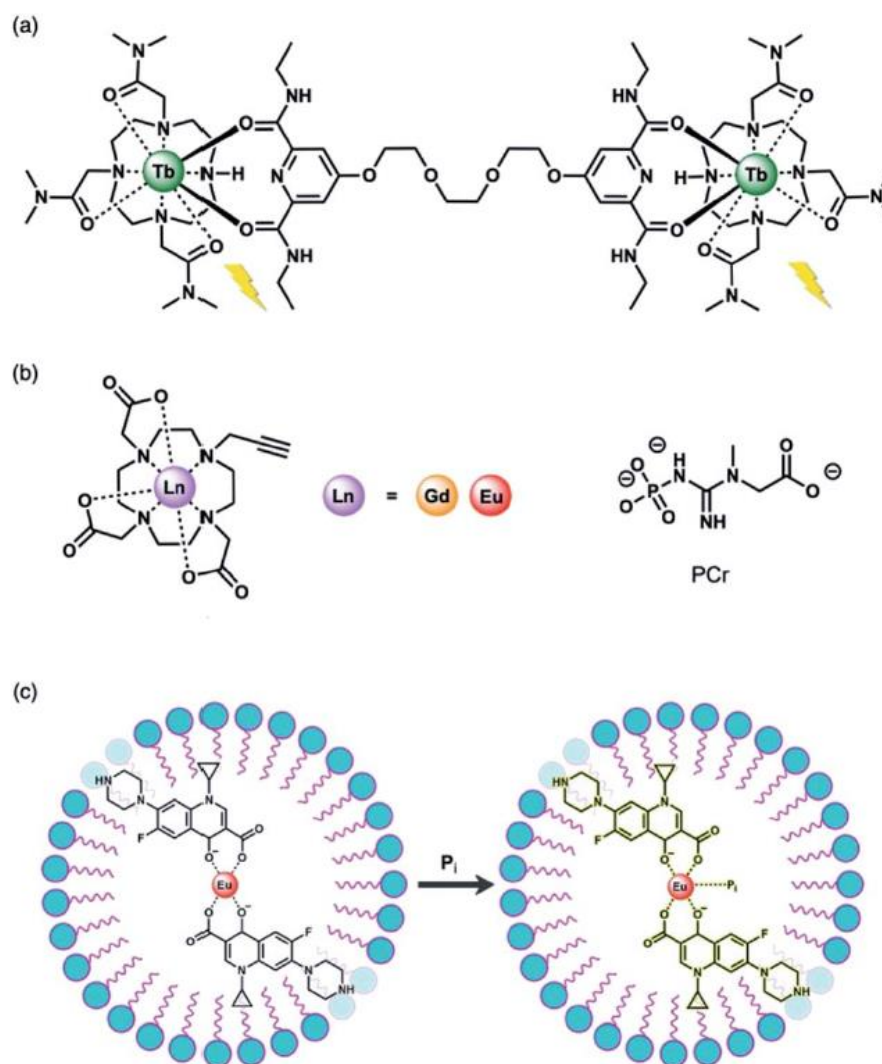
Figure 1.27 Tb-based receptor (a), cyclen-based Ln³⁺ receptor (b) and a complex detection system constructed from Eu³⁺, ciprofloxacin (CIP) and a surfactant (c) for the detection of inorganic phosphate.[70]

In contrast with the tripodal ligands, in cyclen-based ligands phosphate was found to bind in monodentate manner leaving one water molecule coordinated at the inner-sphere metal centre.[72] Inorganic phosphate bound the Eu cyclen ligand (**Figure 1.27** b) with association constant log K_A = 2.29. The same ligand was found to bind ATP with log K_A = 2.30 and PCr (**Figure 1.27** b) with K_A = 2.08. [72] In the case with ciprofloxacin (CIP) – Eu^{3+}−surfactant system the ratio between the metal and ciprofloxacin was $[Eu^{3+}]/[CIP]$ = 3:2.[68] This meant that each Eu^{3+} ion was ligated by less than one CIP molecule. Each CIP ligand had two oxygen coordination sites and lanthanide ions such as Eu^{3+} have a coordination number 8-9, typically shown to be nine. This leaves 7-8 water molecules coordinated to the metal centre affording a large binding pocket for phosphate.[68] The exact binding mode was not investigated, however the requirement for a larger binding space for phosphate was reinforced. Because the intensity of the transition at 415 nm grew linearly with increasing phosphate concentration association constant could not be calculated.

A recent development in phosphate sensing was developed by Butler and co-workers, who reported a new synthetic class of lanthanide probes incorporating an oxyquinoline moiety into the cyclen structure (**Figure 1.28**).[66,67] This new type of pendant arm had three important functionalities which prove advantageous over other examples in the literature: to provide bidentate binding to the metal ion through the oxygen and nitrogen atom; to introduce steric demand and deter oxyanions such as bicarbonate from

binding (to preserve specificity); and to protect the complex from citrate binding (a common bio-anion). Typically, side arms in cyclen-based ligands bind the central lanthanide ion in a monodentate fashion, meaning that all four *N*-sites of cyclen must be functionalised in order to saturate eight of the nine coordination spaces on the metal and produce an inert complex. As discussed above phosphate demands a large binding pocket and so in all examples above to fulfil this requirement complexes were synthesised with hydration numbers larger than one. This means that the metal ion is held in the pocket by weaker Columbic interactions which has the potential to affect stability. By incorporating a side arm capable of binding the metal in a bidentate fashion, the larger binding pocket for phosphate is still present, however the hydration number remained lower than 2. In the example of [Eu.Bn]$^+$, the oxyquinoline arm was completed with a benzyl moiety introducing steric bulk to protect against oxyanion binding and shape the binding pocket for phosphate. Citrate showed preferred binding to the quinoline arm over the metal centre which reinforced the selectivity of the metal-binding site for phosphate. Lastly, the complex had an overall charge of +1, complementing the -1 charge on phosphate. This intelligent synthetic design produced a luminescent probe highly selective towards phosphate binding over selection of biologically relevant oxyanions. Binding to inorganic phosphate was mediated with an association constant log K_A = 3.56, whereas AMP and ADP showed log K_A of 4.02 and 3.65 respectively. [67,70]
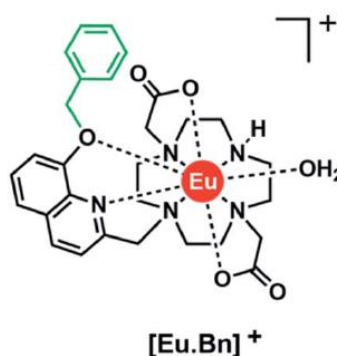
Figure 1.28 *Oxyquinoline DO2A ligand for the selective detection of inorganic phosphate.* [67]

   Binding of phosphate present in larger biological molecules has also been investigated.[67] Adenosine triphosphate (ATP), adenosine diphosphate (ADP) and adenosine monophosphate (AMP) all differ just by the number of phosphate molecules present in a chain which presents an interesting challenge for their specific detection. Sophisticated and innovative synthetic design would be required for the selective detection of each of these biomolecules. More interestingly, lanthanide-based detection systems were also synthesised for the detection of phosphorylated insulin receptors which can be found inside cells and not as soluble proteins in the blood. [73] Fluorescent/phosphorescent probes engineered to penetrate inside cells would be ideal for the successful fluorescent microscopy detection of these important biological molecules.

Mailhot *et al.* reported a cyclen-based ligand completed with two quinoline arms in a *trans* manner for the selective detection of ATP and ADP over AMP and inorganic phosphate.[66] ATP/ADP bind the metal core through the γ-phosphate and the selectivity arose from extra stabilization of the interaction through hydrogen bonding of the quinoline arms with the β-phosphate group (**Figure 1.29** a)). This binding mode was confirmed through high resolution mass spectrometry.[66] An important feature of the ligand shown in **Figure 1.29** a) were the amide-containing side arms of the complex. When these were replaced by carboxylate arms such as the ones present in DOTA, DO3A and DO2A the affinity for ATP and ADP was reduced due to the less electropositive nature of the metal ion.[70] Selective detection of AMP was reported by Bodman *et al.* by slight modification of the oxyquinoline receptor shown on **Figure 1.28**. The benzyl moiety of the benzyloxy quinoline arm was decorated with boronic acid to produce [Eu · *m*BOH$_2$]$^+$ ligand (**Figure 1.29** b)). The function of the boronic acid was to strengthen binding through the interactions with the ribose of AMP at the *cis*-diol. Incorporating a boronic acid onto the benzyl resulted in lower affinity for inorganic phosphate with log K_A = 3.31 and increased affinity for AMP with log K_A = 4.07 and ADP with log K_A = 3.84.[67]
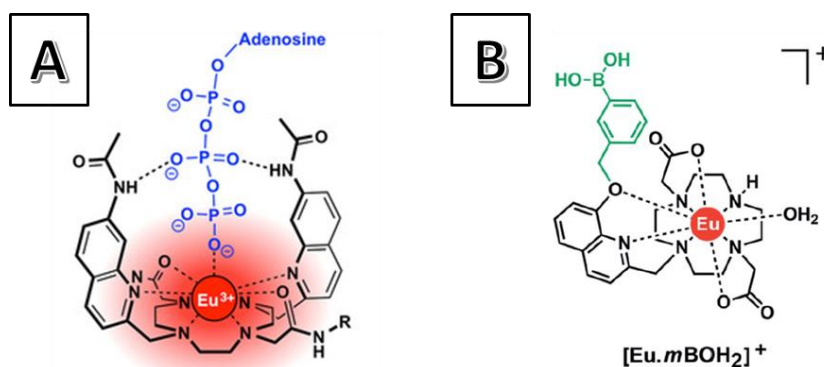
Figure 1.29 *A: Quinoline-functionalised cyclen-based receptor for selective detection of ADP and ATP.* [66] *B: Oxyquinoline DO2A ligand with boronic acid for the selective detection of AMP.* [67]

Phosphorylation is an important post-translational modification in proteins. It plays a crucial role in cell signalling and protein function regulation. Parker and co-workers developed series of acridone-functionalised cyclen ligands for the selective detection of phosphorylated tyrosine.[74] The ligand shown in **Figure 1.30** showed selective binding to phosphotyrosine over phosphoserine.
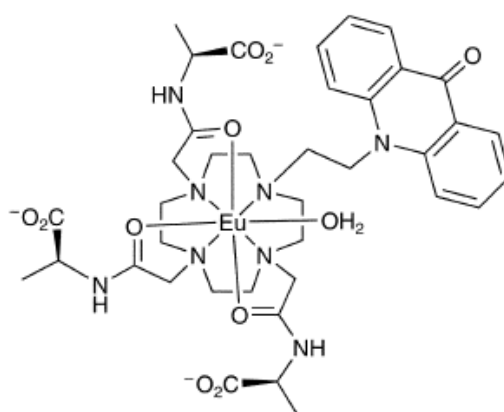
Figure 1.30 *Cyclen-based ligand with acridone side arm for the selective detection of phosphorylated insulin receptors.* [74]

It is therefore clear that there are a number of design features of lanthanide chelates which can aid in selectivity and binding of phosphate-based groups, and fluorimetry has been shown to be a useful method of assessing binding behaviour. Monitoring phosphates is a very useful approach for mimicking nerve agent adducts and the examples above are a useful guide to designing a selective probe for these substances.

1.4.2 Detection of molecules using NMR Relaxometry/MRI

Although fluorimetry has been proven a valid method for the detection of species binding to a metal chelate centre, it is clear that these structures could easily be adapted to facilitate monitoring using MRI, through exploiting changes in the water behaviour at the metal centre simply by replacing the central emissive lanthanide with Gd^{3+} ion. There are a number of examples of this in the literature where changes in the hydration number q due to metal binding are used to produce a change in signal. These are extensively discussed in a number of review articles,[31,42] and here, a selection of pertinent examples will be described.

One example of using the hydration number to perturb change in MRI signal is by using a type of ligand which physically blocks the hydration site (q=0). For example in the probe (1-(2-(β-galactopyranosyloxy)propyl)-4,7,10tris(carboxymethyl)-1,4,7,10-tetraazacyclododecane)gadolinium(III) (EGadMe), a galactopyranose fragment is blocking the nineth coordination space.[75] Upon exposure to β-Galactosidase (an enzyme important in gene

expression) the blocking fragment is enzymatically cleaved, resulting in 200%
increase in relaxivity from 0.90 to 2.72 mM^{-1} s^{-1} (as q changes from 0 to 1,
Figure 1.31, A).[75]

Increase in MRI signal can also be achieved if the q number is increased by
a conformational change in the lanthanide chelate. One example is a contrast
agent based on Gd^{3+}–DOTA, bearing a pendant β-D-glucopyranuronic acid arm
($q = 2$). This molecular probe was designed to bind β-glucuronidase, which
causes cleavage of the pendant arm and reduction of the hydration number
from $q = 2$ to $q = 1$. This causes a decrease in the MRI signal upon binding
from 4.75 to 3.90 mM^{-1} s^{-1} (20 % decrease, **Figure 1.31**, B).[76]

It is clear that all these examples have been used for the detection of
biomolecules as 'on/off' switches', however, not so much has been done in
terms of determining binding behaviour and K_A using MRI signal changes.[77]
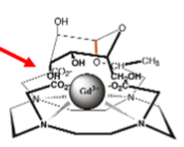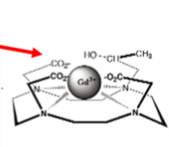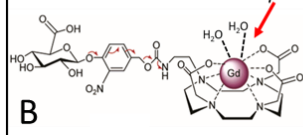
Molecular CAs			r_1 change, mM^{-1} s^{-1}	% change
A	$q=0$	β-galactosidase → $q=1$	0.90 to 2.72	200% increase
B	$q=2$	β-glucoronidase → $q=1$	4.75 to 3.90	20% decrease

*Figure 1.31 **A**– EGadMe with galactopyranose blocking q (left) activated by β-
Galactosidase. EGadMe with coordinated water (right).*[75] ***B**– Self-immolative
Gd^{3+}-chelate complex with q=2 (right) triggered by β-glucuronidase, resulting
in lower relaxivity complex (left).* [76]

1.5   Silica-based nanomaterials as contrast agents

Current contrast agents used in the clinical setting are characterised with low sensitivity.[78] This is in part due to their low molecular weight and limited coordination sites for the chelation of the lanthanide metal. As shown in section 1.3.2 the spectral density function depends on the correlation time (τ_c, s) which is in turn dependant on several parameters, namely the electronic relaxation times (T_{1e}, s), the reciprocal of the water exchange rate (τ_m, s) and the rotational correlation time (τ_R, s). These can be perturbed to increase the relaxivity of the probe and hence deliver selective enhancement of the signal-to-noise ratio.[31] The rotational correlation time is a relatively easy to change as it depends on the tumbling of the complex and therefore on the size of the contrast agent. Carniato *et al.* have shown that for given set of parameters in the fast exchange regime ($\tau_m = 30$ ns) the rotational correlation has a significant effect on longitudinal relaxation times, especially for B_0 in the range $0.5 - 2.0$ T.[78] To date, several strategies have been developed to increase τ_R, especially in systems used for detection.[79, 80, 81, 82] Proteins and nanoparticles which tumble slowly in solution have shown great enhancement in relaxation times when complexed with gadolinium contrast agents. This becomes particularly important in the development of responsive MRI probes for detection because the increased relaxivity translates into an increased response in signal upon detection. Some examples include the receptor-induced magnetisation effect (RIME), involving the complexation of a molecular contrast agent with targeted protein, which dramatically changes

the rotational corelation times and the relaxivity of the complex upon detection.

This has been shown by Breckwoldt *et al.* which designed a probe (Gd-bis-5HT-DTPA) for the detection of the inflammation biomarker Myeloper-oxidase (MPO) secreted by neutrophils.[80] In the presence of the biomarker MPO, the oxygen on the 5-hydroxyindole moiety of the Gd-bis-5HT-DTPA forms a radical and undergoes polymerisation and protein binding.[83] This led to increase in molecular weight and τ_R, dramatically shortening longitudinal relaxation times (T_1, s) manifesting as light areas on the MR image where inflammation is present. Relaxivity of the Gd-bis-5HT-DTPA probe increased from 5.6 mM^{-1} s^{-1} to 9.52 mM^{-1} s^{-1} in inflammation site.[83]* Other examples of RIME include the work of Peter Caravan *et al.*[81] They developed a molecular contrast agent based on Gd^{3+}−DTPA termed MS-325. This molecular contrast agent featured a diphenylphosphinamide satellite group for the binding of human serum albumin (HSA). Because this protein is abundant in the blood, MS-325 offers and excellent method for monitoring blood flow through 800 % increase in longitudinal relaxivity in the presence of HSA (from 5.6 mM^{-1} s^{-1} to 50.8 mM^{-1} s^{-1}).

Mesoporous silica nanoparticles (MSNs) functionalised with gadolinium chelates have been widely used as MRI contrast agents. Due to their large size, surface-to-volume ratio and pore size, MSNs exhibit high

---

* "After" relaxivity value based on the before/after ratio (1.7) provided by the authors and the relaxivity on the "before" complex.

rotational correlation time τ_R and low mean lifetime of water residence time τ_m.[78,84,85] Mobile composition of matter No. 41 (MCM–41) are a type of mesoporous silica nanoparticles that are easily synthesised using a standard sol-gel methods,[86] with a structure that can be controlled by selecting a suitable surfactant template[87] and post-grafting methods.[88] An interesting example of increase in τ_R was developed by Carniato *et al.* by anchoring Gd^{3+}–DOTA-like molecular agents on the surfaces of mesoporous silica materials.[89] A six-fold increase in relaxivity (27 mM^{-1} s^{-1}, 20 MHz, 310 K, 0.1 wt% xanthan gum) was observed for the hybrid material incorporating MCM-41 MSNs and the molecular gadolinium agent. In fact, the relaxivity enhancement mediated by analogous hybrid material featuring a different silica framework SBA-15 was only 6.7 mM^{-1} s^{-1}, measured at equivalent conditions. This relaxivity is more comparable to molecular contrast agents, such as Gd^{3+}–DTPA.[90] This excellent work showcased that MCM-41 mesoporous silica nanoparticles have advantageous properties over other silica materials in the context of MRI contrast agents. From the examples above it is clear that incorporating nanostructures into the design of the MRI detection system for nerve agent-protein adducts can be advantageous.

Another class of interesting silica-based materials are silsesquioxanes. Silsesquioxanes[†] are silica-based cage-like structures that have been used as catalysts, for the synthesis of hybrid materials with enhanced thermal

---

[†] *sil-* (silicon), *sesqui-* (one-and-a-half), *ox-* (oxygen) *-ane* (alkane), empirical formula is $(RSiO_{1.5})_n$

properties and as fluorescent probes.[91–93] Polyhedral oligomeric silsesquioxanes (POSS) are three-dimensional materials which have an inorganic cage-like framework (polyhedral), with one silicon atom connected to one and a half oxygen atoms in a cube-like structure, where every 'edge' of the cube represents a Si-O-Si bond. The corners of the polyhedral frame are functionalised with organic groups, typically alkanes. Silsesquioxanes can be coordinated to metals either by utilising open-corner POSS to form metallasilsesquioxanes (M-POSS, functional group Si–O–M) as ligands, or by functionalising the organic part of the cage with metal chelates. [92-94]

In a recent example, a silsesquioxane cage with imidazolium-based corners was functionalised to generate a novel fluorescent probe by incorporating a lanthanide complex $Eu(tta)_4$, (tta: 2-thenoyltrifluoroacetone) into the organic layer of the POSS (**Figure 1.32**). This functionalised silsesquioxane was designed to detect ions, with a high sensitivity to Cu^{2+}.[92] The POSS cage served to generate a significant enhancement in the $^5D_0 \rightarrow {}^7F_2$ emission intensity through the antenna effect. The hybrid material displayed higher fluorescence intensity, higher thermostability and longer lifetime in comparison with the corresponding molecular lanthanide complex $Eu(tta)_4$. When the probe was exposed to ions, the fluorescent signal was significantly reduced. In the presence of Cu^{2+} the signal was completely quenched, potentially due to the exchange interaction between Cu^{2+} and Eu^{3+}.[92]
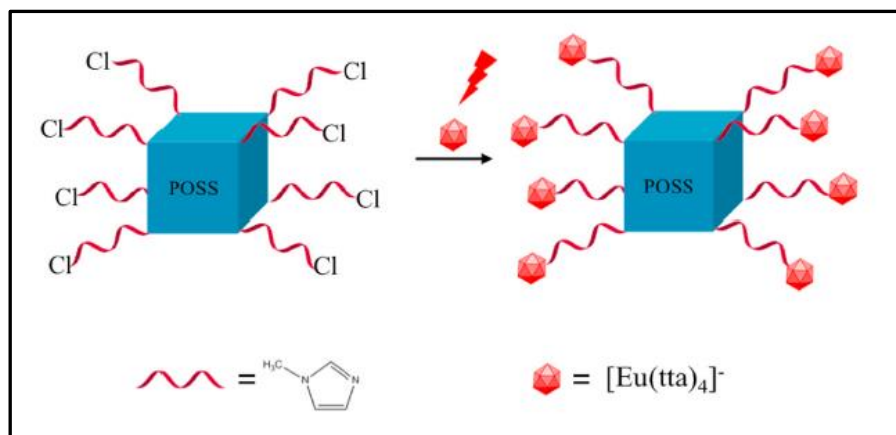
Figure 1.32 *Final step of the synthesis of POSS-min[Eu(tta)₄]⁻ showing the building blocks of the hybrid material: imidazolium arms (left) and the fluorescent lanthanide complex (right) attached to the Si–O–Si cage.* [92]

Replacement of fluorescent Eu^{3+} ions with Gd^{3+} ions enabled an MRI active probe to be produced. [94] The corners of aminopropyl substituted silsesquioxane $T_8(CH_2CH_2\text{-}CH_2NH_2)_8$ were functionalised with molecular MRI contrast agents 1,4,7,10-tetraazacyclododececane, 1-(glutaric acid)-4,7,10-triacetic acid (DOTAGA) and 1,4,7,10-tetraazacyclododecane-1-(4-(carboxymethyl)benzoic)-4,7,10-triacetic acid (DOTABA) to yield two novel MRI contrast agents (*vide infra* Chapter 4 and **Figure 4.2**). [94]

Silsesquioxanes are great precursors for porous nanomaterials. Octa carboxyl polyhedral oligomeric silsesquioxane was used to prepare mesoporous nanostructures containing iron or cobalt.[95] Fe–POSS and Co–POSS nanoparticles were synthesised using solution chemistry. Specifically, the octa carboxy–POSS and the transition metal compounds were refluxed at 60 °C in a coordination reaction to yield the product, which was characterised. The pore diameters were calculated from the desorption branch isotherm using the

Barret–Joyner–Halenda (BJH) method and were found to be between 20 and 30 nm for both M–POSS nanoparticles. The size of the nanoparticles was reported to be 50 nm, however nanoparticles have formed an 'assembly' or nanoparticle clusters (**Figure 1.33**).[95]

An alternative method for the preparation of mesoporous nanoparticles from silsesquioxane cages is thermolysis. An example involved the synthesis of luminescent rare earth doped silica nanoparticles from open-corner trisilanol (c-C_6H_{11})$_7$Si$_7$(OH)$_3$.[96] Instead of the simplistic synthesis involving direct corner-capping with metal oxides or chlorides this open-corner POSS was reacted with the chelated Eu^{3+} species [(THF)$_3$Li(μ-Cl)Eu[N(SiMe$_3$)$_2$]$_3$]. The resultant structure contained the lanthanide ion chelated by two open-corner POSS (M-[POSS]$_2$) (**Figure 1.34**). In the next step the nanoparticles were synthesised by thermolysis at 300 °C under inert atmosphere (N$_2$). TEM analysis showed spherical nanoparticles with size 13.5 ± 4.0 nm (**Figure 1.34**). Pore size was not shown.
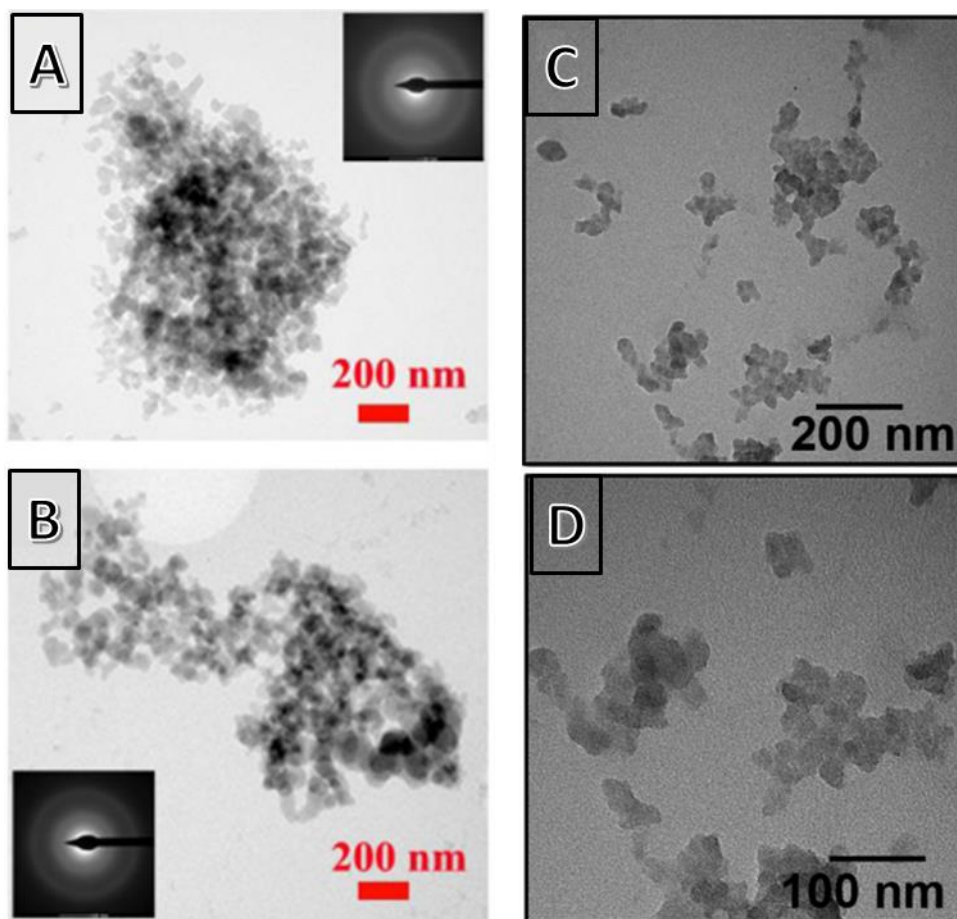
Figure 1.33 *TEM images of Fe-POSS (A) and Co-POSS (B) nanoparticles* [95] *and Eu-POSS nanoparticles.*[96]
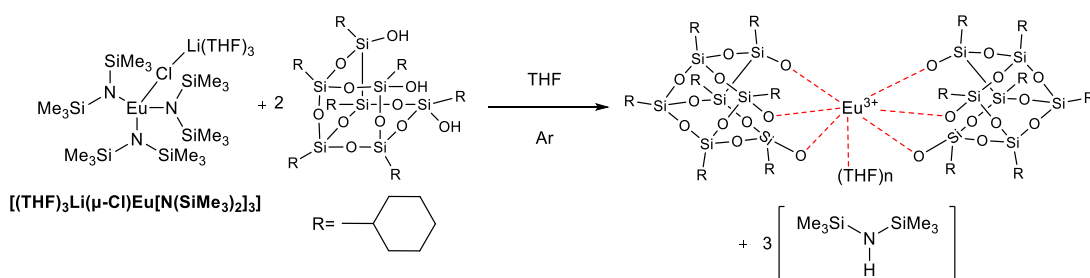
Figure 1.34 *The formation of M-[POSS]₂ from [(THF)₃Li(μ-Cl)Eu[N(SiMe₃)₂]₃] lanthanide chelate. The europium centre is apparently coordinated to six POSS oxygens, leaving three empty coordination spaces.*[96]

1.6   Research question, aims, objectives and hypothesis

There is an unmet need for developing a rapid method of detection for nerve agent exposure. Sarin-tyrosine adducts with structure similar to those shown on **Figure 1.35** are present in blood samples following exposure to the nerve agent sarin that may be accessible for novel imaging-based detection techniques, e.g., MRI. The aim of this project was to develop an MRI-based detection system for sarin-tyrosine adducts in biological samples. Lanthanide-based chelates have been shown to associate with negatively charged functional groups, such as carboxyl and phosphate, which are present in sarin-protein adducts.[63,65,97,98] Gadolinium-based molecular contrast agents have been shown to induce MRI signal change upon association with negatively charged groups/molecules due to a change in their q value.[31] This property may be utilised as a detection system whereby the chelate is designed to specifically bind desired moieties and a change in signal is indicative of binding and hence the presence of a nerve agent adduct (**Figure 1.35**). Furthermore, these molecular systems can be mapped onto mesoporous silica nanoparticles to amplify the signal in-part through altering the rotational correlation time (τ_R) of the contrast agent. Silsesquioxane nanoparticles could be explored as an alternative nano contrast agent to MSNs as their larger hydration number ($q > 1$) is expected to produce high relaxivity. In addition, the bigger binding pocket could potentially accommodate larger guest molecules in the inner sphere of the contrast agent. Therefore, the following research question was formulated:

How can MRI contrast agents be exploited for innovative detection of nerve agent-protein adducts?

The hypothesis of this research was that:

Sarin-tyrosine adducts can bind MRI contrast agents and be detected using MRI through change in relaxivity (r_1), providing a fast method for positive detection of patient exposure to the nerve agent sarin, and providing an approach which could be modified for other nerve agent species.
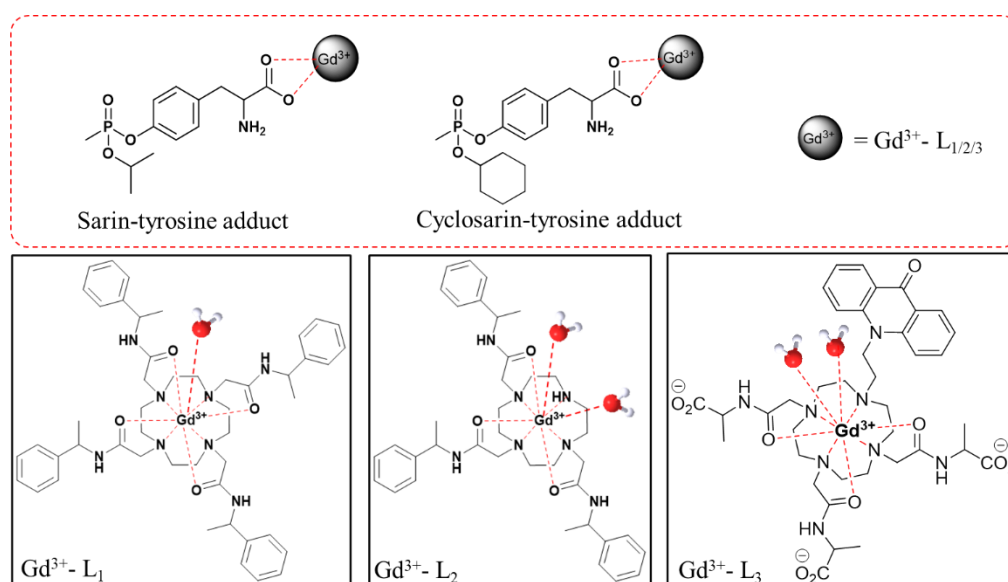
Figure 1.35 *Structure of target complexes for detection in this work and proposed binding mechanism to Gd^{3+} chelates. Both adducts were synthesised and provided by Dstl, Porton Down.*

This aim will be achieved through investigating the interactions between known contrast agent (Gd^{3+}–DOTA) and model molecules containing carboxyl and phosphate groups such as phosphate, ibuprofen, lysine, tyrosine, and phosphoserine. Spectrofluorimetry will be used to validate the changes in MRI signal observed during titrations with guest molecules. More interestingly, the binding at higher frequency (*i.e.* FFC-NMR) will be tested to investigate frequency effects on the MRI signal. Nuclear magnetic resonance (NMR) and nuclear magnetic resonance dispersion (NMRD) techniques will be utilised to better understand the interactions between chelates and guest molecules in aqueous solution and MRI signal amplification by nano contrast agents such as Gd^{3+}–DOTA−MSNs will be investigated. Finally, chelates L_{1-3} will be synthesised and tested for binding to sarin- and cyclosarin-tyrosine adducts (**Figure 1.35**).

2 Experimental and Characterisation Techniques

2.1 Experimental

2.1.1 General experimental

The solvents used were HPLC grade, water was passed through Elga PureLab system to collect Ultrapure® water with resistivity of 14.0 MΩ·cm. Unless specified otherwise chemicals were used as received and purchased from Sigma–Aldrich. The lanthanide ions were obtained as trichloride salts ($LnCl_3$) with purities higher than 98%. 2,2',2",2'''-(1,4,7,10-tetraazacyclododecane-1,4,7,10-tetrayl) tetraacetic acid (DOTA) and 1,4,7,10-tetraazacyclododecane-1,4,7,10-tetraacetic acid mono-N-hydroxysuccinimide ester (DOTA-NHS-Ester) were purchased from Chematech (Dijon, France). All measurements were conducted in water and change in pH was achieved by spiking the measured sample solution with hydrochloric acid (HCl) or sodium hydroxide (NaOH) solution in water.

Hydrodynamic size and zeta potential were measured in water at 25 °C using Zetasizer Nano ZS instrument produced by Malvern Panalytical, equipped with a helium-neon laser module with power rating of 4 mW. Light back-scattered from the zeta cell was measured at an angle of 173°. Reported values were derived from an average of three measurements. Samples were prepared at concentrations of 2 mg/ml in ultrapure water.

[1]H, and ^{13}C spectra were recorded on Bruker Avance III 600 (600 MHz), Bruker Avance Neo 500 (500 MHz) and Bruker Avance Neo 700 (700 MHz), the frequency specified for each spectrum. ^{29}Si NMR data were recorded on Bruker Avance Neo 700 machine, operated at 700 MHz. Spectra were recorded in deuterated solvents and chemical shifts (δ) were reported in ppm. The following abbreviations were used to describe multiplicity: s-singlet, d-doublet, t-triplet, q-quartet, m-multiplet.

Transmission electron microscope (TEM) images were recorded on JEOL 2100 200 kV instrument fitted with a LaB_6 filament giving a point resolution of 0.13 nm (UCL) and 0.23 nm (University of Warwick). Samples were prepared by drop-casting a suspension of material in water onto copper mesh TEM grids coated with formvar carbon, supplied by EM Resolutions. Energy dispersive X-Ray spectroscopy (EDX) were collected on an Oxford Instruments detector.[‡]

Phosphorescent titrations for phosphate, lysine, tyrosine and phosphoserine were recorded on Cary Eclipse Fluorescence Spectrometer by Agilent with excitation wavelength of 280 nm, Delay time 0.2 ms and Gate time 5 ms. Emission was recorded between 550 and 750 nm. Phosphorescent titration for ibuprofen at pH 8-9 was recorded on Fluorolog-QM by HORIBA with excitation wavelength of 392 nm. Emission was recorded between 500 and 700 nm.

[‡] Imaging and EDX of silsesquioxane nanoparticles were recorded by Dr Gemma-Louise Davis at the University of Warwick.

The benchtop relaxometer used in this work was Oxford Instruments MQC+ benchtop NMR analyser equipped with a permanent magnet operating at a resonant frequency of 23.4 MHz which is an equivalent of 0.55 Tesla for ^{1}H nuclei. MRI studies at Dstl were performed on Avance III 600MHz/14T Wide-bore Spectrometer and MRI Scanner.

2.1.2   Experimental for Chapter 3

2.1.2.1 Preparation of $Ln^{3+}-DOTA$ (Ln = Gd, Eu)

LnCl$_3$ (0.10 mmol, 1 equiv.) was dissolved in Ultrapure water (50 mL). DOTA (0.10 mmol, 1 equiv.) was added to the solution and the mixture was stirred at 80 °C for 18 hours. Free Ln^{3+} ions were measured using Arsenazo III assay.

2.1.2.2 Arsenazo III calibration curve
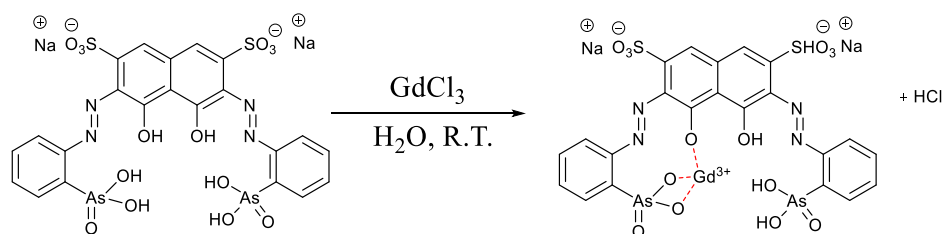
Arsenazo III (39.13 mg, 0.05 mmol) was dissolved in Ultrapure water (250 mL) to give a solution of 0.2 mM concentration. GdCl$_3$ (0.74 mg, 2 μmol) was dissolved in Ultrapure water (10 mL) to give a concentration of 0.2 mM, and this was used as a stock solution. Serial dilutions were used to prepare 25 concentrations of Gd^{3+} in water between 0.2 and 0.0002 mM. Each concentration of Gd^{3+} was analysed using UV-Visible spectrometer by mixing

100 µL of Arsenazo III (0.2 mM), 100 µL of the relevant Gd^{3+} concentration and 800 µL of water. 'Blank' sample was prepared by mixing 100 µL of Arsenazo III (0.2 mM) with Ultrapure water (900 µL). The absorbance was recorded between 500 and 700 nm (**Figure 2.1**, A). The absorbance of peak at 655 nm was plotted against Gd^{3+} concentration (mM) to generate the calibration curve (**Figure 2.1**, B). The linear region was found to be between 0.200 mM and 0.025 mM of gadolinium. All samples showed free Gd^{3+} content of < 10 %.

The absorbance of the pure reagent showed a single broad peak at 540 nm due to the symmetry of the complex. Addition of Gd^{3+} ions removed the symmetry and resulted in two additional peaks corresponding to the complexed reagent with gadolinium. The peak at $\lambda = 605$ nm can belongs to the analytical functional group unbound to the metal, whereas the more colour-intense band at $\lambda = 655$ nm belongs to the part of the molecule bound to Gd^{3+}.
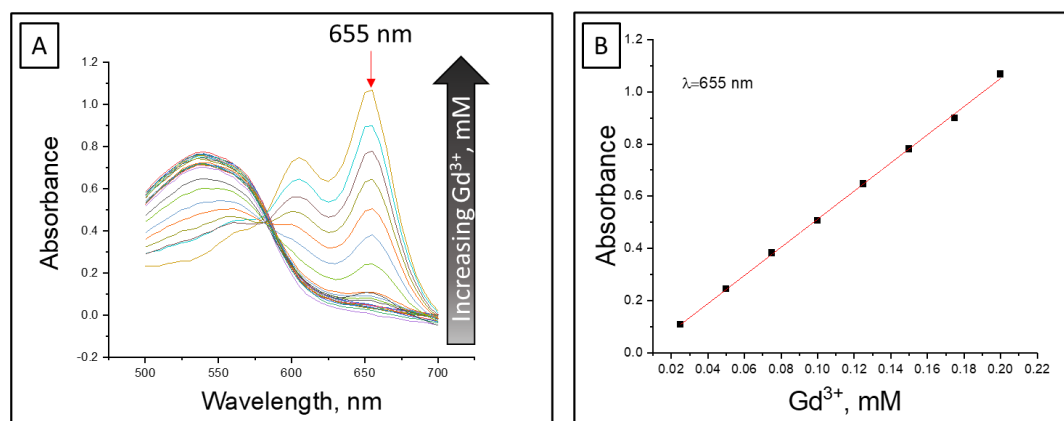
***Figure 2.1 A**– Absorbance of Arsenazo III at increasing Gd^{3+} concentration measured between 500 and 700 nm. The red arrow points at the binding sensitive peak at 655 nm. **B**– Linear region of the Arsenazo III calibration curve was detected between 0.025 and 0.2 mM of Gd^{3+}. Samples were prepared by mixing Arsenazo III solution (0.2 mM) with the solution of the desired Gd^{3+} concentration in water. The absorbance was recorded at 25 °C using a UV-Vis spectrometer at wavelength λ=655 nm.*

2.1.2.3 Calibration curve for Eu^{3+} detection

Calibration curve for the detection of free Eu^{3+} using Arsenazo III was generated in a similar manner to the calibration curve for Gd^{3+}. This was so to ensure that effects observed during fluorescent titrations were due to the interactions between the Eu^{3+}−DOTA and guest species, not Eu^{3+} metal ion with the guest species. The binding of Eu^{3+} to Arsenazo III was expected to be the same as Gd^{3+} as both are rare earth metals of charge 3+, and therefore the spectrum was expected to be representative of similar 1:1 complex between Arsenazo III and the metal ion.

To generate the calibration, curve the absorption spectrum of eight concentrations of Eu^{3+} with Arsenazo III was recorded between λ = 500 and λ

= 700 nm was recorded (**Figure 2.2** A). The spectrum was recorded after using Arsenazo III (0.2 mM) solution as a blank, which caused the broad Arsenazo III peak at $\lambda = 540$ nm to appear negative. This did not influence the peaks corresponding to the bound complex, at $\lambda = 610$ nm and $\lambda = 655$ nm. The intensity of the peak at 655 nm for eight concentrations of Eu^{3+} between 0.2 mM and 0.025 mM was plotted and used as a calibration curve (**Figure 2.2** B).
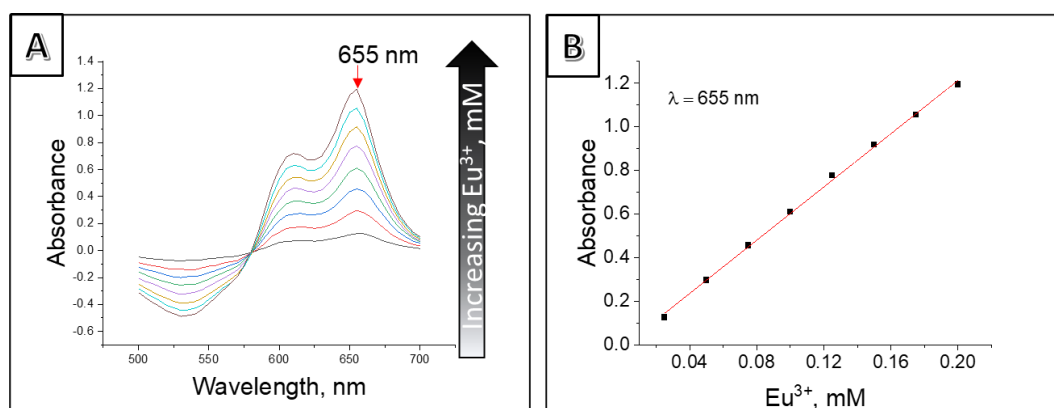
Figure 2.2 A*: Absorbance of Arsenazo III at increasing Eu³⁺ concentration measured between 500 and 700 nm. The red arrow points at the binding sensitive peak at 655 nm. **B**: Linear region of the Arsenazo III calibration curve was detected between 0.025 and 0.2 mM of Eu³⁺. Samples were prepared by mixing Arsenazo III solution (0.2 mM) with the solution of the desired Eu³⁺ concentration in water. The absorbance was recorded at 25 °C using a UV-Vis spectrometer at wavelength λ=655 nm.*

2.1.2.4 *Kinetic study with Arsenazo III and optimised synthetic procedure, Gd^{3+} chelation to DOTA at 18, 50 and 80 °C.*

DOTA (0.04 g, 0.1 mmol) was dissolved in water (50 mL). GdCl$_3$ (0.026 g, 0.1 mmol) was added to the solution with stirring at room temperature. The mixture was aliquoted into vials and the reaction let to proceed at three different temperatures – three vials at 18 °C, three vials at 50 °C and the remaining mixture was refluxed at 85 °C in a round bottom flask equipped with an air condenser. Aliquots (10 µL) of each mixture were taken at 15 time points between 0 and 291 minutes. Time zero was recorded as the time when the required temperatures were reached for all reactions. The aliquots were diluted where required and analysed using UV-Vis spectrometer by mixing 100 µL of Arsenazo III (0.2 mM), 10 µL of reaction aliquot at time t_n (n=0–15) and 890 µL of water. The absorbance was recorded between 500 and 700 nm. The absorbance of the peak at 655 nm was used to interpolate the Gd^{3+} concentration from the calibration curve using Origin software.

In order to determine the presence, if any, of free Gd^{3+} ions following chelate preparation, an Arsenazo III assay was carried out for each sample. Arsenazo III is a metal ion chelator which binds free Gd^{3+} to form Gd^{3+}–Arsenazo complex. This complex can be quantified colorimetrically. This molecule does not bind complexed metal ions which makes it an excellent tool for the determination and quantification of unchelated gadolinium in magnetic nanoparticles and molecular chelates, such as Gd^{3+}–DOTA.[99]

Here, the Arsenazo III assay enabled a study on the effects of time and temperature on the chelation reaction. The chelation of Gd^{3+} was carried out at three temperatures and different time periods to assess the optimal temperature for chelation reactions. This aimed to determine whether long reaction times or higher temperatures had more profound effects on the successful chelation of Gd^{3+} (and hence reduction of 'free' Gd^{3+}) during the reaction as well as the amount of free Gd^{3+} remaining at the end of each chelation. The optimum amount of time required for the completion of the reaction was also investigated so that the synthesis can be more energy efficient and, therefore, environmentally friendly.

Chelation reactions of Gd^{3+}−DOTA at 18, 50 and 80 °C were set up and the reaction progress was monitored by UV-Visible spectroscopy for five hours (**Figure 2.3**). Samples for Arsenazo assay were prepared in an equivalent way to the calibration curve and were diluted where necessary. Interpolation using Origin software allowed the absorbance to be converted into concentration of free Gd^{3+} and this was plotted against time (**Figure 2.3**). At all temperatures the reaction was completed in about two hours (122 minutes). At the lower temperature of 18 °C after 291 minutes (about five hours) the concentration of free Gd^{3+} was 0.4 mM or 20 % of the starting concentration. In comparison, at 50 °C the final concentration of free Gd^{3+} was 0.18 mM or 9 %. The lowest final concentration was observed at the higher temperature (80 °C) where only 3 % of the Gd^{3+} was not chelated (0.06 mM). As a result of these initial

experiments, an 80 °C chelation was employed throughout this thesis to minimize the presence of free Eu^{3+}/Gd^{3+} ions.
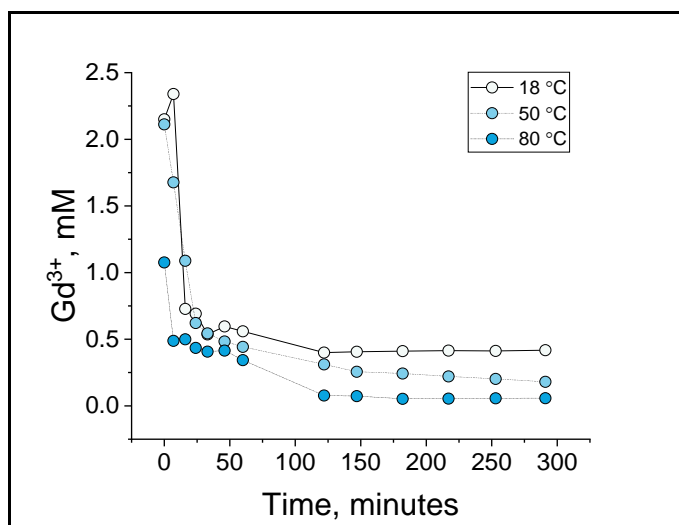
Figure 2.3 *The chelation reaction of Gd^{3+} and DOTA set up at 80 °C showed lowest final concentration of unchelated Gd^{3+}ions (3% of starting concentration at 291 minutes time) compared with the same reaction set up at 18 and 50 °C (20% and 9% remaining at 291 minutes time, respectively). The concentration of the free Gd^{3+} was obtained from absorbance.*

2.1.2.5 Measuring relaxivity of 1:1 ratio of chelated Gd^{3+} and guest molecules

Gd^{3+}–DOTA samples prepared according to Section 2.1.2.1 and were used neat for the measurement of Gd^{3+}−DOTA relaxivity. For the 1:1 guest molecule measurement ibuprofen, lysine, phosphate, phosphoserine and tyrosine were added to the 2 mM Gd^{3+}−DOTA solutions in appropriate amounts. Where binding molecule was present its ratio to the Gd^{3+}–DOTA complex was 1:1. Subsequently, the longitudinal relaxation rate (R_1, s^{-1}) of the sample was recorded for minimum of six different concentrations of Gd^{3+} achieved by the addition of water aliquots to the original sample. The longitudinal relaxation rate (R_1, s^{-1}) was plotted as a function of gadolinium concentration (Gd^{3+}, mM) and the slope was recorded as longitudinal relaxivity (r_1, mM^{-1} s^{-1}). The data points represent the average measurement of three separate samples.

2.1.2.6 Spectrofluorimetric titrations of $Gd^{3+}-DOTA$ with ibuprofen, phosphate, lysine, tyrosine, and phosphoserine

A sample of Eu^{3+}–DOTA (6 mM) and a stock solution of guest molecule: phosphoserine, ibuprofen, tyrosine, phosphate, and lysine (200 mM) in Eu^{3+}–DOTA (6 mM) were prepared. At the start of each titration measurement of 2 mL Eu^{3+}–DOTA (6 mM) was taken, followed by aliquot addition of the stock solution (T1, T2 etc. indicate the data points where fluorescence was recorded). Every time when 3.2 mL of volume was reached, the volume was reduced back to 2 mL due to limitations of the quartz cuvette volumes. Phosphorescent scans were taken with λ_{ex} = 280 nm and emission spectrum was recorded between 550 nm and 750 nm. Scan rate was 600 nm/min with data intervals at 1 nm.

2.1.2.7 Association constants

Association constants were derived using titration data fitted with DynaFit software. DynaFit uses the typical Michaelis-Menten binding model, whereby the association constant K_a, mM^{-1} is the reciprocal of the dissociation constant K_d, mM (K_a=1/K_d) and K_d follows Equation (2.1):

$$K_d = \frac{[Ln^{3+} - DOTA][salt]}{[Ln^{3+} - DOTA:salt]}, mM \qquad (2.1)$$

DynaFit script was used from the literature. [63]

2.1.2.8 Nuclear Magnetic Resonance Relaxometry (NMRR) titrations

Gd^{3+}–DOTA samples prepared according to Section 2.1.2.1 and were used neat (1 mL) to measure the initial data point D0. Stock solutions of each guest molecule: phosphoserine, ibuprofen, tyrosine, phosphate and lysine (200 mM) were prepared by adding the correct amount of solid to the Gd^{3+}−DOTA (2 mM) solution. Aliquots were added and the longitudinal relaxation times (T_1, s) recorded. Relaxivity (r_1, mM^{-1} s^{-1}) was calculated by dividing the relaxation rate ($1/T_1 = R_1$, s^{-1}) by the Gd^{3+} concentration (2 mM), which was kept constant throughout the titration.

2.1.2.9 SAP/TSAP NMR measurements

Eu^{3+}−DOTA (2 mM) samples in D_2O were prepared using the method described in Section 2.1.2.1 and appropriate amounts of gust molecules (phosphoserine, ibuprofen, tyrosine, phosphate and lysine) were added to achieve Eu^{3+}−DOTA (2 mM) + guest molecule (40 mM) samples. ^1H NMR spectra were recorded at 25 °C, 500 MHz.

2.1.2.10 Diffusion-Ordered Spectroscopy (DOSY)

Eu^{3+}−DOTA (50 mM) sample in D_2O were prepared using the method described in Section 2.1.2.1 and diluted to give 5 mM solution. Lysine was added to give Eu^{3+}−DOTA (5 mM) + lysine (5 mM) sample. DOSY spectrums of lysine (5 mM) in D_2O and Eu^{3+}−DOTA (5 mM) + lysine (5 mM) in D_2O were recorded at 25 °C, 500 MHz using a standard Bruker pulse program (dstebpgp3s).

2.1.3 Experimental for Chapter 4

2.1.3.1 Synthesis of aminated MSN

Absolute ethanol (1.84 mL, 30 mmol), ultrapure® water (16.02 mL, 0.89 mmol) and cetyl trimethyl ammonium bromide (0.64 g, 1.75 mmol) were mixed and heated up to 80 °C. Triethanolamine (1.03 g, 6.90 mmol) and dropwise tetraethoxysilane (1.45 mL, 6.49 mmol) were added and the mixture was stirred for 1 hour at 80 °C. Next, 1:1 molar ratio of tetraethoxysilane and (3-aminopropyl) triethoxysilane (total 4.7 µL, 0.02 mmol) was added and the reaction left to proceed for another hour at 80 °C. After this time the reaction was cooled to room temperature, centrifuged and the supernatant discarded. The milky-white pellet was washed with acidic ethanol [§] (3×15 mL) to remove the surfactant from the pores, followed by ethanol washes (10×15 mL) to restore the pH to neutral.[**]

2.1.3.2 DOTA-NHS-Ester Attachment

Aminated MSNs (0.23 g, 3.86 mmol) were centrifuged (20 min, 12, 139 RCF) and the supernatant removed. The pellet was dispersed in anhydrous dimethylformamide (DMF) (30 mL) and stirred. DOTA-NHS-Ester (0.02 g, 0.025 mmol, 0.7 %) and triethylamine (0.2 mL, 1.43 mmol) were added to the suspension and stirred at room temperature for 20 hours.

[§] Acidic ethanol was prepared from 20:3 v/v ratio of EtOH:HCl (47%).
[**] The washes consisted of forming a pellet by centrifugation (20 min, 12,139 RCF), discarding the supernatant and re-dispersing the nanoparticles using alternating vortex and sonication (~30 minutes).

Next, the functionalized MSNs were washed with ethanol (3×20 mL) and dispersed.

2.1.3.3 Gd^{3+} Chelation by DOTA

DOTA-NHS functionalised MSNs (0.23 g, 3.86 mmol) were dispersed in ethanol (20 mL). $GdCl_3$ (0.01 g, 0.0386 mmol) was added with stirring to the suspension and the reaction was left to proceed for 24 hours at room temperature. The mixture was placed in SnakeSkin dialysis tubing (3.5 K, 35 mm) and left in water (2.5 L) for 2 days with stirring to remove any excess unchelated metal. The suspension was then centrifuged (20 min, 12 139 RCF) and dispersed in ethanol (15 mL).

2.1.3.4 Synthesis of [(THF)₃Li(μ-Cl)Gd[N(SiMe₃)₂]₃]
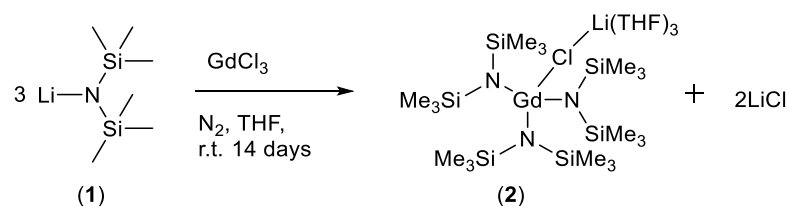
Synthetic procedures were carried out using standard glovebox and Schlenk techniques. Lithium bis(trimethylsilyl)amide (**1**) (0.46 g, 2.74 mmol, 3.3 equiv.) and anhydrous gadolinium chloride (0.22 g, 0.83 mmol, 1 equiv.) were weighed in a glove box. Each solid was removed from the box and dissolved in anhydrous THF (~30 mL) with stirring. The THF solution of lithium bis(trimethylsilyl)amide was added dropwise to the gadolinium chloride slurry. The mixture was left to stir for 14 days at room temperature under an N_2 atmosphere. The white precipitate was allowed to settle before filtration of the transparent liquid containing [(THF)₃Li(μ-Cl)Gd[N(SiMe₃)₂]₃]. The transparent liquid was characterised. v_{max}/cm⁻¹ (neat) 2960 (CH), 2900 (C-H), 1435 (CH bend), 1250 (SiC) cm⁻¹; δ_H (700 MHz, C₆D₆): 3.65 (12H, s, OC*H*₂), 1.29 (12H, s,OCH₂C*H*₂), 0.33 (54H, s, Si(C*H*₃)); δ_C (176 MHz, C₆D₆): 68.73 (O*C*H₂), 25.18 (OCH₂*C*H₂), 6.16 (Si(*C*H₃)); δ_{Si} (139 MHz, C₆D₆): -11.81(N*Si*(CH₃)).[††]

[††] IR spectrum recorded by master student Julie Kalmoni.

*2.1.3.5 Synthesis of Gd³⁺–silsesquioxane chelate (**4**)*

Heptacyclohexyl trisilanol polyhedral oligomeric silsesquioxane **(3)** (0.07 g, 65.0 μmol, 2 equiv.) was mixed with [(THF)$_3$Li(μ-Cl)Gd[N(SiMe$_3$)$_2$]$_3$] **(2)** (0.02 g, 32.5 μmol, 1 equiv.) under nitrogen. The mixture was stirred at 65 °C for 3 days. NMR showed that the reaction did not go to completion and the mixture was refluxed for additional two weeks. The solvent was removed under reduced pressure and the transparent oil was analysed (0.2314g, 89 %). v_{max}/cm^{-1} (neat) 1080 (Si-O-Si sym), 510 (Si-O-Si asym), 420 (O-Si-O bend) cm^{-1}; δ_H (700 MHz, C$_6$D$_6$): 1.60 – 2.10 (m, CH2, c-C$_6$H$_{11}$), 1.28 – 1.60 (m, CH_2, c- C$_6$H$_{11}$), 0.92 - 1.05 (m, SiCH, c-C$_6$H$_{11}$). δ_C (700 MHz, C$_6$D$_6$): 28.0, 27.9, 27.8, 27.7, 27.6, 27.5, 27.4, 27.3. δ_{Si} (700 MHz, C$_6$D$_6$): -71.08, -70.96, -70.45, -70.02, -69.89, -69.82, -69.76, -69.68, -69.05, -69.00, -68.52, -68.11, -67.87, -67.50, -67.38, -67.32, -67.00, -66.87 (*Si*CH, c-C$_6$H$_{11}$).‡‡

---

‡‡ NMR and IR spectra recorded by master student Julie Kalmoni.

2.1.3.6 Relaxivity measurements of Gd³⁺−DOTA−MSN

Relaxivity (r_1, mM^{-1} s^{-1}) of Gd^{3+}-loaded mesoporous silica nanoparticles (Gd^{3+}−DOTA−MSN) was obtained by diluting the original sample with water aliquots (50, 60 or 100 μL) five times to achieve six different Gd^{3+} concentrations. The relaxation rate (R_1, s^{-1}) was then plotted as a function of gadolinium concentration (mM) and fitted with Origin software. The slope of the linear fit was obtained as r_1, mM^{-1} s^{-1} according to equation (2.1) to normalise the relaxation rate to the concentration of the paramagnetic ion:

$$r_1 = \frac{\Delta R_1}{[Gd^{3+}]}, mM^{-1}, s^{-1} \qquad (\ 2.2)$$

The concentration of the metal ion (Gd^{3+}, ppm) from MSN samples was obtained from inductively coupled plasma atomic emission spectroscopy measurements (ICP-AES) using a Varian 720 ICP-AES machine. Each sample was prepared by digesting 500 μL of sample with hot nitric acid which was then diluted in a volumetric flask using ultrapure water to either 10 mL or 25 mL of volume. The samples were measured against standards of known concentrations by Connor Wells.

2.1.3.7 Titrations of Gd³⁺−DOTA−MSN with lysine

The Gd^{3+} concentration of a Gd^{3+}−DOTA−MSN was measured using ICP-AES as described in Section 2.1.3.6. The correct amount of lysine was

added to the sample and relaxivity measurements were undertaken analogously to the molecular species as described in Section 2.1.2.8.

2.1.4 Experimental for Chapter 5

2.1.4.1 Synthesis of (S)-2-chloro-N-(1-phenylethyl) acetamide (Side arm S1) following published procedure.[100]
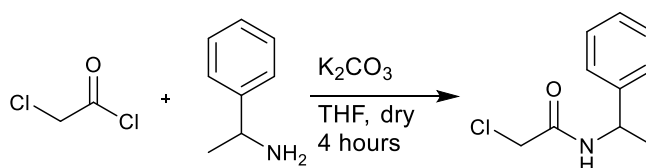
(S)-1-phenylethanamine (3.8 mL, 30 mmol) and anhydrous potassium carbonate (5.4 g, 39 mmol) were dissolved in anhydrous THF (102 mL) and stirred under nitrogen gas. The flask was placed in a water bath and the temperature was maintained under 18 °C. An anhydrous THF solution of 2-chloroacetyl chloride (2.6 mL, 33 mmol) under nitrogen was added dropwise using a glass syringe over half an hour. The reaction was monitored by TLC. After two hours the reaction was finished, the solid was filtered off and washed with THF. The filtrate was concentrated under reduced pressure and quenched with water to form white precipitate which was the final product. 3.35 g, 57 %; δ_H (600 MHz, CDCl$_3$) 1.54 (3H, d, *J* 6.90, C*H*$_3$), 4.05 (2H, dd, *J$_1$* 15.40, *J$_2$* 15.17, C*H*$_2$Cl), 5.13 (1H, p, *J* 7.1, C*H*), 6.79 (1H, br s, N*H*), 7.38-7.27 (5H, m, Ph); δ_C (600 MHz, CDCl$_3$) 21.84 (*C*H$_3$), 42.80 (*C*H$_2$), 49.41 (*C*H), 126.23, 127.82, 128.97, 142.42 (Ph-*C*), 166.12 (*C*=O).

2.1.4.2 Synthesis of four arms ligand (L₁) following published procedure.[101]
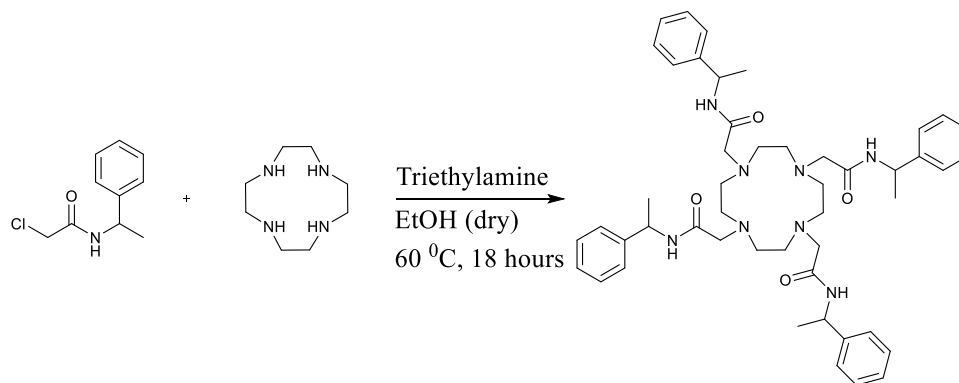
(S)-2-chloro-N-(1-phenylethyl) acetamide, Side arm S1 (1.58 g, 8 mmol) was dissolved in anhydrous EtOH (20 mL), stirred and heated to 60 °C. Solution containing cyclen (0.17 g, 1 mmol) and triethylamine (1.12 mL, 8 mmol) in anhydrous EtOH (10 mL) was added dropwise to the side arm solution over 2 hours. Next, the reaction was left to proceed at 60 °C for 18 hours. The resulting peach-coloured solution was concentrated under reduced pressure, poured over HCl (0.1 M, 40 mL), the aqueous phase washed with diethyl ether (3×30 mL) and neutralised with 1 M NaOH until pH 13 was reached. The crude was extracted from the aqueous phase with dichloromethane (3×30 mL), dried over K_2CO_3, filtered and concentrated under reduced pressure to yellow oil that was purified by chromatography on neutral alumina (100% CH_2Cl_2 to 5 % MeOH/CH_2Cl_2) yielding a hygroscopic yellow solid (280 mg, 34 %). δ_H (600 MHz, CDCl₃): 7.15-7.40 (20H, m, Ar*H*), 7.00 (4H, d, N*H*), 5.11 (1H, quin, NHC*H*(CH₃)), 3.71 (2H, q, *J* = 6.6 Hz, COC*H₂*), 2.57 (16H, m, NC*H₂*), 1.56 (12 H, d, *J* = 7.0 Hz, NHCH(C*H₃*)); δ_c (600 MHz, CDCl₃): 170.5, 170.4, 143.5, 128.8, 127.5, 126.5, 57.2, 53.6, 49.7, 48.5, 22.0, 21.7.

2.1.4.3 Synthesis of three arms ligand (L₂) following published procedure.[101]
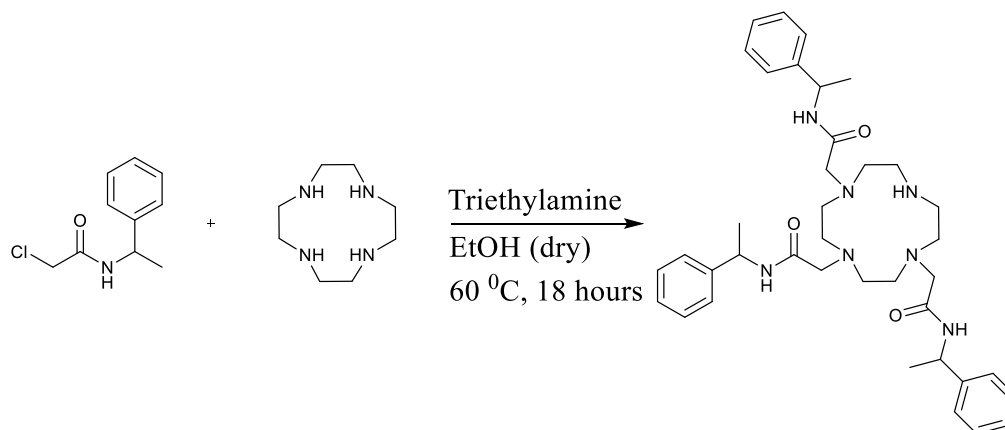
Triethylamine (0.83 mL, 5.9 mmol) was added dropwise to a stirring solution of cyclen (0.34 g, 2 mmol) in anhydrous ethanol (30 mL) and the mixture was heated to 60 °C. A solution of side arm S1 (1.17 g, 5.9 mmol) in anhydrous ethanol (10 mL) was placed in a syringe pump AL-1000 and dripped into the cyclen mixture at rate 20 µL/min. The reaction was left to proceed for 18 hours at 60 °C. The resulting solution was concentrated under reduced pressure, poured over aqueous HCl (0.1 M, 40 mL), the aqueous phase washed with diethyl ether (3×30 mL) and neutralised with 1 M NaOH until pH 13 was reached. The crude was extracted from the aqueous phase with dichloromethane (3×30 mL), dried over K_2CO_3, filtered and concentrated under reduced pressure to yellow oil that was purified by chromatography on neutral alumina (100% CH_2Cl_2 to 2 % $MeOH/CH_2Cl_2$) yielding a hygroscopic pale-yellow solid (300 mg, 23 %); δ_c (600 MHz, $CDCl_3$): 170.9, 170.4, 144.0, 128.5, 127.2, 126.8, 60.7, 54.3, 49.7, 49.1, 46.8, 46.0, 22.6, 21.8. (m/z): $[M + H]^+$ 656.42827. Found; $C_{38}H_{54}N_7O_3$ requires 656.428.

2.1.4.4 Synthesis and characterisation of Gd^{3+}−L$_3$

Step 1: Formation of N-(2-Hydroxyethyl)-acridone **1**, following a published procedure.[74]
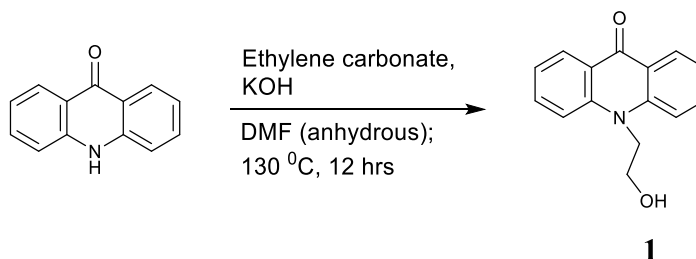
To a suspension of acridone (2.50 g, 12.8 mmol) and ethylene carbonate (2.25 g, 25.5 mmol) in dry DMF (20 mL) was added a catalytic amount (*ca.* 1%) of potassium hydroxide. The mixture was heated at 130 °C under nitrogen for 22 hours. The solvent was removed under reduced pressure and the crude product was precipitated from the residual oil by adding water. The solid was filtered, washed with water and recrystallised from methanol to yield a yellow solid, (1.50 g, 50 %); δ_H (DMSO-d$_6$, 600 MHz): 8.35 (2 H, dd, Ar$H_{1,8}$), 7.90 (2 H, d, Ar$H_{4,5}$), 7.81 (2 H, td, Ar$H_{2,7}$), 7.33 (2 H, td, Ar$H_{3,6}$), 5.07 (1 H, br, OH), 4.60 (2 H, t, CH_2OH), 3.89 (2 H, t, NCH_2); δ_C (DMSO-d$_6$, 600 MHz) 176.7 (*C*O), 140.4 (Ar *C*), 134.1 (Ar *C*), 127.6 (Ar *C*), 121.9 (Ar *C*), 116.4 (Ar *C*), 115.3 (Ar *C*), 60.26 (*C*H$_2$), 47.8 (*C*H$_2$);

Step 2: Formation of N-(2-(ethanotosyl))-acridone **2**, following a modified published procedure. [74]
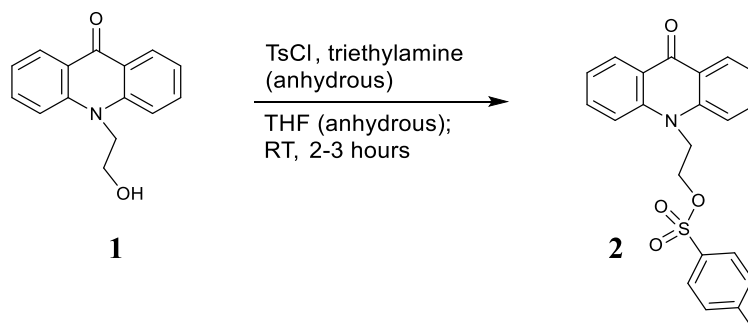
To a suspension of N-(2-hydroxyethyl)-acridone (1.50 g, 6.27 mmol) in dry THF (25 mL) under nitrogen was added toluenesulfonyl chloride (1.49 g, 7.84 mmol) and triethylamine (1.25 mL, 7.9 mmol). The mixture was stirred at room temperature under nitrogen for 4 hours. The solvent was removed under reduced pressure, the resulting solid dissolved in dichloromethane (20 mL), and the solution washed with 1% aqueous hydrochloric acid (10 mL), 50% saturated aqueous sodium bicarbonate solution (10 mL) and water (10 mL), dried ($MgSO_4$), filtered and evaporated to dryness to afford the product as a yellow solid, (1.12 g, 50 %), which was used without further purification. δ_H (CDCl$_3$, 600 MHz): 8.50 (2 H, dd, H_{1-8}), 7.71 – 7.66 (4 H, m, $H_{2-3; 6-7}$), 7.34 (2 H, d, ArH), 7.29 (2 H, t, ArH), 6.94 (2 H, d, ArH), 4.67 (2 H, t, CH_2–OS), 4.55 (2 H, t, CH_2–N), 2.30 (3 H, s, CH_3); δ_C (CDCl$_3$, 600 MHz): 177.7 (C$_9$); 146.9, 141.8, 134.2, 129.7, 128.0, 122.5, 121.8, 114.2, 68.0, 65.8, 44.0; (m/z): [M + H]$^+$ 394.34. Found; C$_{22}$H$_{20}$NO$_4$ requires 394.10.

Step 3: Formation of N-(2-Acridylethyl)-1,4,7,10-tetraazacyclododecane (**3**), following a published procedure. [74]

A solution of N-(2-(ethanotosyl))-acridone **2** (1.12 g, 2.85 mmol) and excess cyclen (0.98 g, 5.69 mmol, 2 eq.) in dry acetonitrile (20 mL) was boiled under reflux for 72 hours. After removal of the solvent, the residue was partitioned between hydrochloric acid (2 M, 75 mL) and dichloromethane (75 mL). The acidic layer was separated, basified to pH 13.5 with concentrated aqueous sodium hydroxide solution and extracted with dichloromethane (3 × 50 mL); under these conditions the excess cyclen remains in the aqueous layer. The combined organic extracts were dried ($MgSO_4$), filtered and evaporated to dryness to give the title compound as a hygroscopic yellow solid **3**, 0.70 g, 62 %, mp 110–112 °C. (m/z): $[M + H]^+$ 394.42. Found; $C_{23}H_{32}N_5O$ requires 394.25.

Step 4: Formation of ethyl (2-chloroacetyl)alaninate (**S2**), following a published procedure. [74]
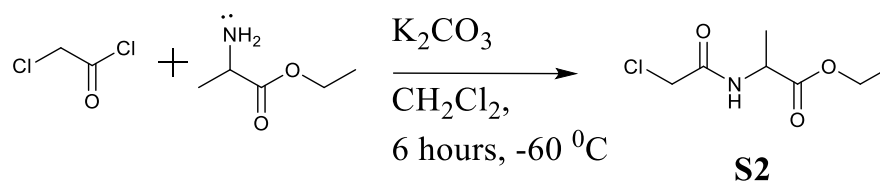
DL-alanine ethyl ester (1.40 g, 10 mmol) and K_2CO_3 (2.76 g, 20 mmol) were dissolved with stirring in dichloromethane (50 mL) under nitrogen gas at –60 °C. Chloroacetyl chloride (0.80 mL, 10 mmol) was dripped into the mixture over 15 minutes. After the dripping was over, the reaction was warmed to 0 °C and allowed to react for six hours at this temperature. The reaction was quenched with water, The organic layer was separated, and the aqueous layer was extracted with dichloromethane (2×100 mL), washed with brine and concentrated under reduced pressure to yield the final product as a colourless oil (1.1 g, 57 %) which was used without further purification. δ_H (CDCl$_3$, 500 MHz): 1.26 (3 H, t, C*H*$_3$CHN), 1.42 (3 H, d, J = 7.2 Hz, C*H*$_3$CH$_2$), 4.04 (2 H, s, C*H*$_2$Cl), 4.19 (2 H, q, C*H*$_2$CH$_3$), 4.53 (1 H, m, CH$_3$C*H*N), 7.26 (1 H, br, N*H*). δ_C (CDCl$_3$, 500 MHz): 172.4, 165.7, 61.7, 48.5, 42.5, 18.1, 14.1.   (m/z): [M + H]$^+$.194.21. Found; $C_7H_{13}ClNO_3$ requires 194.05.

Step 5: Formation of L$_3$ (**4**), following a published procedure. [74]
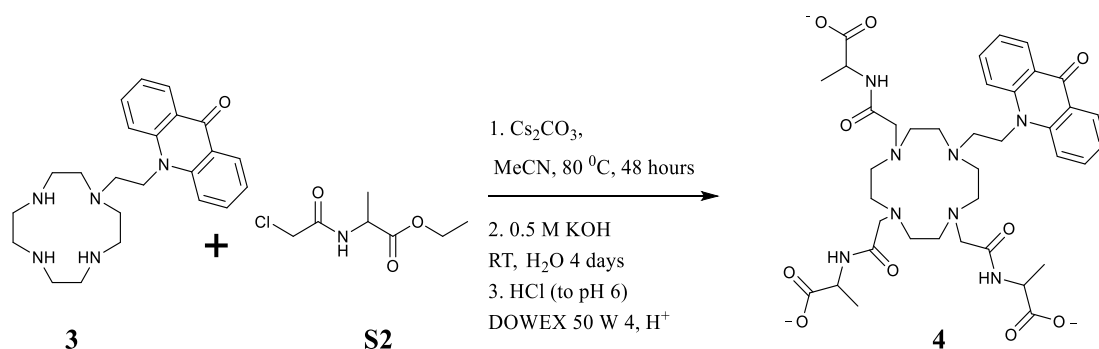
N-(2-Acridylethyl)-1,4,7,10-tetraazacyclododecane **3** (0.7 g, 1.77 mmol), ethyl (2-chloroacetyl)alaninate **S2** (1.1 g, 5.68 mmol) and caesium carbonate (1.8 g, 5.52 mmol) were dissolved in acetonitrile (10 mL) and heated up with stirring to 80 °C for two days. The mixture was concentrated under reduced pressure, purified over neutral alumina (100% CH_2Cl_2 to 0.5% EtOH–CH_2Cl_2) and the yellow solid was stirred in 0.5 M NaOH (20 mL) at room temperature for four days. The pH was adjusted to 6 using 37 % HCl, concentrated under reduced pressure and passed down a strong cation exchange column (DOWEX 50 W, H$^+$ form), eluting with 12% aqueous ammonia solution. The product was concentrated under reduced pressure to oily residue, dissolved in water and freeze dried to give the final product **4** as a hygroscopic yellow powder (650 mg, 47 %). (m/z): [M + H]$^+$ 953.3888. Found; requires 953.3893.

2.1.4.5 Complexation of L$_1$, L$_2$ and L$_3$ with Gd^{3+}

Complexation of L$_1$, L$_2$ and L$_3$ with Gd^{3+} was achieved analogously to the complexation of Gd^{3+}−DOTA described in Section 2.1.2.1.

2.2 Characterisation techniques

2.2.1 Single field NMR Relaxometry

NMR Relaxometry (NMRR) is a technique used for the measurement of relaxation times (T$_i$, i=1,2) of proton nuclei in liquid samples. The benchtop relaxometer used in this work was Oxford Instruments MQC+ benchtop NMR analyser equipped with a permanent magnet operating at a resonant frequency of 23.4 MHz which is an equivalent of 0.55 Tesla for the ^{1}H nuclei. The general schematic of the instrument is shown on **Figure 2.4**.
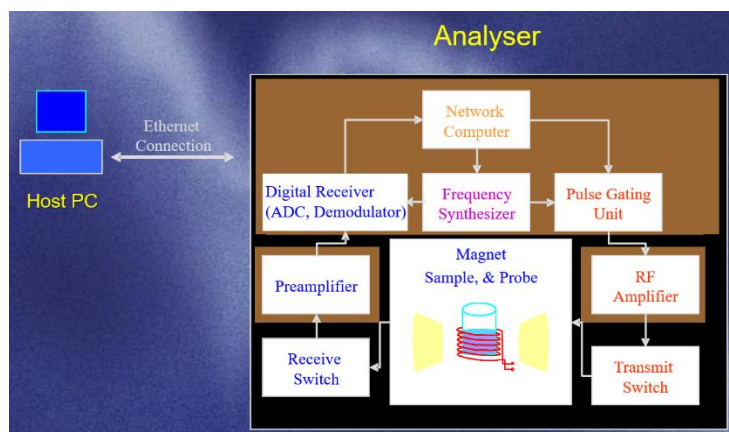
Figure 2.4 *General schematic representation of a benchtop NMR Relaxometer provided by Oxford Instruments.*

The instrument consists of a computer, sample holder, permanent magnet, input module and an output module. The computer contains an integrated

software that operates the Relaxometer. The magnet has a magnet yoke design and provides the static magnetic field B_0. Several channels of shim coils located between the poles of the permanent magnet ensure magnetic field homogeneity. The sample holder is designed for 10 mm inner diameter glass NMR tubes, which are inserted manually. The input module consists of a Frequency Synthesizer, Pulse Gating Unit, Radiofrequency (RF) Amplifier, and a Transmit Switch. The output module contains the Receive Switch, Preamplifier and a Digital Receiver, which includes the analogue-to-digital converter (ADC) and Demodulator.

The Frequency Synthesiser unit creates the initial signal to be used for an excitatory RF pulse (B_1). This signal is then passed through the Pulse Gating Unit which controls the RF Amplifier.[35] The pulse is then modulated by an "envelope" to achieve the desired pulse shape and amplified through the RF Amplifier Unit. Post-excitation, the weak FID signal generated from the nuclei in the sample goes through the Preamplifier Unit to increase the signal-to-noise ratio. Next, the analogue FID is converted to a digital signal by an analogue-to-digital converter (ADC). The original information carried by the FID is recovered by a Demodulator Unit. Both excitation of the sample and detection of the signal are achieved by the same hardware, termed transceiver coil (red wire on **Figure 2.4**). The excitation pulse (B_1) is orders of magnitudes more powerful than the sample signal and in order to avoid damage to the transceiver coil by the excitation RF, the system is equipped

with transmit and receive switches which can switch very rapidly the routing

of the signals (**Figure 2.4**).[37]

The software is operated by python console for command input and both

pulse sequences used to measure T_1/T_2 were written in Python. For the

measurement of T_1, the standard inversion-recovery (IR) method was employed

with a typical 180° pulse (10.91 µs) followed by 90° pulse (5.45 µs). The

recovery delay between the repetition of the pulse sequences was varied

between 400 and 1000 ms to accommodate the recovery of M_z to M_0. The time

constant T_1 (s) was obtained by fitting 512 datapoints acquired per scan (two

dummy and four actual scans per measurement) in accordance with equation (

2.3):

$$M_z(t) = M_{z,eq}(1 - 2e^{\frac{-t}{T_1}})$$ (2.3)

2.2.2 Fast Field-cycling (FFC) NMR and NMR Dispersion (NMRD)

curves

Fast Field-cycling NMR is a powerful tool for the investigation of the

properties of MRI contrast agents. Data are collected by record of the solvent

(water) relaxation rate at varied fields, typically between 0.1 and 100 MHz.

Data analysis enables extraction of structural and dynamic parameters which

affect the overall relaxivity of NMR probes due to the field-dependency of the

relaxation rates (Equations in Section 1.4).[56,57,102]

In a typical FFC NMR relaxometry (FFC NMRR) experiment proton spins are initially polarised using a strong polarisation field (B_{pol}) which is applied for a set time (T_{pol}) until the net magnetisation has reached saturation (**Figure 2.5**). Next, the magnetic field is switched (in few milliseconds) to a desired magnetic field value (B_{relax}) which can be varied throughout the experiment, for a time τ. The magnetic field is then switched again to an acquisition field (B_{acq}) and magnetisation is measured by the application of a 90° pulse followed by acquisition of the free induction decay (FID). To obtain the longitudinal time constants (T_1, s) the FID is recorded for each B_{relax} at varied τ, just like in a standard inversion-recovery pulse sequence. This clever procedure enables the record of the longitudinal relaxation times at varied fields, without changing the field of the spectrometer.[103]
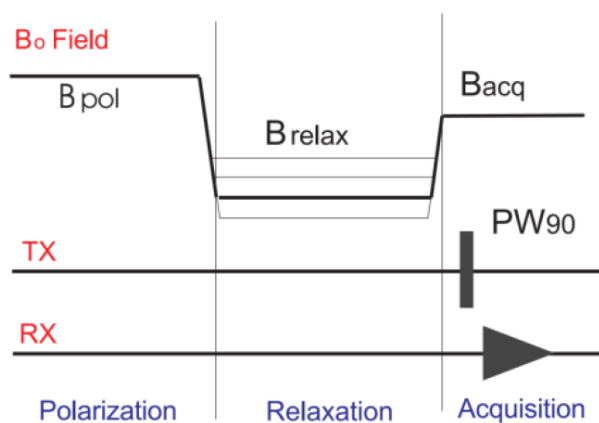
Figure 2.5 *Pulse sequence for fast field-cycling NMR experiment provided by Stelar NMR.*

2.2.3 Spectrofluorimetry (SF)

Spectrofluorimetry, or Fluorescence spectroscopy is an electromagnetic technique used to study materials which emit radiation upon absorbing a photon. It has been widely used across many disciplines, including biotechnology, medical diagnostics, forensics, materials chemistry, and others. Luminescence is the property of materials to emit light as a result of relaxation from an electronically excited state to ground state. When luminescence originates from a singlet excited state, meaning that the electron in the excited state is of the opposite spin to the electron in the ground state, the phenomena is termed fluorescence. This process is allowed and occurs rapidly, with emission rates in the region of 10^8 s^{-1}.[104] Fluorescent lifetimes are around 10 ms. However, when the spin of the electron in the excited electronic state is the same as the spin in the ground state, the excited state is termed a "triplet state", and relaxation to ground state is forbidden. These phenomena are termed phosphorescence and have low emission rates (10^3-10^0 s^{-1}), as well as long lifetimes – from milliseconds to seconds. [104]

In this work photoluminescent measurements on chelated Eu^{3+} liquid samples were carried out on Cary Eclipse Fluorescence Spectrometer in 3.5 mL quartz cuvettes.

2.2.4 Dynamic Light Scattering (DLS)

2.2.4.1 Hydrodynamic diameter

Dynamic Light Scattering is a technique used to measure particle size in the submicron size domain. When particles move in suspension (Brownian motion), they collide with solvent molecules and are forced to take random trajectories. The trajectories of smaller particles are more easily displaced by collisions with the solvent than those of larger particles. Therefore, larger particles diffuse more slowly and have a large translational diffusion coefficient (D).[105] In DLS, the suspension is illuminated with a laser, and the Brownian motion of the particles is followed by recording the backscattering of the laser light (173° in this work). The scattering pattern (fluctuations) over time is analysed using a correlator, which relates the fluctuations in the laser light intensity at various time intervals. The correlation between the patterns is plotted. The faster the patterns loose correlation, the faster the particles diffuse. The rate of particle diffusion is related to the exponential decay of the correlation function.

The correlation function allows for the calculation of the hydrodynamic diameter and polydispersity index of particles. The hydrodynamic diameter, d(H) is defined as a sphere, with the same diffusion coefficient (*D*) as the particle. The value of d(H) is typically a factor of ten larger than the "dry" size obtained my transmission Electron Microscopy (TEM). The polydispersity index (PDI) is a measure of the size distribution of the sample. Values between

0.1 and 0.7 indicate a narrow size distribution, which is within the measurable range of the DLS algorithms. For monodispersed samples within this range, the z-average algorithm is used to calculate diffusion coefficient (D) by fitting a single exponential to the correlation function. [105,106]

The diffusion coefficient is used to calculate d(H) by rearranging the Stokes-Einstein equation (Equation (2.4)):

$$d(H) = \frac{k_B T}{3\pi\eta D} \qquad (2.4)$$

Where k_B is the Boltzmann constant (1.380648×10^{-23} J K^{-1}), T is the temperature and η is the viscosity of the solution. In this works the solvent used was water and samples were measured at 25 °C for all measurements.

2.2.4.2 Zeta potential

The DVLO (Derjaguin, Verwey, Landau and Overbeek) theory states that the stability of colloidal suspensions depends on the balance between the energy of repulsion and the energy of attraction between the particles. When particles approach each other owing to Brownian motion, it is important for the repulsion potential V_R to be larger than the attraction potential V_A. The repulsion potential is a complex function which depends on the particle radius (*r*), solvent permeability (*p*), the ionic composition (k), the translational diffusion (D) and the ζ-potential:

$$V_R = 2pr\zeta^2 e^{-kD} \qquad (2.5)$$

The ʒ-potential is the potential on the surface of the electric double layer (**Figure 2.6**), and it provides information about the stability of the colloidal system. Large positive or negative ʒ-potential indicates that particles will repel each other in suspension resulting in higher colloidal stability. Generally, negatively charged particles with zeta potentials greater than or equal to 30 mV are considered stable.[105,107]

The DLS instrument measures electrophoretic mobility which is related to zeta potential by Henry Equation:

$$U_E = \frac{2\varepsilon\zeta F(kr)}{3\eta} \qquad (2.6)$$

Where U_E is the electrophoretic mobility, ε is the dielectric constant, ʒ is the zeta potential, η is the viscosity of the solution, k is the thickness of the electric double layer (Debye length), r is the particle radius and F(kr) is the Henry function.[105]
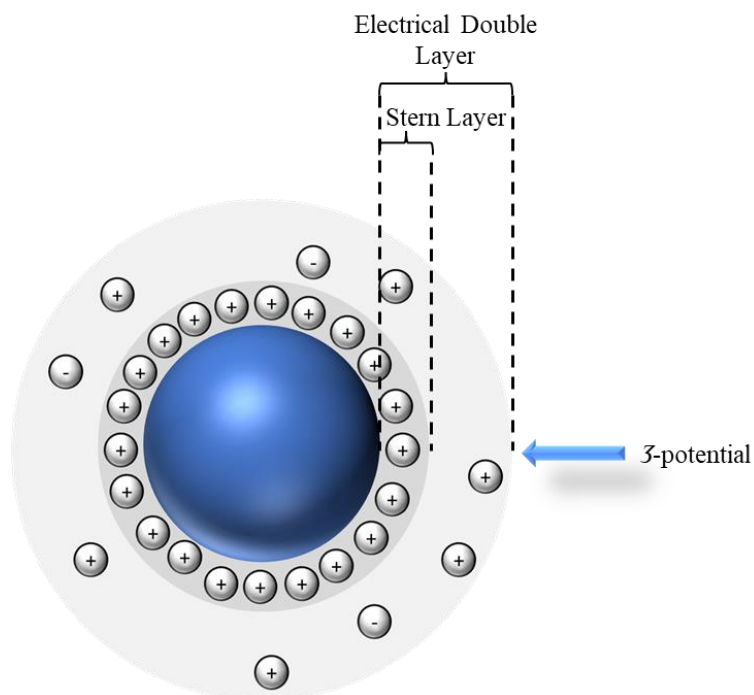
Figure 2.6 *Schematic representation of a negatively charged nanoparticle (blue sphere) in suspension. The ȝ-potential is measured at the surface of the electric double layer.*

2.2.5   Infrared Spectroscopy (IR)

The energy of most molecular vibrations falls within the region of the electromagnetic spectrum associated with infrared radiation. When the samples are exposed to infrared radiation, energy is absorbed at slightly different frequencies by the chemical bonds of different functional groups. Furthermore, symmetric and asymmetric vibrations have different energy gaps between the ground vibrational state and excited vibrational states, indicating that different modes of vibration can be distinguished using IR spectroscopy. For this reason, IR spectroscopy is frequently used by synthetic chemists to confirm the presence of specific functional groups in the molecular structures of synthesized compounds.

In the IR spectrum, the position of the absorption bands is typically expressed in wavenumbers (reciprocal of the wavelength($1/\lambda$), cm^{-1}). Infrared spectrum was recorded using Bruker Alpha ATR-FTIR apparatus, incorporating RockSolid^{TM} dual retroreflecting cube corner mirrors in an inverted double pendulum arrangement eliminating mirror tilt and shear, temperature stabilized deuterated triglycine sulphate (DTGS) detector and platinum attenuated total reflection (ATR) with durable monolithic diamond measurement interface.

2.2.6 Diffusion-Ordered Spectroscopy (DOSY)

DOSY is a type of NMR technique whereby molecules receive spatial encoding with the help of gradient coils. As molecules diffuse, NMR scans are taken in time intervals and the spatial encoding helps to record the speed of molecular translational diffusion, or their translational diffusion coefficient D_T.

In detail, the way that D_T is calculated from peaks is by using a gradient pulse sequence which encodes a spatial information into molecules through series of gradients.[108] An initial gradient has the role to encode spatial information in the molecules. After time τ, a second gradient is applied, which reverses completely the phase encoded by the first gradient. However, because the molecules have diffused, their spins won't be completely refocused, and some of the spatial encoding would be lost. Using the Stejskal-Tanner formula, the peak decay over time can be fitted, and the translational

diffusion coefficient calculated.[109,110] In practice, the fitting can be performed in both TopSpin and Mestrenova software by integrating the peak of interest in a DOSY stacked file. Small molecules typically have D_T of 10^{-10} to 10^{-8} m^2 s^{-1}.

In this work fits were performed using TopSpin software.

2.2.7 Transition Electron Microscopy (TEM)

Transition electron microscopy (TEM) is an analytical technique frequently utilised in materials chemistry to characterise physical properties of nanomaterials. It is an excellent method for the observation of the presence of mesopores in MCM-41 materials and assessment of particle size, stability (crosslinking) and shape. In TEM a high energy electron beam is focused by lenses and apertures and passed through a thin sample, typically positioned on copper grids. Some of the electrons are absorbed or scattered, but some pass straight through the sample, onto a phosphor screen, causing light emission and visualization of the image. Because electrons have much shorter wavelength than visible light, the TEM images have much higher resolution than images produced by standard light microscopy, making TEM perfect for the study of nanomaterials. Because of the direct observation of the materials, nanoparticular sizes obtained by TEM are true of solid MSN, unlike the hydrodynamic size obtained by DLS, which includes the hydration sphere around the particle.

2.2.8   Ultraviolet-visible Spectroscopy (UV-vis)

UV-Vis is a type of light absorption technique, whereby a sample is irradiated by ultraviolet or visible light causing absorption of photons. These photons possess the correct frequency to cause electronic transitions from the ground to the excited states of the irradiated material. The Beer -Lambert Law (Equation 2.5) demonstrates that the absorbance (*A*) of a sample is proportionate to the concentration of the studied material. This makes UV-Vis spectroscopy a very useful tool for the quantification of unknown solution concentrations, provided that the path of the cell used for the measurement (*l*) and the extinction coefficient of the sample (*ε*) are known:

$$A = \varepsilon c l \qquad\qquad (2.5)$$

A common practice in the determination of unknown sample concentrations is to create a calibration curve in advance, relating known concentrations of the studied material to its absorbance. This enables calculations of the unknown concentrations from the measured absorbance of the studied sample.

In this work, Cary 4000 spectrometer by Agilent was used to collect UV-Vis data. Unknown concentration values were extracted using the Interpolation function in Origin software.

3   Gd^{3+}–DOTA in the Presence of Guest Molecules

3.1   Introduction

When designing a detection system, it is desirable to understand how each component of the system affects the generated signal. Relating structural differences in the detection target to the modulation of MRI signal is the first logical step towards designing MRI-based detection systems for sarin-tyrosine adducts. For example, the tyrosine adduct has two potential binding sites to an MRI contrast agent – the phosphonate and the carboxyl groups, which may displace water from the inner-sphere. Phosphonate is more difficult to detect due to its neutral charge, and most likely binding mode will occur through carboxylate, as shown in **Figure 1.35**. Chapter 1 had discussed in length the general structural features of ligands binding to the phosphate group. Even though these rules do not apply to the charge-neutral phosphonate, phosphate binding was also investigated.

A series of powerful characterisation techniques have been developed to explore the MRI signal modulation in the presence of MRI contrast agents. Because of the complexity of the paramagnetic MRI theory described in section 1.3, each of these techniques is able to reveal only a small part of the complete picture. NMR Relaxometry (NMRR) is a very useful technique for the evaluation of the efficacy of contrast agents through the calculation of the relaxivity term (r_1, mM^{-1} s^{-1}). Any perturbation of the relaxivity due to

external stimuli can be detected using NMRR. For example, changes in the

hydration number q and other parameters due to binding and/or water

displacement can either increase or decrease longitudinal relaxivity through

complex mechanisms. In turn, changes in these parameters can be studied

using NMRR. Spectrofluorimetry is frequently used to quantify inner-sphere

binding events to contrast agents through ratiometric titrations with guest

molecules of phosphorescent analogues to gadolinium contrast agents. It is

possible to monitor emission directly from gadolinium ions, however this is

not an easy task due to the large energy gap between the ground and excited

states of Gd^{3+} (**Figure 3.1**). Emission can be induced in Gd^{3+} ions by

electronic transitions between $^8S_{7/2} \rightarrow {}^6I_J$, however the excitation wavelength

for these is very short, around $\lambda_{ex} = 275$ nm and requires high energy source.

On the other hand, Eu^{3+} analogues are easily achieved because of the

chemical similarity between the MRI active gadolinium and phosphorescent

europium. The energy gap between Eu^{3+} ground and excited states is much

smaller and excitation wavelengths are around $\lambda_{ex} = 390$ nm (**Figure 3.1**).

Figure 3.1 *Energy levels of trivalent lanthanide ions.* [111]

Dynamic parameters such as rotational correlation (τ_R), residence time of the inner-sphere water molecule (τ_m) and inner-sphere water molecule relaxation times (T_{1m}) can be obtained using a variety of NMR and NMRR techniques. Diffusion Ordered Spectroscopy (DOSY) allows for the calculation of the diffusion coefficient of molecules in solution (D_T), which is inversely proportional to the rotational correlation time τ_R.[112] The water exchange regime can be accessed through temperature dependent NMRR. Because the behaviour of IS and OS contributions to relaxivity are well known, plotting the relaxivity as a function of temperature can reveal whether a complex is in a fast or intermediate/slow exchange regime. In a fast exchange regime both OS and IS contributions decrease with increasing temperature (**Figure 3.2**, left). The OS contribution to relaxivity always decreases with increasing temperature exponentially because both the electronic relaxation times T_{ie} and the correlation time for the relative translational diffusion τ_D (Equations 1.9 – 1.11, Section 1.3.1) decrease with increasing temperature. The IS contribution decreases with increasing temperature in the fast exchange regime because of longer τ_{ci} (Equations 1.14 and 1.15, Section 1.3.2). In the intermediate/slow exchange regime the IS contribution of low molecular weight contrast agents increases with increasing temperature (**Figure 3.2**, right). This trend is opposite to the OS contribution and becomes more obvious above room temperature. Quantitatively in the fast exchange regime, τ_m is in the nanosecond region,

whereas in the intermediate/slow exchange regime, τ_m is in the microsecond region.[57,58]
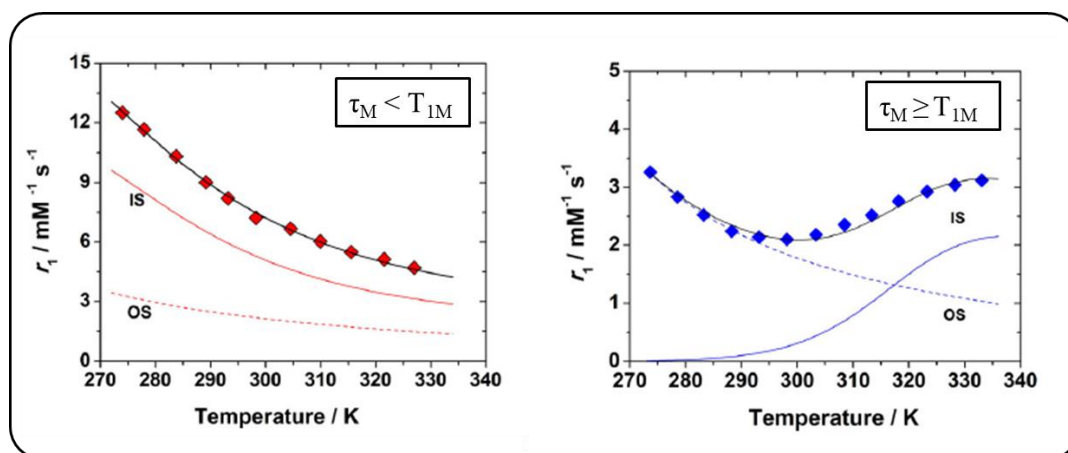
Figure 3.2 *Fast water exchange mode (red, left) and intermediate to slow water exchange modes.*[57]

Possibly the best way to separate inner-sphere from outer-sphere contributions in relaxivity is through fast-field cycling NMR (FFC-NMR). This technique produces NMR dispersion (NMRD) profiles which show the dependency of the r_1 relaxivity on the magnetic field.[56,57,113–116] Changes in the r_1 relaxivity observed at lower frequency can be related to changes in the electronic relaxation times, whereas those at higher frequencies are indicative of the water exchange.[57] Increased relaxivity across all frequencies is indicative of increase in hydration number. Fitting of the NMRD profiles can provide a quantitative measurement of the different parameters governing the paramagnetic MRI theory. Because of the complexity of the equations governing IS and OS relaxation, it is important that most parameters of the contrast agent studied by NMRD are known and only three to four parameters are left free for fitting.

Gd^{3+}–DOTA is commercially known as Dotarem$^®$ and is one of the approved and most frequently used MRI contrast agents in the clinical setting. It has been studied extensively in the literature and most structural and dynamic parameters of this contrast agent are well known.[42,43,57,116] Gd^{3+}–DOTA has a q value of one, meaning that it has a single water molecule coordinated to its inner coordination sphere. This water molecule is coordinated directly to the metal centre at a distance of 3.5 Å. The relaxivity enhancement of this contrast agent is due to the close proximity of the water protons to the metal centre, forming dipole-dipole interactions between the magnetic moments of the proton nucleus and the magnetic moments of the seven unpaired electrons of Gd^{3+} metal. The contrast agent affects many protons in the solution due to water exchange with the bulk water in the outer coordination spere, as well as protic exchange at the coordinated water. Relaxivity is strongly dependent on the distance between the water molecule and the metal core, therefore any competitive binding displacing the inner-sphere water would produce a change in relaxivity. Changes in q and τ_R perturb relaxivity and examples were detailed in Sections 1.4.2 and 1.5. However, detailed understanding of how interactions of Gd^{3+}−DOTA with common biological molecules or, indeed, nerve agent adducts, perturb relaxation is currently well mapped and understood. This makes Gd^{3+}−DOTA a perfect candidate to be studied in the presence of guest molecules, such as amino acids, containing the functional groups present on sarin-tyrosine adducts.

3.2　Aims

The main aim of this Chapter was to investigate the interactions between the functional groups present on nerve agent adducts and a typical Gd^{3+}-based contrast agent. $Gd^{3+}-DOTA$ was chosen as the contrast agent and five commonly-found molecules containing carboxylic and phosphate groups were chosen to represent the functional groups on the nerve agent-tyrosine adducts including ibuprofen, lysine, phosphoserine, tyrosine, and phosphate. It was expected that the presence of these guest molecules in $Gd^{3+}-DOTA$ solution will cause changes in the hydration number of the contrast agent, or other parameters, due to binding interactions. This was expected to cause a decrease or increase in the longitudinal relaxivity. In order to achieve this aim, a variety of characterisation methods such as single field relaxometry (NMRR), nuclear magnetic resonance (NMR), fast-field cycling NMR (FFC NMR) and spectrofluorimetry (SF) were used to construct a complete picture of these interactions in solution.

This work ultimately aims to provide us with a clear understanding of how different functional groups interact with $Gd^{3+}-DOTA$ and will enable us to predict and design chelates capable of amplified relaxation changes as well as specific interactions with nerve agent adducts, which is investigated in later chapters.

3.3 Results and discussion

The investigations of single field relaxometry at 1:1 ratio between guest and host at three different pH values aimed to evaluate the binding strength between the guest molecules and Gd^{3+}−DOTA. ANOVA was used to identify any significant interactions resultant from the relaxometry data. It was expected that if the inner water molecule of Gd^{3+}–DOTA is displaced by competitive binding of a guest molecule to the Gd^{3+} ion, the relaxivity would significantly decrease. This is due to the decrease in q number from 1 to 0. (**Figure 3.3**). It was important to assess the relaxation behaviour of Gd^{3+}–DOTA in the presence and absence of guest molecules at different pH ranges as pH can affect the relaxivity due to variation of H^+ availability in solution and protonation/deprotonation of binding functional groups. Because Gd^{3+}–DOTA is a non-specific ligand and guest binding depends solely on Coulomb attraction,[42] measurements at lower pH would be expected to display a lower change in loss of relaxivity. This is due to protonation of the guest binding molecules and, therefore, weaker binding at Gd^{3+} compared with measurements conducted at higher pH, where carboxylic and phosphate groups are more likely to be deprotonated and to form a stronger binding in the inner sphere of the complex.
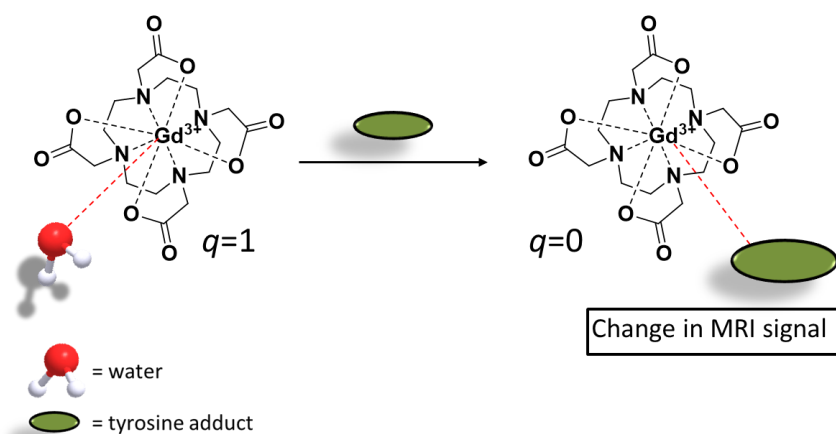
Figure 3.3 *Schematic illustration of possible MRI signal change due to change in hydration number q.*

Five molecules were selected for testing. In order to develop a detection system for nerve agent adducts, phosphoserine was used as the model (**Figure 3.4**). Phosphoserine is an excellent candidate as it contains both carboxylic and phosphate groups. The challenge with this molecule arises from the inability to attribute binding behaviour and subsequent change in MRI signal to either the phosphate or the carboxyl group as they both possess the potential to compete for binding. For this reason, ibuprofen was selected as another binding salt. Ibuprofen has a single binding site, a carboxyl group (**Figure 3.4**). In addition, the behaviour of ibuprofen with Gd^{3+}–DOTA and MSNs is well understood and comparison with the literature can be drawn.[78,87,117,118] Tyrosine and lysine were also selected in order to gain understanding of the carboxyl group binding behaviour in amino acids and investigate if and how the overall structure and size of the binding moiety affects the MRI signal. Finally, disodium phosphate was chosen to give an

insight into the binding behaviour of the phosphate group and highlight potential differences between the COO^- and PO_4^{2-} groups binding behaviour.
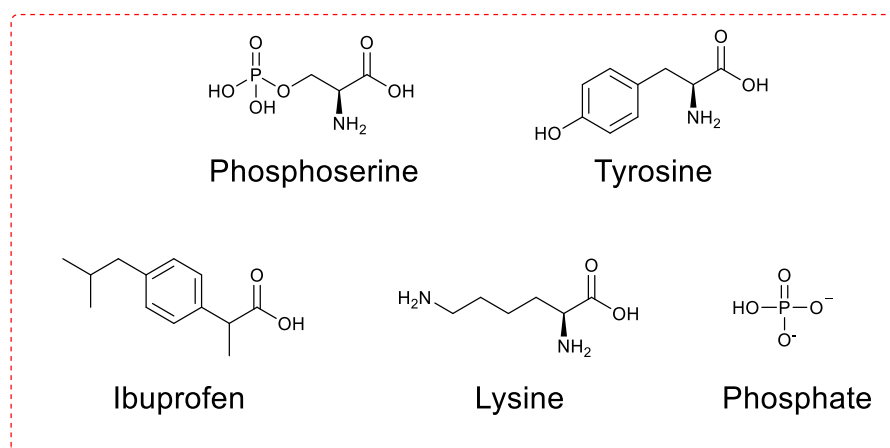
Figure 3.4 *Five molecules used throughout the study to investigate MRI behaviour as a result of binding to Gd³⁺–DOTA.*

3.3.1   1:1 ratio of Gd³⁺–DOTA and guest molecules

The ability of the five guest molecules to displace the inner sphere water molecule of Gd³⁺−DOTA was tested using NMR Relaxometry. First, the relaxivity enhancement induced by the pure contrast agent was recorded. Next, solutions of 1:1 ratio of the contrast agent and each guest molecule were recorded at three different pH (**Figure 3.5**). Every measurement was repeated for three separately prepared samples and the relaxation rate for each sample was measured for five concentrations of Gd³⁺−DOTA and plotted against gadolinium concentration, with the linear fit of the slope providing the r_1 values (as per Equation 1.9, Section 1.3).

The pH of solutions was controlled by additions of up to 50 μL HCl/NaOH. The relaxivity of the pure contrast agent Gd³⁺–DOTA at low pH

(pH 2-3) was found to be 3.99 ± 0.14 mM^{-1} s^{-1}. At neutral pH (pH 6-7) the relaxivity was 3.57 ± 0.16 mM^{-1} s^{-1} and at high pH (9-10) the relaxivity was 3.55 ± 0.21 mM^{-1} s^{-1} which is in good agreement with literature values.[42] The small decrease in relaxivity with increasing pH can be explained in terms of proton availability in solution. At lower pH the higher availability of protons in solution can speed up the protic exchange around the complex and slightly increase the relaxivity value as more protons could experience the effect of Gd^{3+} for given time.[119] This trend would be expected to remain true for the 1:1 solutions too.

At low pH the relaxivity of a solution of Gd^{3+}–DOTA and phosphate at a 1:1 ratio was 3.35 ± 0.15 mM^{-1} s^{-1}, which showed a 0.64 mM^{-1} s^{-1} decrease from the value of pure Gd^{3+}–DOTA solution at the same pH. Gd^{3+}–DOTA in the presence of phosphoserine showed smaller decrease of 0. 17 mM^{-1} s^{-1} (r_1= 3.82 ± 0.20 mM^{-1} s^{-1}) and a Gd^{3+}–DOTA and tyrosine solution showed an even lower decrease of 0.10 mM^{-1} s^{-1}. At the same pH, addition of ibuprofen and lysine to the solution of Gd^{3+}−DOTA resulted in signal increase by 0.17 and 0.64 mM^{-1} s^{-1} respectively, yielding relaxivity values of 4.16 ± 0.13 and 4.50 ± 0.48 mM^{-1} s^{-1}, which could not be explained by the simple dehydration mechanism of the inner sphere.
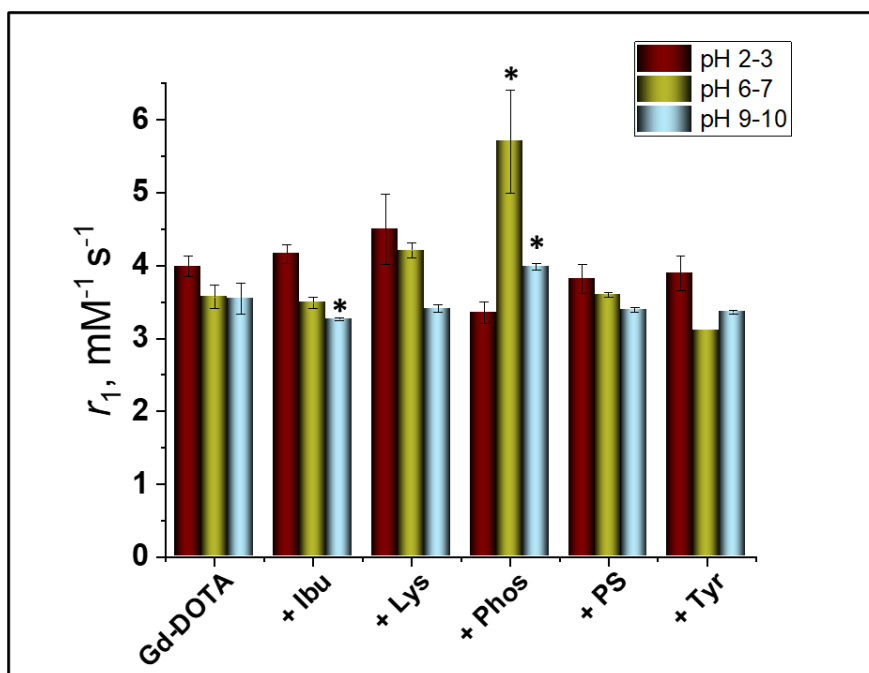
Figure 3.5 *Longitudinal relaxivity (r_1, $mM^{-1}s^{-1}$) measured at 23 MHz and 25 °C of molecular Gd^{3+}–DOTA (2 mM) in the absence and the presence of five guest molecules at the same concentration (ibuprofen, lysine, phosphate, phosphoserine, and tyrosine) at 1:1 molar ratio. Each column represents the r_1 value derived from the gradient of the linear fit of measured longitudinal relaxation rate (R_1) of a minimum of five Gd^{3+}−DOTA concentrations. The error bars represent the error associated with the average of three measurements. Asterisks indicate statistically significant differences with respect to Gd^{3+}−DOTA at the same pH (p-values to follow in **Figure 3.6** and* ***Figure* 3.7***).*

At neutral pH, Gd^{3+}–DOTA with tyrosine showed the greatest decrease in signal by 0.46 mM^{-1} s^{-1}. Ibuprofen showed a relaxivity decrease of 0.08 mM^{-1} s^{-1} (r_1=3.49 ±0.08) from the pure Gd^{3+}–DOTA solution at the same pH. Increased relaxivity was observed at neutral pH for lysine by 0.64 mM^{-1} s^{-1} (r_1=4.21±0.10 mM^{-1} s^{-1}) and phosphate by 2.13 mM^{-1} s^{-1} (r_1=5.70±0.71 mM^{-1}

s^{-1}). Phosphoserine showed a negligible change of 0.03 mM^{-1} s^{-1} (r_1=3.60±0.03 mM^{-1} s^{-1}).

At high pH adding ibuprofen to the Gd^{3+}–DOTA solution caused the greatest decrease in signal by 0.29 mM^{-1} s^{-1} from the pure Gd^{3+}–DOTA solution. Next was tyrosine with 0.19 mM^{-1} s^{-1} decrease in signal (r_1=3.36±0.03 mM^{-1} s^{-1}) followed by phosphoserine with decrease of 0.16 mM^{-1} s^{-1} (r_1=3.39 ±0.03 mM^{-1} s^{-1}) and lysine with decrease of 0.14 mM^{-1} s^{-1} (r_1=3.41±0.05 mM^{-1} s^{-1}), although it should be noted that these samples were all within error of one another. The relaxivity of Gd^{3+}–DOTA with phosphate at pH 9-10 was 3.99 ± 0.05 mM^{-1} s^{-1}, an increase of 0.44 mM^{-1} s^{-1} from the relaxivity of pure Gd^{3+}–DOTA solution for pH 9-10.

This unusual behaviour of some guest molecules causing an increase in signal was interesting and required further investigation. However, it was first important to understand whether or not the signal increase was significant.

One-way ANOVA was used to identify significant changes in signal between Gd^{3+}−DOTA and Gd^{3+}−DOTA + guest molecules from **Figure 3.5**. First, the relaxivity values at neutral pH were compared as they are most relevant for blood sample analysis. The only significant change in signal was the increase upon binding with phosphate by 2.13 mM^{-1} s^{-1}, which could indicate that some parameters governing the paramagnetic relaxation different than the hydration of the inner sphere were changed in the presence of this anion. (**Figure 3.6**). Phosphate was also found to have a significantly different signal from phosphoserine, indicating a different binding mechanism is at play.

It can be seen in **Figure 3.6** that not only did phosphoserine have the smallest positive deviation from the control, but also had a very narrow population distribution.
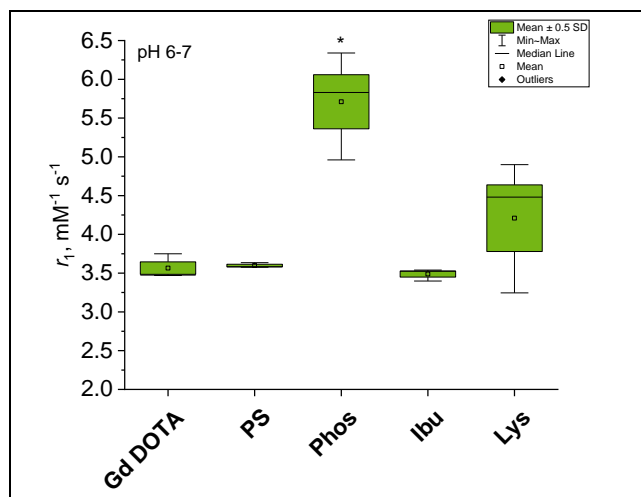
Figure 3.6 *One-way ANOVA analysis of the longitudinal relaxivity (r_1, mM^{-1}s^{-1}) of the control Gd^{3+}–DOTA in the absence and the presence of five guest molecules (ibuprofen, lysine, phosphate, phosphoserine, and tyrosine) in 1:1 molar ratio at pH 6-7. The error bars represent the error associated with the average of three measurements. Asterisks indicate statistically significant differences in relaxivity between the control (Gd^{3+}-DOTA only) and the sample treated with phosphate ($p < 0.01$).*

ANOVA analysis of the samples measured at high pH (***Figure 3.7***) revealed that both phosphate and ibuprofen had a significant increase in signal compared with the corresponding control of Gd^{3+}-DOTA at the same pH. The phosphate and ibuprofen were not significantly different to each other, despite their different binding chemistries. Overall, it was clear that the simple hypothesis of *q* displacement was not supported by this set of data. Furthermore, some potentially interesting and unexpected mechanisms could be causing a significant increase in signal for some of these samples.

Equation 1.12 in section 1.3.2 shows that the inner-sphere relaxivity (r^{IS}) depends on q, τ_m and T_{1m}. It is not possible to explain the increase in signal in terms of q as for Gd^{3+}−DOTA this cannot be more than one, based on its structure.[42] The water exchange or the mechanism of the inner-sphere water molecule relaxation therefore must have been altered upon addition of the guest molecules, or alternatively the overall relaxivity could have been increased through enhanced second/outer sphere relaxation mechanisms (Equations 1.9, 1.10 and 1.11). To investigate this further it would be useful to separate the inner and outer sphere contributions to relaxivity.
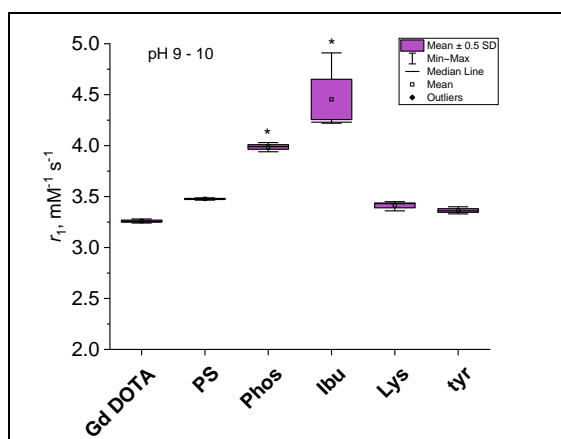
Figure 3.7 *ANOVA analysis of the longitudinal relaxivity (r_1, mM^{-1}s^{-1}) of molecular Gd^{3+}–DOTA in the absence and the presence of five guest molecules (ibuprofen, lysine, phosphate, phosphoserine, and tyrosine) in 1:1 molar ratio at pH 9-10. The error bars represent the error associated with the average of three measurements. Asterisks indicate statistically significant differences in relaxivity between the control (Gd^{3+}-DOTA) and the samples treated with phosphate ($p < 0.01$) and ibuprofen ($p < 0.01$) calculated by Origin software.*

151

3.3.2 Spectrofluorimetric Titrations

Ratiometric studies using spectrofluorimetry aimed to identify any binding interactions causing changes in close proximity to the metal centre and, therefore, affecting the phosphorescence of Eu^{3+}. Spectrofluorimetry is generally regarded as the standard method for detection of inner sphere binding in lanthanide complexes.[63,120,121,65] It has been used to show binding of small anions such as bicarbonate, citrate, inorganic phosphate and others as well as large molecules such as adenosine triphosphate and phosphorylated insulin receptor peptides to fluorescent lanthanide complexes.[98] This technique offers the ability to screen for specific binding as well as compare binding of different molecules at the metal centre. Fluorescent titrations generate binding isotherms which can be fitted and allow for the calculation of association (affinity) constants K_A. This is an excellent way to quantify and compare chemical interactions of anions with the lanthanide core.

Europium (Eu^{3+}) is a good fluorescent analogue to Gd^{3+} as both sit next to each other in the periodic table and have similar size and binding properties, as previously described. Eu^{3+}−DOTA has a characteristic emission spectrum arising from *f*-orbital transitions in the millisecond region.[104] There are two important transition peaks in the emission spectra of Eu^{3+}–DOTA: the forced electric dipole transition peak $^5D_0 \leftarrow \, ^7F_2$ ($\Delta J=2$, J_2) which is hypersensitive to binding at the Eu^{3+} core, and $^5D_0 \leftarrow \, ^7F_1$ ($\Delta J=1$, J_1) which is an environmentally insensitive magnetic dipole transition peak, and it is used as an internal reference. Plotting the peak intensity of J_2 divided by J_1 against

increasing guest concentration provides a binding curve which is independent on the amount of Eu^{3+} ions in solution and can be used to examine a binding event ratiometrically.[63]

Since the presence of ibuprofen at a 1:1 molar ratio with Gd^{3+}−DOTA at pH 9-10 showed a statistically significant change in relaxation, and to show that this could not be due to changes in hydration number q, luminescent titration of Eu^{3+}−DOTA with ibuprofen at pH 9-10 was executed. The emission spectrum at each titration point was recorded (**Figure 3.8**, left) and the ratio of J_2/J_1 was plotted against ibuprofen concentration (**Figure 3.8**, right). The titration data showed no binding of ibuprofen to the metal centre even in its deprotonated form, which was in line with the changes observed in relaxation investigations (Section 3.3.1). The titration covered ibuprofen concentrations between 0 and 42 mM which corresponds to 21 equivalents of the guest molecule. The lack of inner-sphere binding was indicative that the increase in signal observed in the 1:1 NMR relaxometry of Gd^{3+}−DOTA with ibuprofen at high pH was not due to change in q, as predicted.
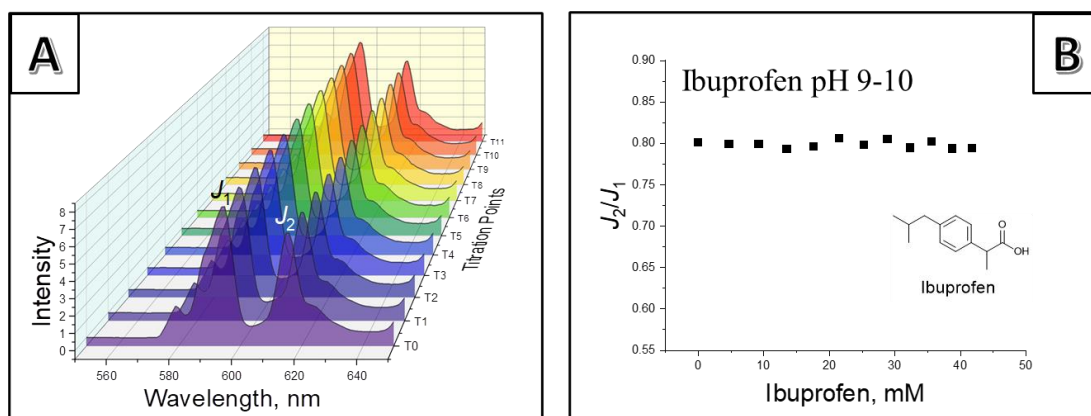
Figure 3.8 A: *Emission spectra of Eu^{3+}–DOTA on its own and in the presence of different concentrations of ibuprofen (denoted as titration points). Spectra were recorded in water at [Eu^{3+}] = 2 mM, 25° C and pH 9-10. Excitation wavelength λ_{ex}= 392 nm.* ***B****: Binding profile of Eu^{3+}−DOTA + ibuprofen generated by plotting J$_2$ transition normalised by J$_1$ transition, against ibuprofen concentration.*

Next, fluorescent titrations of phosphate, lysine, tyrosine, and phosphoserine at neutral pH were performed. For phosphoserine, lysine and tyrosine, no binding curve was expected, since there was no observed difference in the 1:1 relaxation data in section 3.3.1. This was true for lysine and tyrosine and was consistent with the hypothesis of no change in hydration number (Section 3.3.1), (**Figure 3.9**). Interestingly, in the titration of Eu^{3+}−DOTA with tyrosine, the fluorescent intensity of both peaks declined with high tyrosine concentration (**Figure 3.9**, A). This resulted in noisier data towards the end of the titration, most likely due to precipitation. (**Figure 3.9**, F). Phosphate, in the 1:1 relaxation study, demonstrated an increase in r_1 values. Here, the spectrofluorimetry binding titrations indicated no change in q value again, in line with the relaxometry data (although not yet corroborating why there is an observed increase in r_1).

154
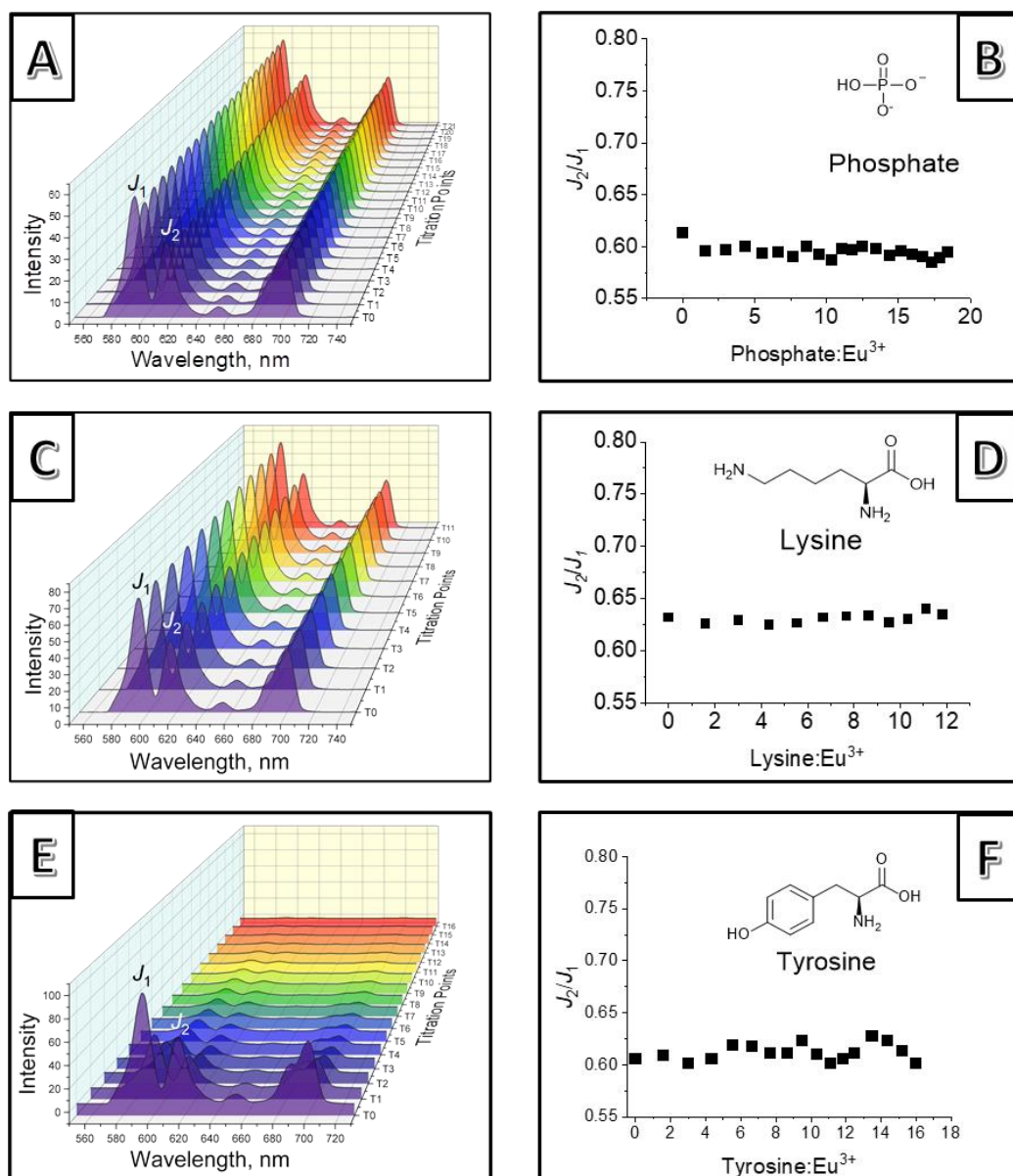
Figure 3.9 *Emission spectra of Eu^{3+}–DOTA on its own and in the presence of different concentrations of phosphate (**A**), lysine (**C**) and tyrosine (**E**), denoted as titration points. Spectra were recorded in water at $[Eu^{3+}]$ = 2 mM, 25° C and pH 6-7. Excitation wavelength λ_{ex}= 392 nm. Binding profiles of Eu^{3+}−DOTA + phosphate (**B**), lysine (**D**) and tyrosine (**F**) were generated by plotting J_2 transition normalised by J_1 transition, against guest molecule concentration.*

Binding of simple carboxylate anions (malonate and aspartate) was previously reported for a bis-Eu^{3+} type fluorescent probe, one of the Eu^{3+} caged in a crown ether macrocycle and the other in a cyclen-based macrocycle (Figure S1). [122] Association constants were reported as log K_A = 4.61 for malonate and log K_A = 4.58 for aspartate. However, binding was only observed when the crown ether moiety was present, and there was no binding when only the cyclen moiety was present, indicating that perhaps cyclen-based mono − Eu^{3+} probes are not always capable of detecting carboxylate binding. On the other hand, binding of amino acids (*e.g.*, glycine and glutamic acid) was successfully detected using relaxometric titrations with Gd^{3+}–DOTA ligand attached to a crown ether (without lanthanide inside it) decorated on a G4 dendrimer.[77] This suggested that relaxometry titrations might be a more suitable way to detect carboxylate binding.

In contrast, the titration of Eu^{3+}−DOTA with phosphoserine yielded a positive binding curve (**Figure 3.10**). The increase in signal intensity for both J_1 and J_2 was small (**Figure 3.10**, left), however the titration curve showed a small increase in their ratio with increased phosphoserine concentration from around 0.6 to about 0.8 (**Figure 3.10**, right). This was an indication of inner-sphere binding. The curve was fitted using DynaFit software, and the affinity constant was calculated as log K_A = 3.60. This value is in line with values obtained for weak binding of phosphate anions to Eu^{3+} complexes available in the literature. For example, association constants of cyclen-based Eu^{3+}

complexes binding to ATP, ADP and phosphate were reported in the range of $\log K_A = 5.2\text{-}5.5$.[98]

Binding of phosphoserine to the inner sphere of DOTA metal chelate was unexpected, based on the ANOVA data from **Figure 3.6** where the signal change in the presence of phosphoserine was negligible. This was the first indication that perhaps 1:1 ratio is not always useful when dealing with weak interactions. Phosphoserine titration showed that the metal was saturated at about 10 equivalents of phosphoserine and showed that titration data is much more informative of binding behaviour, however a method capable of detecting interactions beyond inner-sphere would be required.
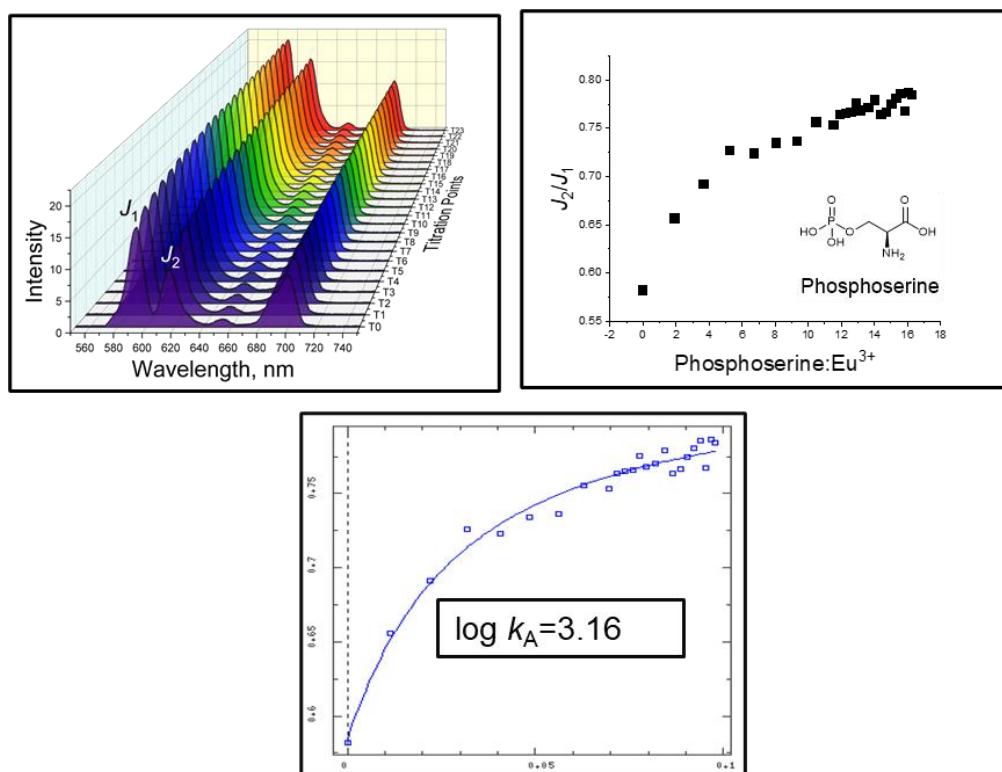
Figure 3.10 A: *Emission spectra of Eu^{3+}–DOTA on its own and in the presence of different concentrations of phosphoserine (denoted as titration points). Spectra were recorded in water at [Eu^{3+}] = 2 mM, 25° C and pH 6-7. Excitation wavelength λ_{ex}= 392 nm.* ***B:*** *Binding profile of Eu^{3+}−DOTA + phosphoserine generated by plotting J$_2$ transition normalised by J$_1$ transition, against phosphoserine concentration.*

Since the increase in signal was likely not due to changes in *q*, the next logical step would be to investigate whether the τ_m and T_{1m} had influenced the r^{IS} signal. First, possible effects of change in solvent properties on τ_m due to addition of guest molecules was investigated.

3.3.3　NMR Relaxometry Titrations

Relaxometry titrations were next performed to investigate how the relaxation rate of water protons changes as a function of guest molecule

concentration and to quantify these changes through calculations of the association constants. Relaxometric titrations of Gd^{3+}–DOTA can deliver both: the combined complex signal from all three hydration spheres and the information about how the signal changes at higher equivalents, to marry with the spectrofluorimetry binding data. They are not common in literature and have been mentioned only once with no discussion on the nature of the relaxometry signal in comparison to other techniques.[77] Fitting of the data in a similar manner to fluorescent titrations can provide quantitative means of examining signal changes and comparing the interactions between the contrast agent and guest molecules.

The titration plot resultant from the titration of Gd^{3+}−DOTA with lysine is shown in **Figure 3.11**, **A**. Upon addition of lysine, the relaxivity signal decreased sharply and reached a plateau after about five equivalents; such behaviour would logically imply that dehydration of the inner sphere is taking place due to binding. The data were fitted using DynaFit and the binding affinity constant was calculated as $\log K_A = 3.16$. These values are an order of magnitude higher than $\log K_A$ values reported for the binding of glycine, glutamic acid, γ-aminobutyric acid (GABA) and carbonate to Gd^{3+}–DOTA dendrimer measured using relaxometry titrations.[77] However, these titrations were performed at much higher field (7.05 T as opposed to our machine operating at 0.55 T) which has been shown to lead to decrease in relaxivity.[57] Similar trend was observed for tyrosine (**Figure 3.11**, B) with slightly lower affinity constant of $\log K_A = 2.83$. Interestingly, the titration

against tyrosine showed a small increase in r_1 at higher concentrations of tyrosine (>30:1 tyrosine: Gd^{3+}). This reflects the behaviour observed in spectrofluorimetry, where both J_1 and J_2 peaks decreased, indicating precipitation. Here, that precipitation results in small increases in r_1, as τ_R increases due to the presence of precipitates.

The reduction in relaxivity was interesting as ANOVA analysis of the 1:1 ratio relaxometry data from Section 3.3.1 did not show any significant change for lysine or tyrosine. This indicated that relaxometric titrations are much more informative of binding than 1:1 relaxivity data "snapshots". This is especially true in cases where the binding behaviour of molecules is not well understood. Herein, relaxometry showed a decrease in longitudinal relaxivity with increased equivalents of guest molecules (lysine and tyrosine) which logically could be attributed to changes in the hydration number q. This was not supported by the spectrofluorimetry data from Section 3.3.2 which implies that either spectrofluorimetry was not sensitive enough to see what clearly are very weak interactions (as evidenced by the K_A values here), and/or relaxivity titrations are indicating some other type of interaction than changes in q/water dehydration.
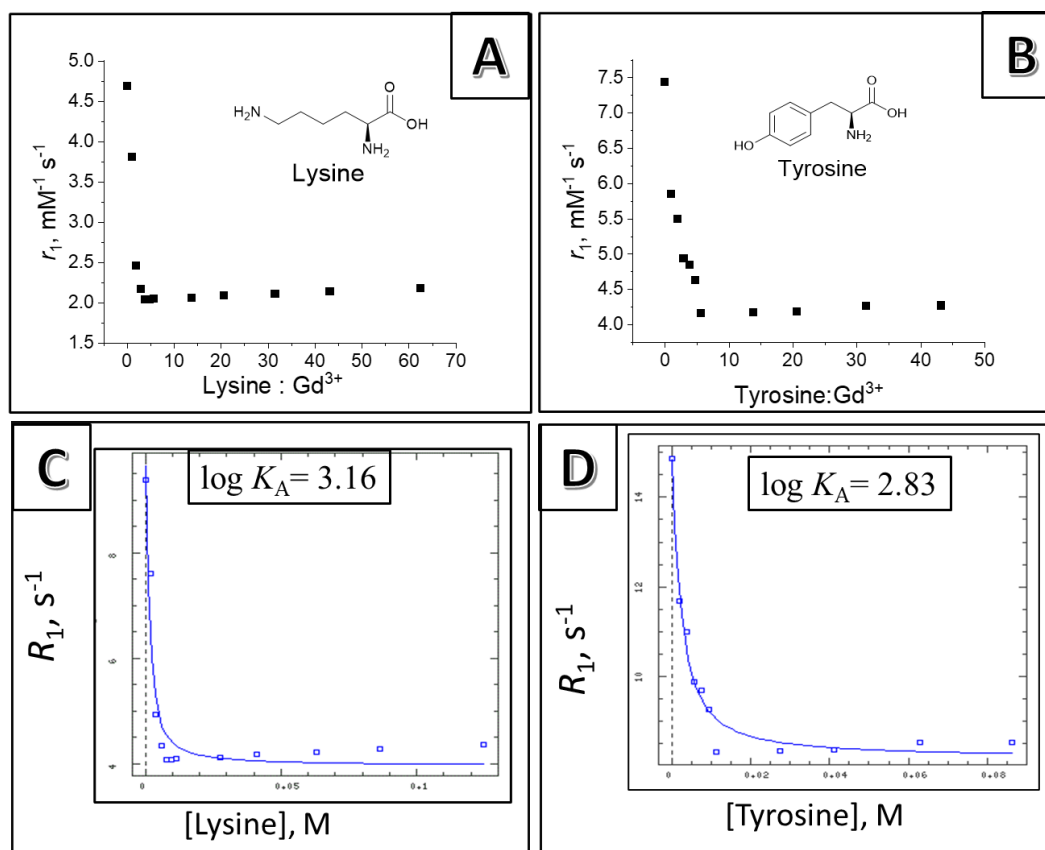
Figure 3.11 *Longitudinal relaxivity (r_1) of (A): $Gd^{3+}−DOTA–lysine$ and (B): $Gd^{3+}−DOTA−tyrosine$ recorded at different guest molecule concentrations (Gd^{3+} = 2 mM) and measured in water at pH 7.4, T = 25° C, B_0 = 23 MHz. (C): $Gd^{3+}−DOTA–lysine$ data fitted with DynaFit. (D): $Gd^{3+}−DOTA–tyrosine$ data fitted with DynaFit.*

Interestingly, titrations of $Gd^{3+}−DOTA$ with ibuprofen and phosphoserine displayed a signal increase followed by a plateau (**Figure 3.12**). The affinity constants were K_A = 4.52 for ibuprofen and K_A = 3.16 for phosphoserine. The trend of relaxivity increasing with ibuprofen addition was consistent with the data collected from the 1:1 NMR Relaxometry. Spectrofluorimetry showed that ibuprofen does not bind to the inner-sphere of $Eu^{3+}−DOTA$, so it was hypothesised that the signal increase was evidence for second/outer sphere effects.

Phosphoserine also caused an increase in signal even though spectrofluorimetry indicated displacement of the inner-sphere water molecule. The increase in relaxometry signal was relatively small (*ca.* 0.30 mM^{-1} s^{-1} with K_A of 3.16) so it is possible that strong second-sphere effects overpowered the partial displacement of the inner-sphere water molecule evidenced in the spectrofluorimetry titrations. Unfortunately, the data generated from relaxometric titrations alone was not conclusive to support or reject this hypothesis, although the similar K_A values obtained for all samples imply that a similar mechanism may be at play for all the different guest molecule species. Titration with phosphate also resulted in consistent small increases in signal which did not plateau even after 40 equivalents and, therefore, could not be fitted to generate a K_A value (**Figure 3.13**). Overall, the data pointed towards second-/outer-sphere effects, since these are not necessarily self-limiting, depending on structural organization surrounding the chelate. This is most likely due to the lack of binding specificity of Gd^{3+}−DOTA resulting in more interesting interactions between the contrast agent and guest molecules. A clear distinction between inner- and outer-sphere contributions were required to investigate this further and the best technique for this is fast-field cycling NMR.[57]
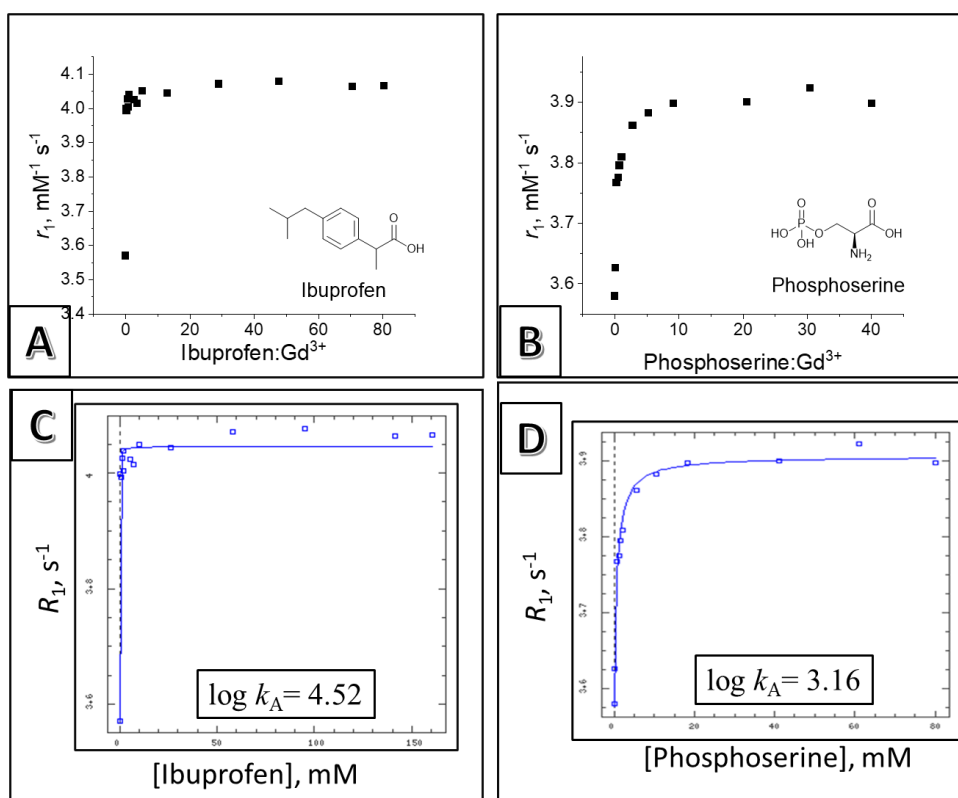
Figure 3.12 *Longitudinal relaxivity (r_1) of (A): $Gd^{3+}-DOTA$–ibuprofen and (B): $Gd^{3+}-DOTA-$phosphoserine recorded at different guest molecule concentrations ($Gd^{3+}= 2$ mM) and measured in water at pH 7.4, T = 25° C, B_0 = 23 MHz. (C): $Gd^{3+}-DOTA$–ibuprofen data fitted with DynaFit. (D): $Gd^{3+}-DOTA$–phosphoserine data fitted with DynaFit.*
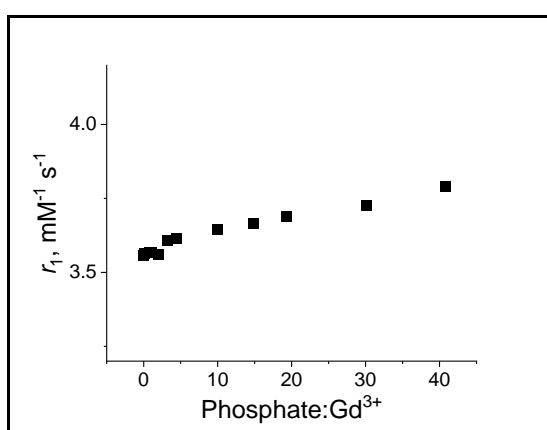
Figure 3.13 *Longitudinal relaxivity (r_1) of $Gd^{3+}-DOTA$–phosphate recorded at different phosphate concentrations ($Gd^{3+}= 2$ mM) and measured in water at pH 6-7, T = 25° C, B_0 = 23 MHz.*

3.3.4 SAP/TSAP

Structured water with higher degree of hydrogen bonding could affect relaxivity through changes in water exchange and Brownian motion of the contrast agent.[123] Changes in the water structure due to the addition of the guest molecules were investigated using ^{1}H NMR and integrating the peaks corresponding to the square antiprism (SAP) and the twisted square antiprism (TSAP) isomers of DOTA.[124] This particular section aimed to cover possible effects on the relaxivity not only due to structural and dynamic changes of the contrast agent itself, but also external factors that could affect the relaxation rates of the water protons. It has been noted that the properties of water are also important in the discussion of the efficiency of MRI contrast agents. Water can form ice-like structures owing to increased hydrogen bonding in the presence of substances termed kosmotropes. The resultant micro viscosity of water can slow down the Brownian motion of contrast agents and result in longer rotational correlation times, τ_R, as well as more ordered water in the second and outer hydration spheres of the complex.[124] From equations 1.14 and 1.15 (section 1.3.2) it can be seen that longer rotational correlation times τ_R would result in higher relaxivity, r_1 due to IS and OS contributions.

Payne *et al.* reported that the addition of kosmotropes (such as NaCl, $CaCl_2$) to the molecular MRI contrast agent Gd^{3+}−TETA resulted in a relaxivity enhancement across all frequencies in its NMR dispersion profile.[124] Gd^{3+}−TETA is a $q = 0$ contrast agent, and relaxivity is a result purely of the second sphere and outer sphere contributions. For example, the addition of

a relatively weak kosmotrope, NaCl, resulted in a uniform increase in relaxivity across all frequencies, which is consistent with the increase in the number of water molecules in the second hydration sphere. In contrast, the addition of a stronger kosmotrope, $CaCl_2$, resulted in a small peak at high frequencies, which is typical of increased τ_R.[124] This demonstrated that kosmotropes can increase relaxivity through increased rotational correlation times.

In molecular complexes with $q > 0$, such as Gd^{3+}–DOTA, τ_R is typically short and has a significant influence on the inner-sphere water molecule relaxivity. If τ_R increases because of the addition of kosmotropes, then the inner-sphere relaxivity r^{IS} would also depend on the residence time of the inner-sphere water molecule τ_m. One factor that affects τ_m is the ratio between the two structural isomers of Gd^{3+}–DOTA: square antiprism (SAP) and twisted square antiprism (TSAP). This is because the TSAP isomer has been shown to have 1-2 orders of magnitude smaller τ_m compared with the SAP isomer and so a larger fraction of TSAP can lower the average τ_m.[123] This ratio can be easily determined from the Eu^{3+}–DOTA ^1H NMR spectrum by integrating the peaks corresponding to the NCH_2 protons of the SAP isomer (at *ca.* 33.0 ppm), and TSAP isomer (at *ca.* 12.4 ppm).[125,126]

Phosphate is considered an ionic kosmotrope and, in theory, can alter the SAP/TSAP ratio of Gd^{3+}–DOTA. This would alter the inner-sphere relaxation dynamics, as discussed above. To investigate whether the concentration of phosphate used previously had any effect on the water

structure, a spectrum of the analogue Eu^{3+}−DOTA in D_2O on its own and in the presence of phosphate was obtained (**Figure 3.14**). The spectra were also recorded in the presence of lysine, tyrosine, ibuprofen, and phosphoserine for comparison, and the peaks corresponding to the SAP and TSAP isomers were integrated.

The SAP/TSAP ratio for the pure complex Eu^{3+}−DOTA (2 mM) calculated from the integration of the peaks at 33.0 ppm and 12.4 ppm was 2.38 (**Figure 3.14**). This corresponds to 70.4 % Eu^{3+}−DOTA in the SAP form and 29.6 % in the TSAP form. These results differ slightly from those in the literature, where SAP isomer was reported to comprise just below 80 % of Eu^{3+}−DOTA (150 mM) solution.[125] This difference could be due to small differences in the experimental conditions (pH, temperature, instrumentation, etc.). In general, higher TSAP content could lead to slightly higher relaxivity due to water exchange when τ_R is large.[124]

The addition of 20 equivalents of phosphate to the Eu^{3+}−DOTA solution led to a negligible decrease in TSAP by 6 % to a value of 24 %, indicating that an increase in relaxivity due to the altered SAP/TSAP ratio would not be expected. [123,127–129] Generally, the addition of all the guest molecules (lysine, phosphate, tyrosine, ibuprofen and phosphoserine) to Eu^{3+}−DOTA led to negligible differences in the SAP content, between 70.4 % and 76 % (**Figure 3.14**). Therefore, it was concluded that the amounts of phosphate and other molecules used in this study were not sufficient to cause changes in the relaxivity owing to the water structure. Interestingly, lysine,

phosphate, tyrosine and ibuprofen showed downfield chemical shift perturbation, consistent with de-shielding of the NCH_2 protons, possibly due to coordination of these salts to Eu^{3+}−DOTA. This was consistent with the trends observed for tyrosine and lysine in the NMRR titrations Section 3.3.3. The lack of chemical shift perturbation in phosphoserine was consistent with the increase in relaxivity observed in the NMRR titrations (Section 3.3.3). To explore this further lysine was chosen as a representative and diffusion-ordered spectroscopy was employed to test this hypothesis.
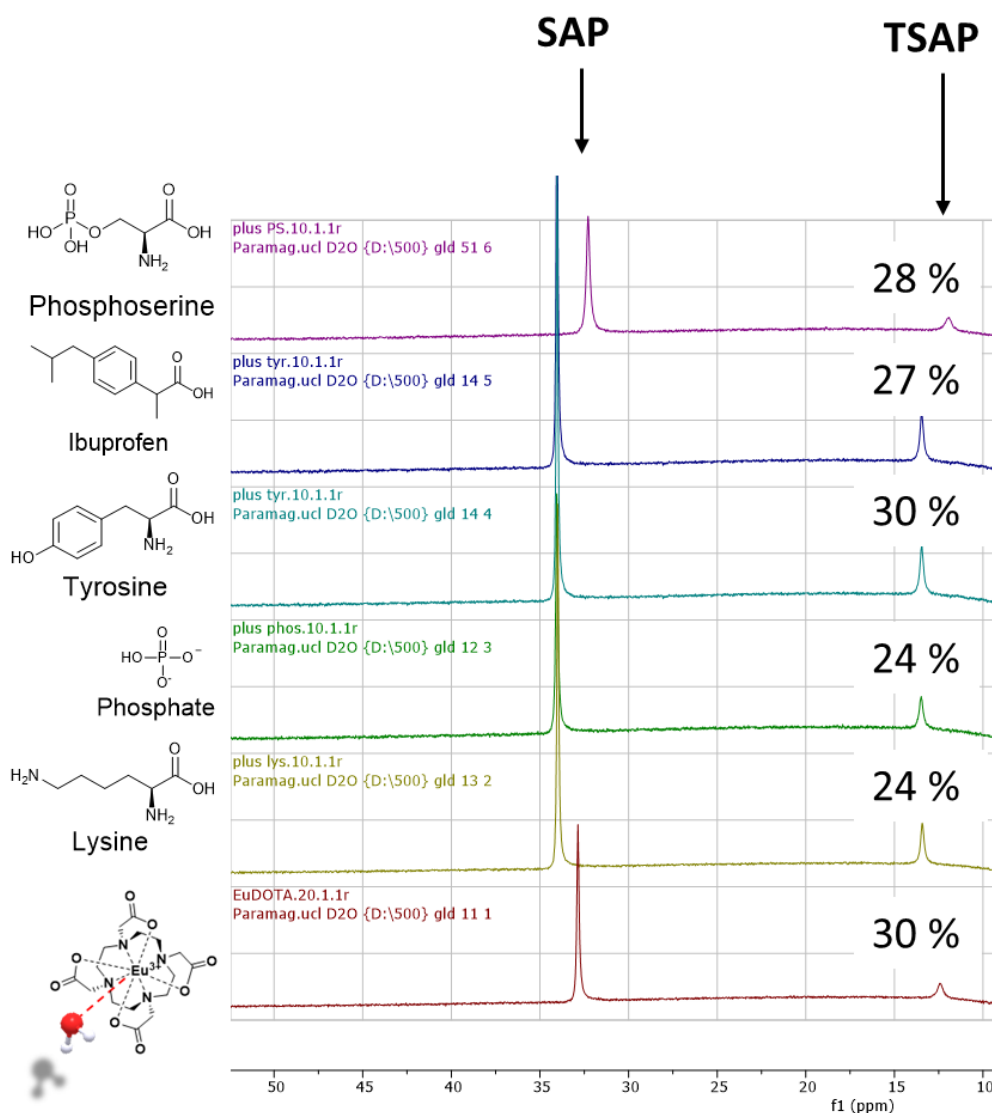
Figure 3.14 *^{1}H NMR (500 MHz, 25 °C, D$_2$O) of Eu^{3+}–DOTA on its own (bottom, red) and in the presence of phosphoserine, ibuprofen, tyrosine, phosphate and lysine in 1:20 ratio. The peaks corresponding to SAP and TSAP isomers are labelled. The percent contributions of the TSAP isomer for each mixture is indicated above each TSAP peak.*

3.3.5 Diffusion-Ordered Spectroscopy (DOSY)

DOSY is an NMR technique that is very useful for calculating the diffusion coefficients of individual resonances in the NMR spectra. It is frequently used to identify compounds in mixtures based on their translational diffusion coefficients (D_T). Because small molecules diffuse faster than larger molecules, DOSY is also very useful for testing complexation. Fast-diffusing molecules alter their diffusion coefficients upon complexation with another molecule.

The diffusion of Gd^{3+}−DOTA would be difficult to calculate due to paramagnetic shift and peak broadening. However, a simple molecule such as lysine has well-defined peaks, and its spectrum can be easily resolved and analysed. Therefore, the binding of lysine to Gd^{3+}−DOTA was investigated by using the lysine spectrum as a reference. It was expected that if no IS binding occurs, lysine's diffusion coefficient (D_T) would remain the same even in a solution containing Gd^{3+}−DOTA. However, lysine's D_T would be lowered if complexation with Gd^{3+}−DOTA took place due to the increase of molecular weight of the newly formed complex.

In order to collect the reference spectra a solution of lysine (5 mM) in D_2O was prepared, and spectra assigned (**Figure 3.15**, bottom). The average diffusion coefficient from all four ^{1}H NMR peaks was calculated as $D = 6.64 \pm 1.12 \times 10^{-10}$ m^2/s. This value is in agreement with literature.[110,109]

To avoid the severe broadening caused by Gd^{3+} the europium analogue Eu^{3+}−DOTA was prepared. A range of Eu^{3+}−DOTA concentrations were tested and 1:1 ratio of Eu^{3+}−DOTA with lysine (5 mM) was chosen for analysis due to the clarity of signal (**Figure 3.15**, top). The diffusion coefficient was calculated for all four peaks. The average translational diffusion coefficient was $D_T = 7.49 \pm 0.98$ x 10^{-10} m^2/s. An independent-samples two-tailed t-test was used to show that there is no difference between the translational coefficients for the lysine ^1H NMR peaks and lysine + Eu^{3+}−DOTA ^1H NMR peaks ($p = 0.30$). The slight reduction in diffusion coefficient upon Eu^{3+}−DOTA addition was assigned to signal broadening errors.
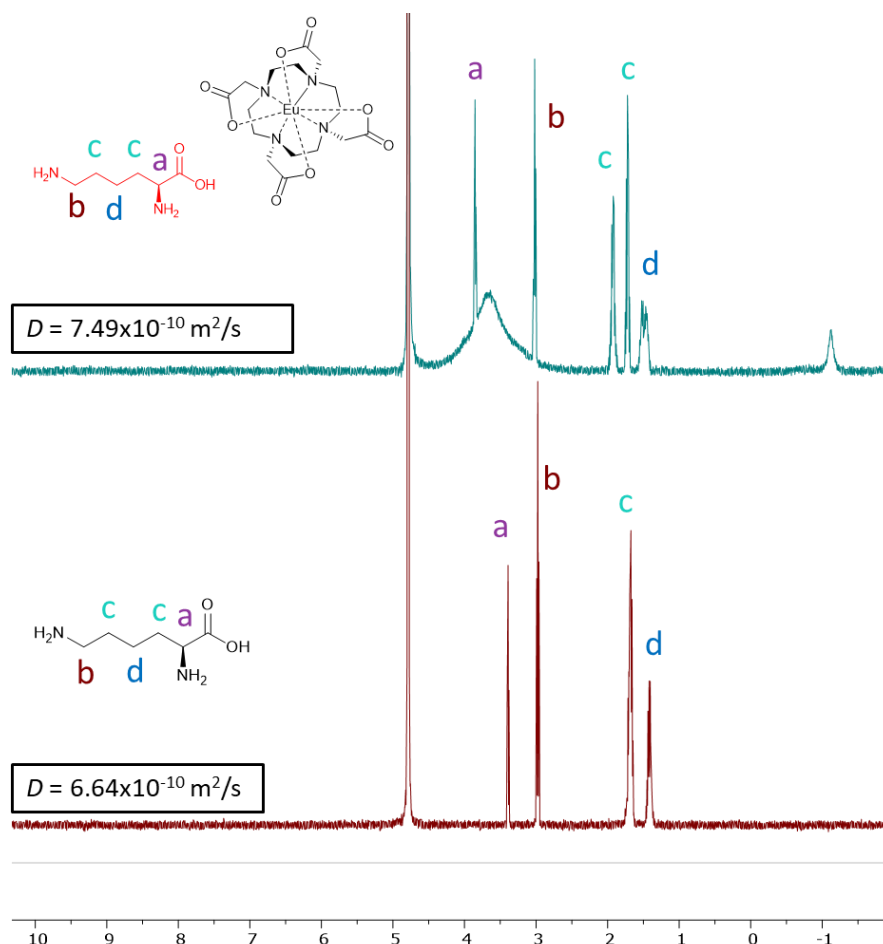
Figure 3.15 *¹H NMR (500 MHz, 25 °C, D₂O) of lysine (5 mM, bottom) and Eu³⁺−DOTA (5 mM) + lysine (5 mM, top). The average translational diffusion coefficients (Dᴛ) calculated from DOSY experiments for each mixture are indicated on the left.*

A slight paramagnetic shift was observed in lysine's spectrum for the peak corresponding to the proton closest to the binding site of the molecule (**Figure 3.15**, peak "a"). This peak migrated downfield by 0.47 ppm upon addition of lysine to Eu³⁺−DOTA, from 3.39 ppm to 3.86 ppm. This was interesting, as it indicated that the proton might be shifted due to close proximity to the Eu³⁺ ion, *i.e.*, this could indicate some alternative mode of binding or interaction with the chelate species. This was consistent with the

peak shifting behaviour observed in NMR when SAP/TSAP ratio was investigated. (Section 3.3.4). The diffusion coefficients of peak "a" (**Figure 3.15**) alone and in the presence of Eu^{3+}−DOTA were also compared as this peak was positioned closest to the binding site with Eu^{3+}−DOTA and would be expected to show biggest change in translational diffusion upon binding. However, D_T for peak "a" in a pure lysine sample was 8.28 x 10^{-10} m²/s and in the presence of Eu^{3+}−DOTA peak "a" showed D_T = 8.68 x 10^{-10} m²/s. A change of only 0.4 x 10^{-10} m²/s indicated that the mode of binding that took place between lysine and the contrast agent was not detectible by DOSY (**Table 3.1**).[108] The only parameter that affects inner-sphere relaxivity which hasn't been explored so far was the balance between the water diffusion and the relaxation of the inner-sphere water molecule.

Table 3.1 *Translational diffusion coefficients D_T for each lysine peak in the absence and presence of Eu^{3+}−DOTA calculated from DOSY measurements.*

Peak	D, x 10^{-10} m²/s Lysine	D, x 10^{-10} m²/s Eu^{3+}−DOTA + lysine
a	8.28	8.68
b	6.47	7.85
c	5.85	6.95
d	5.97	6.46

3.3.6 Temperature-dependent NMR Relaxometry

Temperature-dependent NMRR was used to investigate the balance between τ_m and T_{1m} in the presence of lysine in order to evaluate if this balance remained the same as in pure $Gd^{3+}-$DOTA. Temperature-dependent NMR Relaxometry is an excellent technique for the investigation of water exchange regime in Gd^{3+} complexes.[57] It does so by measuring and analysing the relaxivity dependence on temperature at a single frequency. Water exchange can affect relaxivity by changing the balance in equation 1.12 between the water exchange and the inner-sphere relaxation time.

There are two main water exchange regimes – fast water exchange regime and intermediate/fast exchange regime. Most small molecule contrast agents are in the fast exchange regime, where the water residence time τ_m is much shorter than the time required for the inner-sphere water molecule to relax (T_{1m}). For these systems τ_m is in the nanosecond region. In the intermediate/slow exchange regime τ_m is equal to or longer than T_{1m} and it is on the microsecond timescale.[57,58]

In both exchange regimes the outer-sphere contribution to relaxivity decreases with increasing temperature. This is because both the electronic relaxation times of Gd^{3+}, T_{ie} and the correlation time for relative diffusion τ_D (Equation 1.10-1.11) are decreased with increasing temperature. [57] In the fast exchange regime ($\tau_m < T_{1m}$) r^{IS} also decreases with temperature because the exchange of the water molecule at the metal centre gets faster and faster and

the protons experience less of the enhancing properties of gadolinium's seven unpaired electrons. Fast exchange shows an overall curve which decreases exponentially with increasing temperature.[58]

In the intermediate/slow exchange regime ($\tau_m \geq T_{1m}$) the inner-sphere contribution to relaxivity starts to increase with increasing temperature until it cancels out the outer sphere decrease of relaxivity and overpowers the curve with an increase of overall relaxivity at higher than room temperatures. This results in overall relaxivity-temperature profiles resembling an s-shaped curve. This curve begins with relatively high relaxivity at around 0 °C (273.15 K) which decreases to a point, typically around room temperature (298.15 K) and this is followed by a decrease in relaxivity.[58] In their review Aime *et al.* have reported an excellent comparison between the temperature-dependent NMR relaxometry profiles of the fast exchange contrast agent GdOBETA[-] and the intermediate/slow exchange GdDOTAM (τ_m = 35 μs). The relaxivity for both complexes was recorded between 275 K and 335 K (from 1.85 °C to 61.85 °C) at 20 MHz.[57]

It is well known that Gd^{3+}−DOTA is in the fast exchange regime with τ_m = 244 ns.[90,116] To test whether the addition of lysine changed this condition, the relaxivity of Gd^{3+}−DOTA with lysine (1:10 molar ratio) was recorded at varied temperature (**Figure 3.16**, pink squares, ■). Relaxivity was recorded between 0 °C (273.15 K) and 62 °C (335.05 K). For each datapoint the relaxation rate of five different concentrations of Gd^{3+} were recorded and the relaxivity r_1, mM^{-1} s^{-1} was derived from the linear fit of the straight-line curve

in Origin. The error bars represent the errors of the fit line. Control study was also recorded (**Figure 3.16**, purple triangles, ▲) with solutions of gadolinium chloride ($GdCl_3$) and lysine in 1:10 molar ratio.

The control (▲) showed a straight line at low temperatures between 273.15 K and 300.05 K (0 °C and 27 °C) with r_1 slightly varying between 2.5 and 2.7 mM^{-1} s^{-1}. Between 305.05 K (32 °C) and 335.05 K (62 °C) the relaxivity was slightly lower varying between 1.8 and 1.6 mM^{-1} s^{-1}. Overall relaxivity varied by around 1 mM^{-1} s^{-1}.

In contrast, the relaxivity of a sample containing Gd^{3+}−DOTA and lysine (■) showed a uniform decrease in signal from 4.33 mM^{-1} s^{-1} to 2.01 mM^{-1} s^{-1}. This exponential decrease with increasing temperature was consistent with fast exchange regime and showed that the balance between τ_m and T_{1m} was not changed upon addition of lysine. The fast exchange regime was described in more detail in Section 1.3.2. This exhausted possible inner-sphere effects and pointed towards second-/outer-sphere effects. As mentioned in section 3.3.2 it is possible that the 1:1 ratio between guest molecules and Eu^{3+}−DOTA was not enough to induce binding and a new way to detect the interactions of Gd^{3+}−DOTA with guest molecules across all hydration spheres and at higher ratios was desirable.
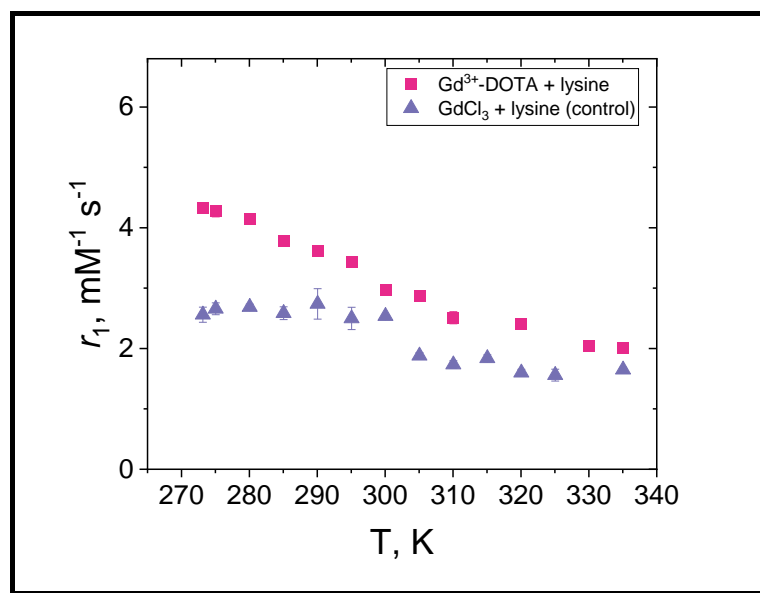
Figure 3.16 *Longitudinal relaxivity enhancement (r_1, $mM^{-1}s^{-1}$) as a function of temperature for $Gd^{3+}-DOTA+$ lysine (■) and the control $GdCl_3$ + lysine (▲) at 1:10 molar ratio at neutral pH. Each datapoint represents the r_1 value derived from the gradient of the linear fit of measured longitudinal relaxation rate (R_1) at minimum of five Gd^{3+} concentrations. The error bars represent the error associated with the linear fit in Origin.*

3.3.7 FFC NMR and NMRD profiles

Possibly the best method to investigate the nature of ^{1}H relaxation signal and access fundamental structural and dynamic properties of Gd^{3+} chelates in solution is by analysis of NMR dispersion (NMRD) profiles generated from fast-field cycling NMR (FFC NMR). The frequency-dependant behaviour of longitudinal relaxivity is well-investigated. Typically, fast-tumbling low molecular weight contrast agents display steady relaxivity values at the low-field region, dispersion between 2-10 MHz and another stabilised region of lower relaxivity at high fields. For contrast agents of higher molecular weight, including but not limited to nano-sized agents, a broad peak appears in the high-field region corresponding to slow rotational correlation τ_R. Fitting of the data allows for the separation of inner-sphere contributions from outer-sphere contributions and the extraction of important parameters such as water diffusion and rotational correlation times.[57,113,114]

In order to investigate the inner-/outer-sphere contributions to relaxivity, NMRD profiles between 0.1 – 105 MHz were recorded of Gd^{3+}−DOTA chelate alone and in the presence of the five guest molecules (lysine, tyrosine, ibuprofen, phosphoserine and phosphate) at a 1:20 molar ratio. The signal was normalised for the diamagnetic water contribution ($R = 0.4$ s^{-1}) and for the gadolinium concentration, as calculated from inductively-coupled plasma optical emission spectroscopy (ICP-OES). The resultant data were plotted, representing the x-axis in logarithmic form in order to obtain typical NMRD profiles (**Figure 3.17**).
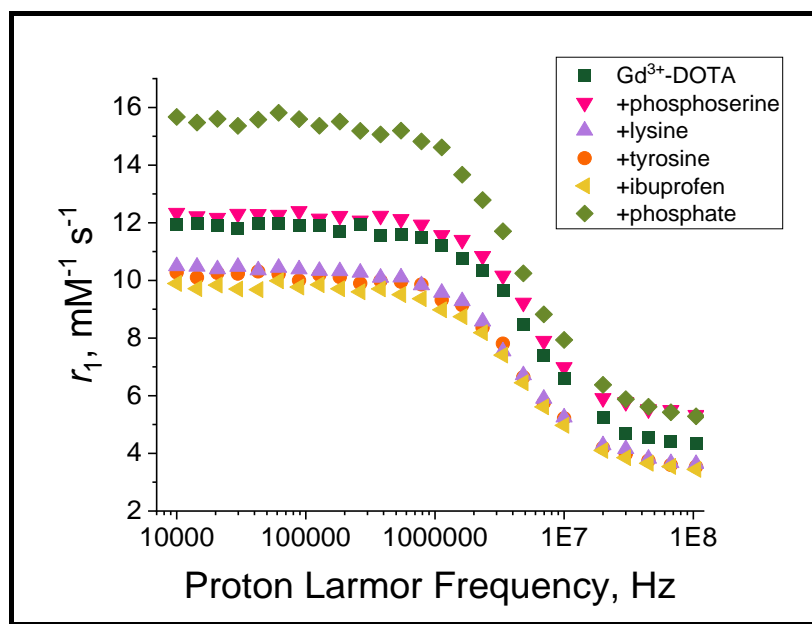
Figure 3.17   *NMRD profiles of Gd^{3+}–DOTA on its own (■) and in the presence of phosphoserine (▼), lysine (▲), tyrosine (●), ibuprofen (◀) and phosphate (◆) at 1:20 molar ratios, measured from 10 KHz to 105 MHz at 27°C, pH 6-7.*

The NMRD profiles showed a typical shape for molecular contrast agents with a plateau in the low-field region, dispersion between 2-10 MHz and another stable region of lower relaxivity at high fields (10-105 MHz).[57] The overall relaxivity enhancement was slightly lower for samples containing lysine, tyrosine and ibuprofen compared with pure Gd^{3+}−DOTA throughout all frequencies, which was consistent with the results observed during single-field titrations for lysine and tyrosine and is attributed to possible complete or partial displacement of the inner-sphere water molecule. Samples containing phosphoserine had a very similar dispersion curve to the Gd^{3+}−DOTA alone at low fields (0.1-2 MHz). At high field (10-105 MHz) the relaxivity of the

sample containing phosphoserine was higher than the Gd^{3+}−DOTA control, which typically indicates a change in τ_R or τ_m. Phosphate also showed a significant increase in relaxivity at both lower frequencies and the dispersion region which could be indicative of changes in electronic relaxation times. In order to extract the parameters governing these results and attribute inner-/outer-sphere contributions, data were fitted using Fitteia software.

Data for Gd^{3+}−DOTA (**Figure 3.18**, **A**) were fitted using Fitteia software by fixing the inner-water residence time τ_m (300 ps), the distance between the Gd^{3+} ion and the water protons (3 Å), the hydration number ($q = 1$) and other parameters listed in **Table 3.2**. Fitting of Gd^{3+}−DOTA was assisted by Prof. Mauro Botta and verified using his in-house fitting software. The fitting of the rest of the data were performed by Viliyana Lewis, using Gd^{3+}−DOTA as a template. The data was in close agreement with previous NMRD profiles published by Stelar NMR.[130] The inner sphere contribution was clearly higher than the outer-sphere contribution at lower fields, as would be expected for this chelate species. At higher fields (20 MHz) the IS/OS contributions were equal (2.25 mM^{-1} s^{-1}). These data were used as a control and a point of reference.

Table 3.2 *Fixed parameters in NMRD fitting in Fitteia, their units and values.*

Parameter	Symbol, Unit	Fixed Value
Distance between proton and electron spins, IS	r, Å	3
Distance between proton and electron spins, OS	a, Å	4.1
Self-diffusion coefficient	D, m^2/s	2.24×10^{-9}
Hyperfine coupling constant	$A/\hbar$, rad/s	1
Concentration of the contrast agent	C, mM	1
Electronic spin	S	3.5
Molar mass of the solvent	m_s, kg/mol	0.018
Density of the solution	ρ, kg/L	1
Diamagnetic contribution to the relaxation rate	R_1 (H$_2$O), s^{-1}	0.4

The relaxation rate for Gd^{3+}–DOTA with lysine, tyrosine and ibuprofen (at a 1:20 molar ratio) samples were fitted in a similar manner to Gd^{3+}–DOTA (**Figure 3.18 B**, **C** and **D**). The hydration number q, the rotational correlation time τ_R, and the mean time of water residence lifetime τ_m, were left as free parameters in order to investigate the effect of excess amounts of each guest molecule on Gd^{3+}–DOTA. The values of the correlation time of the zero-field splitting fluctuations (τ_v, s) and the means square fluctuation of the zero-field splitting (Δ^2, s^{-2}) which were previously calculated for Gd^{3+}–DOTA were used and fixed for these experiments. The correlation time of the zero-field splitting fluctuations was fixed at 15 ps, and Δ^2 was fixed at 7.1 x 10^8 s^{-2}. The rest of the parameters were fixed in accordance with **Table 3.2**.

The hydration number for all three samples was less than one, consistent with the lower relaxivity observed across all frequencies (**Table 3.3**, **Figure 3.17**). The water exchange remained consistent with the control sample, unlike τ_R which showed slight increase from the control (60 ps), with lysine showing the largest change (70.6 ps), followed by ibuprofen (67 ps) and tyrosine (64 ps), indicative of the formation of larger complex, *i.e.*, binding of the oxy anions to Gd^{3+}–DOTA. This was in agreement with the relaxivity data collected in Section 3.3.3 for lysine and tyrosine. Although the NMRR titration in this section did not show inner-sphere binding for ibuprofen, the chemical shift perturbation for all three molecules observed in Sections 3.3.4 and 3.3.5 indicated inner sphere binding and were in agreement

with these NMRD data. Due to due to small discrepancies between these measurement techniques this may be indicative of weak, reversible binding interactions.

At 20 MHz the inner-sphere and outer-sphere contributions to relaxivity for Gd^{3+}−DOTA were equal (2.25 mM^{-1} s^{-1}). At the same frequency for all three samples (containing lysine, tyrosine, and ibuprofen) the outer-sphere contribution remained the same, while the inner-sphere contribution decreased between *ca.* 1 mM^{-1} s^{-1} and 1.7 mM^{-1} s^{-1} (**Figure 3.18**). This was consistent with the hypothesis that relaxometric titrations with lysine and tyrosine cause reduction in inner sphere effects.

Table 3.3 *Fitted ("free") parameters in Fitteia for Gd^{3+}−DOTA in the presence of lysine, tyrosine and ibuprofen. Corresponding values for the control sample Gd^{3+}−DOTA are also shown for ease of comparison and fixed parameters for this sample are indicated with asterisk (*).*

	τ_R, ps	τ_m, ns	q
Gd^{3+}–DOTA	60.0 ± 3.8	*300	*1
+lysine	70.6 ± 6.0	300 ± 29	0.6 ± 0.04
+tyrosine	64.0 ± 5.3	300 ± 31	0.7 ± 0.05
+ibuprofen	66.9 ± 9.2	300 ± 49	0.4 ± 0.04
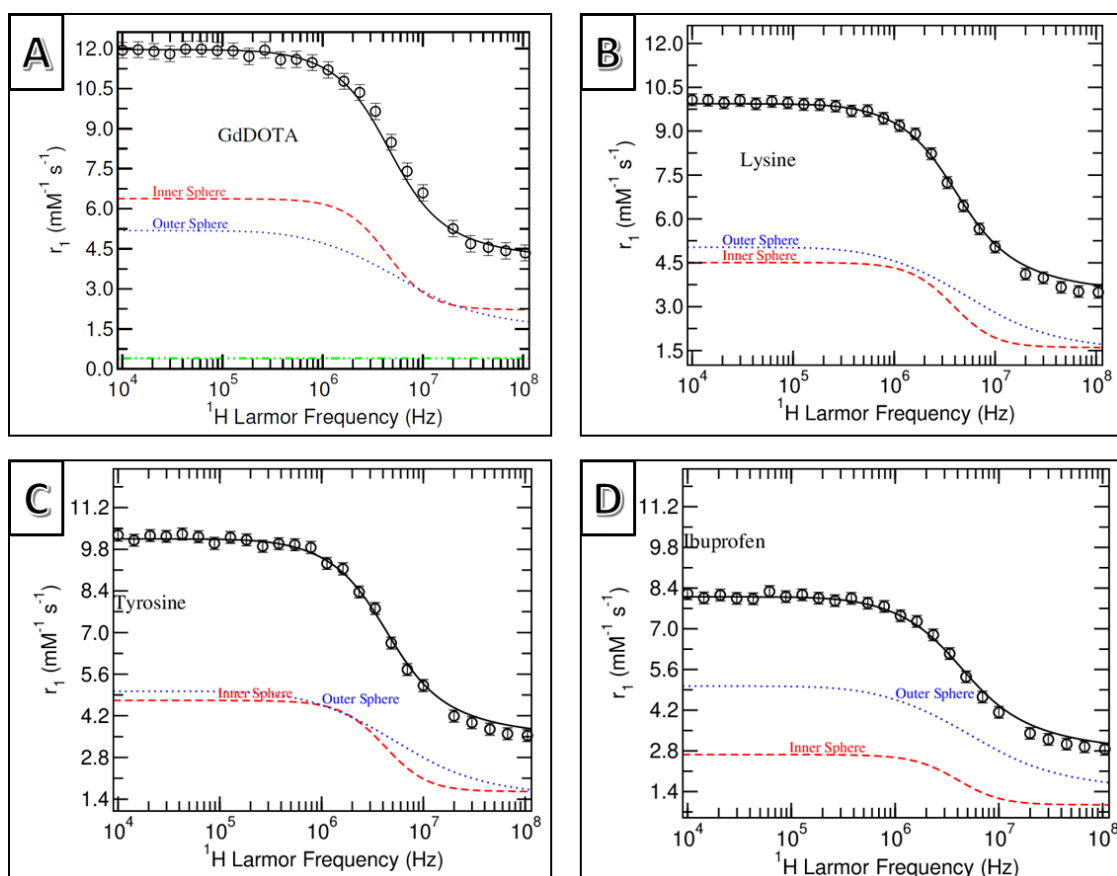
Figure 3.18 *NMRD profiles of* ***A****: Gd^{3+}−DOTA control sample;* ***B****: Gd^{3+}–DOTA + lysine (1:20 molar ratio);* ***C****: Gd^{3+}–DOTA + tyrosine (1:20 molar ratio);* ***D****: Gd^{3+}–DOTA + ibuprofen (1:20 molar ratio). All samples were measured from 10 KHz to 105 MHz at 27°C, pH 6-7(open black circles ○) and fitted in Fitteia software. The black line represents the fit of the data (−) dashed red line (--) represents the inner-sphere contribution to relaxivity, the dotted blue line (…) represents the outer-sphere contribution to relaxivity. The dash-dot green line (-..-) in Gd^{3+}−DOTA sample represents the diamagnetic contribution of water.*

The relaxation rate for Gd^{3+}−DOTA with phosphoserine and phosphate (at a 1:20 molar ratio) samples were fitted using Fitteia similarly to lysine, tyrosine and ibuprofen by fixing all parameters listed in **Table 3.2** as well as τ_v and Δ^2 fitted to 15 ps and 7.1 x 10^8 s^{-2} respectively. The rotational correlation remained the same as the control Gd^{3+}−DOTA for both samples (60 ps) which was the first indication that no direct inner sphere binding occurred (**Table 3.4**). However, the hydration of both complexes increased by <1 (q = 1.8 for phosphoserine and q = 1.6 for phosphate) which is not possible for Gd^{3+}−DOTA which can only accommodate a single water molecule in its inner-sphere. Based on this and the data from the relaxometry titrations (Section 3.3.3), which showed a modest overall increase in signal for phosphoserine and continuous increase for phosphate, it was suspected that the addition of phosphoserine/phosphate induced second-sphere effects. The fitting of phosphoserine showed a dramatic decrease of water exchange with the lifetime of water τ_m shifting in the millisecond region (τ_m = 2.1 ms), consistent with slow exchange regime. This is expected for systems with increased hydrogen bonding and reduced mobility of water in the second sphere of the complex.[131] Because the binding pocket of Gd^{3+}−DOTA is relatively small, it is possible that phosphoserine formed hydrogen bonding through both carboxylic and phosphate groups in the vicinity of the second hydration sphere.
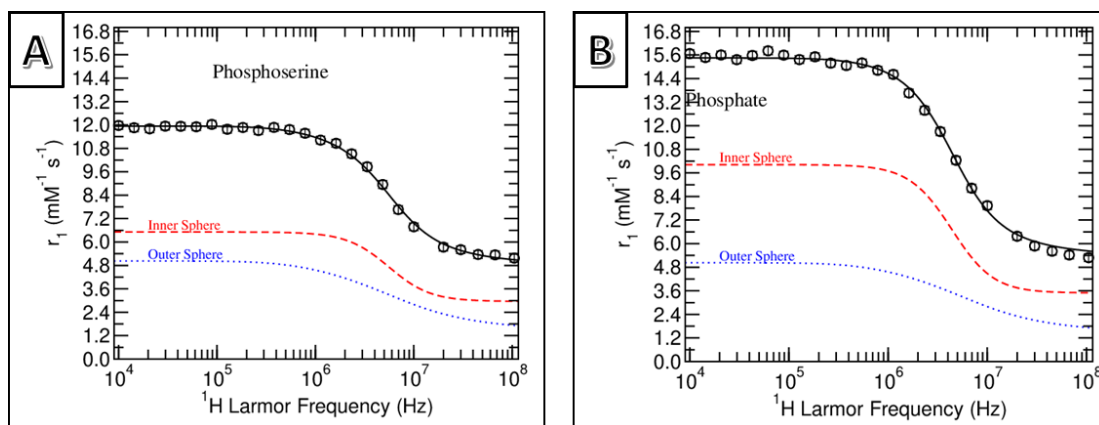
Figure 3.19 *NMRD profile of **A**: Gd^{3+}–DOTA + phosphoserine and **B**: Gd^{3+}–DOTA + phosphate measured from 10 KHz to 105 MHz at 27°C, pH 6-7(open black circles ○) and fitted in Fitteia. The black line represents the fit of the data (−) dashed red line (--) represents the inner-sphere contribution to relaxivity, the dotted blue line (...) represents the outer-sphere contribution to relaxivity.*

On the other hand, the water exchange for Gd^{3+}−DOTA + phosphate sample remained in intermediate/fast exchange regime with τ_m fitted at 300 ±2.5 ns (**Table 3.4**). The rotational correlation also remained similar to the control sample with τ_R fitted at 61 ± 2.5 ps. The only difference between the control sample and Gd^{3+}−DOTA + phosphate remained the higher hydration number q = 1.6 which indicated second-sphere effects, consistent with the ability of phosphate to form hydrogen bonding. Unfortunately, Fitteia software is only capable of separating inner from outer-sphere effects and is not designed to calculate second-sphere effects.

One way to artificially stimulate second-sphere effects in NMRD fitting is by increasing the distance r between the proton and electron spins. Payne *et al.* reported the NMRD profiles of pure Gd^{3+}−TETA and of

Gd^{3+}−TETA in the presence of the kosmotropic salt $CaCl_2$, where Gd^{3+}−TETA + $CaCl_2$ showed an increase in relaxivity, which could not be ascribed to inner-sphere effects because Gd^{3+}−TETA has no inner-sphere water molecule.[131] To account for the water-ordering effects of $CaCl_2$ a second coordination sphere was simulated in the NMRD fitting by increasing the number of water molecules to $q = 3$ and increasing the distance r from 3 Å to 3.7 Å.

In a similar manner phosphate was re-fitted with all other parameters remaining the same, keeping τ_R, τ_m and q free and only changing the distance between the Gd^{3+} and the water proton to $r = 3.7$ Å (**Figure 3.20**). This fit showed slightly faster water exchange with $\tau_m = 400 \pm 29$ ns, which is expected for second hydration sphere. The fitting revealed 5 water molecules situated at 3.7 Å (**Table 3.4**). The fit showed a large error bar for τ_m of 72 %, which underlined the inability of Fitteia to deal with second-sphere fitting. Nevertheless, the linear increase of relaxivity with phosphate equivalents (in NMRR, Section 3.3.3) was consistent with the formation of hydrogen-bonded network through phosphate's four oxygens and the appearance of predominant second-sphere effects.

Table 3.4 *Fitted ("free") parameters in Fitteia for Gd^{3+}−DOTA in the presence of phosphoserine and phosphate. Gd^{3+}−DOTA + phosphate was also fitted for second-sphere effects (SS). Fixed parameters for the control sample Gd^{3+}−DOTA are indicated with asterisk (*).*

	τ_R, ps	τ_m, ns	q
Gd^{3+}–DOTA	60.0 ± 3.8	*300	*1
+phosphoserine	54.4 ± 4.2	2100 ± 239	1.76 ± 0.11
+phosphate	60.9 ± 2.5	300 ± 21	1.55 ± 0.05
+phosphate (SS)	60.0 ± 1.7	400 ± 287	5.19 ± 0.15
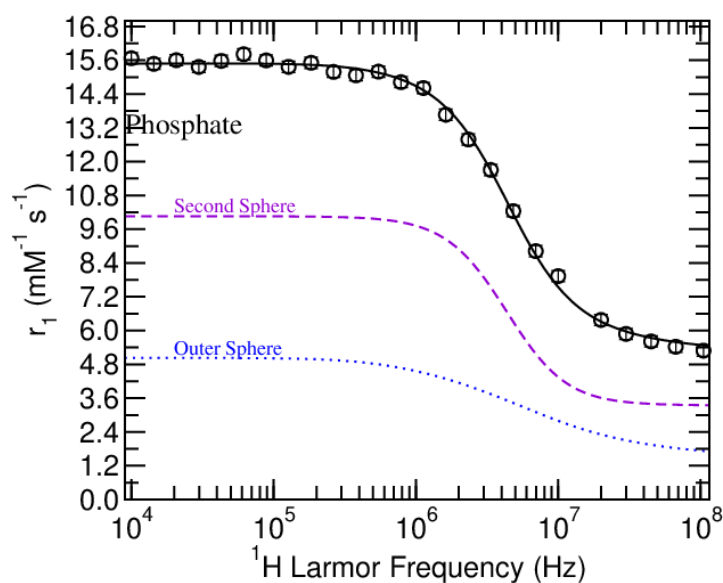
Figure 3.20 *NMRD profile of Gd^{3+}–DOTA + phosphate measured from 10 KHz to 105 MHz at 27°C, pH 6-7(open black circles ○) and fitted in Fitteia. The black line represents the fit of the data (−) dashed violet line (--) represents the second-sphere contributions to relaxivity, the dotted blue line (…) represents the outer-sphere contribution to relaxivity.*

Fitting of the NMRD profiles using Fitteia software provided important insights into the dynamic environment of Gd^{3+}−DOTA in the presence of the five guest molecules. For 20 equivalents of lysine, tyrosine and ibuprofen, a higher contribution of the outer hydration sphere to the relaxivity compared with Gd^{3+}−DOTA was observed. Fitting of Gd^{3+}−DOTA + phosphoserine/phosphate suggested that the increase in relaxivity with increasing phosphate for both NMRR titrations and NMRD was due to the formation of hydrogen-bonded water in the second hydration sphere. These findings were interesting and encouraging as they showed that the richness of the MRI signal boosted by contributions from all hydration spheres enabled detection of much weaker interactions than current techniques are able to detect.

3.4   Conclusion

The interactions between Gd^{3+}−DOTA and five guest molecules were investigated using a range of spectroscopic and relaxometric techniques. Characterisation of the relaxometry signal due to these interactions was challenging due to the weak binding which appeared to be taking place, however distinct contributions of the relaxivity due to inner-sphere, second-sphere and outer-sphere effects were separated with the help of the paramagnetic relaxation theory described in Section 1.3.

NMRR titrations of Gd^{3+}−DOTA with the guest molecules revealed that these weak interactions are best observed at and above 1:10 ratio between

the contrast agent and the binding moiety. This was of particular importance for the experimental design of future investigations of these types of interactions. NMRR titrations were much more appropriate for the evaluation of the MRI contrast agent interactions than fluorimetric titrations due to the difference in signal origin in the two techniques. The NMRR signal was more sensitive to structural changes around the complex because unlike spectrofluorimetry, NMRR is representative of changes in all hydration spheres. This makes MRI ideal for the detection of weak reversible binding interactions which was encouraging in the context of designing novel detection of sarin poisoning, where the structure of the adducts existing in the body present similar functional groups to those species investigated herein. This was emphasised quantitatively by the higher association constants produced by fitting of the titration curves generated by NMRR compared with equivalent titrations in SF which showed no binding or smaller association constants. NMRR was used only once before in the literature,[77] however the results were not compared with other techniques before.

In order to investigate the origin of the relaxivity signal at the end of each titration, FFC NMR of Gd^{3+}−DOTA alone and in the presence of excess guest molecules was measured. Fitting the NMRD profiles in Fitteia software revealed predominantly inner-sphere effects upon addition of excess lysine, tyrosine and ibuprofen and an increased hydration of the Gd^{3+}−DOTA + phosphate/phosphoserine complexes possibly due to hydrogen bonding forming a well-defined second hydration sphere. This could be caused by the

size of the guest anionic species, as well as the charge. This correlated well with the NMRR titration data, as well as chemical shift perturbation observed in the SAP/TSAP and DOSY experiments. Due to the limitations of the software, fitting of phosphoserine and phosphate containing samples was challenging. A strategy previously applied only to $q = 0$ contrast agent $Gd^{3+}−TETA$ revealed the formation of a strong second hydration sphere around the $Gd^{3+}−DOTA$ complex when 20 equivalents of phosphate were added. This equated to five water molecules at a distance of 3.7 Å.

From this research it can be concluded that amino acids bind weakly to $Gd^{3+}−DOTA$ through displacement of the inner-sphere coordinated water molecule. In contrast, phosphoserine displayed second-sphere interactions. In the future it would be interesting to test the binding of other phosphate-containing molecules, such as phosphotyrosine and ATP, ADP etc. to $Gd^{3+}−DOTA$ and investigate whether they also display this second-sphere binding behaviour. This type of study will give a better understanding of the behaviour of this frequently used contrast agent *in vivo*.

4   Towards Magnetic Resonance Active Nanoparticles

4.1   Introduction

Porous silica materials are versatile materials which have been widely used for a number of applications, such as for polymer fillers, pharmaceutical excipients, in acid-base catalysis, pollutant sorbents and others.[132] Notably, porous silica nanoparticles have been found to be very useful for medical applications, including drug delivery,[87,133–137], fluorescent imaging [138,139] and magnetic resonance imaging (MRI), when appropriately modified.[138,140–143] Silica nanoparticles have become an attractive target for the synthesis of novel nano-sized gadolinium-based contrast agents due to their large surface area, ease of preparation and good biocompatibility.[140] The large surface area allows the surface functionalisation with large number of molecular Gd^{3+}-based molecular contrast agents and the presence of porous structure in some types of silica nanoparticles provides the perfect environment for impregnation with insoluble drugs for the preparation of theranostic materials.[144] Due to their generally acceptable biocompatibility silica nanoparticle-based contrast agents have the potential to be used *in vivo*, which is crucial for their applications in bioimaging.

Mesoporous silica nanoparticles (MSNs) are class of silica materials with pore diameter arrays (which can be ordered or disordered) between 20 and 500 Å.[86,145] These structures are typically synthesised using a modified

Stöber process, which yields highly stable and monodispersed colloidal suspensions. The conventional Stöber process involves a one-pot reaction, with a silica precursor, a base, and water/alcohol mixture. First, the water and ammonia hydrolyse the silica precursor to silicic acid. This leads to subsequent particle nucleation and growth due to condensation of the silica monomers and seed aggregation.[132] Low catalyst (ammonia) concentration leads to high polydispersity, whereas high concentration leads to large particle sizes.[132,146] Therefore, the reaction conditions have to be carefully controlled for uniform nanoparticle synthesis. Silanol surfaces of silica nanoparticles lend themselves to ready functionalisation. For example, using any functional ethoxysilane, the same condensation chemistry allows the surfaces to be grafted and modified with a variety of chemical moieties, including, for example, Gd^{3+}-cyclen-based MRI chelates. These types of MRI active agents typically have a higher relaxivity than their molecular counterparts mainly due to their larger size (nanometres), which leads to increased τ_R. When sizes start approaching a micron, longitudinal relaxation rates become slow again as τ_R assumes values of nanoseconds.[59] For example, MSNs post-grafted with gadolinium-chelates are MRI active and experience enhanced longitudinal relaxation times through changes in the rotational correlation time τ_R.[31]

A recent example of novel magnetic silica nanoparticles as positive MRI contrast agents involved the synthesis of Gd_2O_3 nanoparticles (5.7 nm) which were subsequently dotted on the surface of non-porous silica nanoparticles with overall diameter of 60 nm.[142] The relaxivity of this

material was $r_1 = 39.08$ mM^{-1} s^{-1}, measured in 0.5 wt% agar, 0.55 T, (temperature not specified). This is a significant enhancement compared with molecular contrast agents which are restricted to relaxivity values between 4 and 5 mM^{-1} s^{-1}.[42]

The Stöber process can be modified with an additional step to produce porous colloidal silica. This is achieved by the formation of a micelle template at the beginning of the synthesis for the development of the mesopores. The micelle template is typically formed using a surfactant, the size of which determines the particle pore diameter. The silica precursor condenses around the template following the standard Stöber process, after which the template can be removed thermally, through calcination, or chemically, through acid/base removal.[132] In a similar example to the one above, the synthesis of MSNs decorated with Gd_2O_3 was reported.[140] These nanoparticles however bore mesopores with a pore size of 3.5 nm and an overall size of 90 nm. They displayed a very high relaxivity of 51.85 ± 1.38 mM^{-1} s^{-1} (1% agarose, 37 °C, 0.5 T), suggesting that porosity could be important for achieving higher relaxivity. A high hydration number for Gd^{3+} of $q = 2$-3 was reported, just like in the previous example, and additionally contributed to the high relaxivity value. Toxicity evaluation after 48 hours at range of pH showed that leaching of toxic Gd^{3+} ions was $< 1\%$.

Molecular gadolinium chelates can also be incorporated within the structure of silica nanoparticles by utilising a co-condensation method which typically attaches an anchoring unit which bears the Gd^{3+}-species.[143] An

example of Gd^{3+} chelates embedded into a silica network in mesoporous nanoparticles with size 75 nm and pores between 1.4 – 2.9 nm was reported. Despite the τ_R enhancement, these materials yield relatively low relaxivity, between 4.1 to 8.4 mM^{-1} s^{-1} (3 T, temperature not specified, solvent not specified), which is only a slight improvement over molecular contrast agents.[143] Similarly, embedding Gd^{3+}−DTPA into a silica matrix increased the relaxivity enhancement only by 1.69 mM^{-1} s^{-1}, from 4.09 mM^{-1} s^{-1} for molecular Gd^{3+}−DTPA to 5.78 mM^{-1} s^{-1} (30 °C, 1.2 T, solvent not specified) when embedded on silica nanoparticles with sizes of 6.6 nm.[138] The reason for the lower relaxivity was not reported, however it is likely that most Gd^{3+} ions in the MSNs are "hidden" (embedded in the pores) and have no direct contact with water, resulting in lower relaxivity enhancement which is defined "per gadolinium ion".

A more popular strategy is to decorate the surfaces of MSNs with gadolinium chelates which enlarges their τ_R and maintains the water access to the ions. This is the approach often used to produce MRI active MSNs – through the covalent surface modification of the particles such as Gd^{3+}–DOTA.[140] The attachment to the nanoparticles typically occurs through one of the pendant arms of the chelate utilising an amide into the structure instead of carboxylate. The amide enables chelation to Gd^{3+} through the carbonyl oxygen, retaining octadentate coordination to the metal. This could reduce slightly the stability of complexes as the central metal is held less tightly by the cage. This type of material is more easily modified to serve as

detection systems due to the ability to vary the functional groups present on the molecular ligand. This means that ligands tailored to specific targets can be easily produced.

Characteristically, attachment is accomplished by functionalising the MSN surfaces with amine groups which are reacted with an NHS-ester version of the molecular ligand. The size of the linker can affect relaxivity as it induces a local motion (τ_{RL}) through bond rotation in addition to the overall tumbling of the complex (τ_{RG}). Unreacted amine groups on the nanoparticle surface aid the formation of a hydration sphere close to the gadolinium complex, which can increase hydrogen bonding and lower τ_m values. Carniato *et al.* reported post-grafting of the external surfaces of MSNs of the type MCM-41 with a DOTA-like ligand featuring a long linker (**Figure 4.1**).[89] The relaxivity of the nanoparticle composite was reported as $r_1 = 27 \pm 2$ mM^{-1} s^{-1} in 0.1 wt% xanthan gum solution, 20 MHz, 310 K (36.85 °C). This was described as a six-fold increase in relaxivity compared with the molecular agent shown in **Figure 4.1**.
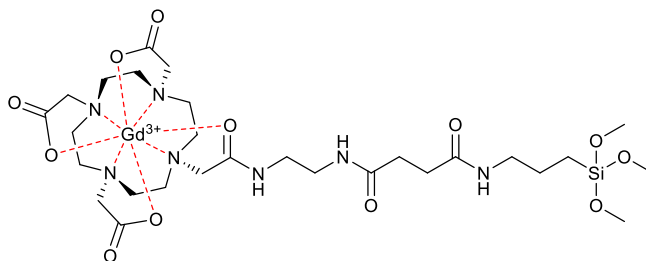
Figure 4.1 *Structure of Gd^{3+}−DOTA-like complex Gd^{3+}−DOTAMA anchored to MCM-41 by Carniato et al.* [89]

Another desirable property of MSNs is their ability to host large payloads of guest molecules in their pores due to their high surface area-to-volume ratio. For this reason, MSNs have been extensively studied as an inorganic framework for biomedical applications.[147,148,149,84] This type of material has been also explored as a theranostic probe, by loading their pores with therapeutics and functionalising their surfaces with molecular contrast agents.[144] Interactions of the drugs with the contrast agent during release enable real-time monitoring and potential quantification of the drug release, based on the changes in MRI signal. Previous studies showed that interactions between guest molecules and molecular contrast agents are preserved when the contrast agent is attached to MSNs, however the overall absolute relaxivity is much higher compared to their molecular analogues.[144] This is encouraging in the context of developing a detection system as utility of MSNs can significantly increase detection sensitivity.

Another interesting class of nanomaterials are silsesquioxane nanoparticles. They have been previously reported as potential fluorescent probes, as described in Section 1.5, by incorporating Eu^{3+} in their structure.[96] Replacement of fluorescent Eu^{3+} ions with Gd^{3+} ions enabled an MRI active probe to be produced.[94] In a literature example, the corners of aminopropyl substituted silsesquioxane $T_8(CH_2CH_2\text{-}CH_2NH_2)_8$ were functionalised with molecular MRI contrast agents 1,4,7,10-tetraazacyclododececane, 1-(glutaric acid)-4,7,10-triacetic acid (DOTAGA) and 1,4,7,10-tetraazacyclododecane-1-

(4-(carboxymethyl)benzoic)-4,7,10-triacetic acid (DOTABA) to yield two novel MRI contrast agents (**Figure 4.2**). [94]

The relaxivity of the hybrid materials were higher than the relaxivity of the corresponding molecular agents, due in-part, to slower Brownian motion (lower τ_R). The relaxivity of the molecular DOTAGA agent measured at 20 MHz and 25 °C was 5.18 mM^{-1} s^{-1} The silsesquioxane alternative Gadoxane G generated a higher value of $r_1 = 12.13$ mM^{-1} s^{-1}. Measurement of DOTABA under the same conditions (20 MHz, 25 °C) returned a relaxivity value (r_1) of 5.87 mM^{-1} s^{-1} for the molecular species, in comparison to $r_1 = 17.11$ mM^{-1} s^{-1} for Gadoxane B, the POSS complex.[93]
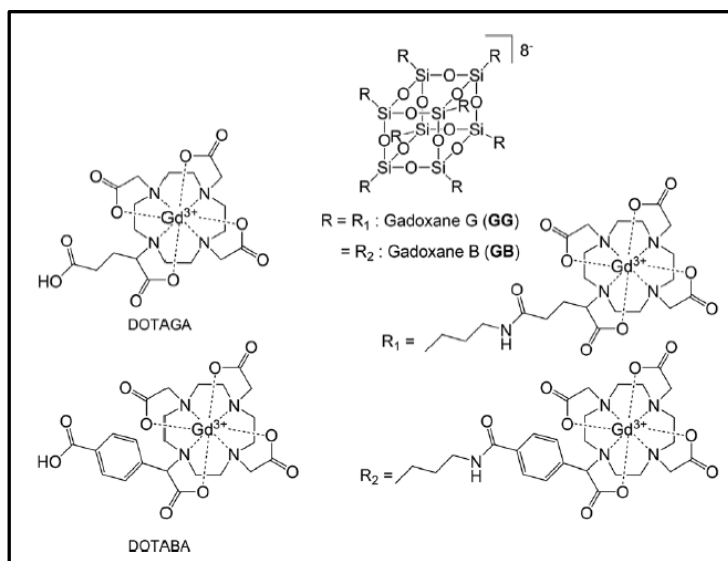
***Figure 4.2** Structures of the molecular MRI contrast agents DOTAGA and DOTABA (left) and their POSS-based alternatives(right).*[93]

Open-corner polyhedral oligomeric silsesquioxanes (OC-POSS) are characterised by incompletely condensed silanol groups and are often used for the chelation of metals. This chelation can be achieved by reaction of the open-

corner POSS with metal alkoxides or metal chlorides to form metalosilsesquioxanes (M-POSS).[91,95] Examples of M-POSS predominantly incorporate transition metals, however, silsesquioxanes doped with rare earth metals have been demonstrated. [96]

One example of using open-corner POSS for metal chelation is through direct corner-capping.[91] Trisilanolisobutyl-POSS was capped with Ti^{IV} and V^{V} transition metals to yield Ti-isobutyl-POSS and V-isobutyl-POSS. The reaction progress of the corner-capping was monitored in solution by FTIR spectroscopy. It was found that the metals in M-POSS adopted a tetrahedral coordination geometry. Embedding of these structures in polypropylene significantly enhanced thermal stability under oxidative conditions.[91] The natural porosity arising from the cage-like structure of partially uncondensed POSS makes them attractive candidates for MRI contrast agents.

In this structure the metal centre could be coordinated to six oxygens originating from the POSS (coordination number = 6) and there remain three possible spaces which could be exploited as a binding pocket for solvent or possible guest molecule binding. Therefore, silsesquioxane-based nanomaterials can be used as alternative species for MRI contrast agents and could enhance the MRI signal by varying the coordination number around the metal centre and in this way, increasing the hydration number (q). A bigger binding pocket would mean greater signal change upon chelation when guest molecules are present in the solution. The high hydration number ($q = 3$) could lead to increased relaxivity in solvent and the large binding pocket can

accommodate larger guest molecules in the inner sphere. This prospect was investigated in this project.

4.2   Aims

The aim of this chapter was to explore nano-contrast agents as potential detection systems for nerve agent adducts. In the first part a well-known type of silica nanoparticles was synthesised and modified with a $Gd^{3+}-$DOTA species, and their ability to serve as a detection system for oxyanions was evaluated. The second part of this chapter aimed to synthesize novel nano-contrast agents based on silsesquioxane structures and the ability of these nanoparticles to enhance relaxivity was evaluated.

4.3   Mesoporous Silica Nanoparticles for MRI Detection

4.3.1   Synthesis and characterisation

Mesoporous silica nanoparticles (MSNs) were synthesised using a modified Stöber bottom-up approach.[117,133] Tetraethyl orthosilicate (TEOS) was used as a silica precursor and cetrimonium bromide (CTAB) was used as a template to form the silica matrix (**Figure 4.3**). The surface of the nanoparticles was partially aminated through co-condensation with 3-aminopropyltriethoxysilane (APTES). The micellar template was subsequently removed using acid extraction and the nanoparticles were washed until neutral pH was restored. Next, the MSN were post-grafted with

DOTA–NHS–ester using carbodiimide chemistry and with GdCl₃ to form

Gd³⁺–DOTA–modified MSNs (Gd³⁺–DOTA–MSN).
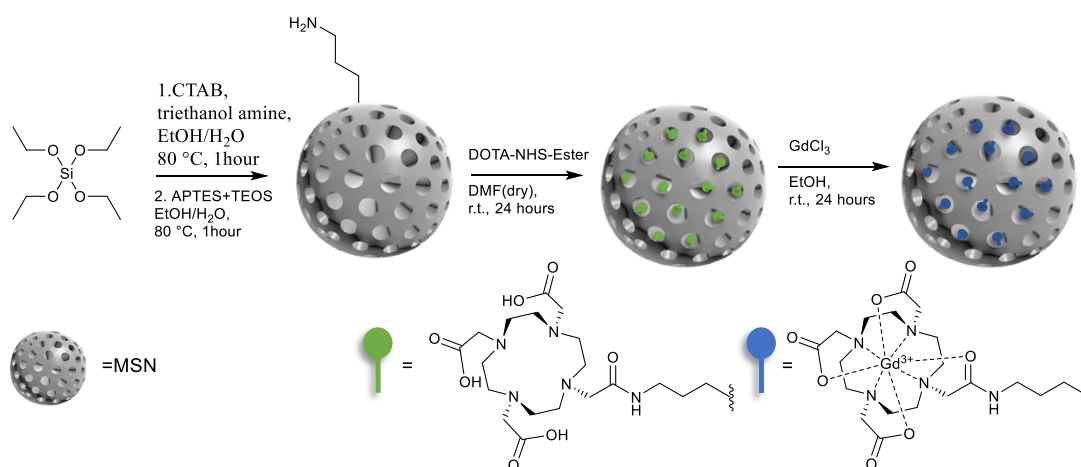
Figure 4.3 *Synthetic route to Gd³⁺–DOTA–MSNs. The first step was a surfactant templated hydrolysis and condensation which formed the particles; APTES modification allowed the decoration with amino functionalities during the synthesis and then carbodiimide coupling to DOTA-NHS-ester afforded embellishment of the chelate, which was then ligated to Gd³⁺.*

4.3.2 Characterisation

The size of the uniform spherical nanoparticles was measured using transmission electron microscopy (TEM) and it was *ca*. 50 nm in diameter (**Figure 4.4**). The TEM micrograph showed an array of mesopores. It has been shown that this type of MCM-41 materials using CTAB as a template have a characteristic pore size of 2.0-2.5 nm.[87] The stability of the colloidal suspension was tested using dynamic light scattering (DLS). The zeta potential of the nanoparticles was found to be -22.6 ± 0.5 mV which indicated a stable suspension. The average hydrodynamic diameter, d(H), was found to

be 190.4 ± 3.7 nm which is typical for these type of materials.[144] The

hydrodynamic diameter size measured by DLS is always an estimation of the

actual nanoparticle diameter of the hard sphere observed by TEM. This is

because d(H) of the particle includes the diameter of the hard sphere

surrounded by a thin electric dipole layer meaning that d(H) is defined as a

sphere, with the same diffusion coefficient as the particle (Section 2.2.3). The

polydispersity index (PDI) of 0.19 ± 0.01 indicated a highly monodispersed

sample. Infrared spectroscopy (IR) was used to verify that the template had

been successfully removed followed chemical extraction. The infrared

spectrum captured after the first synthetic step showed symmetric and

asymmetric Si-O-Si stretches at ν_{max} = 1060 cm^{-1} and ν_{max} = 790 cm^{-1}

respectively.[150] CTAB peaks usually found at ν_{max} = 2950 cm^{-1} and ν_{max} =

1460 cm^{-1} (red dash line, **Figure S2**) were not present in the spectra. This

confirmed successful removal of the surfactant template.[151]

The relaxivity of the Gd^{3+}−DOTA−MSNs was evaluated at 23.4 MHz,

25 °C and found to be 40.65 ± 0.21 mM^{-1} s^{-1}. This value is higher than the

relaxivity of other MSNs decorated on the surface with similar molecular

chelate but much larger linker.[89] This is possibly due to short local rotational

correlation τ_{RL} arising from rotation of the long linker and lowering the

relaxivity. In fact, the relaxivity of the Gd^{3+}−DOTA−MSNs was comparable

to Gd$_2$O$_3$ doped non-porous materials, which have a three-times higher

hydration number (q = 3).[142]
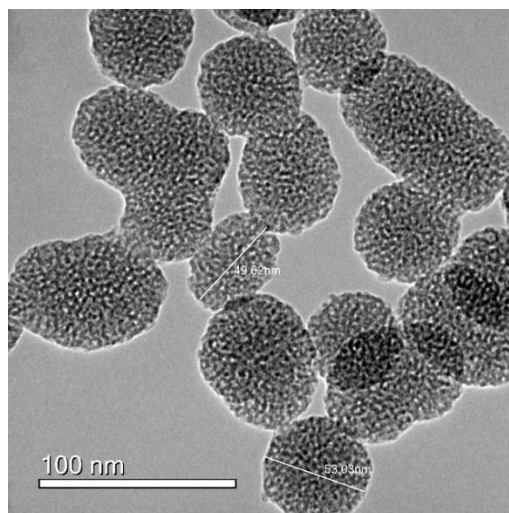
Figure 4.4 TEM of MSNs showing spherical nanoparticles of size ca. 50 nm displaying array of pores.

4.4   Relaxometry Titration of Gd^{3+}−DOTA−MSN with Lysine

The Gd^{3+}−DOTA functionalised nanoparticles were titrated with lysine in a similar manner to the molecular Gd^{3+}−DOTA species as described in Section 3.3.3. A stock solution containing lysine was prepared and the relaxation rate was recorded after every aliquot addition to the original Gd^{3+}−DOTA−MSN sample. The relaxation rate (R_1) drastically increased from 12.45 s^{-1} to 16.41 s^{-1} after the first aliquot addition of lysine, which raised the lysine concentration of the sample to 20 mM (**Figure 4.5**). Following this initial strong increase, the value varied between 15.7 s^{-1} and 17.5 s^{-1} around an apparent steady state. One reason for this could be that the addition of lysine may have influenced the colloidal stability of the particles slightly, although they appeared to remain homogenous in suspension and did not precipitate during the measurement. One of the differences between the

molecular agent titrations and the nanoparticle titrations is that in the second case the exact gadolinium concentration at the time of titration was unknown. Therefore, precise calculations of the salt equivalents to the Gd^{3+} ions were undetermined for the initial experiments. The sharp initial increase in relaxation rate between 0 and 20 mM of lysine indicated that there were not enough titration points in the early part of the titration, and addition of additional lower concentrations of lysine were required for the binding curve to be observed. The experimental procedure was therefore adjusted to cover lower lysine concentrations and for each datapoint the relaxivity (r_1, mM^{-1} s^{-1}) rather than the relaxation rate, (R_1, s^{-1}) of the sample was measured with the intention to improve accuracy, with accurate [Gd] concentrations confirmed using inductively coupled plasma atomic emission spectroscopy (ICP-AES). The ICP-AES was recorded by Connor Wells, a PhD student from the group.
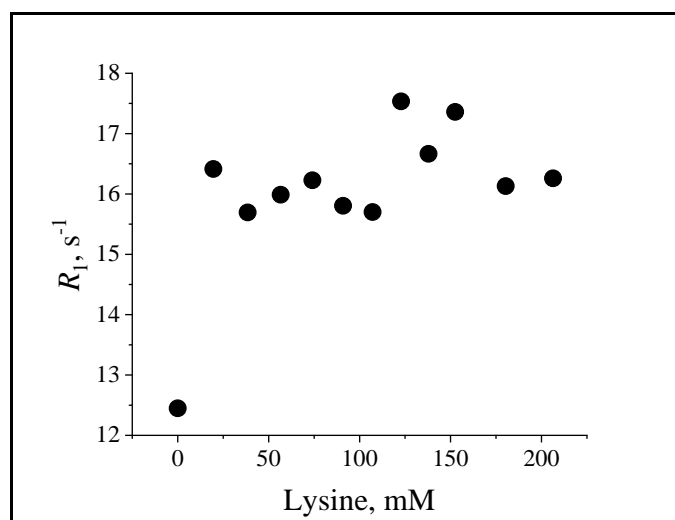
Figure 4.5 *Relaxation rate (R_1, s^{-1}) of Gd^{3+}– MSNs increase with increasing lysine concentration. Datapoints represent the recorded relaxation rate at each lysine stock addition. Data were recorded in water at pH 7, T = 25° C, B_0 = 23 MHz.*

Six different lysine concentrations were chosen between 0.0002 and 20 mM and added to a fixed concentration of Gd^{3+}-modified MSNs with known [Gd] and the relaxivity was recorded as a function of lysine concentration (**Figure 4.6**). The concentrations were chosen based on **Figure 4.5**, to fill the gap between rapidly increased relaxivity (between 0 and 20 mM) where binding was expected to be seen. For each concentration of lysine, the relaxation rate (R_1, s^{-1}) was first recorded at six different Gd^{3+} concentrations to yield relaxivity (r_1, $mM^{-1}s^{-1}$), in accord with equation 1.12, Section 1.3.2. As predicted, a clearer binding curve was observed at low lysine concentrations between *ca.* 0 and 10 mM of lysine (**Figure 4.6**). The signal increased from 40 mM^{-1} s^{-1} to 59 mM^{-1} s^{-1}. Interestingly, when the binding curve was fitted using DynaFit, the association constant of the chemical interactions was very similar to the K_A for the molecular titration described in Section 3.3.6. The association constant for the lysine with the nano contrast agent was log K_A = 3.71 *vs.* the association constant of lysine with the molecular Gd^{3+}−DOTA species, which was log K_A = 3.16, assuming 1:1 binding mode.
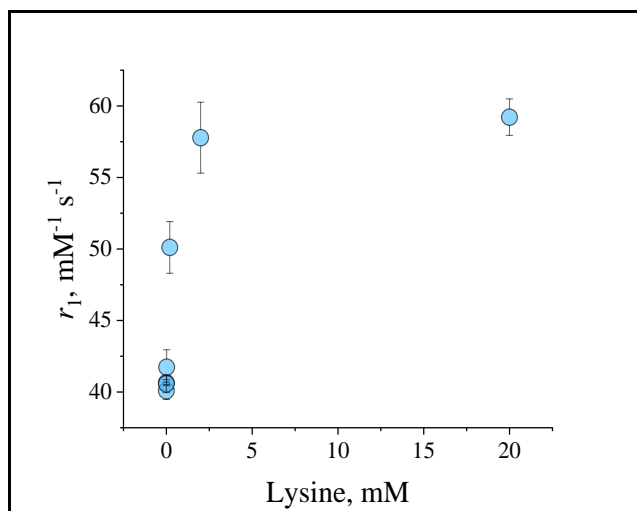
Figure 4.6 *Relaxivity (r_1, $mM^{-1}s^{-1}$) of Gd^{3+}–DOTA– MSN increase with increasing lysine concentration. Each datapoint was obtained by plotting the relaxation rate vs six different concentrations of gadolinium and obtaining the slope of the linear fit. Data were recorded in water at pH 7, T = 25° C, B_0 = 23 MHz and fitted using Origin software. The error bars represent the error associated with the linear fit.*

The increase in signal with increasing concentration of lysine observed in **Figure 4.5** and **Figure 4.6** suggested that the IS binding effects previously observed in molecular Gd^{3+}−DOTA + lysine (where a decrease in relaxation rate occurred) were overpowered in the nanosized contrast agent. Evidently the embodiment of the molecular species into the silica matrix has altered the solution dynamics between lysine and Gd^{3+}−DOTA. Most likely this would be a result of the interactions between lysine and the surface functional groups of MSNs resulting in changes of one or more of the key parameters governing relaxivity. It has been previously shown that the local ionic environment of a similar complex, Gd^{3+}−DOTAMA (**Figure 4.1**), can change in the presence of guest molecules such as ibuprofen, as described in the introduction.[144] This

in turn can influence key parameters governing the relaxivity enhancement, such as local rotational correlation time, τ_{RL} and parameters related to water exchange, such as τ_m.[144] Gd^{3+}−DOTA has a shorter linker than Gd^{3+}−DOTAMA and so the effects of local rotational correlation would not be expected to have a large influence on the relaxivity in the system herein. On the other hand, changes in the water exchange are very likely due to the plethora of silanol groups and water hydration layers within the porous network and could explain the signal increase.

Lysine has two amine groups capable of forming hydrogen bonding with the surrounding water and has a larger surface area accessible to water compared with ibuprofen, which was the guest molecule used in the literature with Gd^{3+}−DOTAMA. The amine groups on lysine can assist in the formation of a larger hydration sphere around the nanoparticles aided by the amine and siloxane groups on the surface of the MSNs. It was hypothesised that the increase in relaxivity upon the addition of lysine was a result of changed water dynamics (faster water exchange) due to the interactions between lysine and the surface of the particles influencing its interaction with the Gd^{3+} species. Moreover, it was previously reported that titration of a Gd^{3+}–DOTA functionalised dendrimer with glutamate resulted in a decrease in relaxivity.[77] Glutamate has a very similar molecular structure to lysine, with large hydrophilic area and the only difference is that the dendrimer lacks the same surface functionality as the MSNs, suggesting that the observed increase relaxivity was due to MSN surfaces interacting with lysine and Gd^{3+}−DOTA.

In future works this hypothesis could be tested by NMRD analysis, following Lipari-Szabo fitting. Nonetheless, there is clearly an observable interaction, with a similar K_A to the molecular species, despite the different mechanism. The large change in r_1 observed is also much bigger than that observed for the molecular species, meaning that this may have promise as a tool for observing detection more clearly than the molecular chelates.

4.5   Towards silsesquioxanes as contrast agents for MRI

The synthesis of fluorescent silica nanoparticles prepared from silsesquioxanes (SSNPs) have been reported in the literature as described in section 4.1.[96] Gadolinium doped SSNPs based on this research have the potential to be used as MRI CAs and could offer increased relaxivity through higher rotational correlation time, τ_R (slower tumbling) due to larger sizes compare with molecular contrast agents, similarly to MCM-41 MSNs. A disadvantage of silsesquioxane materials is their high sensitivity to air, which means that their synthesis and characterisation is more demanding compared with other silica precursor materials. With Gd^{3+} embedded in the structure from the first step, characterisation using standard methods, such as NMR is challenging due to potential paramagnetic shifting and peak broadening.

However, the intrinsic properties of these materials make them an extremely attractive candidate for novel MRI contrast agent probes. A great advantage of gadolinium doped POSS NPs is that they are made of stable hexadentate gadolinium chelate monomers with hydration number of three (compound **(4),**

Figure 4.8), which would be expected to provide concomitant increase in relaxivity in agreement with equation 1.12, section 1.3.2. An interesting property of silsesquioxanes is their cage-like structure which can form pores in the nanoparticles without the need of a template. For this reason, this type of materials is expected to have a unique water dynamics, which can either lead to increase or decrease of relaxivity.

Compound (**2**) was prepared following a modified literature procedure (reaction scheme shown in Figure 4.7), by utilising Gd^{3+} instead of Eu^{3+}, Sm^{3+}, Nd^{3+} which were previously used.[152] It should be noted that all compounds were air and moisture sensitive and were kept and handled under inert conditions. Previous work demonstrated that $[(THF)_3Li(\mu$-$Cl)Ln[N(SiMe_3)_2]_3]$ (Ln=Eu, Sm, Nd) were present as isostructural products with three amide ligands coordinated to the lanthanide centre and a chlorine bridging between Ln and Li. Three THF molecules were shown to be attached to the Li atom.[152] This pattern was also observed in the present research as confirmed by NMR analysis. ^1H NMR of compound (**2**) showed a peak at 3.65 ppm and a peak at 1.29 ppm each corresponding to 12 THF protons belonging to the 3 THF molecules (a and b in Figure 4.7). A peak at 0.33 ppm corresponded to the methyl protons adjacent to the silicon atoms (c, Figure 4.7). This assignment confirmed the proposed structure of (**2**) shown in Figure 4.7 which is consistent with the literature as described above.[152] Carbon NMR (**Figure S4**) Showed peaks at 68.76 and 25.21 ppm which were assigned to the THF carbons and a peak at 6.19 assigned to the carbon of the methyl

group. The symmetry of the compound was reflected by the single peak of ^{29}Si NMR at -11.81 ppm (**Figure S5**).
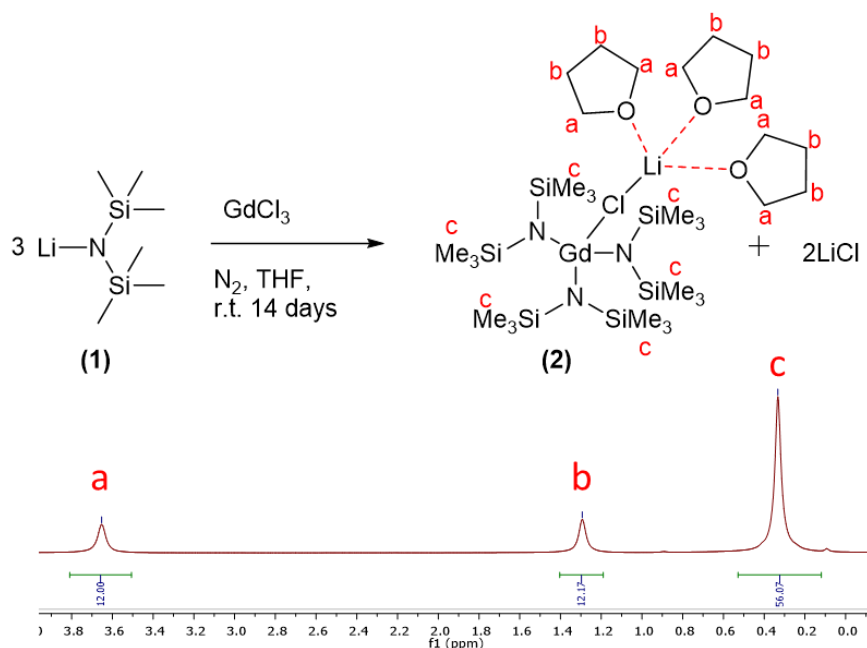
Figure 4.7 ^{1}H NMR of compound (2) recorded in at 700 MHz, 25 °C.

In order to produce the metallasilsesquioxanes containing the Gd^{3+} metal centre, the open-corner heptacyclohexyl trisilanol silsesquioxane (**3**) was next refluxed at 65 °C under inert conditions with compound (**2**) to yield the hexadentate gadolinium chelate (**4**), as shown in **Figure 4.8**. ^{1}H and ^{29}Si NMR indicated that the reaction has not gone to completion. More specifically, ^{29}Si NMR showed a large broad peak at -113.52 ppm and a smaller sharp peak at -67.79 ppm indicating higher symmetry of the product than expected. The ^{1}H NMR of the reaction showed the presence of peaks a, b and c corresponding to the starting material (compound (**2**)) and some additional peaks most likely corresponding to an intermediate product. Therefore, the complex was refluxed for additional couple of weeks and the

resultant ^{1}H spectrum is shown in **Figure 4.9** in blue. The spectrum shows broad peaks corresponding to the protons from the silsesquioxane cage. These peaks can be observed as sharp multiplets in the ^{1}H spectrum of the starting material **(3)**. The peak broadening shows that Gd^{3+} was successfully incorporated into the silsesquioxane cage.
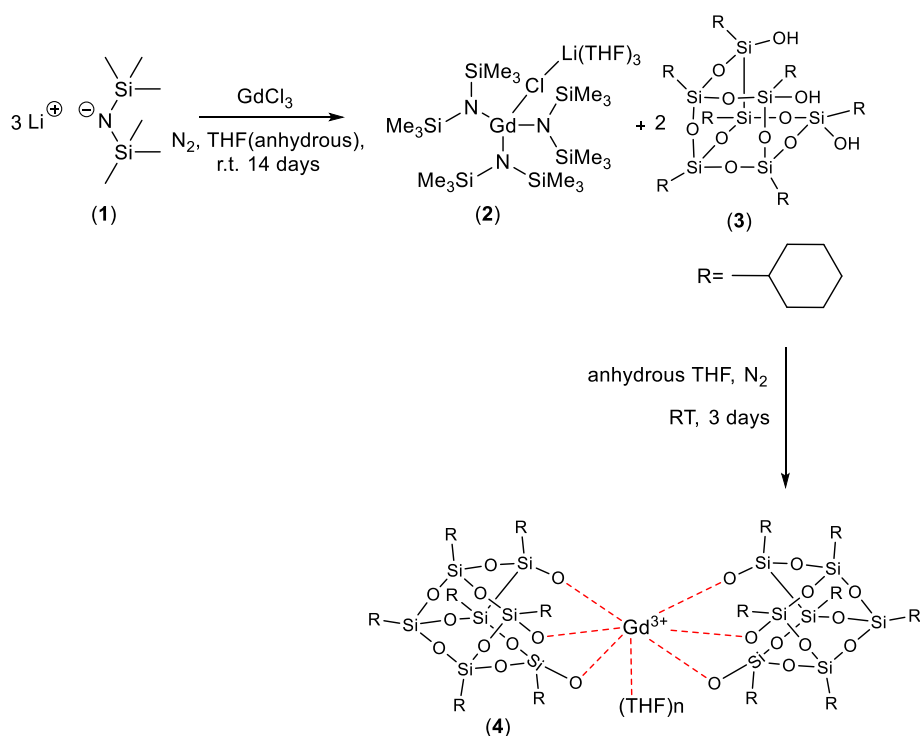
Figure 4.8 Formation of POSS Gd^{3+}chelate (4), including a proposed structure.
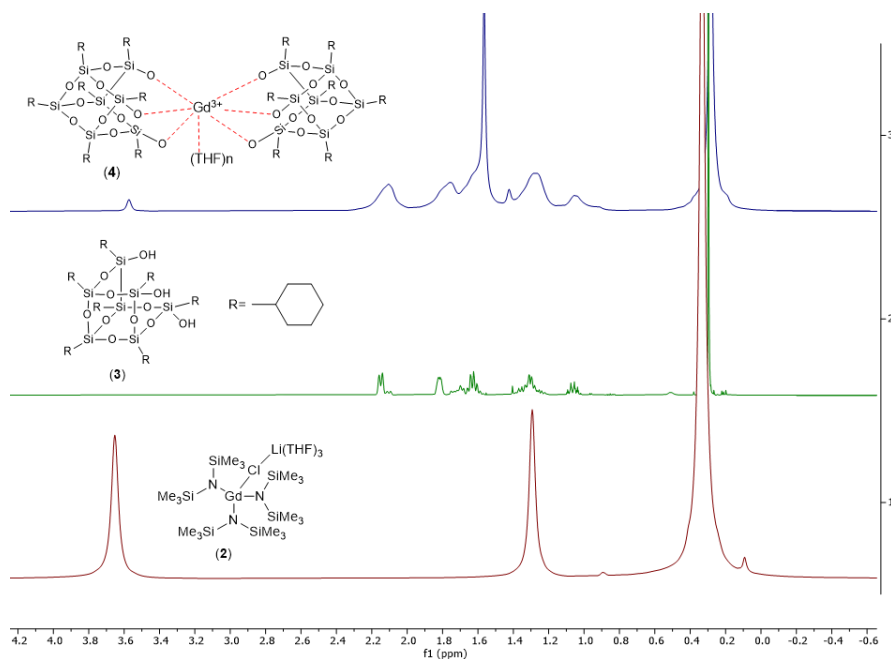
Figure 4.9 *Stacked ^1H NMR spectrum of starting materials (**2**) and (**3**) and the product (**4**), recorded in C_6D_6 at 700 MHz, 25 °C.*

Next, thermogravimetric analysis (TGA) was performed to assess the thermal stability of compound **(4)**. About 30 % of the sample weight was lost between 45 and 160 °C, attributed to the thermal desorption of coordinated solvent molecules.[153] Another 3.5 wt% was lost between 170-230 °C and less than 1 % above this temperature attributed to loss of organic fragments and possible rearrangement of the structure (**Figure 4.10**).

From the TGA it was concluded that the best temperature for thermolytic formation of nanoparticles was 300 °C and so a fresh sample of compound **(4)** was heated to 300 °C using a TGA to yield Gd^{3+}−SSNPs nanoparticles following a published procedure.[96] The resulting slurry was washed with water three times to remove any molecular impurities by centrifugation and sonication. TEM images of Gd^{3+}−SSNPs are shown in

(**Figure 4.11**, A, B). They revealed severe crosslinking between the individual Gd^{3+}−SSNPs, which indicated low stability of the sample in water. However, these images were very similar to previously reported TEM images of Fe-POSS, Co-POSS and Eu-POSS nanoparticles which also showed significant particle aggregation (Section 1.5, **Figure 1.33**).[95,96] Energy Dispersive X-Ray Analysis (EDX) was also carried out on the TEM sample (**Figure 4.11**, C) which confirmed the presence of silicon and oxygen from the silsesquioxane cage, as well as very low peaks representing Gd, which may indicate some successful incorporation of Gd^{3+} into the nanostructures.

The relaxivity of the nanoparticles dispersed in water was measured at 23.4 MHz, 25 °C and was found to be 3.32 ± 0.25 mM^{-1} s^{-1} (**Figure 4.12**). This low value per Gd^{3+} can be explained partially through the internalisation of most gadolinium ions in the silsesquioxane structure, just like in materials where Gd^{3+} chelates are embedded in the silica structure and also by the severe aggregation of the sample in water as shown by TEM, wherein water would be less able to access the MRI centres to facilitate strong relaxation. In fact, the value is comparable to the relaxivity of mesoporous silica nanoparticles with embedded Gd^{3+} chelate, described in Section 4.1.[143] Due to the low relaxivities and poor water stability, guest molecule interaction experiments were not carried out.
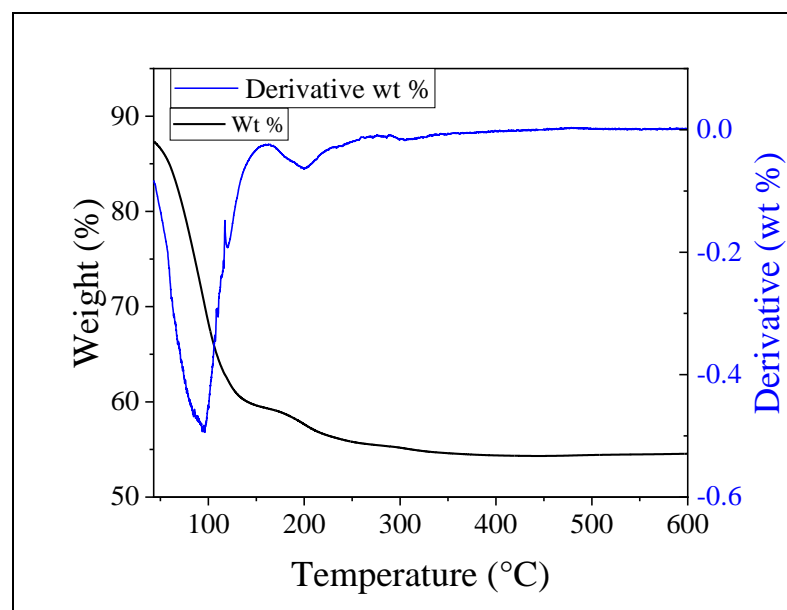
Figure 4.10 *Thermogravimetric analysis and first derivative of gadolinium doped POSS NPs (black line) and first derivative (blue line).*
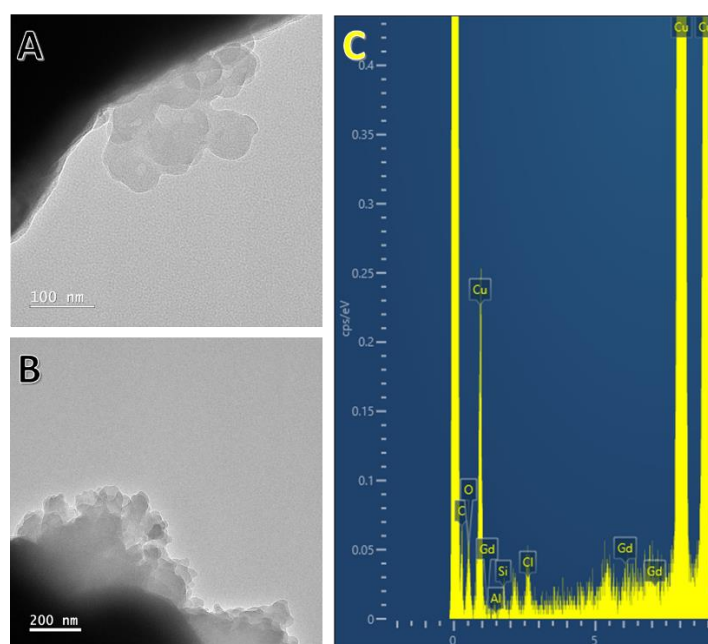
Figure 4.11 *A, B: TEM images of gadolinium doped POSS NPs. C: EDX data recorded from the TEM images.*
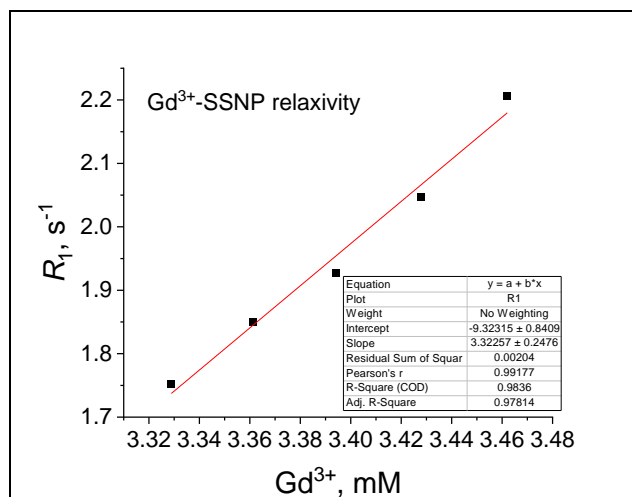
Figure 4.12 *Relaxivity of $Gd^{3+}-SSNP$ (r_1 = 3.32 $\pm$ 0.25) measured at 23.4 MHz (0.55T), 25 °C.*

4.6   Conclusion and Future Work

Mesoporous silica nanoparticles were shown to be advantageous in oxyanion detection by significantly increasing proton relaxation times. Their ability to show change in signal upon interaction with guest molecules, such as lysine, on a much greater scale than well-known molecular contrast agents make them a highly promising candidate for future detection systems. The versatility of their surface modification offers a pathway for tailoring them for specific anion detection, for example by embedding a ligand with anion selectivity (*vide infra*, Chapter 5), hence providing responses with significantly larger amplifications for diagnostic purposes. Further work is required for the clearer understanding of the interactions of guest molecules with the MCM-41 surface, especially changes in behaviour dependent on the hydrophilicity/hydrophobicity of the guest molecules. This could be achieved by NMRD studies and fitting using the Lipari-Szabo model.[57]

214

The synthesis of the gadolinium precursor (2) for the production of Gd^{3+}−POSS-NPs was successful as confirmed by proton NMR, however the remaining steps of the synthesis were challenging and require optimisation. Future work must include specialised TGA thermolysis, where samples are prepared and sealed in a glove box prior to burning. Nanoparticle purification must be incorporated into the synthesis with removal of impurities through solvent washes and centrifugation. With such improvements potentially boosting their colloidal and relaxation properties, these materials have a fantastic potential as MRI contrast agents and further insight into their behaviour, especially their water exchange dynamics, could be gained using NMRD.

5   Chemoselective Chelates for Nerve Agent Adduct Detection

5.1   Introduction

Research into lanthanide ligands tailored for the chemoselective detection of anionic species has enabled the detection and monitoring of biological processes and early disease progression. The design and synthesis of lanthanide-based mono-aqua and di-aqua complexes binding to phosphorylated amino acid residues have been explored.[74,97,154–156] Both the nature of the lanthanide centre and the surrounding ligand have been found to impact the affinity and selectivity towards reversible binding in solution.[154] Although there have not been direct studies wherein nerve agent adducts bind to lanthanide chelates (to provide either emissive or MRI generated perturbations in signal), the body of research into various anionic species binding to lanthanide chelates can provide a rich body of evidence for the potential to produce chemoselective ligating species.

In the design of MRI active chemoselective species towards sarin-tyrosine adducts the perturbation of the lanthanide is not possible. However, the structural properties of ligands can be selected to complement the size, shape and charge of sarin-tyrosine adducts. For example, as discussed in Section 1.4, binding to the metal centre through the phosphate group would require a contrast agent with a large binding pocket. This could be a coordinatively unsaturated Gd^{3+} complex with a hydration number $q = 2$. This

is not a requirement for the nerve agent adducts as they contain neutral phosphonate functional group. On the other hand, binding through the tyrosine side of the nerve agent adduct (**Figure 5.1**) would be enhanced by the presence of aromatic groups on the lanthanide-chelate for the formation of π-π interactions with the benzene ring on tyrosine and might also be affected by a larger binding pocket. Most lanthanide phosphorescent probes contain aromatic groups in their structure as they are used as sensitisers for lanthanide emission so binding to aromatic anions would be expected. [155]
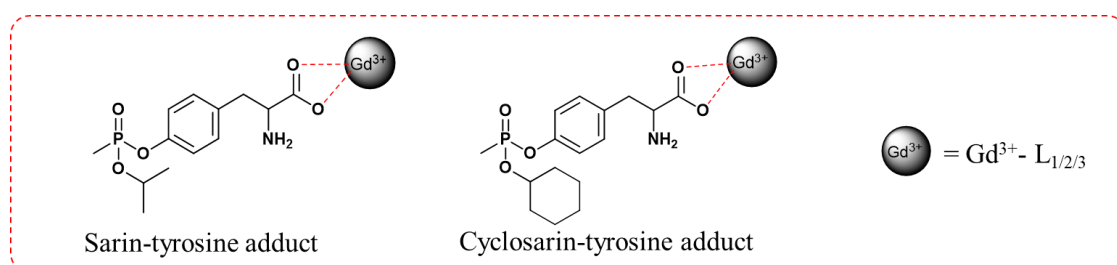
Figure 5.1 Expected binding modes for the target adducts with Gd^{3+}-based chelates in agreement with Butler et al. [98]

Variations of the DOTAM ligand, which were used in the experimental part of this work, are shown in **Figure 5.3** and were previously characterised and tested for binding to oxy anions, including phosphate and phosphorylated amino acids.[74,101,154–158] It was found that lanthanides with high Lewis acidity, such as Tm^{3+}/Yb^{3+}−L$_2$ display strong binding to simple amino acids.[65,154] Furthermore, binding to phosphorylated amino acids occurs with competition between phosphate and amino acid coordination to Tm^{3+}/Yb^{3+}−L$_2$(**Figure 5.2**).
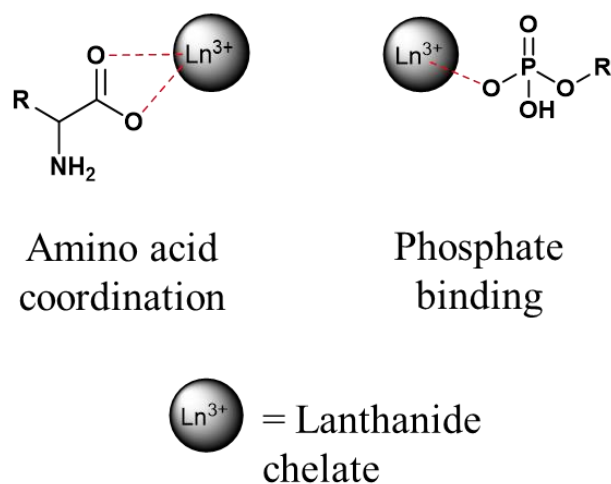
Figure 5.2 Competitive binding modes in phosphorylated amino acids.[98]

Interestingly, proton NMR studies showed a preference of $Yb^{3+}-L_2$ for phosphorylated tyrosine over phosphorylated serine.[156] In contrast, L_2 analogues containing less acidic lanthanides, such as Eu^{3+} and Tb^{3+} can bind weakly to simple amino acids with the carboxylic group remaining protonated in the ternary adduct.[156] Binding of $Eu^{3+}-L_2$ to histidine ($K_A = 3, 500 \ M^{-1}$) and phenylalanine ($K_A = 120 \ M^{-1}$) was quantified from the changes in intensity of $\Delta J = 2$ transition with increasing amino acid concentration. Hydration number calculations revealed the different mode of binding of $Eu^{3+}-L_2$ in ternary adducts with different oxy anions. In detail, a bidentate binding mode was exhibited in ternary adducts with carbonate, lactate and citrate species, evident from the change in hydration number, q from 2 to 0. The complex of $Eu^{3+}-L_2$ with citrate was crystallised and X-Ray studies showed a well-defined hydrogen bonded structure of water around the complex which could enhance the activation energy barrier for dissociative water exchange and enlarge τ_m.[158] In contrast, adducts with fluoride, acetate and phosphate were

bound in a monodentate manner to the lanthanide Eu^{3+} centre with a single water molecule remaining in the axial position.[65] The affinity for phosphate was quite low, with $K_A > 7$ x 10^{-4} M^{-1} (log K_A = -3.15), however preference for phosphate binding by $Eu^{3+}-L_2$ was retained in the presence of proteins and endogenous ions.[65,156–158] The preference for phosphate anions by $Eu^{3+}-L_2$ was evident in the NMR studies with a simple peptide (Gly-Ala-Pro-Tyr(OP)-Lys-Phe), where $Eu^{3+}-L_2$ selectively complexed with phosphotyrosine (Tyr−OP).[154] Furthermore, the interactions between $Eu^{3+}-L_2$ and a peptide fragment of an insulin receptor was studied by TOCSY (Total Correlation Spectroscopy). $Eu^{3+}-L_2$ exhibited a weak binding to a non-phosphorylated equivalent of the peptide with no changes in the spectrum. On the contrary, the presence of tri-phosphorylated peptide (with Tyr−OP) in the $Eu^{3+}-L_2$ solution caused large shifts in the resonances corresponding to the Tyr−OP fragments indicating binding to the lanthanide centre. Shifts were also observed for lysine, however this was assigned to the proximity to Tyr−OP.[155] The binding to Tyr−OP was confirmed with ^{31}P NMR by the appearance of a new peak at -136 ppm corresponding to the newly formed ternary adduct. The same peak was observed when $Eu^{3+}-L_2$ was mixed with Tyr−OP alone.[155]

L₁: R=CH₂CONHCH(Me)Ph
L₂: R=H

L₃
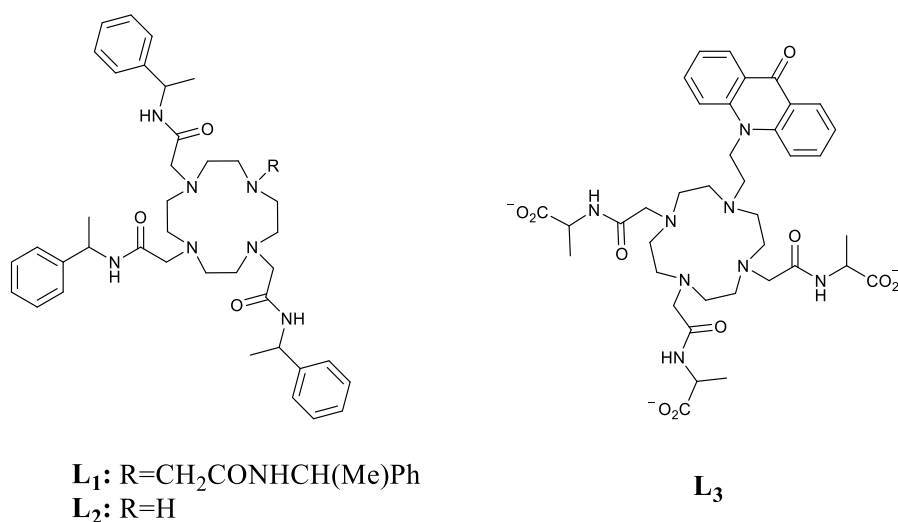
Figure 5.3 *Structures of DOTAM ligands L₁₋₂ and acridone ligand L₃ to be synthesised and used in this study.*[155]

It is clear from the literature[65,74,97,154,155,157,159] that there are opportunities to produce chemoselective ligands which may assist in generating selectivity to nerve agent adducts (containing carboxylic and phosphate residues). There is nothing in this arena, however, which describes the binding of nerve agent adducts to such lanthanide chelates, despite the various different anionic binding modes which are analogous to how a nerve agent adduct may bind. Lanthanide probes can easily be permuted to become MRI active by replacing the central (usually fluorescent/emissive) lanthanide with an MRI-active Gd^{3+} ion. Thus, the task of developing an MRI-based detection system for sarin-tyrosine adducts is feasible as it allows for utility of the excellent research into chemoselective binding of phosphorylated tyrosine. With this in mind, Gd^{3+} analogues of ligands L_{1-3} were synthesised and tested for reversible binding to sarin-tyrosine adducts.

5.2   Aims

The aim of this section was to synthesise MRI contrast agents with the potential to specifically bind sarin-tyrosine adducts. The first part of this chapter aims to confirm the successful synthesis of three cyclen-based complexes following published procedures by analysis of the characterisation data (NMR, mass spectrometry). The second part of this Chapter aims to investigate the relaxivity of each ligand tested by NMRR and evidence for their binding to guest molecules. The relaxivity of each ligand was recorded and discussed in the presence and absence of guest molecules introduced in Chapter 3. The final part of this Chapter aims to investigate the ability of $Gd^{3+}- L_{1-3}$ to bind sarin-tyrosine adducts in the nerve agent testing facilities at Dstl, Porton Down. This part of the thesis aims to assess the effectiveness of the contrast agents on the high-field MRI machine in the specialised facilities and their binding to two G-type nerve agent adducts – sarin-tyrosine (GB−Tyr) and cyclosarin-tyrosine (GF−Tyr), which were produced by Dr Claire Mitchell, Dstl.

5.3   Synthesis of ligands $Gd^{3+}-L_{1-3}$

Ligand L_2 was synthesised following the procedure provided by Bruce *et al.*[101] The procedure was slightly modified for the synthesis of L_1. The side arm (S1) which is common for both ligands was synthesised using a procedure published by Cui *et al.*[100] Ligand L_3 was synthesised using the

procedure detailed by Bretonniere *et al.* and the side arm S2 was synthesised following the procedure written by Hirota *et al.*[160,97] Finally, all ligands were chelated to Gd^{3+} according to the procedure described in the Experimental Chapter. All data mentioned below can be found in the Experimental Chapter in Section 2.2.3.

The structure of side arm S1 is shown in **Figure 5.4**. For this reaction chloroacetyl was reacted with (*S*)-1-phenylethanamine. Chloroacetyl chloride can react through the carbonyl group (S_N2 mechanism) or through the primary chloride following an S_N1 reaction mechanism. To encourage the formation of the desired thermodynamic product following an S_N2 pathway the reaction was kept under 20 °C. Similarly, for the synthesis of the ester (side arm S2, **Figure 5.5**) from chloroacetyl chloride and alanine ethyl ester, the reaction was kept at -60 °C during the addition of chloroacetyl chloride which was dripped slowly over 30 minutes. The compound was added dropwise to both reactions to slow down the rate of formation of ionic intermediates which in large amounts can impair stirring. Additionally, chloroacetyl chloride can react violently with water, so both reactions were kept under inert conditions to avoid exposure to moisture in the air. Successful synthesis was confirmed using NMR and mass spectrometry. The Yield of S1was lower than the literature –57 % in this study and 96 % reported by Hu *et al.*[100] This could be due to the low temperatures used resulting in less efficient reaction. For S2 the yield was 57 % and it was not reported in the literature.[160]
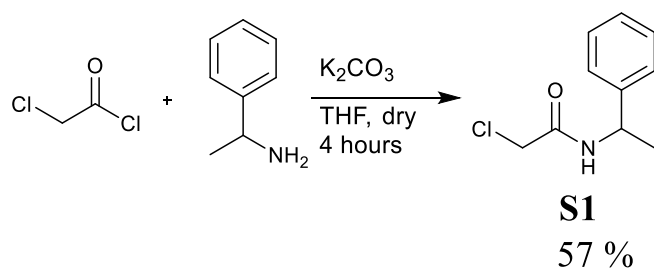
***Figure 5.4** Synthesis of2-chloro-N-(1-phenylethyl) acetamide (side arm S1).*
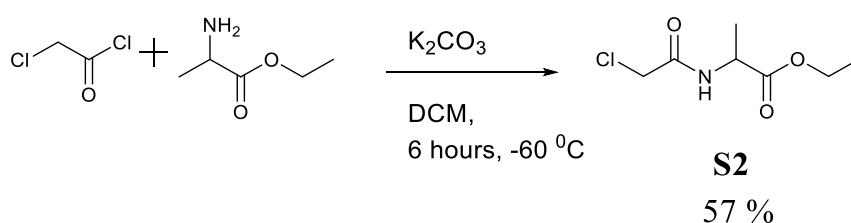
***Figure 5.5** Synthesis of ester side arm S2.*

The ^{1}H NMR spectrum of side arm S1 is shown in **Figure 5.6** and **Figure 5.7**. Even though peak "d" was reported as a quartet by Cui *et al.*,[100] in this research two distinct coupling constants were calculated ($J_1 = 15.40$ Hz and $J_2 = 15.17$ Hz). This indicated that the resonances belonged to a doublet of doublets rather than a quartet. The pattern could be explained by the presence of two rotamers due to the restricted rotation along the C−N bonds of the amide (**Figure 5.8**). This behaviour was observed previously by Gavriel *et al.* in carbamides.[161] In his paper a similar *syn-anti* rotamer equilibrium was observed due to restricted rotation along the C−N bond of carbamate causing splitting of nearby proton resonances.[161] Analogously, it is likely that the aliphatic protons adjacent to the amide in S1 form rotamers causing a splitting of the resonance "d" into doublet of doublets.
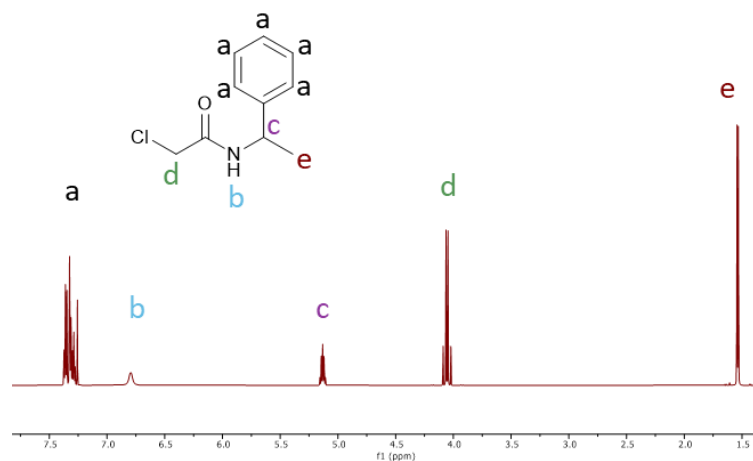
Figure 5.6 *Proton NMR spectra of side arm S1 recorded at 600 MHz, CDCl₃,*

25 °C.
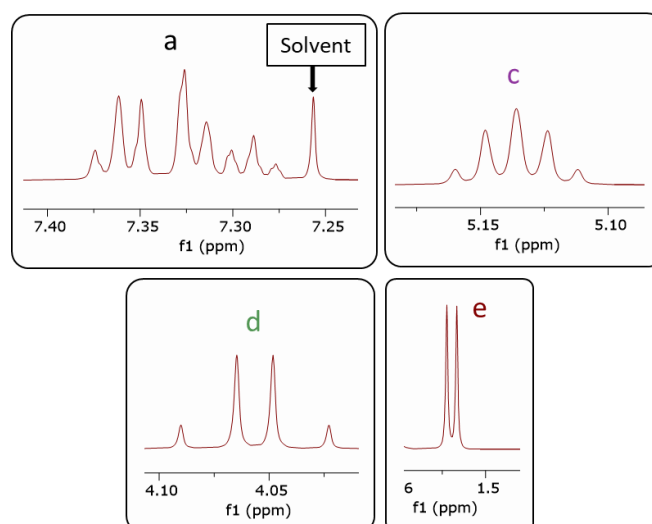
Figure 5.7 *Enlarged spectrum of ¹H NMR spectra of side arm S1 peaks: a (top,*

left), c (top, right), d (bottom, left) and e (bottom, right).
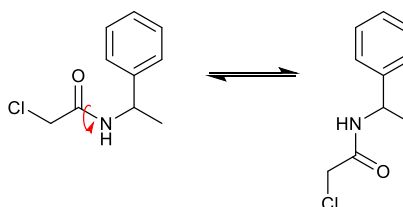
Figure 5.8 *Proposed rotamer equilibrium due to restricted rotation of the*

amide C−N bond.

Side arm S1 attachment to cyclen in L_1 and L_2 (**Figure 5.9**) differed slightly. The synthesis of L_1 was straightforward with dropwise addition of cyclen to excess of the side arm and subsequent purification of the ligand on neutral alumina. Yield was not reported in any of the literature articles[74,157,158], however, in this study it was 34 %. The yellow viscous oil was analysed using MS and NMR which confirmed successful formation of the product.

The synthesis of ligand L_2 was more challenging because in L_2 cyclen is coordinatively unsaturated, with a single nitrogen atom left unfunctionalized. Controlling the molar ratio of cyclen to S1 at 1:3 alone is not enough for the successful synthesis. There is a danger of formation of different species in solution with one, two, three and four side arms which can be avoided if the rate of addition is carefully controlled. To accommodate this requirement L_2 was synthesised using a syringe pump with a very slow addition of S1 overnight to a cyclen solution, aiming to slowly functionalise all cyclen molecules with a single arm first, two arms next and finally three arms. The product was purified and analysed using MS and NMR. The yield was 23 %, which is similar to the literature reported value of 29 %.[101]

L₁: n = 4
L₂: n = 3

L₁: R=CH₂CONHCH(Me)Ph, 34 %
L₂: R=H, 23 %
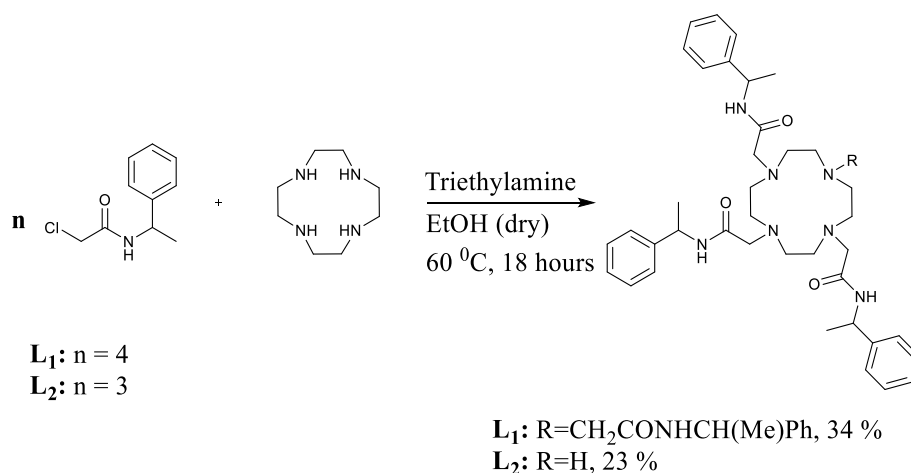
Figure 5.9 *Schematic representation of synthetic procedure for L₁ and L₂.*

The synthesis of the acridone ligand L_3 (**Figure 5.10**) involved the preparation of the acridone moiety (**1**, **Figure 5.11**, **Figure 5.10**) with subsequent attachment to cyclen. In the final steps, the three remaining amine groups on cyclen were functionalised with side arm S2 and deprotected to yield a negatively charged ligand. The final product was purified, freeze-dried and the successful synthesis confirmed using mass spectrometry following the procedure provided by Bretonniere *et al.*[74]
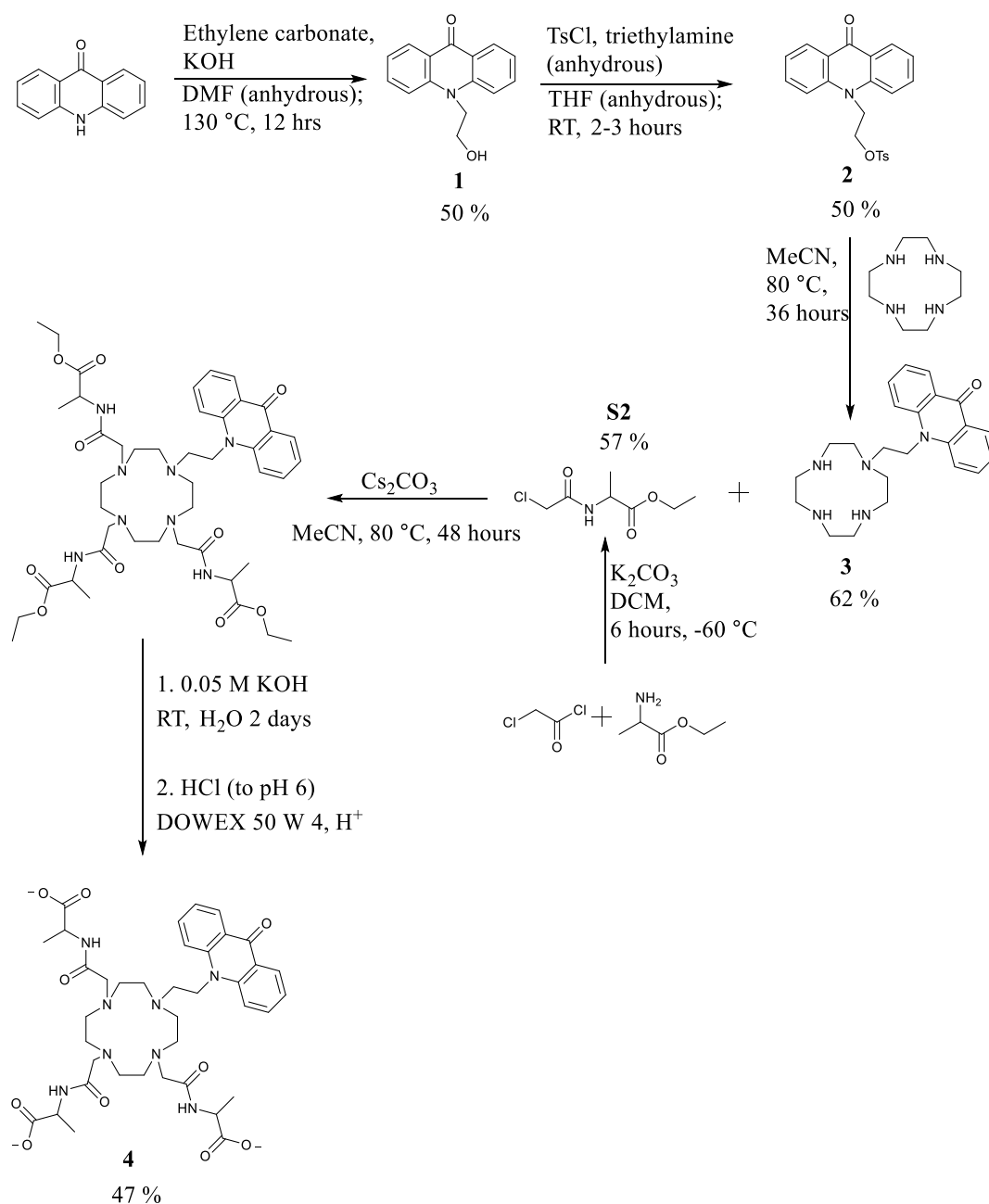
Figure 5.10 *Schematic representation of the synthetic route towards L₃.*

In detail, the reaction between acridone and ethylene carbonate afforded N-(2-hydroxyethyl)-acridone **1**. The proposed mechanism for this reaction is shown in **Figure 5.11**. The n-alkylation of acridone proceeds *via* ring-opening of ethylene carbonate catalysed by potassium hydroxide. Electron delocalisation of the negatively charged acridone makes it a soft

nucleophile and ring-opening of ethylene carbonate occurs through nucleophilic attack at the soft electrophilic carbon and not at the carbonyl. The formation of the final alcohol product **1** is driven by the release of carbon dioxide.
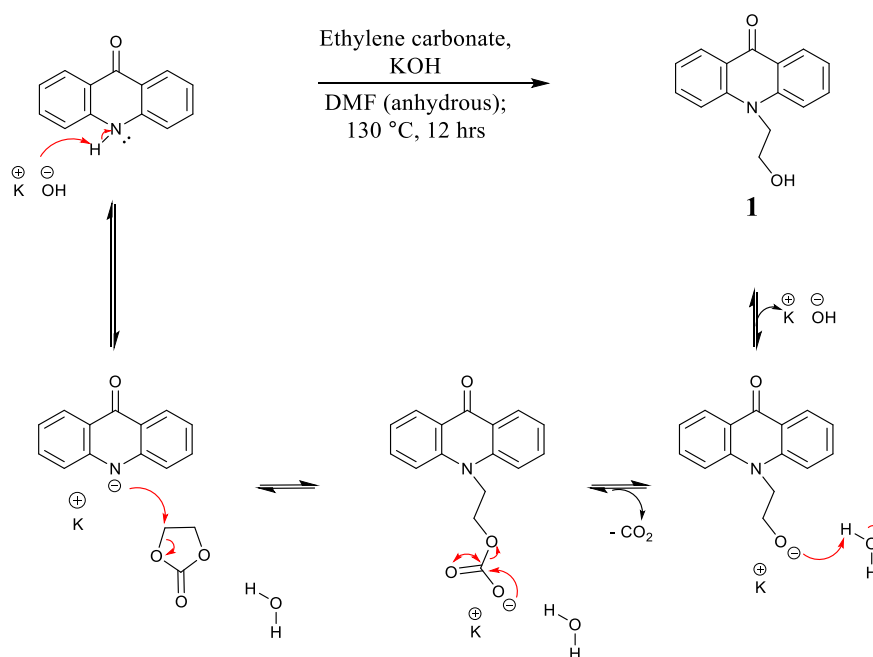
***Figure 5.11** Proposed mechanism for the formation of N-(2-Hydroxyethyl)-acridone **1** from the reaction between acridone and ethylene carbonate.*

NMR and MS analysis after re-crystallization from methanol suggested the successful synthesis of **1** with yield of 50 %. This was much lower than the literature reported value of 70 % possibly due to differences in the laboratory technique.[74] ^{1}H NMR revealed the disappearance of the proton resonance at 11.72 ppm, corresponding to the N*H* proton of acridone, suggesting successful functionalisation at the nitrogen atom. The n-alkylation was further confirmed by the appearance of two new triplets at 3.89 ppm and 4.60 ppm corresponding to the aliphatic protons NCH$_2$C*H*$_2$OH and

NC*H₂*CH₂OH respectively, as well as a broad peak at 5.07 ppm originating from the alcohol proton. Attachment of the acridone moiety to cyclen directly through the alcohol group would not be favoured as ⁻OH is not a good leaving group. Bretonniere *et al.* avoided this problem through conversion of the alcohol group to a sulfonate group using methanesulfonyl chloride (MsCl).[74] In this work, *p*-toluenesulfonyl (*p*-TsCl) was used instead to produce **2** (**Figure 5.12**), as it is safer to handle. The reaction was conducted following the method provided by Bretonniere *et al.* with increase of reaction times to account for the lower reactivity of *p*-TsCl compared with MsCl.[162] The synthesis of compound **2** was confirmed using mass spectrometry and NMR analysis and gave yields of 62 %, which was slightly lower than the yield reported by Bretonniere *et al*. This is consistent with the lower reactivity of *p*-TsCl compared with MsCl.[74] In ¹H NMR a new singlet peak corresponding to the aliphatic protons of tosylate was observed at 2.30 ppm. Doublet resonances of the aromatic tosylate protons were observed at 7.34 ppm and 6.94 ppm, their coupling confirmed by COSY.

2
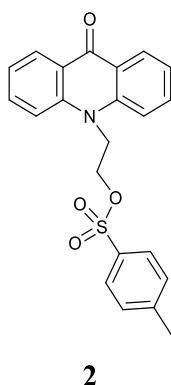
Figure 5.12 *Structure of N-(2-(ethanotosyl))-acridone, compound 2.*

The acridone moiety **2** was attached to cyclen *via* nucleophilic substitution of the OTs group to form product **3** (**Figure 5.10**). Next, the free N-coordination sites left on cyclen were functionalised with **S2**. The ester was deprotected and passed through hydrogen form ion exchange column to yield 47 % L_3, a value very similar to the literature value of 46 % (**Figure 5.10**).[74] The synthesis was confirmed using mass spectrometry. All three ligands were complexed with Gd^{3+} and their contrast agent properties were examined in the next Section. The complexation was conducted at 80 °C for 24 hours and confirmed using Arsenazo III assay, which showed less than 10 % free Gd^{3+} in solution.

5.4   NMR Relaxometry of $Gd^{3+}-L_{1\text{-}3}$

Ligands L_1 and L_2 were previously studied in literature by NMR and X-Ray crystallography.[157] Both L_1 and L_2 adopt a square antiprismatic structure with 40° between their O_4 and N_4 planes (Figure S8).[163] It was found that the nature of the chelated lanthanide plays a key role in the binding and water exchange of the ligand. It has been reported that the ligand $Ln^{3+}-L_1$ is in a slow exchange regime, with τ_m values ranging between 0.6 – 280 μs dependent on the lanthanide cation. The mean residence lifetime of the single coordinated water in the inner hydration sphere in the europium analogue of the ligand was found to be τ_m = 280 μs, whereas ytterbium which has higher Lewis acidity displayed much faster water exchange with τ_m = 0.6 μs. The overall slow water exchange was a result of the large hydrophobic surface of

L_1 leading to high-energy transition state.[157] Therefore, any process which lowers the energy of the transition state of water exchange would be expected to lead to higher relaxivity in accord with equation 1.12, Section 1.3.2.

The relaxivity and binding of $Gd^{3+}-L_1$ to five guest molecules was investigated using NMRR. In this study, the relaxivity of $Gd^{3+}-L_1$ at neutral pH was obtained from the linear fit of the relaxation rates of six concentrations of Gd^{3+} and found to be 9.67 ± 0.21 mM^{-1} s^{-1} (**Figure 5.13**). This value was much higher compared with the relaxivity enhancement induced by $Gd^{3+}-DOTA$, which can be attributed to the higher molecular weight of $Gd^{3+}-L_1$, thereby increasing τ_R. High values of the rotational correlation time cause higher relaxivity as described by equations 1.12 to 1.15 (Section 1.3.2). It was expected that when excess of tyrosine is introduced to $Gd^{3+}-L_1$ solution, it will form π-π interactions with the aromatic groups on the guest and displace the inner-sphere water molecules more efficiently than other molecules. To test this hypothesis, $Gd^{3+}-L_1$ was mixed with each of the guest molecules introduced in Chapter 3 (phosphoserine, phosphate, tyrosine, lysine, and ibuprofen) in excess of 1:20 ratio and the relaxivity of the solutions was recorded from the linear fit of six Gd^{3+} concentrations. The ratio was chosen to ensure binding saturation using as a guidance the NMRR titration data from Chapter 3.

As expected, introducing 20 equivalents of tyrosine to $Gd^{3+}-L_1$ caused the greatest reduction in signal signifying high affinity of $Gd^{3+}-L_1$ for tyrosine. The relaxivity of $Gd^{3+}-L_1$ + tyrosine was 2.18 ± 0.08 mM^{-1} s^{-1},

typical for a $q = 0$ complex with only an outer-sphere contribution to the relaxivity (77 % decrease in signal).[97] Interestingly, it was also observed that lysine appeared to displace the inner-sphere water molecule in a very similar manner to tyrosine, reducing the signal to 2.42 ± 0.09 mM^{-1} s^{-1} or by 75 %. This was attributed to the small size of lysine, being able to fit well in the small binding pocket of Gd^{3+}−L$_1$. The lysine blood levels in healthy adults are between 0.12 mM and 0.22 mM, therefore detection of sarin poisoning using Gd^{3+}−L$_1$ would be possible only in concentrations above 0.22 mM, unless competitive binding assay shows a strong preference for sarin adducts over lysine. Addition of phosphate also led to a reduction in relaxivity by 54 %, to $r_1 = 4.43 \pm 0.33$ mM^{-1} s^{-1}, although this was to a lesser degree than tyrosine and lysine. This finding was surprising considering the large binding pocket requirements for phosphate described in Chapter 1 and demonstrated by the NMRR data of Gd^{3+}−DOTA with phosphate (Chapter 3, which showed no binding in terms of q displacement), however it was noted that tyrosine has a lower hydration energy and hence higher binding affinity. However, phosphate has been shown to bind in a monodentate manner to similar lanthanide probes in the literature, which is less sterically demanding and therefore the observed binding to phosphate is in line with literature.[97,101] This reduction in signal was very encouraging as it suggested that sarin-tyrosine adducts can potentially bind to Gd^{3+}−L$_1$ through both binding sites *i.e.*, the amino acid side and the phosphate functional group. This type of competitive binding to the metal centre was previously observed in Tm^{3+} and Yb^{3+}

analogues of similar DOTAM ligands.[154] In contrast to lysine, tyrosine and phosphate, phosphoserine induced an increase in relaxivity when added to $Gd^{3+}-L_1$. This behaviour was previously observed with $Gd^{3+}-DOTA$ and, therefore, it is consistent with the findings presented in Chapter 3. When phosphoserine was added to $Gd^{3+}-L_1$ the signal increased by 22 % to $r_1 = 12.1 \pm 0.23$ mM^{-1} s^{-1}, which was attributed to the ability of phosphoserine to form strong second hydration sphere around contrast agents as demonstrated by the NMRD fitting shown in Section 3.3.7. Furthermore, considering the slow exchange regime of L_1, it is also possible that the presence of this strong second hydration sphere lowered the free energy barrier of the water exchange transition state, thereby increasing relaxivity enhancement.[157]   It would be useful to compare the binding of tyrosine to $Gd^{3+}-L_1$ with other molecules forming aromatic oxy anions, such as ibuprofen. However, the relaxivity of $Gd^{3+}-L_1$ + ibuprofen could not be recorded as addition of ibuprofen to $Gd^{3+}-L_1$ caused sedimentation and resulted in an opaque solution (**Figure 5.14**).
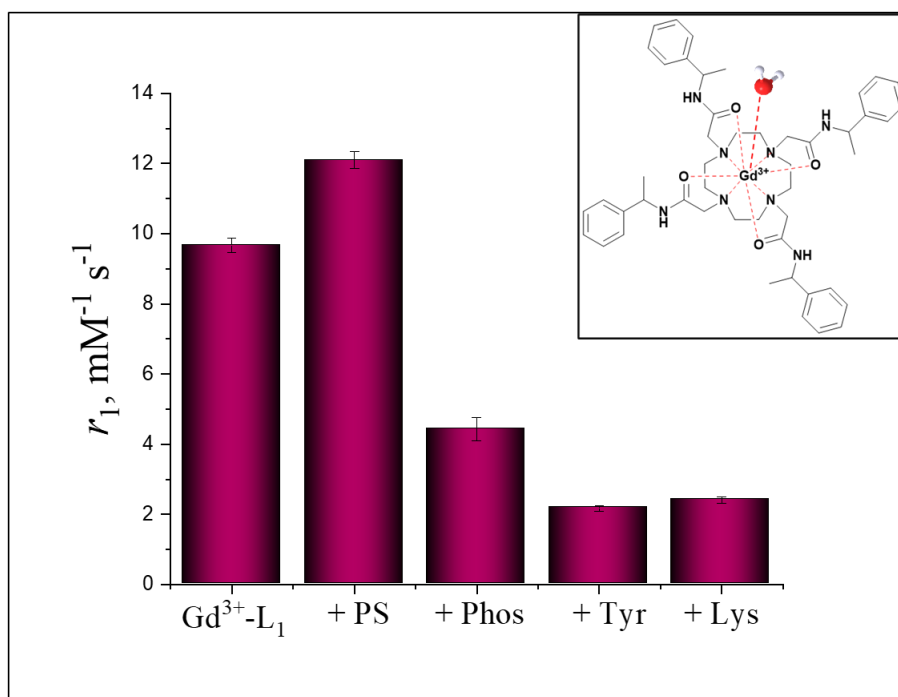
Figure 5.13 *Relaxivity of Gd³⁺−L₁ in the presence and absence of phosphoserine (PS), phosphate (Phos), tyrosine (Tyr), and lysine (Lys) recorded at 23.4 MHz, 25 °C. Guest molecules were introduced to Gd³⁺−L₁ in 20 equivalents. The error bars represent the linear fit error obtained in Origin software.*

Figure 5.14 *Sedimentation in Gd³⁺−L₁ + ibuprofen sample.*

Previous studies of L_2 in the literature showed that binding to the metal centre depends on the Lewis acidity of the ion, related to its ionic radius.[156]

For example, Eu^{3+} was not acidic enough to induce strong binding to amino acids due to smaller lanthanide contraction compared with ions later in the lanthanide series, such as Yb^{3+}. Gd^{3+} is slightly smaller than Eu^{3+}, by 10 Å, so it is possible that it possesses enough Lewis acidity to accommodate binding to phosphate and oxyanions.[156]

The relaxivity of $Gd^{3+}-L_2$ was found to be 10.11 ± 0.11 mM^{-1} s^{-1}, which was slightly higher than the relaxivity of $Gd^{3+}-L_1$ due to the extra water molecule in the inner hydration sphere (**Figure 5.15**). The effect of increased hydration number was slightly offset by the lower molecular weight of $Gd^{3+}-L_2$ compared with $Gd^{3+}-L_1$ due to the missing fourth side arm. The lower molecular weight causes a faster molecular tumbling and shorter τ_R values lowering the relaxivity and resulting in small overall gain in relaxivity (Section 1.3.2). There was a discrepancy with the relaxivity value reported by Dickens *et al.* for $Gd^{3+}-L_2$ which was $r_1 = 8.5$ mM^{-1} s^{-1} at 20 MHz and 25 °C.[158] It was not clear what technique was used to determine this value, which was contradicted by the NMRD data presented in the same paper, showing longitudinal relaxivity enhancement above 9 mM^{-1} s^{-1} .[158] NMRD can give a good approximation of the relaxivity, however it is not an accurate way to measure it because it can carry errors. The reason for this is the way that the relaxivity is derived in NMRD measurements. A single value of the relaxation rate, R_1, s^{-1} at given frequency is taken and divided by the concentration of the paramagnetic ion in the measured solution. On the contrary, in this work relaxivity was recorded from the change in relaxation rate at 23.4 MHz as a

function of six paramagnetic concentrations (Gd^{3+}) in accord with equation 1.7, Section 1.3. Further to this, slight differences in set up (*e.g.,* frequency, temperature) and instrumentation can altogether account for the marginally different relaxivity values presented in this works and the literature.

Upon addition of excess phosphate and phosphoserine to $Gd^{3+}-L_2$ the relaxivity decreased to 3.9 ± 0.07 mM^{-1} s^{-1} and 3.11 ± 0.13 mM^{-1} s^{-1} respectively (**Figure 5.15**). These values are typical for $q = 1$ molecular contrast agents consistent with a monodentate binding of phosphate in agreement with previously reported binding behaviour of L_2. For example, Dickins *et al.* reported a decrease in q from 2 to 1 in $Gd^{3+}-L_2$ when phosphate was introduced to the solution in variable-temperature NMR.[158] Binding of $Gd^{3+}-L_2$ to phosphoserine has not been previously reported. However, as previously mentioned, binding of $Yb^{3+}-L_2$ and $Tm^{3+}-L_2$ to phosphoserine has been observed.[154] In these lanthanides later in the series Lewis acidity is higher due to stronger lanthanide contraction effects and phosphate binding competes with binding on the carboxylic site of phosphorylated amino acids. On the other hand, Gd^{3+} has a larger ionic radius and lower Lewis's acidity, similarly to Eu^{3+}. It was shown that binding of amino acids to $Eu^{3+}-L_2$ occurs with very low affinity, with the COOH group remaining protonated. Based on these observations coupled with the similar relaxivity of $Gd^{3+}-L_2$ + phosphoserine to $Gd^{3+}-L_2$ + phosphate it is logical to conclude that phosphoserine binds $Gd^{3+}-L_2$ in a monodentate manner through the phosphate

group with a single water molecule remaining at the axial position of the ligand.[158]

Addition of excess amount of tyrosine to $Gd^{3+}-L_1$ reduced the signal to 1.18 ± 0.05 mM^{-1} s^{-1} (**Figure 5.15**) consistent with purely outer sphere contribution and displacement of both water molecules situated in the centre of the complex. This binding mode supports the hypothesis of π-π stacking between the benzene rings on the ligand and on tyrosine, which can encourage efficient binding of tyrosine to the Gd^{3+} centre, also observed previously with $Gd^{3+}-L_1$.
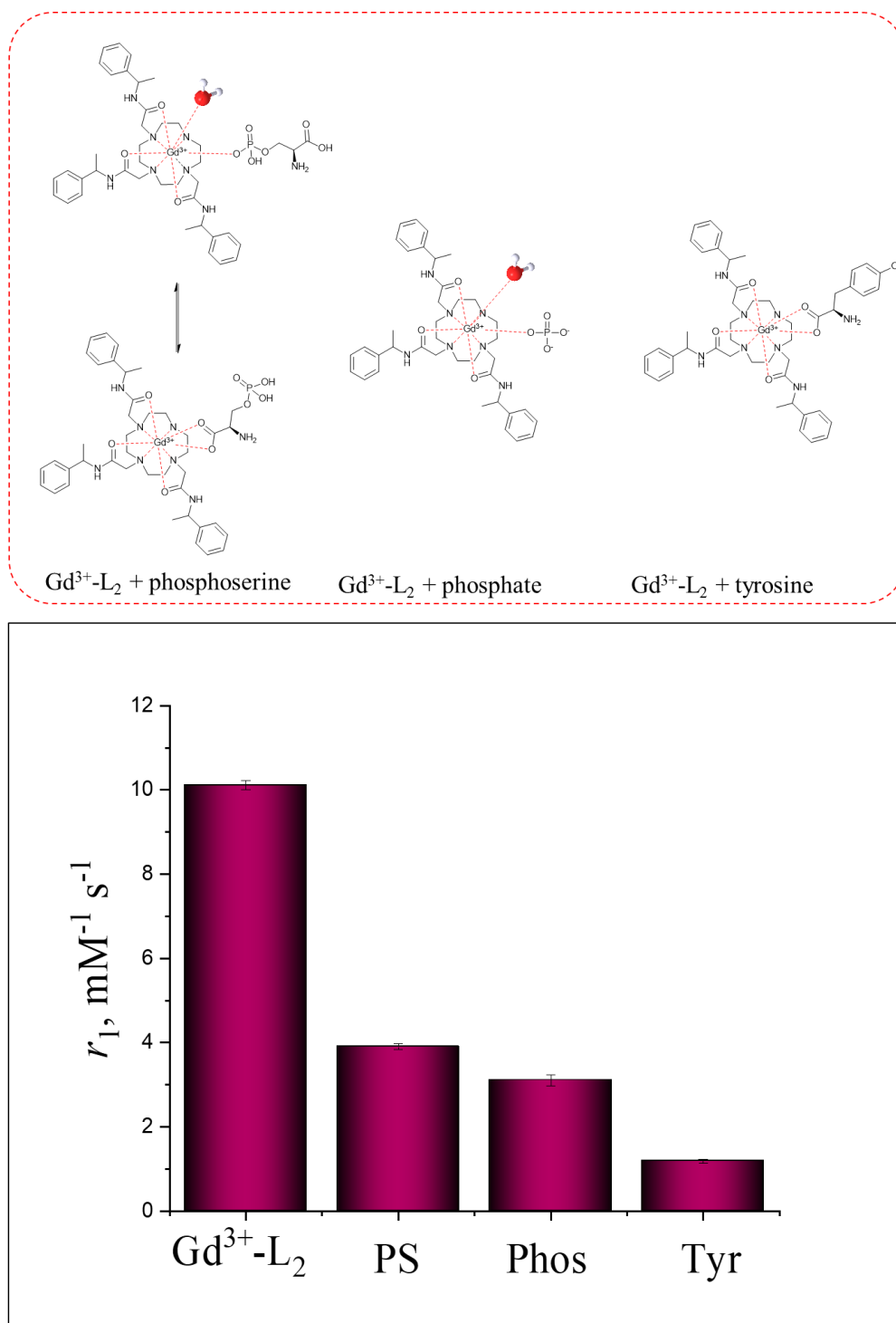
Figure 5.15 *Relaxivity of $Gd^{3+}-L_2$ in the presence and absence of phosphoserine (PS), phosphate (Phos) and tyrosine (Tyr), recorded at 23.4 MHz, 25 °C. Guest molecules were introduced to $Gd^{3+}-L_2$ in 20 equivalents. The error bars represent the linear fit error obtained in Origin software. The proposed binding modes are shown on the top.*

The relaxivity enhancement induced by $Gd^{3+}-L_3$ was recorded at 25 °C and 37 °C using NMRR and the values were very similar, 15.9 ± 0.44 mM^{-1} s^{-1} and 15.5 ± 0.40 mM^{-1} s^{-1} respectively (**Figure 5.16**). This showed that slight differences in temperature for up to 10 °C, for example caused by measurements of physiological samples, would not affect significantly the efficiency of the ligand. The relaxivity of $Gd^{3+}-L_3$ at 25 °C was 1.5-fold higher than the relaxivity of $Gd^{3+}-L_2$ measured in the same conditions (10.1 mM^{-1} s^{-1}). This was attributed to the higher molecular weight of $Gd^{3+}-L_3$ causing longer rotational correlation times and increasing the inner-sphere contribution to relaxivity. Previous studies showed that the europium version of the ligand, $Eu^{3+}-L_3$, had a hydration number $q = 1.2$, however L_3 is a heptadentate ligand and would be expected to have a hydration number $q = 2$.[156] This lower reported value could be due to the presence of the bulky acridone pendant arm which has the potential to prevent water access to the lanthanide ion. Additionally, the large hydrophobic area of the ligand could destabilise the transition state for associative water exchange and lead to longer τ_m as previously shown for this type of DOTAM-based ligands.[157] When excess of phosphoserine was introduced to the solution of $Gd^{3+}-L_3$ the relaxivity decreased to 11.26 ± 0.19 mM^{-1} s^{-1} (**Figure 5.16**), consistent with partial removal of the water molecule. This type of binding to phosphoserine was previously observed in literature with $Eu^{3+}-L_3$ where spectrofluorimetric studies showed a reduction in q from 1.2 to 0.7 upon addition of the phosphorylated amino acid in solution.[156] Therefore, the reduction in

relaxivity observed with phosphoserine is in agreement with previous reports in literature. Addition of excess (20 equivalents) of tyrosine, phosphate and lysine caused sedimentation in the solution which was sinking to the bottom of the test tube before measurements could be completed and as a result relaxation times could not be measured (**Figure 5.17**). Although this (reproducibly occurring) sedimentation behaviour implies that there is some kind of binding interaction, this is qualitative rather than quantitative evidence.
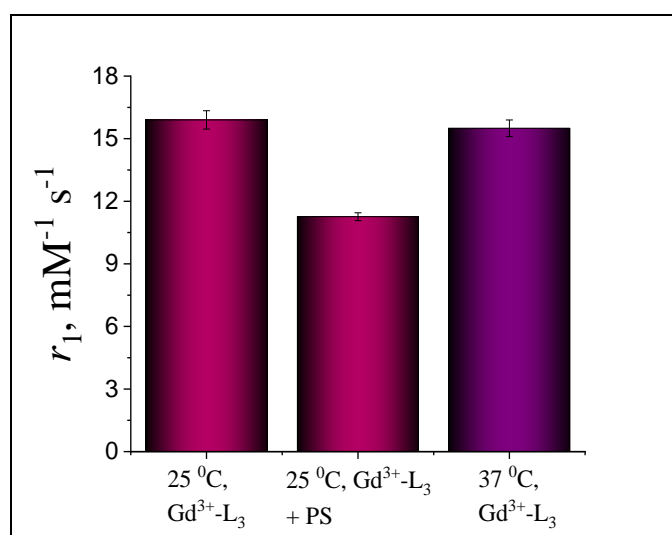
Figure 5.16 *Relaxivity of Gd³⁺−L₃ in the presence and absence of phosphoserine (PS, 20 equivalents) at 25 °C and Gd³⁺−L₃ alone at 37 °C, recorded at 23.4 MHz. The error bars represent the linear fit error obtained in Origin software.*
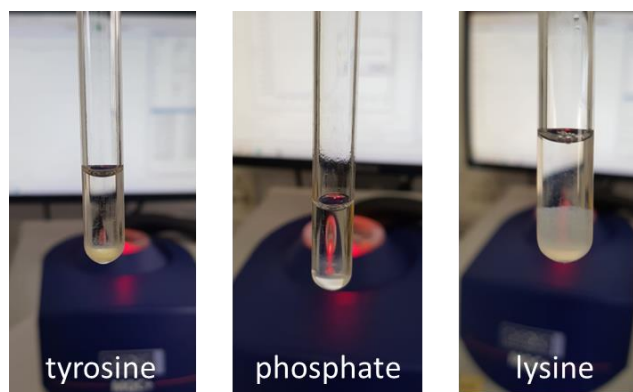
Figure 5.17 *Sedimentation in mixed samples of Gd^{3+}−L$_3$ with tyrosine, phosphate, and lysine.*

The ability of Gd^{3+}−L$_{1,2}$ to bind phosphate and tyrosine and Gd^{3+}−L$_3$ to bind phosphoserine was very promising as it indicated their potential to bind sarin-tyrosine adducts. The similarity of the binding modes observed for Gd^{3+}−L$_2$ to other lanthanide analogues of L$_2$ from the literature was reassuring that selective binding for phosphotyrosine over other oxy anions, including amino acids in solution is likely to be retained. Competitive binding of these ligands to phosphoserine (PS) could be an advantage in sarin poisoning detection because phosphorylation of acetylcholinesterase and other related enzymes occurs at serine residues as a result of sarin poisoning. With this in mind, in the next section Gd^{3+}−L$_{1-3}$ were tested in the nerve agent testing MRI facilities at Dstl Porton Down for binding to two nerve agent adducts.

5.5   MRI of L$_{1-3}$ and testing with sarin adducts

The next set of experiments were conducted at Dstl, Porton Down. The sarin adducts were synthesised by Claire Mitchell, Dstl, Porton Down, and all

MRI experiments were assisted by Dr Stuart Notman and Dr Soumya Roy, Dstl Porton Down. The basic principles governing NMRR, and MRI are the same and both techniques can produce quantitative information on relaxation times. The most obvious differences arise from the ability of MRI to produce images due to 3D spatial encoding unlike NMRR which is used for quantitative assessment of contrast agents and deliver a numerical value for proton relaxation times. Producing images requires a different pulse sequence to the simple inversion-recovery (IR) used to measure T_1 in NMRR, such as Fast Imaging with Steady-state free Precession (FISP). Furthermore, in NMRR the signal (proton relaxation times) is a sum of all signals present in the sample, contrasted by MRI, where the signal is generated in small voxels along all three axes, spatially encoded by gradient coils and processed to produce an image. Relaxation times in MRI can be extracted by defining a region of interest (ROI) on the image and following a set of commands in the software. On the other hand, in NMRR the relaxation times are derived in a mathematical form directly from the measurement. Finally, the two techniques usually differ in magnetic field – typical benchtop NMRR machines operate with a permanent magnet at low frequencies, while MRI systems run on much higher frequencies created by superconducting magnets. All these differences emphasise the necessity for evaluation of the contrast agent properties and binding of ligands L_{1-3} on the MRI machine they will most likely be used in case of nerve agent poisoning.

The following data was collected in the facilities of Dstl, Porton Down on a Bruker 400 MHz MRI machine.[§§] Longitudinal relaxation times (T_1, s) were recorded using a FISP pulse sequence, described in detail in Section 1.2.3. As a reminder, the NMRR measurements described in previous sections were recorded at 23.4 MHz using a simpler inversion-recovery sequence, and so some differences in contrast agent performance due to frequency and pulse sequence effects were expected. The relaxivity of $Gd^{3+}-L_1$ was assessed on the MRI machine at Dstl, Porton Down and compared with the value previously calculated using NMRR at UCL to establish the differences in both techniques. This was achieved by recording phantom images of $Gd^{3+}-L_3$ at 0.1 mM, 0.2 mM and 1 mM using FISP pulse sequence for a slice of 1 mm thickness. The relaxivity of $Gd^{3+}-L_1$ was determined in accordance with equation 1.7, Section 1.3 and was found to be 11.04 ± 0.67 mM^{-1} s^{-1}. This value was in good agreement with the value obtained using NMRR which was slightly lower, 9.67 ± 0.21 mM^{-1} s^{-1}. This difference can be accounted for by considering all factors that could impact performance described above. In addition, the MRI value was derived from the linear fit of only three data points (compared with six data points for NMRR) which would be expected to result in a larger error.

To assess the binding interactions between $Gd^{3+}-L_1$ and the sarin-tyrosine nerve agent adduct (GB−Tyr, **Figure 5.18**) a titration similar to the ones described in section 3.3.3 was performed. The phantom images of

---

[§§] With the help of Dr Stuart Notman and Dr Soumya Roy, Dstl Porton Down.

samples containing 0.02, 0.2, 2 and 10 equivalents of GB−Tyr[***] with

Gd^{3+}−L$_1$ were taken (**Figure 5.19**), the longitudinal relaxation times (T_1, s)

extracted using the Bruker software, and the longitudinal relaxivity (r_1, mM^{-1}

s^{-1}) calculated by dividing the corresponding relaxation rates (R_1, s^{-1} = $1/T_1$)

by the Gd^{3+}−L$_1$ concentration (**Figure 5.20**). At 10 equivalents of GB−Tyr

there was 40 % decrease in signal, from 12.03 mM^{-1} s^{-1} to 7.34 mM^{-1} s^{-1},

consistent with partial removal of the inner-sphere water molecule. In

contrast, in section 5.4 tyrosine induced 77 % decrease in signal at 20

equivalents consistent with amino acid chelation at the metal site, inducing

apparent complete removal of the inner-sphere water molecule. However, the

molecular weights of tyrosine and GB−Tyr are different (with GB−Tyr

estimated to be > 1.5 times larger), so it would be expected that coordination

of GB−Tyr to Gd^{3+}−L$_1$ may have a larger impact on the rotational correlation

τ_R. Therefore, the reduction in signal due to reduction in hydration number in

Gd^{3+}−L$_1$ + GB−Tyr is likely to be slightly offset by signal increase as a result

of longer τ_R times. Previous studies of ligands from the same class as L$_1$

showed that in a competitive binding environment these types of ligands

prefer to coordinate through the phosphate binding site over the carboxylic

acid of their amino acids, therefore it would be expected that binding of

GB−Tyr occurs *via* the phosphorylated site in a monodentate manner.

However, the phosphonate on the adduct bears no negative charge and so the

most likely binding mode would be amino acid chelation.[65,154,156–158] This

---

[***] Synthesised by Claire Mitchell, Dstl, Porton Down.

reduction in longitudinal relaxivity was also visible on the phantoms by the darkening of the image at higher equivalents of GB−Tyr (**Figure 5.19**). This titration showed that ten equivalents of nerve agent adduct were enough to invoke a notable change in proton relaxation rates and so $Gd^{3+}−L_{1-3}$ were tested for binding with ten equivalents of nerve agent adducts GB−Tyr and cyclosarin-tyrosine (GF−Tyr, **Figure 5.18**), which is a cyclosarin-tyrosine adduct version.[†††]

Sarin-tyrosine adduct   **Cyclosarin-tyrosine adduct**
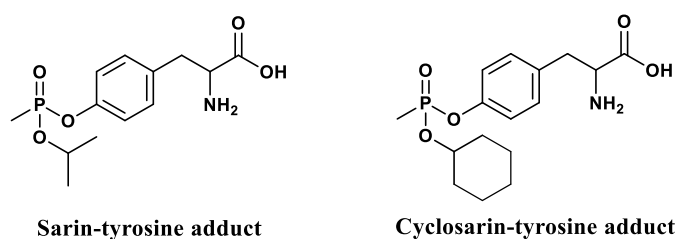
Figure 5.18 *Structures of sarin-tyrosine (GB−Tyr) and cyclosarin-tyrosine (GF−Tyr) nerve agent adducts tested in this study. Compounds were provided by and tested at Dstl, Porton Down.*

GB-Tyr
equivalents   0.02   0.2   2   10

Figure 5.19 *Phantom images of $Gd^{3+}−L_1$ + GB−Tyr in different ratios recorded at 400 MHz, 25 °C.*

[†††] Synthesised by Claire Mitchell, Dstl, Porton Down.
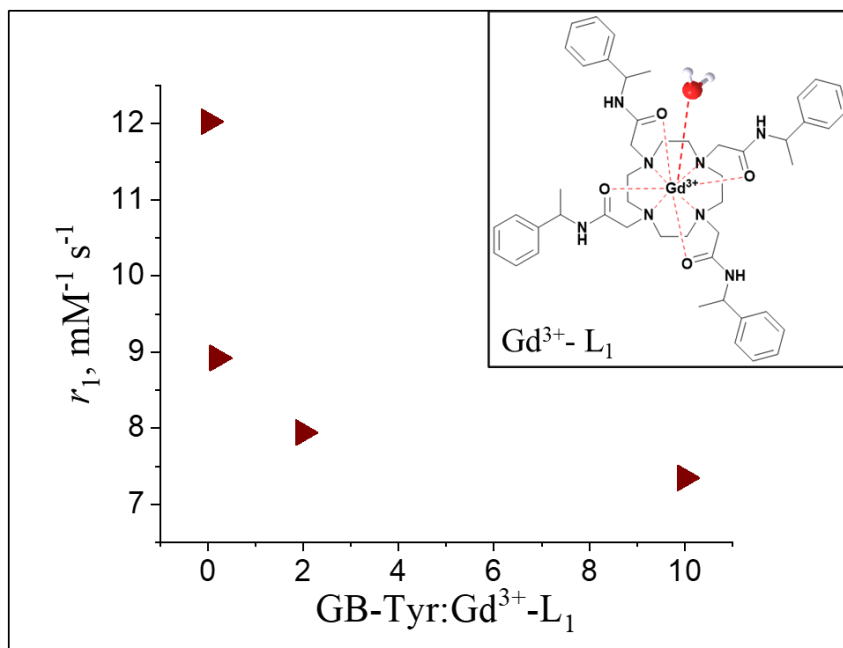
Figure 5.20 *Titration of $Gd^{3+}-L_1$ with GB−Tyr recorded at 400 MHz, 25 °C. The x-axis shows molar equivalents.*

The phantom images of the three ligands in the presence and absence of nerve agent adducts (10 molar equivalents) can be seen in **Figure 5.21**. Addition of both GB−Tyr and GF−Tyr caused images to appear darker, associated with lower longitudinal relaxation. The images were processed, and relaxation times calculated (**Figure 5.22**). In this set of experiments addition of 10 equivalents of GB−Tyr and GF−Tyr to $Gd^{3+}-L_1$ caused a very similar response, a signal decrease by 32 % and 33 % respectively (**Figure 5.22**). Response of $Gd^{3+}-L_2$ and $Gd^{3+}-L_3$ to GB−Tyr and GF−Tyr ranged from 35 % to 43 % with the greatest decrease in signal recorded for $Gd^{3+}-L_3$ + GB−Tyr. Interestingly, the proton relaxation rate of $Gd^{3+}-L_3$ alone showed highest enhancement of 8.40 s^{-1} at 400 MHz; this enhancement compared to $Gd^{3+}-L_1$ and $Gd^{3+}-L_2$ is similar to that observed at 23.4 MHz and attributed to changes in τ_R as previously described. In this experiment, relaxation rate

was used simply for comparison of the response to the nerve agent adducts. As previously noted, relaxivity values derived from a single data point are not as accurate as those measured for multiple concentrations, possibly due to differences in the experimental setting and pulse sequence parameters. However, since this enhancement was broadly in line with the data observed at lower frequencies, this was not a major concern as transferability of contrast agent properties were demonstrated above. Furthermore, the response of all the contrast agents to sarin and cyclosarin nerve agent adducts were notable in both phantom images and relaxation rate calculations. The level of signal decrease (*ca.* 40%) was consistent with monodentate binding, previously observed by NMRR. The trend in relaxation rate enhancement previously noted by NMRR was also preserved in the order $Gd^{3+}-L_1 < Gd^{3+}-L_2 < Gd^{3+}-L_3$. Most importantly, detection of both G-type nerve agent adducts was successful in aqueous solutions. Data acquisition was rapid with very basic sample preparation, including weighing the nerve agent adduct and the contrast agent and mixing them in water by shaking. Qualitative data analysis could be accessed immediately after the scan, which took less than a minute, and could be performed by a non-specialist. Quantitative data analysis was straightforward and involved simply running the software and converting the relaxation times (T_1, s) to relaxation rates ($1/T_1$, s^{-1}). This underlines the potential of MRI as a rapid detection system for nerve agent poisoning.
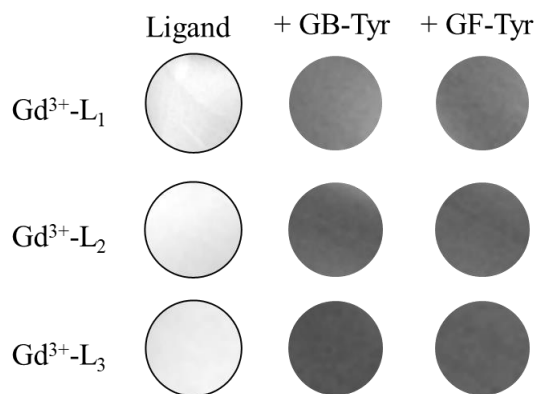
Figure 5.21 *Phantom images of $Gd^{3+}-L_{1-3}$ on their own and in the presence of 10 equivalents of GB−Tyr and GF−Tyr recorded at 400 MHz, 25 °C*
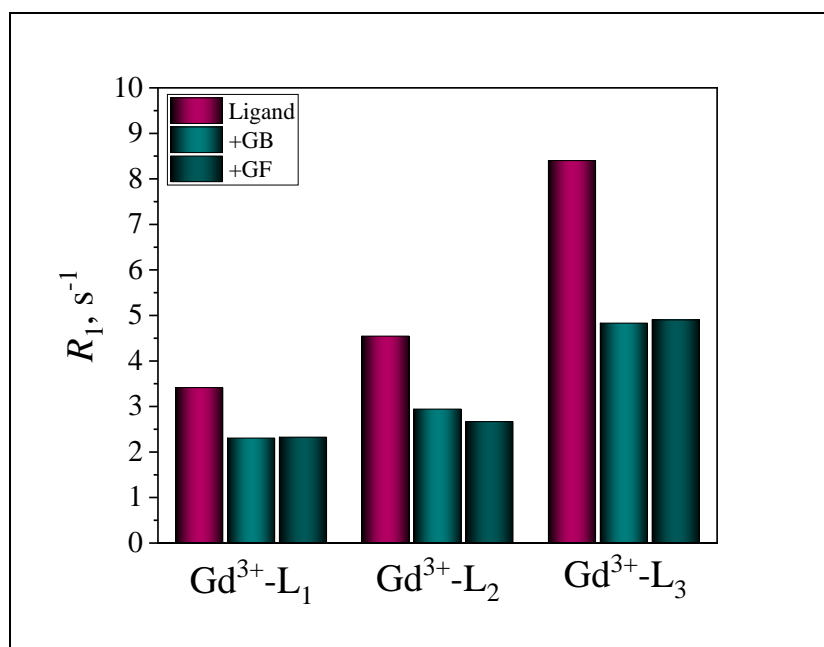
Figure 5.22 *Relaxation rates of $Gd^{3+}-L_{1-3}$ in the presence and absence of GB−Tyr and GF−Tyr recorded at 400 MHz, 25 °C. Nerve agent adducts were introduced to $Gd^{3+}-L_{1-3}$ in 10 equivalents.*

5.6   Conclusion

A series of lanthanide chelates were selected based on their known preference for binding with phosphotyrosine in the literature. These

preferences for binding were of relevance for the development of chelates for nerve agent adduct binding, due to their equivalent binding sites of phosphotyrosine. Herein, the series of L_{1-3} ligands was successfully synthesized and chelated with Gd^{3+} and assessed for their binding interaction with common ligands and nerve agent adducts.

NMRR studies of ligands $Gd^{3+}-L_1$ and $Gd^{3+}-L_2$ showed behaviour consistent with monodentate binding of phosphate and a strong chelation to tyrosine, possibly due to π-π stacking between the pendant arms of the ligands and the benzene ring of tyrosine. It was observed that the availability of a large binding pocket did not affect the successful binding of phosphate, however the phosphorylated amino acid phosphoserine (PS) had different effects on the relaxometry of the mono-aqua ligand ($Gd^{3+}-L_1$) with a relatively small binding pocket and the di-aqua analogue bearing only three pendant arms ($Gd^{3+}-L_2$). When introduced to $Gd^{3+}-L_1$, PS caused an increase in relaxivity, consistent with increased second hydration sphere observed with this molecule in Chapter 3. In the presence of the larger binding pocket, PS behaved very similarly to phosphate, indicating the displacement of a single water molecule from the inner-hydration sphere. This behaviour was not observed with the phosphorylated nerve agent adducts GB−Tyr and GF−Tyr during MRI studies (where relaxation decreases were observed for both ligands), possibly because the interaction with the lanthanide centre was reinforced by π stacking between the ligands and the tyrosine benzene ring on the nerve agent adducts.

$Gd^{3+}−L_3$ showed binding to PS in NMRR which could be advantageous for nerve agent poisoning detection. A good agreement was observed between NMRR and MRI with regards to signal enhancement and binding properties of the contrast agents that were tested, and all three ligands showed binding to two G-type nerve agent adducts when tested on a 400 MHz MRI machine at Dstl. This was evident by the reduction in relaxation rate ranging between 32% and 43%, typical for partial displacement of an inner-sphere water molecule and monodentate binding *via* the phosphate binding site. The phantom images taken with MRI showed a visible change in shade from very light grey to dark grey upon introduction of 10 equivalents of nerve agent adducts to their solutions. $Gd^{3+}−L_3$ induced the highest enhancement of proton relaxation rates and the largest reduction in signal as a response to GB−Tyr binding from 8.40 s^{-1} to 4.83 s^{-1} and seems like the most promising ligand for nerve agent poisoning detection.

6   Summary and Future work

The current state of the art for the detection of nerve agent poisoning, for example by sarin exposure, is limited by the length of time to process samples and requires specialised LC-MS equipment that is often not available in hospitals, which are typically the first point of contact for victims. The focus of this work was to develop proof of principle for an alternative approach to detection of G-type nerve agents poisoning utilising MRI alongside a ligand-capture and contrast enhancement system. This approach has the advantage of rapid detection and does not require laborious and time-consuming sample preparation. An additional benefit of MRI is that scanners are available in most hospitals, offering the option for application to be expanded beyond specialised laboratories, such as at Dstl.

In order to design an MRI-based detection system for nerve agent poisoning, a systematic investigation of how nerve agent adduct analogues interact with the clinically approved MRI contrast agent Dotarem® (Gd^{3+}–DOTA) was undertaken. It became clear that MRI is an excellent technique for uncovering binding interactions in certain binding modes, such was as the case for lysine, tyrosine, and ibuprofen with Gd^{3+}–DOTA. In this case, standard methods such as DOSY, spectrofluorimetry and NMR were not sensitive enough to detect weak interactions, whereas signal change was observed by NMRR . Most importantly, it was noted that in order to observe weak binding interactions with the Gd^{3+} core, a minimum excess of 10

equivalents of the guest moiety were required. Remarkably, the strength of the binding interactions of lysine remained consistent even when Gd^{3+}–DOTA was anchored to the surface of MSNs to yield an MRI-active hybrid nanomaterial. Gd^{3+}–DOTA−MSNs synthesised using a modified Stöber procedure showed a superior enhancement of the MRI signal to similar materials published in the literature (r_1 = 40.65 ± 0.21 mM^{-1} s^{-1}). When titrated with lysine the NMRR response of Gd^{3+}–DOTA−MSNs was much higher compared with the molecular analogue Gd^{3+}–DOTA + lysine, however the association constant (log K_A) remained very similar. The requirement for larger binding pocket led to the synthesis of novel class of MRI nano contrast agents, Gd^{3+}−SSNPs, which offered some potential to be used as contrast agents in the future, albeit requiring some optimisation to assess their full utility.

Interestingly, introducing molecules containing phosphate (*e.g.*, inorganic phosphate and phosphoserine) resulted in increased relaxivity when mixed with molecular Gd^{3+}–DOTA, an observation that could not be explained immediately. Fitting NMRD profiles of 1:20 ratio of Gd^{3+}–DOTA:guest molecule revealed an interesting mechanism of the binding mode, whereby the inability of phosphate anions to bind to the inner coordination sphere of Gd^{3+}–DOTA resulted in increased in signal through the second coordination sphere arising from the small binding pocket of Gd^{3+}–DOTA. This was further confirmed in Chapter 5 when specific ligands with different size binding pockets were tested for binding to phosphoserine.

Since Gd^{3+}–DOTA is not a specific ligand for binding oxyanions and interactions with the model guest molecules were weak and non-specific, data presented in Chapter 5 detailed the synthesis of three selective ligands previously shown in the literature to bind phosphoserine and phosphotyrosine when produced as fluorescent probes. herein, the ligands were chelated to Gd^{3+} and their ability to bind to the guest molecules was investigated using NMRR. Finally, the capability of these ligands to detect G-series nerve agent adducts was investigated with cyclosarin (GF) and sarin (GB) tyrosine adducts on a high-field MRI instrument in the facilities of Dstl, Porton Down. For this series of experiments, samples were simply shaken together in a tube for 10 seconds and an MR image was recorded for additional 30 seconds. The resultant images demonstrated differential signals for all three ligands in the presence of GB−Tyrosine adduct and GF−Tyrosine adduct relative to the control. This qualitative detection offers a powerful tool for the rapid detection of nerve agent poisoning, in particular, due to the simplicity of the experimental methodology and data readouts. Further processing of the MR images to delineate relaxivity can complement the initial qualitative assessment and offer a route towards quantitative analysis. Because MRI is non-destructive, the samples can be retained and further tested by traditional methods such as LC-MS.

Future work should include binding assays using NMRR of the ligands $(Gd^{3+}−L_{1-3})$ with 10-20 equivalents of phosphotyrosine. Saturation transfer difference analysis, which is an NMR technique, could be used to determine

the binding site of small molecules to the Gd^{3+} core and help in the understanding of the mode of binding. Additionally, competitive binding assays of phosphotyrosine and phosphorylated nerve agent adducts in the presence of other oxy anions must be completed at Dstl. This would enable testing in the future in blood/plasma samples which would be the type of samples to be tested in a real-life nerve agent poisoning. Testing on the protein nerve agent adduct as opposed to molecular adducts is also crucial as this will increase, rather than decrease relaxivity. It would be expected that this increase in signal will be large, due to the large rotational correlation times of proteins. Testing on other types of nerve agent adducts, such as Novichock, can reveal if the current ligands, $Gd^{3+}-L_{1\text{-}3}$, bind specifically G-type biomarkers or are more general. Subsequent optimisation of the pendant arms of the ligating chelates could additionally lead to more specific detection. For example, in the binding pocket of albumin adjacent to Tyr411 (the site where nerve agents react) there is an arginine at 410 position (Arg410). At neutral pH, such as the pH in the blood, the guanidine functional group is positively charged. Including a negative charge on one or more of the side arms of the contrast agent could lead to stabilisation of the molecular binding to the nerve agent adduct. To test this hypothesis ligand $Gd^{3+}-L_3$ should be tested with the nerve agent-protein adduct before and after the side arms are negatively charged and the effects of this charge on binding has to be investigated. Furthermore, techniques like DOSY and NMRD can give more insights into the hydration spheres structure around the ternary adducts and

the water dynamics and would be desirable for the better understanding of the relaxivity behaviours observed in this chapter.

Overall, the work showcases insight into the utility of MRI as a kinetic tool for investigating weak interactions between Gd^{3+}−cyclen species, where other 'gold standard' methods have proven less useful. It further demonstrates the promise of such materials for the fast and straightforward detection of nerve agent adducts, requiring minimal processing, yet clear signal changes. Further work to assess selectivity and specificity in the context of relevant biological fluids would be needed in the future, however it provides significant promise as a novel tool for nerve agent poisoning detection.

7 References

1   D. Kaszeta, *Toxic*, 2020.

2   Cometee on Toxicology National Research Council, *Review of Acute Himan-Toxicity Estimates for Selected Chemical-Warfare Agents*, National Acaademy Press, 1997.

3   U. Schmidt, *Camb. Q. Healthc. Ethics*, 2006, **15**, 366–80.

4   T. C. Südhof and R. C. Malenka, *Neuron*, 2008, **60**, 469–476.

5   L. Purves, Dale; Augustine, George; Fitzpatrick, David; Hall, William; LaMantia, Anthony-Samuel; White, *Neuroscience*, Sinauer Associates, Fifth., 2012.

6   Nonaged form of Mouse Acetylcholinesterase inhibited by sarin-Update, https://doi.org/10.2210/pdb2y2v/pdb (Accessed January 2023).

7   Synapse, https://courses.lumenlearning.com/wm-biology2/chapter/chemical-and-electrical-synapses (Accessed January 2023).

8   T. Okumura, T. Hisaoka, A. Yamada, T. Naito, H. Isonuma, S. Okumura, K. Miura, M. Sakurada, H. Maekawa, S. Ishimatsu, N. Takasu and K. Suzuki, *Toxicol. Appl. Pharmacol.*, 2005, **207**, 471–476.

9   OPCW, Mission, https://www.opcw.org/about/missionv(Accessed January 2023).

10   OPCW, 2017, **0455**, 2.

11   KHAN   SHAYKHUN, https://www.opcw.org/sites/default/files/documents/Fact_Finding_Missi on/s-1510-2017_e_.pdf (Accessed January 2023).

12   OPCW, 2021, 1–3.

13   E. J. Hulse, J. D. Haslam, S. R. Emmett and T. Woolley, *Br. J. Anaesth.*, 2019, **123**, 457–463.

14   Y. Z. Q. Y. Y. Ci and Z. G. K. R. W. Chang, *Arch. Toxicol.*, 1995, **69**, 644–648.

15   H. John, M. J. van der Schans, M. Koller, H. E. T. Spruit, F. Worek, H. Thiermann and D. Noort, *Forensic Toxicol.*, 2018, **36**, 61–71.

16   Y. Lin, J. Chen, L. Yan, L. Guo, B. Wu, C. Li, J. Feng, Q. Liu and J. Xie, *Anal. Bioanal. Chem.*, 2014, **406**, 5213–5220.

17   H. H. Bai, L. Guo, J. L. Feng, C. L. Feng, J. Chen and J. W. Xie, *Fenxi Huaxue/ Chinese J. Anal. Chem.*, 2008, **36**, 1269–1272.

18   M. Blanca, A. Shifrovitch, M. Madmon, M. Elgarisi, S. Dachir, S. Lazar, S. Baranes, I. Egoz, M. Avraham, H. Dekel Jaoui, S. Dagan and A. Weissberg, *Arch. Toxicol.*, 2020, **94**, 103–111.

19   Y. Dubrovskii, E. Murashko, O. Chuprina, P. Beltyukov, A. Radilov, N. Solovyev and V. Babakov, *Talanta*, 2019, **197**, 374–382.

20   V. Kumar, H. Kim, B. Pandey, T. D. James, J. Yoon and E. V. Anslyn,

257

Chem. Soc. Rev., 2022, **52**, 663–704.

21   L. Chen, D. Wu and J. Yoon, *ACS Sensors*, 2018, **3**, 27–43.

22   S. Royo, R. Martínez-Máñez, F. Sancenón, A. M. Costero, M. Parra and S. Gil, *Chem. Commun.*, 2007, **46**, 4839.

23   K. Aich, S. Das, S. Gharami, L. Patra and T. Kumar Mondal, *New J. Chem.*, 2017, **41**, 12562–12568.

24   V. Kumar, G. Raviraju, H. Rana, V. K. Rao and A. K. Gupta, *Chem. Commun.*, 2017, **53**, 12954–12957.

25   M. S. J. Khan, Y. W. Wang, M. O. Senge and Y. Peng, *J. Hazard. Mater.*, 2018, **342**, 10–19.

26   Z. Abbas, U. Yadav, R. J. Butcher and A. K. Patra, *J. Mater. Chem. C*, 2021, **9**, 10037–10051.

27   A. Allgardsson, L. Berg, C. Akfur, A. Hörnberg, F. Worek, A. Linusson and F. J. Ekström, *Proc. Natl. Acad. Sci. U. S. A.*, 2016, **113**, 5514–5519.

28   J. L. Major and T. J. Meade, *Acc. Chem. Res.*, 2009, **42**, 893–903.

29   D. Messeri, M. P. Lowe, D. Parker and M. Botta, *Chem. Commun.*, 2001, **1**, 2742–2743.

30   J. L. Major, G. Parigi, C. Luchinat and T. J. Meade, *Proc. Natl. Acad. Sci.*, 2007, **104**, 13881–13886.

31   G. L. Davies, I. Kramberger and J. J. Davis, *Chem. Commun.*, 2013, **49**,

9704–9721.

32   R. R. Zairov, A. V. Yagodin, M. N. Khrizanforov, A. G. Martynov, I. R. Nizameev, V. V. Syakaev, A. T. Gubaidullin, T. Kornev, O. Kaman, Y. H. Budnikova, Y. G. Gorbunova and A. R. Mustafina, *J. Nanoparticle Res.*, 2019, **21**, 12.

33   Y. Shen, F. L. Goerner, C. Snyder, J. N. Morelli, D. Hao, D. Hu, X. Li and V. M. Runge, *Invest. Radiol.*, 2015, **50**, 330–338.

34   J. W. Emsley, J. Feeney and L. H. Sutcliffe, *High Resolution Nuclear Magnetic Resonance Spectroscopy*, Pergamon Press Ltd., Headington Hill Hall, Oxford, 1966.

35   T. C. Farrar and E. D. Becker, *Pulse and Fourier Transform NMR*, Elsevier, 1971, pp. 1–17.

36   S. Currie, N. Hoggard, I. J. Craven, M. Hadjivassiliou and I. D. Wilkinson, *Postgrad. Med. J.*, 2013, **89**, 209–223.

37   P. Rink, *Magnetic Resonance in Medicine*, Blackwell Science, 2001.

38   I. I. Rabi, *Phys. Rev.*, 1937, **51**, 652–654.

39   G. B. Chavhan, P. S. Babyn, B. G. Jankharia, H. L. M. Cheng and M. M. Shroff, *Radiographics*, 2008, **28**, 1147–1160.

40   A. D. Elster, MRI Q and A, https://mriquestions.com/gradient-echo.html (Accessed January 2023).

41   F. Bloch, *Phys. Rev.*, 1946, **70**, 460–474.

42   A. J. Aaron, A. Bumb and M. W. Brechbiel, *Chem. Rev.*, 2010, **110**, 2921–2959.

43   A. D. Sherry, P. Caravan and R. E. Lenkinski, *J Magn Reson Imaging*, 2009, **1248**, 1240–1248.

44   A. N. Oksendal and P. -A Hals, *J. Magn. Reson. Imaging*, 1993, **3**, 157–165.

45   S. Laurent, L. Vander Elst, C. Henoumont and R. N. Muller, *Contrast Media Mol. Imaging*, 2010, **5**, 305–308.

46   M. Port, J.-M. Idée, C. Medina, C. Robic, M. Sabatou and C. Corot, *BioMetals*, 2008, **21**, 469–490.

47   C. Thakral and J. L. Abraham, *J. Cutan. Pathol.*, 2009, **36**, 1244–1254.

48   P. Caravan, N. J. Cloutier, M. T. Greenfield, S. A. McDermid, S. U. Dunham, J. W. M. Bulte, J. C. Amedio, R. J. Looby, R. M. Supkowski, W. D. W. Horrocks, T. J. McMurry and R. B. Lauffer, *J. Am. Chem. Soc.*, 2002, **124**, 3152–3162.

49   G. Angelovski, P. Fouskova, I. Mamedov, S. Canals, E. Toth and N. K. Logothetis, *ChemBioChem*, 2008, **9**, 1729–1734.

50   E. L. Que and C. J. Chang, *J. Am. Chem. Soc.*, 2006, **128**, 15942–15943.

51   I. Solomon, *Phys. Rev.*, 1955, **99**, 559.

52   N. Bloembergen, E. M. Purcell and R. V. Pound, *Phys. Rev.*, 1948, **73**, 679–712.

53 P. Caravan, *Chem. Soc. Rev.*, 2006, **35**, 512–523.

54 M. Botta, *Eur. J. Inorg. Chem.*, 2000, **2000**, 399–407.

55 W. Y. Huang, G. L. Davies and J. J. Davis, *Chem. Commun.*, 2013, **49**, 60–62.

56 F. Omil, C. D. Bakker, L. W. H. Pol and G. Lettinga, *Environ. Technol. (United Kingdom)*, 1997, **18**, 255–264.

57 S. Aime, M. Botta, D. Esteban-Gómez and C. Platas-Iglesias, *Mol. Phys.*, 2019, **117**, 898–909.

58 A. L. Thompson, D. Parker, D. A. Fulton, J. A. K. Howard, S. U. Pandya, H. Puschmann, K. Senanayake, P. A. Stenson, A. Badari, M. Botta, S. Avedano and S. Aime, *J. Chem. Soc. Dalt. Trans.*, **47**, 2006, 5605–5616.

59 P. J. Hore, *Nuclear Magnetic Resonance*, Oxford University Press, Oxford, 2015.

60 F. K. Kálmán, M. Woods, P. Caravan, P. Jurek, M. Spiller, G. Tircsó, R. Király, E. Brúcher and A. D. Sherry, *Inorg. Chem.*, 2007, **46**, 5260–5270.

61 S. Aime, A. Barge, M. Botta, D. Parker and A. S. De Sousa, *J. Am. Chem. Soc.*, 1997, **119**, 4767–4768.

62 A. Beeby, I. M. Clarkson, R. S. Dickins, S. Faulkner, D. Parker, L. Royle, A. S. De Sousa, J. A. G. Williams and M. Woods, *J. Chem. Soc.,*

Perkin Trans, 1999, **2**, 493–503.

63   T. J. Sørensen, L. R. Hill, J. A. Tilney, O. A. Blackburn, M. W. Jones, M. Tropiano and S. Faulkner, *Eur. J. Inorg. Chem.*, 2014, **2014**, 2520–2528.

64   P. Kuzmic, *Methods in Enzymology*, Academic Press, 2009.

65   J. I. Bruce, R. S. Dickins, L. J. Govenlock, T. Gunnlaugsson, S. Lopinski, M. P. Lowe, D. Parker, R. D. Peacock, J. J. B. Perry, S. Aime and M. Botta, *J. Am. Chem. Soc*, 2000, **122**, 9674–9684.

66   R. Mailhot, T. Traviss-Pollard, R. Pal and S. J. Butler, *Chem. - A Eur. J.*, 2018, **24**, 10745–10755.

67   S. E. Bodman, C. Breen, S. Kirkland, S. Wheeler, E. Robertson, F. Plasser and S. J. Butler, *Chem. Sci.*, 2022, **13**, 3386–3394.

68   H. Wu and C. Tong, *ACS Sensors*, 2018, **3**, 1539–1545.

69   V. C. Pierre and R. K. Wilharm, *Front. Chem.*, 2022, **10**, 2296-2646.

70   S. E. Bodman and S. J. Butler, *Chem. Sci.*, 2021, **12**, 2716–2734.

71   D. F. Caffrey and T. Gunnlaugsson, *Dalt. Trans.*, 2014, **43**, 17964–17970.

72   L. R. Tear, M. L. Maguire, M. Tropiano, K. Yao, N. J. Farrer, S. Faulkner and J. E. Schneider, *Dalt. Trans.*, 2020, **49**, 2989–2993.

73   J. F. Youngren, *Cell. Mol. Life Sci.*, 2007, **64**, 873–891.

74   Y. Bretonniere, M. J. Cann, D. Parker and R. Slater, *Org. Biomol. Chem.*, 2004, **2**, 1624–1632.

75   A. Y. Louie, M. M. Hüber, E. T. Ahrens, U. Rothbächer, R. Moats, R. E. Jacobs, S. E. Fraser and T. J. Meade, *Nat. Biotechnol.*, 2000, **18**, 321–325.

76   S.-H. Chen, Y.-T. Kuo, S. Gyan, T.-L. Cheng, Y.-Z. Su, T.-P. Wang, Y.-Y. Chiu, J.-J. Lai, C.-C. Chang, T.-S. Jaw, S.-C. Tzou, G.-C. Liu and Y.-M. Wang, 2012, **51**, 12246–12435.

77   Đ. Toljić and G. Angelovski, *ChemNanoMat*, 2019, **5**, 1456–1460.

78   F. Carniato, L. Tei and M. Botta, *Eur. J. Inorg. Chem.*, 2018, **46**, 4936–4954.

79   M. Giardiello, M. Botta and M. P. Lowe, *J. Incl. Phenom. Macrocycl. Chem.*, 2011, **71**, 435–444.

80   M. O. Breckwoldt, J. W. Chen, L. Stangenberg, E. Aikawa, E. Rodriguez, S. Qiu, M. A. Moskowitz and R. Weissleder, *Proc. Natl. Acad. Sci.*, 2008, **105**, 18584–18589.

81   P. Caravan, N. J. Cloutier, M. T. Greenfield, S. A. McDermid, S. U. Dunham, J. W. M. Bulte, J. C. Amedio, R. J. Looby, R. M. Supkowski, W. D. W. Horrocks, T. J. McMurry and R. B. Lauffer, *J. Am. Chem. Soc.*, 2002, **124**, 3152–3162.

82   A. L. Nivorozhkin, A. F. Kolodziej, P. Caravan, M. T. Greenfield, R. B.

Lauffer and T. J. McMurry, *Angew. Chem. Int. Ed. Engl.*, 2001, **40**, 2903–2906.

83   E. Rodríguez, M. Nilges, R. Weissleder and J. W. Chen, *J. Am. Chem. Soc.*, 2010, **132**, 168–177.

84   F. Carniato, L. Tei, J. Martinelli and M. Botta, *Eur. J. Inorg. Chem.*, 2018, **2018**, 2363–2368.

85   Y. Chen, H. Chen, D. Zeng, Y. Tian, F. Chen, J. Feng and J. Shi, *ACS Nano*, 2010, **4**, 6001–6013.

86   C.T.Kresge, M.E.Lenowicz, W.J.Roth, J.C.Vartuli and J.S.Bech, *Nature*, 1992, **359**, 710–712.

87   B. Muñoz, A. Rámila, J. Pérez-Pariente, I. Díaz and M. Vallet-Regí, *Chem. Mater.*, 2003, **15**, 500–503.

88   J. Park, Y. J. Park, C. Jun and J. Park, *Chem. Commun.*, 2011, **47**, 4860–4871.

89   F. Carniato, L. Tei, W. Dastrù, L. Marchese and M. Botta, *Chem. Commun.*, 2009, **15**, 1246–1248.

90   F. A. Dunand, A. Borel and L. Helm, *Inorg. Chem. Commun.*, 2002, **5**, 811–815.

91   F. Carniato, E. Boccaleri, L. Marchese, A. Fina, D. Tabuani and G. Camino, *Eur. J. Inorg. Chem.*, 2007, **4**, 585–591.

92   F. Zou, H. Ling, L. Zhou, F. F. Wang and Y. Li, *Dye. Pigment.*, 2021,

184, 108840.

93   H. Strauch, J. Engelmann, K. Scheffler and H. A. Mayer, *Dalt. Trans.*, 2016, **45**, 15104–15113.

94   U. Díaz, T. García, A. Velty and A. Corma, *Chem. - A Eur. J.*, 2012, **18**, 8659–8672.

95   W. Zhang, W. Zhang, Y. T. Pan and R. Yang, *J. Hazard. Mater.*, 2021, **401**, 123439.

96   G. L. Davies, J. O'Brien and Y. K. Gun'ko, *Sci. Rep.*, 2017, **7**, 1–8.

97   R. S. Dickins, S. Aime, A. S. Batsanov, A. Beeby, M. Botta, J. I. Bruce, J. A. K. Howard, C. S. Love, D. Parker, R. D. Peacock, H. Puschmann, C. Ifm, V. P. Giuria and V. Uni, *J. Am. Chem. Soc.*, 2002, **124**, 12697–12705.

98   S. J. Butler, D. Parker, A. Werner and S. J. Butler, *Chem. Soc. Rev*, 2013, **42**, 1652–1666.

99   S. E. McNeil, *Methods Mol Biol.*, 2011, **697**, 9-15.

100   S. Cui, T. Wang and X. Hu, *Spectrochim. Acta - Part A Mol. Biomol. Spectrosc.*, 2014, **133**, 778–784.

101   J. I. Bruce, R. S. Dickins, L. J. Govenlock, T. Gunnlaugsson, S. Lopinski, M. P. Lowe, D. Parker, R. D. Peacock, J. J. B. Perry, S. Aime and M. Botta, *J. Am. Chem. Soc.*, 2000, **122**, 9674–9684.

102   E. C. Wiener, M. C. Abadjian, R. Sengar, L. Vander Elst, C. Van

Niekerk, D. B. Grotjahn, P. Y. Leung, C. Schulte, C. E. Moore and A. L. Rheingold, *Inorg. Chem.*, 2014, **53**, 6554–6568.

103   P. Conte and P. Lo Meo, *Agronomy*, 2020, **10**, 1040.

104   J. R. Lakowicz, *Principles of fluorescence spectroscopy*, Springer, New York, 2006.

105   J. Stetefeld, S. A. McKenna and T. R. Patel, *Biophys. Rev.*, 2016, **8**, 409–427.

106   W. I. Goldburg, *Am. J. Phys.*, 1999, **67**, 1152–1160.

107   R. Marsalek, *APCBEE Procedia*, 2014, **9**, 13–17.

108   M. D. Pelta, G. A. Morris, M. J. Stchedroff and S. J. Hammond, *Magn. Reson. Chem.*, 2002, **40**, S147–S152.

109   M. Melia Rodrigo, A. J. M. Valente, M. C. F. Barros, L. M. P. Verissimo, C. Romero, M. A. Esteso and A. C. F. Ribeiro, *J. Chem. Thermodyn.*, 2014, **74**, 227–230.

110   M. W. Germann, T. Turner and S. A. Allison, *J. Phys. Chem. A*, 2007, **111**, 1452–1455.

111   S. V. Eliseeva and J. C. G. Bünzli, *Chem. Soc. Rev.*, 2010, **39**, 189–227.

112   B. Bagchi, *J. Chem. Phys.*, 2001, **115**, 2207–2211.

113   M. Andrews, A. J. Amoroso, L. P. Harding and S. J. A. Pope, *Dalt. Trans.*, 2010, **39**, 3407–3411.

114 P. O. Westlund, *Phys. Chem. Chem. Phys.*, 2010, **12**, 3136–3140.

115 M. Pasin and P. Sebastião, *FFC Appl. Note*.

116 D. H. Powell, O. M. Ni Dhubhghaill, D. Pubanz, L. Helm, Y. S. Lebedev, W. Schlaepfer and A. E. Merbach, *J. Am. Chem. Soc.*, 1996, **118**, 9333–9346.

117 M. Vallet-Regi, A. Rámila, R. P. Del Real and J. Pérez-Pariente, *Chem. Mater.*, 2001, **13**, 308–311.

118 M. Manzano, M. Colilla and M. Vallet-Regí, *Expert Opin. Drug Deliv.*, 2009, **6**, 1383–1400.

119 Y. Matsumoto, M. Harada, Y. Kanazawa, Y. Taniguchi, M. Ono and Y. Bito, *Sci. Rep.*, 2022, **12**, 1–9.

120 G. Blasse, *Chem. Phys. Lett.*, 1973, **20**, 573–574.

121 H. Samelson and A. Lempicki, *J. Chem. Phys.*, 1963, **39**, 110–112.

122 S. E. Plush and T. Gunnlaugsson, *Org. Lett.*, 2007, **9**, 1919–1922.

123 K. J. Miller, A. A. Saherwala, B. C. Webber, Y. Wu, A. D. Sherry and M. Woods, *Inorg. Chem.*, 2010, **49**, 8662–8664.

124 K. M. Payne, J. M. Wilds, F. Carniato, M. Botta and M. Woods, *Isr. J. Chem.*, 2017, **57**, 880–88.

125 S. Aime, M. Botta, M. Fasano, M. P. M. Marques, C. F. G. C. Geraldes, D. Pubanz and A. E. Merbach, *Inorg. Chem.*, 1997, **36**, 2059–2068.

126   S. Avedano, M. Botta, J. S. Haigh, D. L. Longo and M. Woods, *Inorg. Chem.*, 2013, **52**, 8436–8450.

127   S. Aime, M. Botta, Z. Garda, B. E. Kucera, G. Tircso, V. G. Young and M. Woods, *Inorg. Chem.*, 2011, **50**, 7955–7965.

128   S. P. Babailov, E. N. Zapolotsky, A. I. Kruppa, P. A. Stabnikov, I. A. Godovikov, E. V. Bocharov and E. S. Fomin, *Inorganica Chim. Acta*, 2019, **486**, 340–344.

129   J. Blahut, P. Hermann, Z. Tošner and C. Platas-Iglesias, *Phys. Chem. Chem. Phys.*, 2017, **19**, 26662–26671.

130   M. Pasin, R. Steele and G. Ferrante, *FFC Appl. notesFitteia*.

131   K. M. Payne, J. M. Wilds, F. Carniato, M. Botta and M. Woods, *Isr. J. Chem.*, 2017, **57**, 880–88.

132   J. R. H. Manning, C. Brambila and S. V. Patwardhan, *Mol. Syst. Des. Eng.*, 2021, **6**, 170–196.

133   M. H. Lim and A. Stein, *Chem. Mater.*, 1999, **11**, 3285–3295.

134   T. Xia, M. Kovochich, M. Liong, H. Meng, S. Kabehie, S. George, J. I. Zink and A. E. Nel, *ACS Nano*, 2009, **3**, 3273–3286.

135   H. Meng, M. Liong, T. Xia, Z. Li, Z. Ji, J. I. Zink and A. E. Nel, *ACS Nano*, 2010, **4**, 4539–4550.

136   H. Meng, M. Xue, T. Xia, Y. Zhao and F. Tamanoi, 2010, **36**, 12690–12697.

137 N. K. Mal, M. Fujiwara, Y. Tanaka, T. Taguchi and M. Matsukata, *Chem. Mater.*, 2003, **15**, 3385–3394.

138 S. Li, F. Wang, X.-W. He, W.-Y. Li and Y.-K. Zhang, *J. Mater. Chem. B*, 2018, **6**, 3358–3365.

139 L. Jin, X. Li, C.-H. Wong, T.-W. Ng, C.-F. Zhang and K. C.-F. Leung, *Int. J. Nanomedicine*, 2016, **11**, 2471.

140 Z. Li, J. Guo, M. Zhang, G. Li and L. Hao, *Front. Chem.*, 2022, **10**, 1–10.

141 N. Wartenberg, P. Fries, O. Raccurt, A. Guillermo, D. Imbert and M. Mazzanti, *Chem. - A Eur. J.*, 2013, **19**, 6980–6983.

142 J. Yin, X. Wang, H. Zheng, J. Zhang, H. Qu, L. Tian, F. Zhao and Y. Shao, *ACS Appl. Nano Mater.*, 2021, **4**, 3767–3779.

143 K. M. L. Taylor-Pashow, J. Della Rocca and W. Lin, *Nanomaterials*, 2011, **2**, 1–14.

144 F. Carniato, M. Muñoz-Úbeda, L. Tei and M. Botta, *Dalt. Trans.*, 2015, **44**, 17927–17931.

145 J. S. Beck, J. C. Vartuli, W. J. Roth, M. E. Leonowicz, C. T. Kresge, K. D. Schmitt, C. T. W. Chu, D. H. Olson, E. W. Sheppard, S. B. McCullen, J. B. Higgins and J. L. Schlenker, *J. Am. Chem. Soc.*, 1992, **114**, 10834–10843.

146 W. Stöber, A. Fink and E. Bohn, *J. Colloid Interface Sci.*, 1968, **26**, 62–

69.

147 Y. Yang and C. Yu, *Nanomedicine Nanotechnology, Biol. Med.*, 2016, **12**, 317–332.

148 Z. Li, J. C. Barnes, A. Bosoy, J. F. Stoddart and J. I. Zink, *Chem. Soc. Rev.*, 2012, **41**, 2590.

149 L. Pan, Q. He, J. Liu, Y. Chen, M. Ma, L. Zhang and J. Shi, *J. Am. Chem. Soc.*, 2012, **134**, 5722–5725.

150 V. A. Zeitler, C. A. Brown and C. A. Brown, *J. Phys. Chem.*, 1957, **61**, 1174–1177.

151 IR   spectrum   Sigma, https://www.sigmaaldrich.com/spectra/rair/RAIR011468.PDF (Accessed January 2023).

152 S. L. Zhou, S. W. Wang, G. S. Yang, X. Y. Liu, E. H. Sheng, K. H. Zhang, L. Cheng and Z. X. Huang, *Polyhedron*, 2003, **22**, 1019–1024.

153 R. L. Brutchey, J. E. Goldberger, T. S. Koffas and T. D. Tilley, *Chem. Mater.*, 2003, **15**, 1040–1046.

154 P. Atkinson, Y. Bretonnière, D. Parker and G. Muller, *Helv. Chim. Acta*, 2005, **88**, 391–405.

155 P. Atkinson, B. S. Murray and D. Parker, *Org. Biomol. Chem.*, 2006, **4**, 3166–3171.

156 P. Atkinson, Y. Bretonniere and D. Parker, *Chem. Commun.*, 2004, **4**,

438–439.

157   S. Aime, A. Barge, A. S. Batsanov, M. Botta, D. D. Castelli, F. Fedeli, A. Mortillaro, D. Parker and H. Puschmann, *Chem. Commun.*, 2002, **2**, 1120–1121.

158   R. S. Dickins, S. Aime, A. S. Batsanov, A. Beeby, M. Botta, J. I. Bruce, J. A. K. Howard, C. S. Love, D. Parker, R. D. Peacock and H. Puschmann, *J. Am. Chem. Soc.*, 2002, **124**, 12697–12705.

159   P. Atkinson, Y. Bretonniere and D. Parker, *Chem. Commun.*, 2004, **4**, 438–439.

160   S. Hirota, T. Sakai, N. Kitamura, K. Kubokawa, N. Kutsumura, T. Otani and T. Saito, *Tetrahedron*, 2010, **66**, 653–662.

161   A. G. Gavriel, F. Leroux, G. S. Khurana, V. G. Lewis, A. M. Chippindale, M. R. Sambrook, W. Hayes and A. T. Russell, *J. Org. Chem.*, 2021, **86**, 10263–10279.

162   J. Clayden, N. Greeves and S. Warren, *Organic Chemistry*, Oxford University Press, Oxford, 2001.

163   T. J. Clough, L. Jiang, K.-L. Wong and N. J. Long, *Nat. Commun.*, 2019, **10**, 1420.

8   Supplementary Information
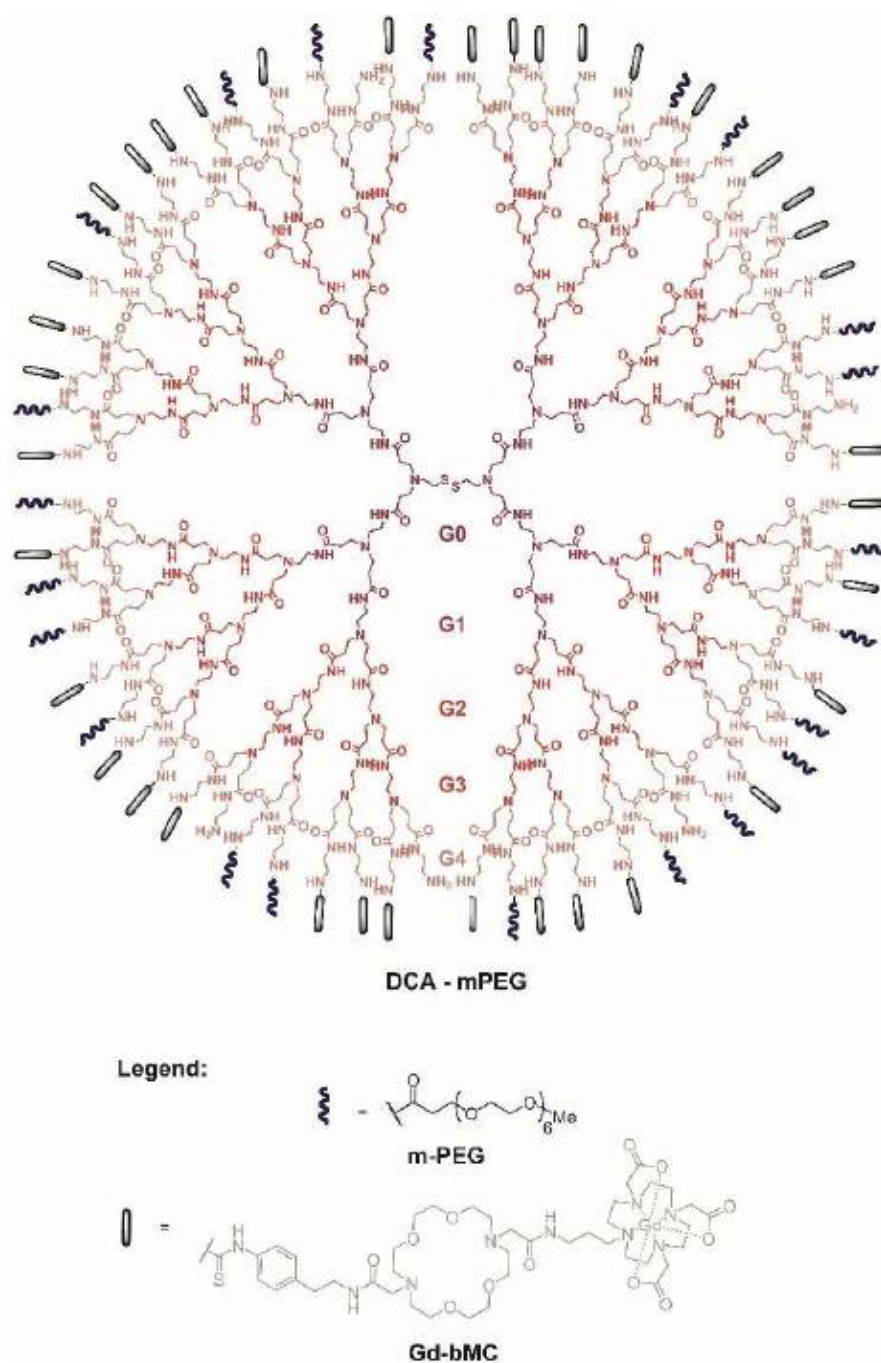
8.1   Supplementary Information for Chapter 3

Figure S1.   *Chemical structure of the G4 PAMAM + Gd-bMC.*[77]
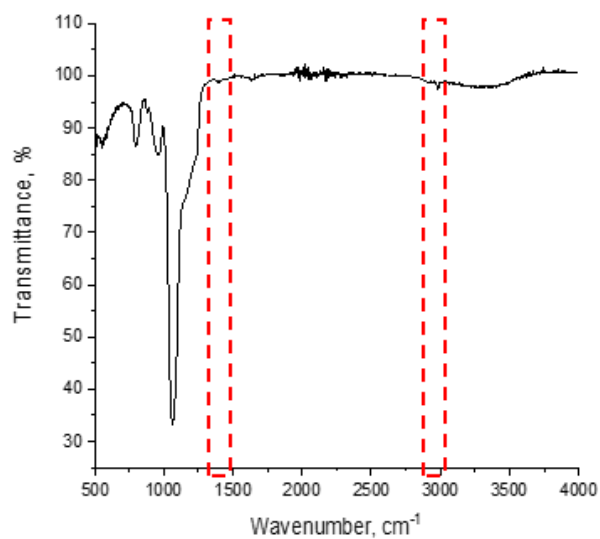
8.2 Supplementary Information for Chapter 4

Figure S2. *Infrared spectroscopy of Gd³⁺–DOTA –MSNs. The stretches at 790 and 2950 cm⁻¹ correspond to Si–O–Si asymmetrical and symmetrical stretch respectively. The red dash line represents the missing CTAB bands.*
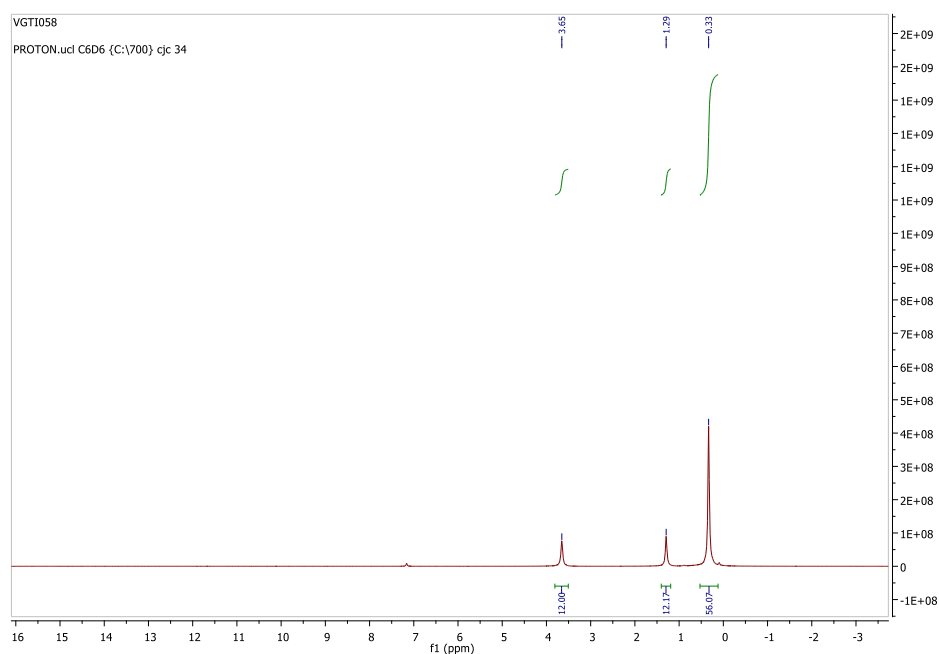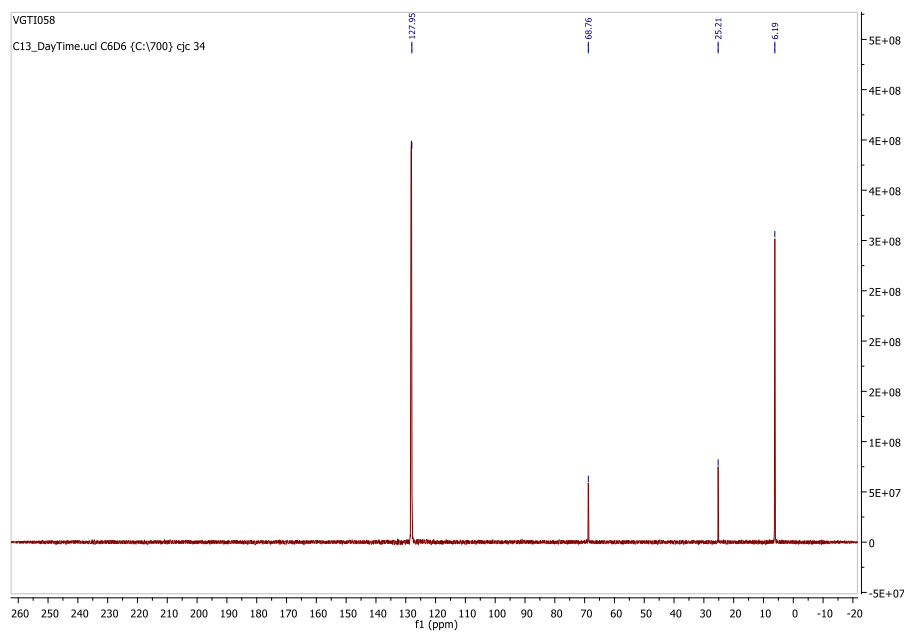

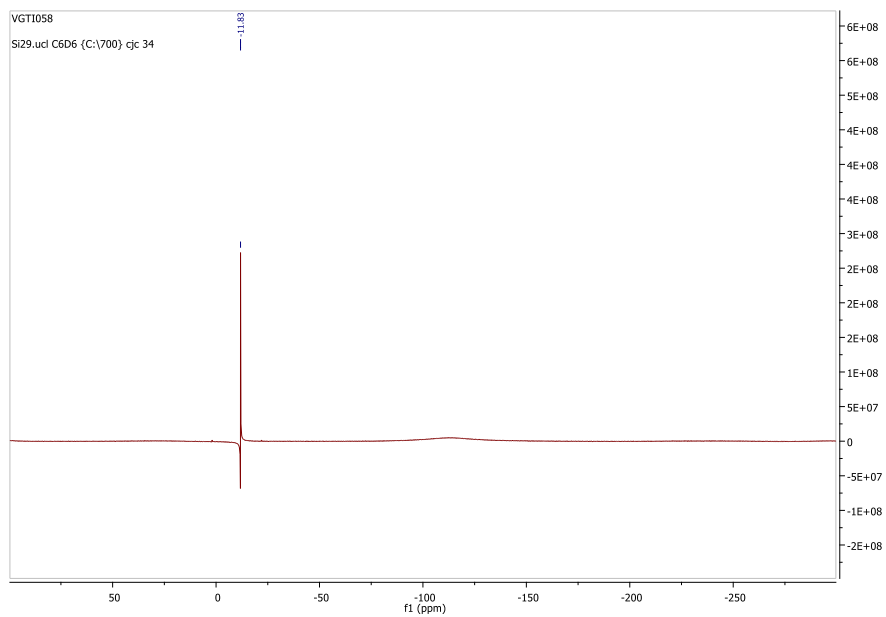***Figure S3.*** *¹H NMR of compound (2)*

Figure S4. *^{13}C NMR of compound (**2**)*

Figure S5. *^{29}Si NMR of compound (**2**)*

Figure S6.   *^{1}H NMR of Step 2*

Figure S7.   *^{29}Si NMR of synthetic Step 2*

8.3   Supplementary Information for Chapter 5
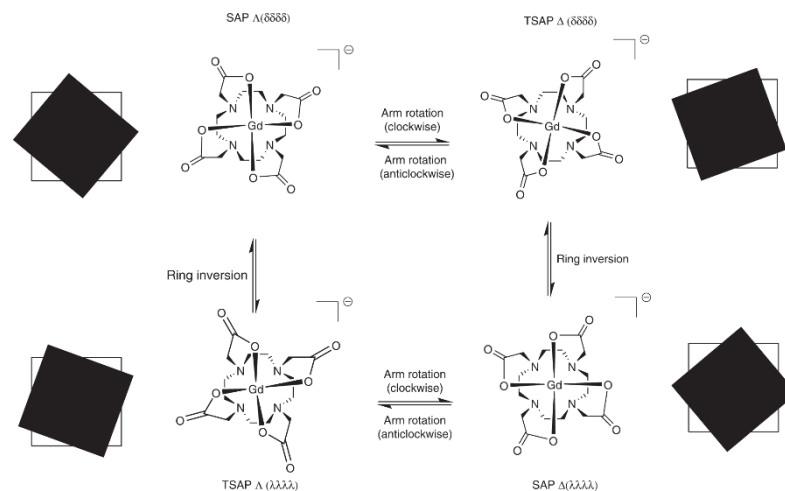

Figure S8.   *Square antiprismatic structure with 40° between their O4 and N4 planes adopted by L_1 and L_2.*[163]
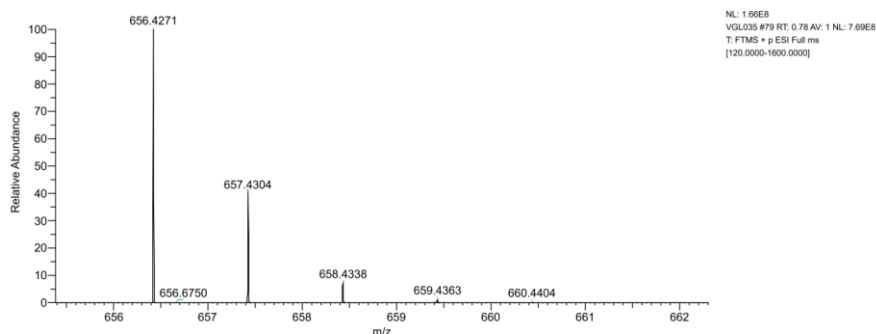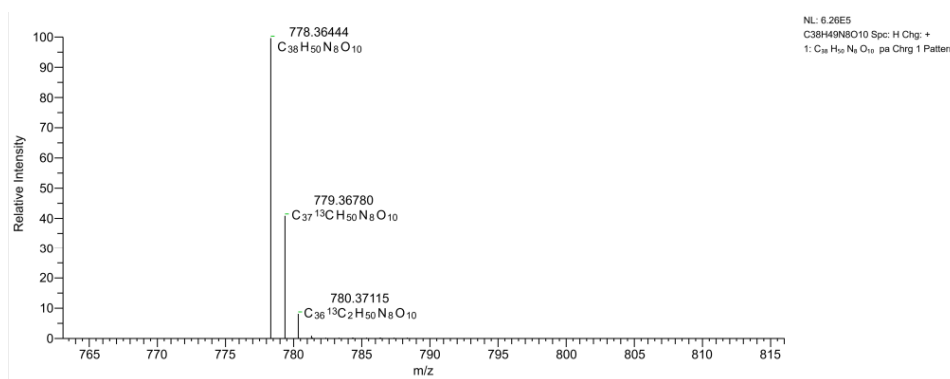

Figure S9.   *Mass spec L_2*

Figure S10.   *Mass Spec L_3*